

**Cardiff University**

**School of Chemistry**



**NEW DERIVATIVES OF NITROIMIDAZOLES FOR THE POTENTIAL  
IMAGING AND THERAPEUTIC TREATMENT OF HYPOXIC TISSUE**

A thesis submitted for the degree of Doctor of Philosophy

By:

**Nuha Mohammad Alghamdi**

August 2019

---

## ACKNOWLEDGEMENT

Firstly, I would like to express my sincere appreciation to my supervisor Dr. Angelo Amoroso for the continuous support of my Ph.D study, for his patience, motivation, time and immense knowledge. His supervision assisted me in all the time. I am also extremely grateful to my second supervise Dr. Ian Fallis for his advice, support and time. I am grateful for them both, this research would not have been possible without them.

My sincere thanks also go to Dr. Simon Pope, who help me to obtain luminescence data for my samples. Without his precious support it would not be possible to conduct this research. Thanks also goes to Prof. David Lloyd for his help in confocal imaging and Dr. Christopher von Ruland for TEM data of the nanoparticles. Without them this work could not be completed.

Huge thanks go to all the technical support staff, in the chemistry department of Cardiff University. None of this would have been possible without them.

My thanks also extended to all people in lab 1.24 for their inspiration, help and friendship throughout my research.

The financial support of Al Baha University, for this research is highly grateful.

My kindest gratitude and love go to my husband, Awn who share with me from the beginning the incredible experience of living and studying abroad. Despite his limited time as he is PhD student, He has always encouraged, inspired and supported me in all aspect of my life. I will be forever grateful for all that you have done.

Deepest thanks go to my daughter Mays, and my sons, Abdullah and Mohammad for their patience, love and understanding during my research. Without them I do not know if I would ever have made it.

Last but not the least, I would like to thank my beloved mother for her endless love and support, these thanks extended to my brothers and sisters for supporting me spiritually throughout my study and my life in general.

---

## ABSTRACT

There is an increasing interest in the development of drugs able to selectively kill and target hypoxic cells. Hypoxic cells are known to exist in numerous tumours and prevent the successful treatment by both radiotherapy and chemotherapy. The goal of this work was to develop a hypoxia-sensitive imaging agent that would identify hypoxic cells based on 2-nitroimidazole or 5-nitroimidazole and compare the reduction potential of these nitroimidazoles. The development of drugs able of selectively killing the hypoxic cells was the additional aim for this research.

In chapter 2, a series of novel luminescent compounds containing 2- nitroimidazole or metronidazole was synthesised as potential probes for use in confocal fluorescence microscopy. The luminescent properties of these compounds (the absorption and emission properties of the compounds) were investigated. The behaviour of these compound in cells were assessed using confocal fluorescence microscopy in order to determine the biological behaviour of these molecules in cells.

In chapter 3 two novel ligands based on terpyridine and containing 2- nitroimidazole or metronidazole was successfully synthesised. A series of novel Fe(II),Co(II), Ni(II), Pd(II), Cu(II) and Zn(II) complexes of these two ligands was synthesised and fully characterised. The electrochemical behaviour of the ligands and complexes was to be studied using cyclic voltammetry to determine the suitability for their intended application.

The synthesis of novel superparamagnetic iron oxide nanoparticles containing 2-nitroimidazole or 5-nitroimidazole were reported in Chapter 4. Fluorescently labelled (2/5) nitroimidazole conjugated to SPIONs were successfully synthesised as potential probes for use in MRI. The photophysical properties of these nanoparticles such as UV-vis and luminescence were investigated.

---

Chapter 5 summarises the conclusions that may be drawn from the three previous chapters. In addition, it highlights future work that is needed for each of these areas of research.

---

## TABLE OF CONTENTS

TITLE	PAGE
<b>New Derivatives of Nitroimidazoles for the potential Imaging and Therapeutic purpose of Hypoxic Tissue</b>	
<b>ACKNOWLEDGEMENT</b>	<b>i</b>
<b>ABSTRACT</b>	<b>ii</b>
<b>TABLE OF CONTENTS</b>	<b>iv</b>
<b>LIST OF TABLES</b>	<b>x</b>
<b>LIST OF FIGURES</b>	<b>xi</b>
<b>LIST OF ABBREVIATIONS</b>	<b>xvii</b>
<b>CHAPTER 1 Introduction and background theory</b>	<b>1</b>
1.1 Background of hypoxia	2
1.2 Introduction	3
1.2.1 Nitroimidazoles	5
1.2.1.1 Nitroimidazoles and nuclear medicine techniques	7
1.2.1.2 Nitroimidazoles and fluorescent probes	9
1.2.1.3 Coordination complexes of nitroimidazoles	11
1.3 Physical Techniques	13
1.3.1 Confocal Fluorescence Microscopy	13
1.3.2 Luminescence spectroscopy	14
1.3.2.1 Autofluorescence and Stokes Shift	17
1.3.3 Cyclic Voltammetry	18
1.4 Aims and Objectives	21

---

1.5	References	22
<b>CHAPTER 2</b>	<b>Fluorescently labelled nitroimidazole</b>	<b>25</b>
2.1	Introduction	26
2.2	Aims	28
2.3	Result and discussions:	30
2.3.1	Synthesis and characterisation of fluorophores (naphthalimide derivatives):	30
2.3.2	Fluorescently labelled Metronidazole	31
2.3.2.1	Tosylation and mesylation process of metronidazole	31
2.3.2.2	Attempted synthesis of 2-(2-((2-(2-methyl-5-nitro-1H-imidazol-1-yl)ethyl)amino)ethyl)-1H-benzo[de]isoquinoline-1,3(2H)-dione 2.5	32
2.3.2.3	Synthesis and characterisation of 2.7, 2.8, 2.9 and 2.10	34
2.3.3	Synthesis and characterisation of (E)-2-(2-((4-hydroxybenzylidene)amino)ethyl)-1H-benzo[de]isoquinoline-1,3(2H)-dione 2.11	39
2.3.4	Synthesis and characterisation of fluorescently labelled 2-nitroimidazole	40
2.3.4.1	Synthesis and characterisation of 2-nitromidazole	40
2.3.4.2	Attempted synthesised of 6-(2-nitro-1H-imidazol-1-yl)-1H,3H-benzo[de]isochromene-1,3-dione	41
2.3.4.3	Synthesis and characterisation of 1-(2-((tert-butyl dimethylsilyl)oxy)ethyl)-2-nitro-1H-imidazole, 2.12	44
2.3.4.4	Synthesis and characterisation of 2-(2-nitro-1H-imidazol-1-yl)ethan-1-ol, 2.13	44
2.3.4.5	Synthesis and characterisation of 2-(2-nitro-1H-imidazol-1-yl)ethyl methanesulfonate, 2.14	45
2.3.4.6	Synthesis and characterisation of 4-(2-(2-nitro-1H-imidazol-1-yl)ethoxy)benzaldehyde, 2.15	45
2.3.4.7	Synthesis and characterisation of (E)-2-(2-((4-(2-(2-nitro-1H-imidazol-1-	

	yl)ethoxy)benzylidene)amino)ethyl)-1H- benzo[de]isoquinoline-1,3(2H)-dione 2.16	47
2.3.5	Synthesis and characterisation of N-(2-(1,3-dioxo-1H- benzo[de]isoquinolin-2(3H)-yl) ethyl)-2-(2-nitro-1H- imidazol-1-yl) acetamide 2.19	50
2.4	Stability of the new compounds	52
2.5	Optical properties	53
2.5.1	UV-vis analysis	53
2.5.1.1	UV-vis analysis of 2.8, 2.9 and 2.10	53
2.5.1.2	UV-vis analysis of 2.16 and 2.17	55
2.5.2	Luminescence analysis	56
2.5.2.1	Luminescence analysis of 2.8, 2.9 and 2.10	56
2.5.2.2	Luminescence analysis of 2.16	57
2.5.2.3	Luminescence analysis of 2.17	58
2.6	Confocal Microscopy	59
2.7	Experimental section	65
2.7.1	Materials	65
2.8	References	77
<b>CHAPTER 3 Design and synthesis of metal complexes based on the terpyridine ligand and nitroimidazole</b>		<b>79</b>
3.1	Introduction	80
3.2	Introduction to terpyridines	83
3.2.1	Synthesis of pyridine	83
3.2.2	Synthesis of terpyridine	84
3.2.3	Coordination Chemistry of Terpy	87
3.2.4	Survey of the Co-ordination of Terpyridine to First Row Late Transition Metals	88
3.3	Result and Discussion	90
3.3.1	Synthesis and characterisation of Ligand 1 (L <sup>1</sup> )	91
3.3.2	Synthesis and characterization of ligand 2 (L <sup>2</sup> )	95
3.3.3	Complexes of L <sup>1</sup>	97
3.3.3.1	Bis( 4'-(4-(2-(2-methyl-5-nitro-1H-imidazol- 1-yl)ethoxy)phenyl)-2,2':6',2"-terpyridine) iron (II)tetra fluoroborate (1)	98

3.3.3.2	Bis( 4'-(4-(2-(2-methyl-5-nitro-1H-imidazol-1-yl)ethoxy)phenyl)-2,2':6',2''-terpyridine) nickel (II) tetra fluoroborate (2)	99
3.3.3.3	Bis( 4'-(4-(2-(2-methyl-5-nitro-1H-imidazol-1-yl)ethoxy)phenyl)-2,2':6',2''-terpyridine) cobalt (II) tetra fluoroborate (3)	100
3.3.3.4	Bis( 4'-(4-(2-(2-methyl-5-nitro-1H-imidazol-1-yl)ethoxy)phenyl)-2,2':6',2''-terpyridine) zinc (II)chloride(4)	101
3.3.3.5	Bis( 4'-(4-(2-(2-methyl-5-nitro-1H-imidazol-1-yl)ethoxy)phenyl)-2,2':6',2''-terpyridine) copper (II)chloride (5)	101
3.3.3.6	( 4'-(4-(2-(2-Methyl-5-nitro-1H-imidazol-1-yl)ethoxy)phenyl)-2,2':6',2''-terpyridine) palladium (II)acetate (6)	103
3.3.4	Spectroscopic Properties of L <sup>1</sup> complexes	104
3.3.4.1	Vibrational Spectroscopy	104
3.3.4.2	<sup>1</sup> H and <sup>13</sup> C NMR of Fe, Pd and Zn complexes of L <sup>1</sup>	105
3.3.4.3	Electronic Absorption Spectroscopy	108
3.3.5	Complexes of L <sup>2</sup>	110
3.3.5.1	Bis (4'-(4-(3-(2-nitro-1H-imidazol-1-yl)propoxy)phenyl)-2,2':6',2''- terpyridine) iron(II) tetra fluoroborate (7)	111
3.3.5.2	Bis (4'-(4-(3-(2-nitro-1H-imidazol-1-yl)propoxy)phenyl)-2,2':6',2''- terpyridine) Ni (II)tetra fluoroborate (8)	111
3.3.5.3	Bis (4'-(4-(3-(2-nitro-1H-imidazol-1-yl)propoxy)phenyl)-2,2':6',2''- terpyridine) cobalt (II)tetra fluoroborate (9)	112
3.3.5.4	Synthesis of bis (4'-(4-(3-(2-nitro-1H-imidazol-1-yl)propoxy)phenyl)-2,2':6',2''- terpyridine) copper(II)chloride (10)	112
3.3.5.5	Synthesis of 4'-(4-(3-(2-nitro-1H-imidazol-1-yl)propoxy)phenyl)-2,2':6',2''- terpyridine zinc (II) chloride (11)	113
3.3.5.6	Synthesis of 4'-(4-(3-(2-nitro-1H-imidazol-1-yl)propoxy)phenyl)-2,2':6',2''- terpyridine palladium (II) acetate (12)	114
3.3.6	Spectroscopic Properties of L <sup>2</sup> complexes	115

---

3.3.6.1	Vibrational Spectroscopy	115
3.3.6.2	$^1\text{H}$ and $^{13}\text{C}$ NMR of Fe, Pd and Zn complexes of $\text{L}^2$	116
3.3.6.3	Electronic Absorption Spectroscopy	120
3.4	Electrochemistry	122
3.4.1	Summary of electrochemistry	129
3.5	Experimental Section	130
3.6	References	144
<b>CHAPTER 4 Fluorescently labelled SPION-coated silica nanoparticles for cell multifunctional imaging probes</b>		<b>148</b>
4.1	Introduction	148
4.2	Theory	150
4.2.1	Nuclear Magnetic Resonance	150
4.2.2	Magnetic Resonance Imaging (MRI)	151
4.2.3	Physical Principles of Magnetism	154
4.2.4	Superparamagnetism	155
4.2.5	Positron Emission Tomography (PET)	156
4.3	SPIONs synthesis	159
4.4	Stabilization of Magnetic Particles	161
4.4.1	Polymer stabilisers	161
4.4.2	Organic Stabilisers	162
4.4.3	Inorganic Material	163
4.4.3.1	Silica coating	163
4.5	Literature Review	164
4.6	Results and discussion	168
4.6.1	Synthesis and characterisations of fluorescently labelled SPIONs	169
4.6.2	Coordination of CA1 with $\text{Cu}^{+2}$	172
4.6.3	Synthesis and characterisation of fluorescently labelled SPIONs conjugated to 5-nitroimidazole	174
4.6.4	The synthesis and characterisation of fluorescently labelled SPIONs conjugated to 2-nitroimidazole	181

---

4.6.4.1	Synthesis and characterisation of 4.14 and 4.15	182
4.6.4.2	Synthesis and characterisation of 4.12 and 4.13	184
4.6.5	SPION diameter analysis	185
4.6.5.1	Transmission electron microscopy (TEM)	185
4.6.6	Optical properties	188
4.6.6.1	UV-Vis absorption spectroscopy	188
4.6.6.2	Luminescence spectroscopy	191
4.6.7	Inductively coupled plasma atomic emission spectroscopy (ICP-AES)	195
4.6.7.1	MP-AES Analysis of Cu <sup>+2</sup> Incorporation	195
4.7	Experimental procedures	197
4.8	References	203
<b>CHAPTER 5</b>	<b>Conclusion</b>	<b>207</b>
5.1	References	212

---

## LIST OF TABLES

TABLE NO.	TITLE	1.	PAGE
<b>Chapter 2</b>			
Table 1:	Luminescence properties of 8, 9, 10, 16 and 17		59
Table 1:	IR stretching frequencies of L <sup>1</sup> and its complexes		105
Table 2:	<sup>1</sup> H NMR spectra of free L <sup>1</sup> , Fe, Pd, and Zn complexes		107
Table 3:	Electronic spectral assignments for L1 and complexes		109
Table 4:	IR stretching frequencies of L2 and its complexes		115
Table 5:	<sup>1</sup> H NMR spectra of free L <sup>2</sup> , Fe, Pd, and Zn complexes		118
Table 6:	Electronic spectral assignments for L2 and complexes		121
Table 7:	Electrochemical parameter for the redox processes exhibited by L1, L2 and their complexes in anhydrous DCM solution (supporting electrolyte: [Bu <sub>4</sub> N][PF <sub>6</sub> ](0.1 mol dm <sup>-3</sup> ); T:20 0C. Measured at 0.1 Vs <sup>-1</sup>		130
<b>Chapter 4</b>			
Table 1:	Calculated diameters of APTES@SPIONs, CA1, CA2, 4.9 and 4.10; particle sizes were calculated using ImageJ software, taking 25 measurements for each sample		186
Table 2:	Luminescence properties of CA1, CA2, 4.10 and 4.13		194
Table 3:	Standard Cu <sup>2+</sup> solutions		196
Table 4:	The percentage of Cu <sup>2+</sup> which coordinated to the nanoparticle.		197

---

## LIST OF FIGURES

FIGURE NO.	TITLE	2.	PAGE
Figure 1.1:	Selective structure of bioreductive prodrugs		3
Figure 1.2:	Structure of 2-nitroimidazole (Azomycin) and metronidazole.		5
Figure 1.3:	The mechanism of the bioreductive metabolisms of nitroimidazoles in both normixic and hypoxic cells. <sup>25,26</sup>		6
Figure 1.4:	Some structures of 2-nitroimidazole derivative doped with fluorine-18		8
Figure 1.5:	Chemical structures of selected radiopharmaceuticals for imaging hypoxia.		9
Figure 1.6:	Chemical structures of selected radiopharmaceuticals for imaging hypoxia. <sup>54</sup>		10
Figure 1.7:	2-Nitroimidazole–naphthalimide derivatives. <sup>55,56</sup>		11
Figure 1.8:	Selective structures of metal-nitroimidazole complexes.		13
Figure 1.9:	The Jablonski diagram.		15
Figure 1.10:	Cyclic voltammogram potential sweep reproduced from reference <sup>69</sup>		19
Figure 1.11:	Typical voltammogram in CV experiment. <sup>69</sup>		20
Figure 2.1:	Naphthalimides moiety containing one or two side chain of 2-nitroimidazole <sup>11</sup>		26
Figure 2.2:	Representation of some metronidazole -Based Schiff Base compounds		27
Figure 2.3:	Synthetic route for producing fluorescently labelled nitroimidazoles		29
Figure 2.4:	Path way synthesis of n-(2-Aminoethyl)-1,8 naphthalimide 1 , 2-(2-aminoethyl)-6-chloro-1H-benzo[de]isoquinoline-1,3(2H)-dione 2.2 and 2-(2-aminoethyl)-6-morpholino-1H-benzo[de]isoquinoline-1,3(2H)-dione 2.3		31
Figure 2.5:	Tosylation 2.4 and mesylation 2.6 of metronidazole.		32
Figure 2.6:	Attempted synthesis of 2-(2-((2-(2-methyl-5-nitro-1H-imidazol-1-yl)ethyl)amino)ethyl)-1H-benzo[de]isoquinoline-1,3(2H)-dione 2.5		33
Figure 2.7:	Multi steps attempted synthesis of 2-(2-((2-(2-methyl-5-nitro-1H-imidazol-1-yl)ethyl)amino)ethyl)-1H-benzo[de]isoquinoline-1,3(2H)-dione		34
Figure 2.8:	Synthesis of compounds: 2.8, 2.9 and 2.10		35

Figure 2.9: High resolution mass spectrometry of 2.9	38
Figure 2.10: <sup>1</sup> H NMR analysis for 2.7 (blue), 2.8 (red), 2.9 (green) and 2.10(purple)	39
Figure 2.11: Synthesis of (E)-2-(2-((4-hydroxybenzylidene)amino)ethyl)-1H-benzo[de]isoquinoline-1,3(2H)-dione 2.11	40
Figure 2.12: Synthesis of 2-aminoimidazole and 2-nitroimidazole.	41
Figure 2.13: Attempted synthesis of 6-(2-nitro-1H-imidazol-1-yl)-1H,3H-benzo[de]isochromene-1,3-dione	43
Figure 2.14: Synthetic pathway of 2.15, 2.16 and 2.17	43
Figure 2.15: <sup>1</sup> H NMR analysis for 2.15 (blue), 2.16(green) and 2.17(red)	49
Figure 2.16: <sup>13</sup> C NMR analysis for 2.15 (blue), 2.16(red) and 2.17(green)	49
Figure 2.17: General mechanism of formation Schiff base compounds	50
Figure 2.18: Synthetic scheme for producing 2.19	51
Figure 2.19: UV-vis absorption profiles of 2.8 ( $2.4 \times 10^{-5}$ mol dm <sup>-3</sup> ), 2.9 ( $2.6 \times 10^{-5}$ mol dm <sup>-3</sup> ) and 2.10 ( $2.9 \times 10^{-5}$ mol dm <sup>-3</sup> ) in chloroform. Inset shows the UV-vis absorption spectrum of metronidazole in DMSO at $8.5 \times 10^{-6}$ M and 2.7 in DCM at $1.3 \times 10^{-5}$ M	53
Figure 2.20: UV-vis absorption profiles of 2.16 ( $2.4 \times 10^{-5}$ mol dm <sup>-3</sup> ) and 2.17 ( $2.8 \times 10^{-5}$ mol dm <sup>-3</sup> ) in chloroform. Inset shows the UV-vis absorption spectrum of 2-nitroimidazole in DMSO at $5.6 \times 10^{-6}$ M and 2.15 in DCM at $1.3 \times 10^{-5}$ M	55
Figure 2.21: luminescence analysis of 2.8 (blue), 2.9 (red) and 2.10 (grey). Inset: excitation spectra	56
Figure 2.22: luminescence analysis of 2.16. Inset: excitation spectra at $\lambda_{exc} = 358$	57
Figure 2.23: luminescence analysis of 2.17. Inset: excitation spectra at $\lambda_{exc} = 436$	58
Figure 2.24: A thin slice electron micrograph of <i>S. pombe</i> . N = nucleus, M= mitochondria, EDV/ETV = electron dense/transparent vacuoles; bar = 1 $\mu$ m. <sup>37</sup>	61
Figure 2.25: <i>C. Utilis</i> N = nucleus, M= mitochondria, V = vacuole ; bar = 1 $\mu$ m. <sup>37</sup>	61
Figure 2.26: Top left: autofluorescence of <i>S. Pombe</i> . Bottom left fluorescence image of <i>S. Pombe</i> exposed to A and B for 10 minutes. Images to the right are the brightfield images of each fluorescent image.	62
Figure 2.27: Top left: autofluorescence of <i>S. Pombe</i> . Bottom left: fluorescence image of <i>S. Pombe</i> exposed to A and B for 18 hours. Images to the right are the brightfield images of each fluorescent image	64
Figure 3.1: Zn-terpy with adenine complex	81

Figure 3.2: Cu-terpy with conjugated morpholine	81
Figure 3.3: Zn-terpy with adenine complex	83
Figure 3.4: Krohnke's synthetic pathway for terpyridine production	84
Figure 3.5: Pott's synthetic pathway for terpyridine production	85
Figure 3.6: Jameson's synthetic pathway for terpy formation	86
Figure 3.7: Synthetic scheme of Raston reaction for terpyridine synthesis	86
Figure 3.8: Synthetic scheme of Stille cross-coupling for terpyridine synthesis	87
Figure 3.9: Alteration in configuration of free and bound ligand	88
Figure 3.10: Distortion in the bond angles of ligand due to complexation	88
Figure 3.11: Illustration presenting the length of central nitrogen-metal bond compared to the terminal bonds	90
Figure 3.12: Illustration presenting attempted synthesis of 4'-(4-(2-(2-methyl-5-nitro-1H-imidazol-1-yl)ethoxy)phenyl)-2,2':6',2''-terpyridine L <sup>1</sup>	91
Figure 3.13: The synthetic pathway of 4'-(4-(2-(2-methyl-5-nitro-1H-imidazol-1-yl)ethoxy)phenyl)-2,2':6',2''-terpyridine L <sup>1</sup>	93
Figure 3.14: <sup>1</sup> H NMR analysis of L <sup>1</sup> in DMSO-d <sub>6</sub>	94
Figure 3.15: Crystal structure of 4'-(4-(2-(2-methyl-5-nitro-1H-imidazol-1-yl)ethoxy)phenyl)-2,2':6',2''-terpyridine	95
Figure 3.16: the synthetic pathway of 4'-(4-(3-(2-nitro-1H-imidazol-1-yl)propoxy)phenyl)-2,2':6',2''-terpyridien L <sup>2</sup>	96
Figure 3.17: <sup>1</sup> H NMR analysis of L <sup>2</sup> in DMSO-d <sub>6</sub>	97
Figure 3.18: Experimental and theoretical mass spectra of 3: (A) theoretical spectrum, (B) experimental spectrum	100
Figure 3.19: Experimental and theoretical mass spectra of 5: (A) theoretical spectrum, (B) experimental spectrum	102
Figure 3.20: <sup>1</sup> H NMR spectra of free L <sup>1</sup> (blue), Fe (red), Pd (green), and Zn (purple) complexes in d <sub>6</sub> -DMSO	106
Figure 3.21: Aromatic region of <sup>1</sup> H NMR spectra of free L <sup>1</sup> (blue), Fe (red), Pd (green), and Zn (purple) complexes in d <sub>6</sub> DMSO	107
Figure 3.22: <sup>13</sup> C NMR spectra of L <sup>1</sup> (blue) and its iron complex (red)	108
Figure 3.23: UV-vis absorption profiles of L <sup>1</sup> and its complexes	109
Figure 3.24: UV-vis absorption profiles 3 (left) and 5 (right)	110
Figure 3.25: Experimental and theoretical mass spectra of 10: (A) theoretical spectrum, (B) experimental spectrum	113

Figure 3.26: $^1\text{H}$ NMR spectra of free $\text{L}^2$ (blue), 7 (red), 12 (green), and 11 (purple) complexes in $d_6$ DMSO	117
Figure 3.27: The aromatic region $^1\text{H}$ NMR spectra of free $\text{L}^2$ (blue), Fe (red), Pd (green), and Zn (purple) complexes in $d_6$ DMSO	117
Figure 3.28: $^{13}\text{C}$ NMR spectra of $\text{L}^2$ (blue) and 7 (red)	119
Figure 3.29: $^{13}\text{C}$ NMR spectra of 12	119
Figure 3.30: $^1\text{H}$ NMR spectra of 1 (blue) and 7 (red)	120
Figure 3.31: $^{13}\text{C}$ NMR spectra of 1 (blue) and 7 (red)	120
Figure 3.32: UV-vis absorption profiles of $\text{L}^2$ and its complexes	121
Figure 3.33: UV-vis absorption profiles of 9 (left) and 10 (right)	122
Figure 3.34: Cyclic voltammogram for $\text{L}^1$ vs (Fc+/Fc)	123
Figure 3.35: Cyclic voltammogram for complex 1 vs (Fc+/Fc)	124
Figure 3.36: Cyclic voltammogram for complex 2 vs (Fc+/Fc)	125
Figure 3.37: Cyclic voltammogram for complex 3 vs (Fc+/Fc)	126
Figure 3.38: Cyclic voltammogram for $\text{L}^2$ vs (Fc+/Fc)	126
Figure 3.39: Cyclic voltammogram for complex 7 vs (Fc+/Fc)	127
Figure 3.40: Cyclic voltammogram for complex 9 vs (Fc+/Fc)	128
Figure 3.41: Cyclic voltammogram for complex 12 vs (Fc+/Fc)	128
Figure 3.42: Cyclic voltammogram for complex 11 vs (Fc+/Fc)	129
Figure 4.1: MRI scans (a), PET images(b), dual MRI/PET images	149
Figure 4.2: (a) Precession of the net magnetisation of the proton around z-axis, (b) the effect of the radio frequency pulse on the net magnetisation, (c) the alteration of transverse resonance over time, and (d) longitudinal signal amplitude over time <sup>15</sup>	150
Figure 4.3: $\text{Gd}^{3+}$ bound by 1,4,7,10-tetraazacyclododecane-1,4,7,10-tetraacetic acid (DOTA)	153
Figure 4.4: Inverse spinel unit cell of magnetite <sup>23</sup>	155
Figure 4.5: Illustration of the physical principle of Positron Emission Tomography (PET) <sup>27</sup>	157
Figure 4.6: 18-Fluorodeoxyglucose (FDG)	158
Figure 4.7: Structure of $^{64}\text{Cu}$ -ATSM	158
Figure 4.8: Published work on SPION synthesis by three different pathways up until 2011. Source: Institute of Science and Technology	160

Figure 4.9: Dextran and polyethylene glycol	162
Figure 4.10: Some examples of monomeric species used for coating iron oxide nanoparticles	162
Figure 4.11: (3-Aminopropyl) triethoxysilane	163
Figure 4.12: Illustration of MRI and PET dual functional probe based on SPIONs <sup>71</sup>	165
Figure 4.13: Diagram of chelator-based radio labelling SPIONs with <sup>89</sup> Zn and DFO as a chelator <sup>70</sup>	165
Figure 4.14: Diagram of the SPIONs@SiO <sub>2</sub> with Cu <sup>+2</sup> and EDTA as a chelator	166
Figure 4.15: Illustration of tri-modal nanoparticles	167
Figure 4.16: IR spectra of uncoated SPIONs, APTES-coated SPIONs, CA1 and CA2	172
Figure 4.17: The suggested mechanism of 4.8	176
Figure 4.18: High resolution mass spectrometry 4.8, (A) theoretical spectrum, (B) experimental spectrum	178
Figure 4.19: Infra-red spectrum of uncoated SPIONs (A) and 4.11 (B)	178
Figure 4.20: Infrared spectra of 4.9 (A) and 4.10 (B)	180
Figure 4.21: Infra-red spectrum of uncoated SPIONs (A) and 4.15 (B)	183
Figure 4.22: Infrared spectrum of 4.12 (A) and 4.13 (B)	185
Figure 4.23: Transmission electron microscopy for SPIONs@APTES, CA1, 4.9, 4.10 and CA2. The scale bar on the bottom right of each image corresponds to 100 nm.	187
Figure 4.24: UV-vis absorption spectra of CA1 and CA2	188
Figure 4.25: UV-vis absorption spectra of 4.9 and 4.10. Inset shows the UV-vis absorption spectrum of metronidazole in DMSO at $8.5 \times 10^{-6}$ M and 2.7 in DCM at $1.3 \times 10^{-5}$ M	189
Figure 4.26 : UV-vis absorption spectra of 4.12 and 4.13. Inset shows the UV-vis absorption spectrum of 2-nitroimidazole in DMSO at $5.6 \times 10^{-6}$ M and 2.15 in DCM at $1.3 \times 10^{-5}$ M	190
Figure 4.27: Luminescence spectra for CA1, inset shows excitation spectra of CA1	191
Figure 4.28: Luminescence spectra for CA2, inset shows excitation spectra of CA2	192
Figure 4.29: Luminescence spectroscopy of 4.10, inset shows excitation spectra of 4.10	193

---

Figure 4.30: Luminescence spectroscopy of 4.13, inset shows excitation spectra of  
4.13 194

---

## LIST OF ABBREVIATIONS

SPECT	Single Photon-Emission Computed Tomography
PET	Positron Emission Tomography
MRI	Magnetic resonance imaging
CT	Computed tomography
CV	Cyclic Voltammetry
NMR	Nuclear Magnetic Resonance
IR	Infrared
HRMS	High resolution spectrometry
UV-Vis	Ultraviolet-visible
MHz	Mega hertz
ppm	Part per million
V	Volt
mV	millivolt
CT	charge transfer
$\lambda_{\max}$	Wavelength of the band at maximum absorption
$T_R$	repetition time
$T_E$	Echo time
$T_1$	Spin lattice relaxation
$T_2$	Spin-spin relaxation
R	relaxivity
$\text{cm}^{-1}$	Reciprocal centimetres/wavenumber
m/z	Mass/charge ratio

---

Mw	Molecular weight
g	Gram
mmol	Millimole
L <sup>1</sup>	4'-(4-(2-(2-Methyl-5-nitro-1H-imidazol-1-yl)ethoxy)phenyl)-2,2':6',2''-terpyridine
L <sup>2</sup>	4'-(4-(3-(2-Nitro-1H-imidazol-1-yl)propoxy)phenyl)-2,2':6',2''-terpyridine
SPIONs	Superparamagnetic iron oxide nanoparticles
CA1	Naphthalimie-edta-APTES@Fe <sub>3</sub> O <sub>4</sub>
CA2	Morpholine-naphthalimie-edta-APTES@Fe <sub>3</sub> O <sub>4</sub>
EDTA	Ethylenediaminetetraacetic acid
CHCl <sub>3</sub>	Dichloromethane
AEDTA	EDTA bisanhydride
APTES	(3-Aminopropyl) triethoxysilane
DMF	N,N'-Dimethylformamide
DMSO <sub>4</sub>	Dimethyl sulfoxide
DCM	Dichloromethane
DMSO <sub>4</sub> -d <sub>6</sub>	Deuterated dimethyl sulfoxide
D <sub>2</sub> O	Deuterated water
CDCl <sub>3</sub>	Deuterated dichloromethane
EtOH	Ethanol
ES-MS	Electrospray mass spectrometry
MLCT	Metal-ligand charge transfer (state)
ml	Millilitre

# **CHAPTER 1**

## **Introduction and Background Theory**

## CHAPTER 1 Introduction and background theory

### 1.1 Background of hypoxia

Oxygen plays a vital role in supporting all physiological functions in the living cells. This is because it works as a terminal electron acceptor in oxidative phosphorylation.  $O_2$  is provided through the respiration process and it is transported all over the living cells as *oxyhemoglobin* ( $O_2Hb$ ). Limitations in oxygen quantity from the vascular supply affect the biological functions of the tissues and this gives rise to hypoxic areas. Hypoxia is a situation of limited  $O_2$  used to support the metabolism occurring in human cells. The level of  $O_2$  in hypoxia lies between the typical physiological concentration of oxygenation (*normoxia*) and the total absence of oxygen (*anoxia*). The oxygen partial pressure ( $pO_2$ ), which is a crucial element of the biological state of a tissue, comes from the balance between oxygen supply and its intake. During medical conditions such as tumours or cardiovascular diseases, the provision of  $O_2$  is disturbed which is linked with a reduction in  $pO_2$  and consequently, hypoxia. Therefore, hypoxia can be defined according to the concentration terms of  $O_2$  (e.g. ppm  $O_2$ ).<sup>1</sup>

Hypoxia can happen quickly when blood vessels are interrupted, such as in a stroke or traumatic wound. It can also occur gradually during the development of some vascular diseases. In general, during the development of some diseases, hypoxia can reduce the probability of an effective treatment. The diffusional walls that stop oxygen from accessing the hypoxic cells of tumours are able to prevent the transmission of reactive medications into the hypoxic tissues. In the case of tumours, the swift growth of some tumours can outgrow their vascular supply, causing local hypoxia, necrosis and increasing the risk of metastasis. This can result in an alteration, which has an undesirable consequence on their response to

therapy and in diagnoses. Therefore, hypoxic tumour cells are three times less responsive towards radiation treatment which relies on a sufficient oxygen concentration for radical generation than normoxic cells. They are more resistant to some chemotherapeutic medications.<sup>2,3</sup>

## 1.2 Introduction

The estimation of the oxygenation level of solid tumours is a significant goal of radiopharmaceutical study. This is because hypoxic tissue is more resistant to conventional radiotherapy and chemotherapy.<sup>2</sup> Therefore, the evaluation of hypoxia becomes a significant factor in therapeutic plans for enhancing better clinical results. One approach to examine hypoxic cells is by using a probe that selectively targets hypoxic cells. It should also be transported to the whole tissue equally without relying on vascular flow and most importantly, to selectively bind to hypoxic cells. There are five categories of bioreductive compounds that have been selectively reduced and trapped in hypoxic regions that have been studied; nitro groups, quinones, aromatic *N*-oxides, aliphatic *N*-oxides and transition metals.<sup>4,5</sup> Some examples of these bioreductive drugs are as shown in **Fig 1.1**.

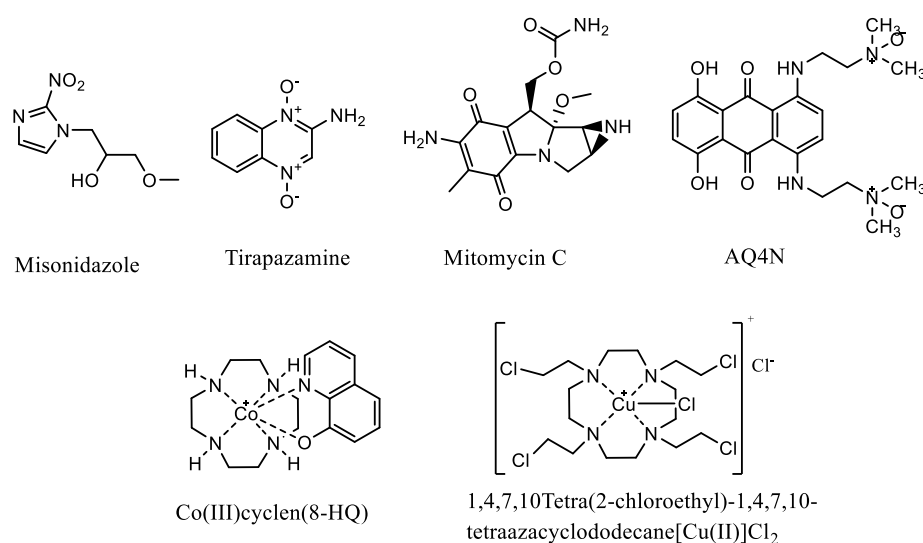


**Figure 1.1: Selective structure of bioreductive prodrugs**

The typical mechanism for these chemical moieties in hypoxic cells involves the reduction of these compounds by a one-electron reduction to form radical species. In the presence of oxygen, these radical species undergo a re-oxidation process to produce a superoxide. The failure of the re-oxidation step causes hypoxia-selective cell killing. This is because the free radicals are more toxic than the superoxide moiety or unreacted bioreductive prodrugs.<sup>4</sup>

The effect of the presence of oxygen on the inhibition of the drugs during the redox mechanism was studied for the first time on nitro compounds.<sup>6</sup> Then it was revealed that nitroimidazoles demonstrated hypoxia-selective cytotoxicity.<sup>7</sup>

Quinones such as mitomycin (**Fig 1.1**) also undergo bioreductive process under hypoxic conditions through a redox cycling mechanism.<sup>8</sup> However, this mechanism occurs with two sequential one-electron reductions. It reduces initially to the semiquinone and then to the hydroquinone.<sup>9</sup>

Aromatic *N*-oxide such as tirapazamine (**Fig 1.1**) reduces to oxidizing hydroxyl or benzotriazinyl radicals arising naturally from the tirapazamine radical in hypoxic tissue through a one-electron reduction to a DNA-damaging free radical.<sup>10,11</sup> The bioreduction of aliphatic *N*-oxides to the corresponding tertiary amines occurs via two-electron reductases by oxygen not by redox cycling,<sup>12,13</sup> for example, AQ4N (**Fig 1.1**).

Transition metals such as cobalt (III)<sup>14,15</sup> and copper (II)<sup>16</sup> can also be bioactivated in the hypoxic regions by the one-electron reductions of the metals to unstable cobalt (II) or copper (I) complexes. These then disconnect and release cytotoxic ligands. Co(III)cyclen (8-HQ) and 1,4,7,10-Tetra(2-chloroethyl)-1,4,7,10-tetraazacyclododecane[Cu(II)]Cl<sub>2</sub> are examples of these complexes (**Fig 1.1**).

In this research, we will only focus on nitroimidazoles, which are well-known for hypoxia directing. This will be discussed in more detailed in the next section.

### 1.2.1 Nitroimidazoles

After the discovery of the effect of 2-nitroimidazole (azomycin) (**Fig 1.2**) against anaerobic infections by Nakamura in 1955, many nitroimidazole analogues have been synthesized as antibiotics against anaerobic bacteria and protozoa.<sup>17</sup> The exceptional properties of nitroimidazoles in hypoxic conditions has drawn attention to studying the behaviour of the molecules to be used in low oxygenated tissue as hypoxic sensitizers. This is in order to enhance the radiation responsiveness of hypoxic cells to radiation and chemical therapy.<sup>18</sup> The concept of using nitroimidazoles for imaging hypoxic tissue has been studied for more than 20 years. However, this idea has only been applied practically in the last decade.<sup>19</sup>

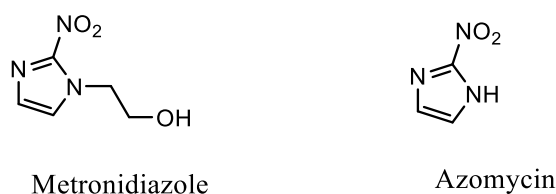


**Figure 1.2: Structure of 2-nitroimidazole (Azomycin) and metronidazole.**

Nitroimidazoles have been investigated intensively for tumour hypoxia via nucleophilic covalent binding to proteins in conditions of low pO<sub>2</sub> (<1.5% O<sub>2</sub>).<sup>20,17</sup> The function of 2-nitroimidazole in hypoxic cells was discovered by Varghese *et al* in 1976. The main factor that determines the diffusion of the nitroimidazoles is the lipophilicity of the compounds. The mechanism of the selective binding of nitroimidazoles to poorly oxygenated cells involves the transfer of one electron to the ring of nitrogen via enzymes and cytochromes. The nitro group of nitroimidazole increases the electron affinity of the molecule, thus giving it suitable reactivity. The nitroimidazoles within the cells behave differently depending on the concentration of O<sub>2</sub> in the cells. The nitro group of this compound experiences an enzymatic reduction resulting in forming a radical anion NO<sub>2</sub><sup>-</sup>. In the normoxic condition, this radical reacts directly with O<sub>2</sub> to form terminal electron products that turn back into nitroimidazole,

resulting in the diffusion of imidazole out of the cell. This step occurs as the electronic affinity of  $O_2$  is higher than that of the nitro group. However, in hypoxic cells, further reductions take place, producing reactive intermediates (amino-) that are able to combine with cellular macromolecules and that form (non-diffusible) molecules trapped in hypoxic cells<sup>21,22,23</sup> The mechanism of a bioreductive metabolism of nitroimidazoles in both normoxic and hypoxic cell mechanisms was considered to be clinical with the development of 5- and 2-nitroimidazoles as radiosensitizers.<sup>24</sup> Compounds with free radicals produced by ionizing radiation or by bioreductive procedure imitate the action of oxygen, forming adducts with nucleophilic cellular macromolecules, a procedure which results in radiosensitization. This stops or slows the access of nitroimidazole (**Fig 1.3**).

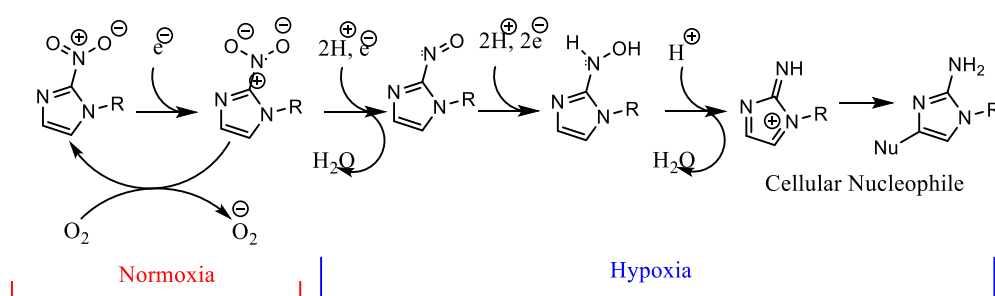


**Figure 1.3: The mechanism of the bioreductive metabolisms of nitroimidazoles in both normoxic and hypoxic cells.**<sup>25,26</sup>

Another nitroimidazole has presented the potential to be used as a hypoxia tracer such as metronidazole. Metronidazole, a 5-nitroimidazole derivative (**Fig 1.2**), is an antiprotozoan and an antibacterial drug. It has been also used as a radiosensitizer for hypoxic cells in pilot radio therapeutic trials. Metronidazole and its derivatives have been studied in both *vivo* and *vitro* as radiosensitizing hypoxia.<sup>26</sup> They have presented selective toxicity towards hypoxic tumour cells.<sup>7,27</sup> Moreover, they possess effective cytotoxic activity in anaerobic but not aerobic microorganisms.<sup>28</sup>

However, 2-nitroimidazole is one of the most widely studied of the nitroimidazole moiety. This is because 2-nitroimidazole has a higher reduction potential (-0.39 V) than 5-nitroimidazole (-0.47 V). The higher value of reducing the potential demonstrates the higher potential to gain electrons and to consequently show a greater reduction ability. Thus 2-nitroimidazole has a higher tendency to undergo the bioreductive process and to accumulate in low oxygenated tissues.<sup>29</sup> It also shows the low toxicity and antibiotic properties in oxygenated tissue.<sup>30</sup>

#### 1.2.1.1 Nitroimidazoles and nuclear medicine techniques

Nitroimidazole has been used widely *in vivo* to increase the effectiveness of radiotherapy by imitating the radiosensitizing features of O<sub>2</sub>.<sup>31,32</sup> Non-invasive imaging of tumor hypoxia is currently being studied using either the nuclear scintigraphy of iodine-labelled 2-nitroimidazoles or PET imaging of <sup>18</sup>F-labelled reagents.<sup>33</sup>

#### Nitroimidazole-containing PET Probes

There are many hypoxia tracers based on 2-nitroimidazoles which are incorporated with PET isotopes and fused with gamma-emitting radionuclides.<sup>34,35,36</sup> The initial development of nitroimidazole for *in-vivo* imaging involved radiohalogenated derivatives of misonidazole. For example, <sup>18</sup>F-FMISO (fluoromisonidazole), <sup>18</sup>F-FAZA (fluoroazomycin arabinoside), <sup>18</sup>F-EF5 (pentafluoropropylacetamide), <sup>18</sup>F-FETNIM and <sup>18</sup>F-HX4 (**Fig 1.4**).<sup>37,38,39,40</sup> All of these compounds are acting similarly in the hypoxic cells. However, they are different in lipophilicity. PET probes decay by emitting a positron which collides with an electron to produce gamma rays which are tracked by the PET scanner.<sup>41</sup>



2-nitroimidazole-based  $^{99m}\text{Tc}$  was synthesised and evaluated in hypoxic tumour cells *in vitro*.  $^{99m}\text{TcO}(\text{PnAO-1-(2-nitroimidazole)})$  BMS181321 (Fig 1.5) was the first  $^{99m}\text{Tc}$ -labelled 2-nitroimidazole complex to be used for imaging hypoxia.<sup>44</sup> The 5-nitroimidazole has been also labelled with Tc-99m. For example, Tc-Ntm-2 (Fig 1.5) was produced by labelling 2-amino-3-{1-(2-(2-methyl-5-nitro-1H-imidazole-1-yl)ethyl)1H-triazole-4-yl}triazole-4-yl}propanoic acid Ntm-2 with  $^{99m}\text{T}$  ion.<sup>43,45,46,47,48</sup> The low cost, availability and an ideal half-life of 6 hours are the most distinguished features of using  $^{99m}\text{Tc}$  in tracking ischemic tissue.<sup>43</sup> There are many examples of technetium-labelled nitroimidazole complexes reported in an excellent previous review.<sup>49</sup>

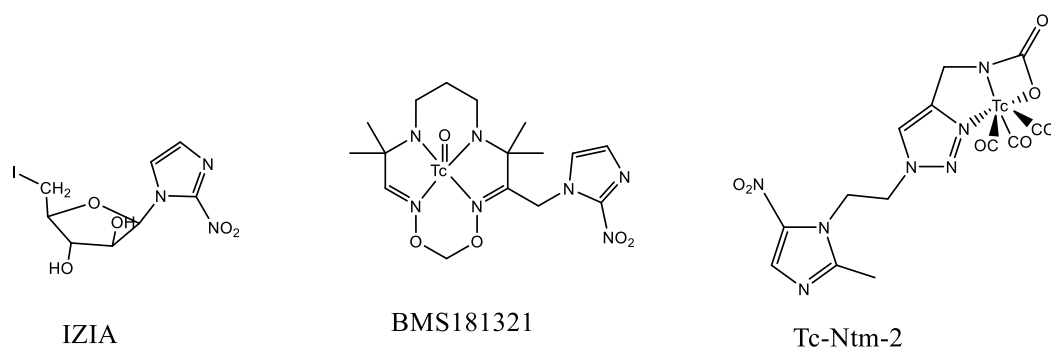


**Figure 1.5: Chemical structures of selected radiopharmaceuticals for imaging hypoxia.**

### 1.2.1.2 Nitroimidazoles and fluorescent probes

Fluorescence imaging has been employed as a diagnostic technique to display various biological processes.<sup>50</sup> Owing to the advantages of fluorescent probes, such as simplicity, high spatial resolutions and possible non-invasive *in vivo* imaging (problematic and depth limited), numerous small molecule fluorescent probes have been developed for detecting low oxygenated tissues and some have proposed the use of fluorescent nitroaromatics.<sup>51, 52</sup> The nitro group quenches the fluorescence of the aromatic ring system in the normoxic

environment. However, referring to the bioreduction of the nitro group in ischemic cells, the molecule develops more fluorescence.<sup>53</sup>

There are several compounds that consist of 2-nitroimidazole and a fluorescent ring system in their molecular structure.<sup>54</sup> The bioreductive processes of these compounds was predicted to show fluorescence in both normoxic and hypoxic cells. However, because of the existence of the nitroimidazole moiety, they would be selectively located in the hypoxic cells. The authors synthesised a series of 2-nitroimidazoles based on several fluorescent compounds. For example, naphthalimide (A), coumarin (B), indolizine (C) and bimane (D) (**Fig 1.6**). When these compounds were studied in V79 Chinese hamster cells, coumarin and bimeane presented more than a 5-fold and 17-fold hypoxic/normoxic fluorescence differential.<sup>54</sup>

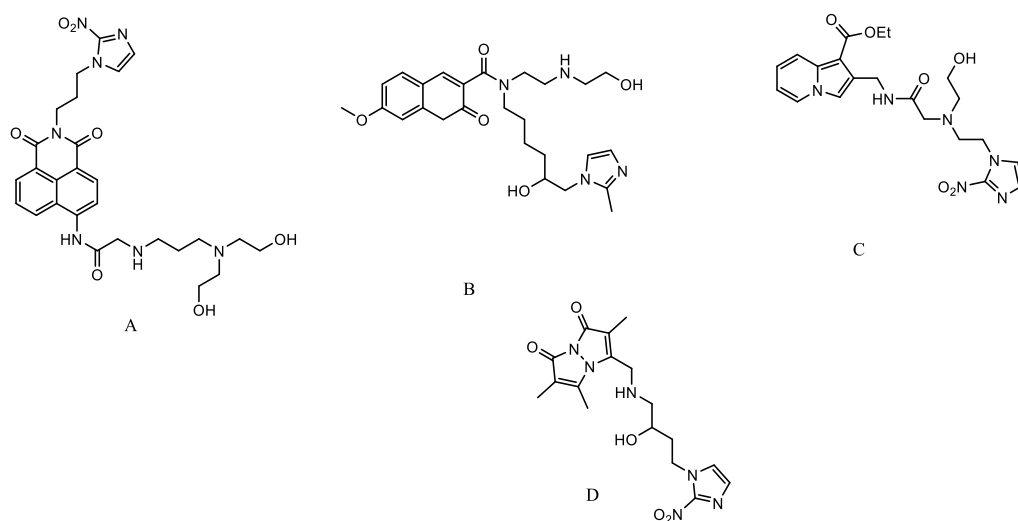


**Figure 1.6: Chemical structures of selected radiopharmaceuticals for imaging hypoxia.**<sup>54</sup>

In this research, we will only focus on 1,8-naphthalimide and its derivatives as a fluorescence moiety to be linked to 2-nitroimidazole in order to form a detecting agent for hypoxia.

There are also several compounds that have 2-nitroimidazoles and 1,8-naphthalimides as prepared by Qian and their co-workers. The strategies of the synthesis of these compounds was reported for the first time by the author which includes 1,8-naphthalimides functionalised with two 2-nitroimidazole moieties (**Fig 1.7**). The investigation of these compounds in V79

Chinese hamster, CHO and 95D cells exhibited a large degree of fluorescence differential between the hypoxic and normoxic cells as evidenced by fluorescence microscopy.<sup>55</sup>

A series of 1,8-naphthalimides functionalised with 2-nitroimidazole moiety were synthesised and evaluated to see if they exhibited increased fluorescence in response to hypoxic conditions (**Fig 1.7**).<sup>56</sup> Fluorescently labelled 2-nitroimidazoles have been the subject of an excellent review.<sup>25</sup>

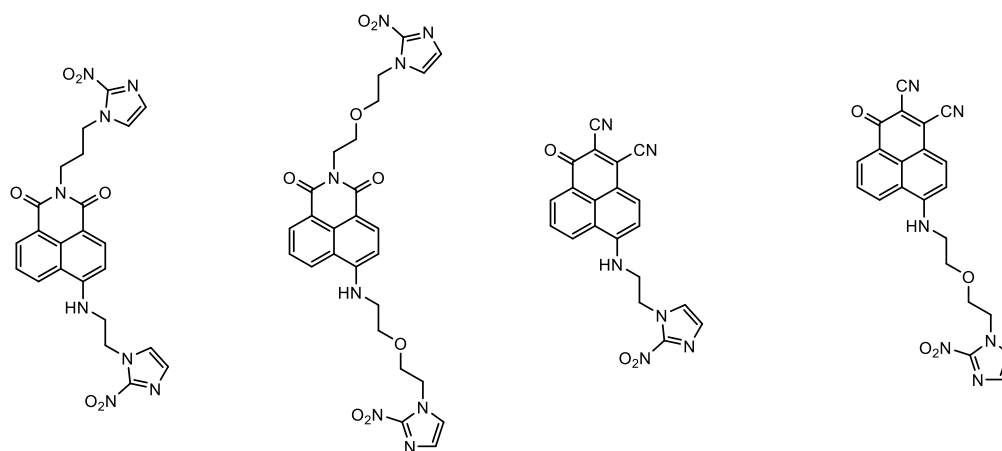


**Figure 1.7: 2-Nitroimidazole–naphthalimide derivatives.**<sup>55,56</sup>

### 1.2.1.3 Coordination complexes of nitroimidazoles

Nitroimidazoles are coordinated to some metal ions via a bifunctional chelator.

Organometallic complexes that include nitroimidazoles may possess one or more reducible centres, for example, nitroimidazole and, depending on the redox chemistry of the metal centre, the metal. This potentially provides better selectivity for low oxygenated cells than either the reducible metal complex alone or the nitroimidazole without a metal ion. Some of the metal ions can be replaced with a radiometallic nuclide in order to produce an imaging agent for hypoxic tissue that is suitable for the PET technique.<sup>49</sup>

Some examples of Cu and Re complexes based on nitroimidazole and a very brief description of their biological activities will be discussed in the following section. However, more detail on nitroimidazole complexes has been extensively reviewed elsewhere.<sup>49</sup>

Nitroimidazole moieties have been conjugated to Cu(II) ion and <sup>46</sup>Cu radiometallic nuclides using bithiosemicarbazones as a ligand to produce a series of complexes that have two reducible sites. An example includes the nitroimidazole derivative (Cu-H2ATSM/A-1) (**Figure 1.4**). *In vitro* studies presented a rapid uptake of this complex by hypoxic cells.<sup>57</sup>

Polyazamacrocyclic is another class of bifunctional ligand that was conjugated to 2-nitroimidazole and coordinated with Cu and <sup>46</sup>Cu radioisotopes for the delineation of tumour hypoxia. There are a range of azomycin-cyclams Cu(II) complexes such as <sup>64</sup>Cu-FC-323 (**Fig 1.8**). Some of them showed good hypoxia-marking potential for tumour cells *in vitro*.<sup>58</sup>

There are several examples of azomycin rhenium complexes that have been reported.<sup>59,60</sup> Mie *et al* reported on the Re-labelled marker MAMA-AA-B2NIL containing 2-nitroimidazole moieties respectively. This complex bears more than just bioreductive moiety. The uptake studies show a high tumour tissue ratio which makes it suitable as a hypoxia marker.

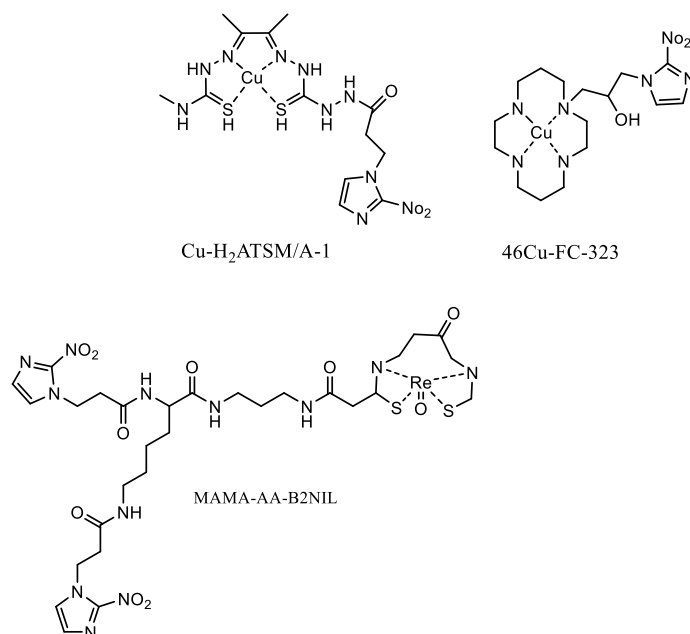


Figure 1.8: Selective structures of metal-nitroimidazole complexes.

### 1.3 Physical Techniques

#### 1.3.1 Confocal Fluorescence Microscopy

Confocal fluorescence microscopy is an important device in biochemical investigations. It is very sensitive, and it has the advantage of being less expensive than other imaging techniques.

High resolution spectra at the nanometre scale can be acquired using this method.

Luminescent moieties can be used to produce a contrast in the image attained and to provide comprehensive data at the sub-cellular level.

The principle of a fluorescent microscope is like that of a typical optical microscope.

However, the only difference between them is that the sample is irradiated with photons of a particular wavelength instead of using ambient light. The wavelength is chosen according to the specific fluorophore that is being studied. The optimal wavelength will be selected in order to induce the most intense emission.<sup>65</sup>

### 1.3.2 Luminescence spectroscopy

#### Luminescence

Luminescence is the emission of light by a molecule in the absence of heat. This can be described using the Jablonski diagram (**Fig 1.9**). The electron of a molecule absorbs the photon of the electromagnetic radiation, and then it is promoted from a ground state singlet ( $S_0$ ) to an excited state singlet ( $S_1$ ). Luminescence occurs when the electron returns to the energetic ground state and emits its excess energy as a photon.

In this decay, the excited species follows two possible pathways, either reductive/non-radiative decay pathways or chemical change.

The reductive pathway includes fluorescence and phosphorescence, as shown in the Jablonski diagram (**Fig 1.9**).

Succeeding the excitation through the absorption of a photon by the electron, namely the excited state made during this process, is unstable and it possesses high energy. Thus, it is important to undergo the deactivation procedure. First, the energy is lost from the excited state singlet to the lowest vibrational level of the excited state through internal relaxation. This process is a non-radiative procedure; it is known as an internal conversion (IC) on the Jablonski diagram. In this stage, the molecule remains in an excited state and it has excess energy. The molecule can lose its excess energy through several methods such as molecular rotations, vibration, heat and light. When this energy is lost as released light, it is called luminescence. This emitted light can be released through two routes, fluorescence or phosphorescence. Both pathways show initial intramolecular energy transfer procedures when the preliminary excess energy is lost through a non-radiative process. There is another non-

reductive pathway that is completed with luminescence and this is known as quenching. This includes the interaction with another molecule, known as a quencher.

## Fluorescence

Fluorescence involves an instant emission of light directly after it is absorbed causing the electron returning from an excited state to the ground state. This process is fast as it is spin-allowed. The process of spin-allowed is comparatively fast and it shows a luminescence lifetime with a range of  $10^{-9}$  to  $10^{-6}$  seconds. A molecule which displays fluorescent photophysical properties is stated as a fluorophore such as poly aromatic hydrocarbons or heterocyclic molecules.

The fluorescence emission occurs as a result of a procedure of three steps inside the molecule. This can be clarified through the simple electronic state diagram of Jablonski (**Fig 1.9**).

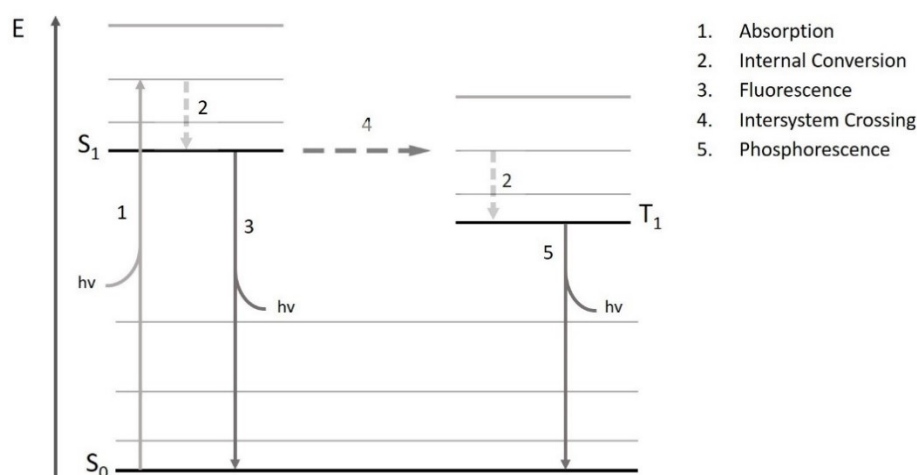


**Figure 1.9: The Jablonski diagram.**

### Step 1: Excitation

The fluorophore absorbs the light energy from the external laser in the form of photons ( $h\nu_{ExA}$ ). This leads to the creation of an excited singlet electronic state ( $S_1$ ). This step differentiates fluorescence from chemiluminescence. In the case of the chemiluminescence, the excited state is formed by the chemical reaction.

### Step 2 Excited-State Lifetime

As a part of this process, the excited state is relative, and it remains only for the nanosecond range. During this time, the fluorophore experiences different conformational transformations that could interact as well with its surroundings in several ways. Accordingly, the excited state can be affected by these interactions. The energy of ( $S_1$ ) is partly degenerated, whereas a relaxed singlet state is created. Moreover, in the first step, not every excited molecule goes back to the ground electronic state ( $S_0$ ) through the emitting of the photons. There are several processes that the excited molecule can follow in order to lose excess energy such as fluorescence resonance energy transfer (FRET) and intersystem crossing. The ratio of the number of photons emitted through fluorescence related to the number of photons absorbed is known as 'fluorescence quantum yield'.

### Step 3: Fluorescence Emission

The energy of the photon after the emission is lower than its original state, owing to the partial dissipation of energy. Therefore, it possesses lower energy and a longer wavelength (red- shifted). The alteration in both energy and wavelength can be expressed by this equation ( $h\nu_{EX}-h\nu_{EM}$ ).

The other parameter in fluorescence is Stokes shift, which simplifies the recording of the photon emission against a low background.

## **Phosphorescence**

Before the explanation of the phosphorescence process, intersystem crossing (ISC) should be understood. This phenomenon happens because the energy of the excited triplet state is lower than that of the energy of the excited singlet state, causing a reverse spin of the excited electron. When the electronic levels of the triplet state interfere with the excited singlet state,

this phenomenon occurs. ISC arises in molecules with a high degree of spin-orbit coupling. This includes the overlapping of the orbital angular momentum and the spin angular momentum of the electron, which permits a forbidden transition between the singlet and triplet states. ISC increases with the mass of the atoms and this can be seen in the heavy atom effect, which is more common in 2<sup>nd</sup> and 3<sup>rd</sup> row transition metals. From this excited triplet state, the electron slowly returns to the singlet ground state, losing energy by emitting a photon. As this process is 'forbidden', it occurs slowly and shows luminescence lifetimes within the range of microseconds up to thousands of seconds.

#### 1.3.2.1 Autofluorescence and Stokes Shift

There are some problems associated with using fluorescence microscopy, such as autofluorescence. Typically, many natural species of the cells have a variety of fluorophores and phosphors which tend to have a small Stokes' shift and a small emission lifetime.

Autofluorescence becomes challenging if the fluorescence of the biological species and that of a fluorophore of interest are emitted at a similar wavelength.<sup>66</sup>

Self-quenching is another problematic issue in fluorescence microscopy. This occurs when there is no considerable difference in wavelength between the absorbed and emitted light of the probe. This causes the emitted light to be reabsorbed and consequently, it reduces the emission intensity in the resulting image.<sup>67</sup>

Autofluorescence may be filtered out from the desired signal by using molecules that have a large Stokes shift and/or a large emission lifetime.<sup>68</sup> This criteria should be considered for designing probes for fluorescence microscopy.

### 1.3.3 Cyclic Voltammetry

This technique was used to study the electrochemical properties of the molecules. This includes the study of the electron transfer and the transport properties of the electrolysis reactions. This is in addition to the reduction and oxidation processes of the molecular species. An electrochemical cell consists of three types of electrodes: working, counter (auxiliary) and reference. These electrodes are linked to potentiostat and the parameter of the CV experiment can be chosen using the potentiostat software.

The working electrode is where the electrochemical action happens. The reference electrode such as (Ag/AgCl) possesses a stable equilibrium potential and it is used as a reference for the applied potential of the other electrodes in the electrochemical cell. A counter electrode such as platinum wire is used to close the electrical circuit. That is because when the potential is applied to the working electrode, the reduction or an oxidation process of the analyte takes place. Then the current starts to flow between the working electrode and the counter electrode.

Through a CV experiment, the electrons transfer from the electrode to the analyte and ions migrate in the solution to balance the charge and to complete the electrical circuit.

A supporting electrolyte is added to the solvent in order to support the reduction of the solution resistance. This mixture is generally called the electrolyte solution.

The fundamentals of CV include plunging a working electrode into a solution of the compound of interest, applying the potential and measuring the change in current. The potential is typically swept as given in (**Fig 1.10**).

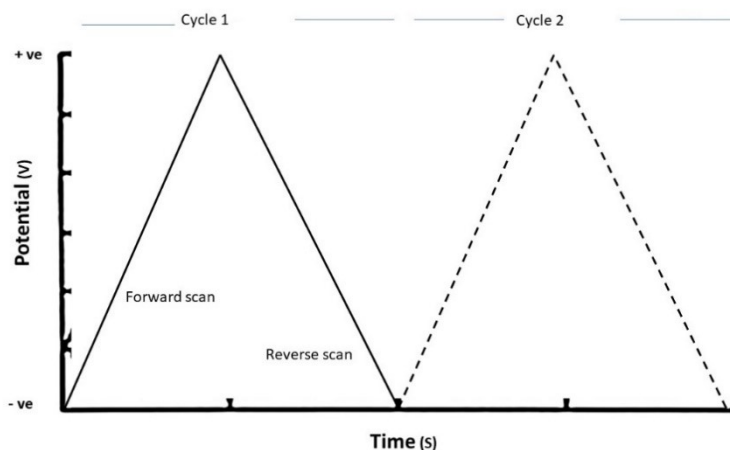
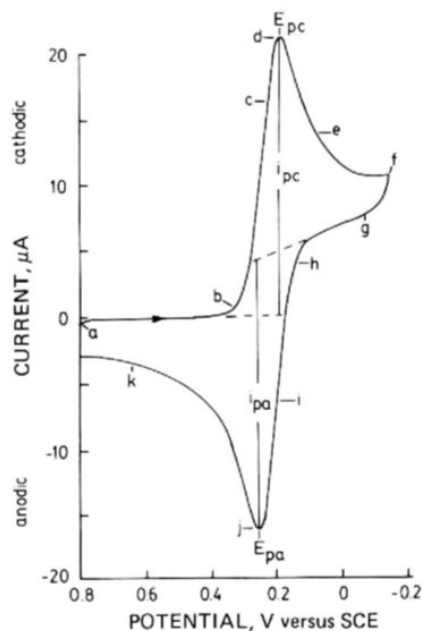


Figure 1.10: Cyclic voltammogram potential sweep reproduced from reference <sup>69</sup>

This graph shows two cycles; each cycle involves a forward and a backward scan. **Fig 1.11** displays a cyclic voltammogram experiment. There are two different factors that control the current. The migration of the redox moiety to the surface of the electrode and the electron transfer reaction. The rate constant for the reduction process is dependent on the applied potential. As a result of the reduction of the species adjacent to the electrode, there will be a less reducible species in the locality of the electrode. For this reason, the peak of the forward scan has a maximum current more than that of the reverse scan. For the reversible reduction, the two peaks are identical. That is because there is a large amount of the reducible species adjacent to the electrode surface which then oxidises back to the starting material. In the reversible redox- process, the concentration of both the reduced and oxidized forms of the analyte are stable. It occurs regularly to form equilibrium at the electrode surface. In this case, the current depends only on the diffusion of the electroactive species.<sup>70</sup> The difference between the peak potentials in the reversible reduction is equal to  $59/n$  mV and it is termed Nernstian according to the Nernst equation:

$$(a) \quad E = E^0 - (RT/nF) \ln ([R]/ [O])$$

F is Faraday's constant, R is the universal gas constant, T is the temperature, n is the number of electrons and [R], [O] are the concentrations of the reduction and oxidation species respectively.  $E^0$  is the standard reduction potential; it is valued as the average of the peak voltages and it is usually termed  $E_{1/2}$ .  $E_{1/2} = (E_{pa} + E_{pc})/2$ .



(b)

Figure 1.11: Typical voltammogram in CV experiment.<sup>69</sup>

If the electron transfer rate is slow, this leads to a large separation of reduction and separating peaks. This separation increases if the scan rate increases. That is because extreme electrode potentials are required to drive the electron transfer in each direction and to record the current on the potentiostat. This process is referred to as quasi-reversible.

In the irreversible process, the reduction and oxidation peaks do not overlap at all and in some cases, there is no corresponding back peak. This is because the reduced species is not able to oxidise into its original form. The peak height can be affected by the scan rate according to the Randles- Sevcik equation.<sup>69</sup>

$$(c) \quad i_p = (2.67 \times 10^5) n^{3/2} A D_0^{1/2} \nu^{1/2} C_0$$

$i$  represents the current (amps),  $n$ : number of electrons,  $A$ : electrode area ( $\text{cm}^2$ ),  $D$ : the diffusion coefficient ( $\text{cm}^2/\text{sec}$ ),  $v$  scan rate ( $\text{V}/\text{sec}$ ) and  $C_0$ : the bulk concentration (mole/ $\text{cm}^3$ ).

According to this equation, the current is directly proportional to the square root of the scan rate. In the reversible system, the ratio of the cathodic current  $i_{pc}$  to the anodic current  $i_{pa}$  should be  $=1$ .<sup>69</sup>

#### 1.4 Aims and Objectives

An interest in the development of drugs that is able to selectively kill hypoxic cells is increasing.<sup>61,62</sup> Hypoxic cells are known to exist in numerous tumours. They are a marker for a poor outcome. They prevent both the radiotherapy and chemotherapy of cancer.<sup>63,64</sup> The goal of this work was to develop hypoxia-sensitive imaging agents that would identify hypoxic cells based on 2-nitroimidazole or 5-nitroimidazole. Another goal was to compare the reduction potential of the nitroimidazoles. The last objective of this work was to develop complex bases on nitroimidazole that have more than one reducible centre potential to selectively kill hypoxic cells.

## 1.5 References

- 1 H.-J. Machulla, *Imaging of hypoxia: tracer developments*, Springer Science & Business Media, 2013, vol. 33.
- 2 A. I. Minchinton and I. F. Tannock, *Nat. Rev. Cancer.*, 2006, **6**, 583-592.
- 3 J. M. Brown and W. R. Wilson, *Nat. Rev. Cancer.*, 2004, **4**, 437-477.
- 4 W. R. Wilson and M. P. Hay, *Nat. Rev. Cancer.*, 2011, **11**, 393-410.
- 5 A. Rauth, R. Marshall and B. Kuehl, *Cancer Metastasis Rev.*, 1993, **12**, 153–164.
- 6 R. P. Mason and J. L. Holtzman, *Biochem. Biophys. Res. Commun.*, 1975, **67**, 1267–1274.
- 7 J. K. Mohindra and A. M. Rauth, *Cancer Res.*, 1976, **36**, 930-936
- 8 K. A. Kennedy, S. Rockwell and A. C. Sartorelli, *Cancer Res.*, 1980, **40**, 2356-2360.
- 9 N. R. Bachur, S. L. Gordon and M. V Gee, *Cancer Res.*, 1979, **76**, 954-957.
- 10 G. Chowdhury, V. Junnotula, J. S. Daniels, M. M. Greenberg and K. S. Gates, *J. Am. Chem. Soc.*, 2007, **129**, 12870-12877.
- 11 S. S. Shinde, M. P. Hay, A. V Patterson, W. A. Denny and R. F. Anderson, *J. Am. Chem. Soc.*, 2009, **131**, 14220–14221.
- 12 L. Patterson, *Cancer Metastasis Rev.*, 1993, **12**, 119–134.
- 13 W. R. Wilson, P. Van Zijl and W. A. Denny, *Int. J. Radiat. Oncol.*, 1992, **22**, 693–696.
- 14 D. C. Ware, B. D. Palmer, W. R. Wilson and W. A. Denny, *J. Med. Chem.*, 1993, **36**, 1839-1846.
- 15 G.-O. Ahn, K. J. Botting, A. V Patterson, D. C. Ware, M. Tercel and W. R. Wilson, *Biochem. Pharmacol.*, 2006, **71**, 1683–1694.
- 16 L. L. Parker, S. M. Lacy, L. J. Farrugia, C. Evans, D. J. Robins, C. C. O’Hare, J. A. Hartley, M. Jaffar and I. J. Stratford, *J. Med. Chem.*, 2004, **47**, 5683-5689.
- 17 A. Nunn, K. Linder and H. W. Strauss, *Eur. J. Nucl. Med.*, 1995, **22**, 265–280.
- 18 J. M. Brown, *Int. J. Radiat. Oncol.*, 1989, **16**, 987–993.
- 19 J. D. Chapman, A. J. Franko and J. Sharplin, *Br. J. Cancer.*, 1981, **43**, 546-550.
- 20 S. Kizaka-Kondoh and H. Konse-Nagasawa, *Cancer Sci.*, 2009, **100**, 1366–1373.
- 21 J. E. Biaglow, M. E. Varnes, L. Roizen-Towle, E. P. Clark, E. R. Epp, M. B. Astor and E. J. Hall, *Biochem. Pharmacol.*, 1986, **35**, 77–90.
- 22 D. I. Edwards, *J. Antimicrob. Chemother.*, 1993, **31**, 201–210.
- 23 G. E. Adams and D. L. Dewey, *Biochem. Biophys. Res. Commun.*, 1963, **12**, 473–477.
- 24 M. B. Mallia, S. Subramanian, A. Mathur, H. D. Sarma, M. Venkatesh and S. Banerjee, 2008, **18**, 5233–5237.
- 25 R. B. P. Elmes, *Chem. Commun.*, 2016, **52**, 8935–8956.
- 26 G. E. Adams, *Int. J. Radiat. Oncol. Biol. Phys.*, **4**, 135- 141.
- 27 J. L. Foster, P. J. Conroy, A. J. Searle and R. L. Willson, *Br. J. Cancer.*, 1976, **33**, 485-490.
- 28 D. I. Edwards, M. Dye and H. Carne, *J. Gen. Microbiol.*, 1973, **76**, 135–145.
- 29 D. L. Church, H. R. Rabin and E. J. Laishley, *J. Antimicrob. Chemother.*, 1991, **28**,

- 221-228.
- 30 A. Mital, *Sci. Pharm.*, 2009, **77**, 497–520.
- 31 G. E. A. Fowler, J.F., *Cancer Treat. Rev.*, 1976, **3**, 227-256.
- 32 S. K. Chitneni, G. M. Palmer, M. R. Zalutsky and M. W. Dewhirst, *J. Nucl. Med.*, 2011, **52**, 165–168.
- 33 L. S. Ziemer, S. M. Evans, A. V Kachur, A. L. Shuman, C. A. Cardi, W. T. Jenkins, J. S. Karp, A. Alavi, W. R. Dolbier and C. J. Koch, *Eur. J. Nucl. Med. Mol. Imaging.*, 2003, **30**, 259-266.
- 34 J. S. Rasey, G. V Martin and K. A. Krohn, in *Imaging of Hypoxia: Tracer Developments*, ed. H.-J. Machulla, Springer Netherlands, Dordrecht, 1999, pp. 85–117.
- 35 and J. S. R. Z. Grunbaum, S.J. Freauff, K. A. Krohn, D. S. Wilbur, S. Magee, *J Nucl Med*, 1987, **28**, 68–75.
- 36 B. S. Mallia MB, Subramanian S, Mathur A, Sarma HD, *Nucl Med Biol*, 2014, **41**, 600–610.
- 37 R. Beck, B. Röper, J. M. Carlsen, M. C. Huisman, J. A. Lebschi, N. Andratschke, M. Picchio, M. Souvatzoglou, H.-J. Machulla and M. Piert, *J. Nucl. Med.*, 2007, **48**, 973-980.
- 38 R. Ali, S. Apte, M. Vilalta, M. Subbarayan, Z. Miao, F. T. Chin, E. E. Graves and J. J. Li, *PLoS One.*, 2015, **10**
- 39 J. Yue, Y. Yang, A. R. Cabrera, X. Sun, S. Zhao, P. Xie, J. Zheng, L. Ma, Z. Fu and J. Yu, *Dis. Esophagus*, 2012, **25**, 54–61.
- 40 Z. Zhang, L. Chen, H. C. Wang and Y. Guan, *J. Nucl. Med.*, 2012, **33**, 1096–1102.
- 41 S. I. Ziegler, *Nucl. Phys. A*, 2005, **752**, 679–687.
- 42 Y. Xu, S. Zanganeh, I. Mohammad, A. Aguirre, T. Wang, Y. Yang, L. Kuhn, M. B. Smith and Q. Zhu, *J. Biomed. Opt.*, 2013, **18**, 66009.
- 43 F. Riche, D. M. D&Apos, A. Hardemare, S. Sepe, L. Riou, D. Fagret and M. Vidal, *Bioorg. Med. Chem. Lett.*, 2001, **11**, 71–74.
- 44 K. E. Linder, Y. W. Chan, J. E. Cyr, M. F. Malley, D. P. Nowotnik and A. D. Nunn, *J. Med. Chem.*, 1994, **37**, 9-17
- 45 S. Fernandez, J. Giglio, A. M. Rey and H. Cerecetto, *Bioorg. Med. Chem.*, 2012, **20**, 4040–4048.
- 46 D. Yang, S. Ilgan, T. Higuchi, F. Zareneyrizi, C.-S. Oh, C.-W. Liu, E. Kim and D. Podoloff, *Pharm. Res.*, 1999, **16**, 743–750.
- 47 M. B. Mallia, A. Mathur, S. Subramanian, S. Banerjee, H. D. Sarma and H. D. Meera Venkatesh, *Bioorg. Med. Chem. Lett.*, 2005, **15**, 3398–3401.
- 48 T. Das, S. Banerjee, G. Samuel, H. D. Sarma, A. Korde, M. Venkatesh and M. R. A. Pillai, *Nucl. Med. Biol.*, 2015, **30**, 127–134.
- 49 C. Ricardo, P. Kumar and L. Wiebe, *J. Diagnostic Imaging Ther.*, 2015, **2**, 103–158.
- 50 J. Wu, B. Kwon, W. Liu, E. V Anslyn, P. Wang and J. S. Kim, *Chem. Rev.*, 2015, **115**, 7893–7943.
- 51 M. Ni, S. Zhuo, P. T. C. So and H. Yu, *J. Biophotonics*, 2017, **10**, 11–23.
- 52 L. Cui, Y. Zhong, W. Zhu, Y. Xu, Q. Du, X. Wang, X. Qian and Y. Xiao, *Org. Lett.*, 2011, **13**, 928–931.

- 53 P. Wardman, E. D. Clarke, R. J. Hodgkiss, R. W. Middleton, J. Parrick and M. R. L. Stratford, *Int. J. Radiat. Oncol.*, 1984, **10**, 1347–1351.
- 54 R. J. Hodgkiss, A. C. Begg, R. W. Middleton, J. Parrick, M. R. L. Stratford, P. Wardman and G. D. Wilson, *Biochem. Pharmacol.*, 1991, **41**, 533–541.
- 55 Y. Liu, Y. Xu, X. Qian, J. Liu, L. Shen, J. Li and Y. Zhang, *Bioorg. Med. Chem.*, 2006, **14**, 2935–2941.
- 56 Y. Liu, Y. Xu, X. Qian, Y. Xiao, J. Liu, L. Shen, J. Li and Y. Zhang, *Bioorg. Med. Chem. Lett.*, 2006, **16**, 1562–1566.
- 57 P. D. Bonnitcha, S. R. Bayly, M. B. M. Theobald, H. M. Betts, J. S. Lewis and J. R. Dilworth, *J. Inorg. Biochem.*, 2010, **104**, 126–135.
- 58 E. L. Engelhardt, R. F. Schneider, S. H. Seeholzer, C. C. Stobbe and J. D. Chapman, *J. Nucl. Med.*, 2002, **43**, 837-860
- 59 M. B. Mallia, S. Subramanian, A. Mathur, H. D. Sarma, M. Venkatesh and S. Banerjee, *Bioorg. Med. Chem. Lett.*, 2008, **18**, 5233–5237.
- 60 L. Mei, Y. Wang and T. Chu, *Eur. J. Med. Chem.*, 2012, **58**, 50–63.
- 61 J. M. Brown and A. Koong, *J. Natl. Cancer Inst.*, 1991, **83**, 178–185.
- 62 E. Jaillette, C. Girault, G. Brunin, F. Zerimech, A. Chiche, C. Broucqsault-Dedrie, C. Fayolle, F. Minacori, I. Alves, S. Barrailler, L. Robriquet, E. Delaporte, D. Thellier, C. Delcourte, A. Duhamel, S. Nseir, X. Valette, I. Desmeulles, B. Savary, R. Masson, A. Seguin, C. Daubin, B. Sauneuf, P. Verrier, V. Pottier, M. Orabona, D. Samba, G. Viquesnel, M. Lermuzeaux, P. Hazera, J.-L. Hanouz, J.-J. Parienti, D. Du Cheyron, A. Demoule, M. Clavel, C. Rolland-Debord, S. Perbet, N. Terzi, A. Kouatchet, F. Wallet, H. Roze, F. Vargas, C. Guérin, J. Dellamonica, S. Jaber, T. Similowski, J.-P. Quenot, C. Binquet, C. Vinsonneau, S.-D. Barbar, S. Vinault, V. Deckert, S. Lemaire, A. A. Hssain, R. Bruyère, B. Souweine, L. Lagrost, C. Adrie, B. Jung, A. Daurat, A. De Jong, G. Chanques, M. Mahul, M. Monnin, N. Molinari, O. Lheureux, E. Trepo, M. Hites, F. Cotton, F. Wolff, R. Surin, J. Créteur, J.-L. Vincent, T. Gustot, F. Jacobs, F. S. Taccone, M. Neuville, J.-F. Timsit, N. El-Helali, A. Le Monnier, E. Magalhaes, A. Radjou, R. Smonig, J.-F. Soubirou, G. Voiriot, R. Sonnevile, L. Bouadma, B. Mourvillier, E. Gélisse, A. Brasseur, S. Roisin, D. De Backer, V. Van Ruychevelt, E. Carlier, M. Piagnerelli, M. Vanhaeverbeek, C. Danguy, P. Biston, S.-M. Au, E. Begot and ..., *Ann. Intensive Care*, 2016, 6.
- 63 *Hypoxia and Cancer Metastasis*, 1st ed. 2019., 2019.
- 64 M. P. Hay, H. H. Lee, W. R. Wilson, P. B. Roberts and W. A. Denny, *J. Med. Chem.*, 1995, **26**, 1928-1941.
- 65 D. A. Peterson, in *Encyclopedia of Movement Disorders*, Elsevier Inc., 2010, pp. 250–252.
- 66 M. Barer, *Int. J. Coal Geol.*, 1994, **26**, 262–264.
- 67 J. B. Pawley, *Scanning*, 1991, **13**, 184–198.
- 68 N. Billinton and A. W. Knight, *Anal. Biochem.*, 2001, **291**, 175–197.
- 69 P. T. Kissinger and W. R. Heineman, *J. Chem. Educ.*, 1983, **60**, 702.
- 70 G. A. Mabbott, *J. Chem. Educ.*, 1983, **60**, 697.

---

## **CHAPTER 2**

### **Fluorescently Labelled Nitroimidazole**

## CHAPTER 2 Fluorescently Labelled Nitroimidazole

### 2.1 Introduction

The use of fluorophore molecules as marker groups for tagging of biomolecules, such as nucleic acids or proteins is a very vital research area.<sup>1</sup> 1,8-Naphthalic anhydride and its derivatives have been proven to be excellent building block for the synthesis of fluorescent labels.<sup>2,3</sup> Because of their good features, such as strong fluorescence, great photostability and electroactivity, these molecules have applications in many areas, for example pharmaceutical agents for the treatment of cancer,<sup>4</sup> fluorescent markers in molecular biology and imaging applications,<sup>5</sup> organic light emitting diodes,<sup>6</sup> optical brighteners in detergent and textiles,<sup>7</sup> fluorescence switches,<sup>8</sup> photo induced electron transfer based sensors,<sup>9</sup> and laser dyes.<sup>10</sup> Naphthalimides with single side chain of 2-nitroimidazole have been synthesised (**Fig 2.1**) as poorly oxygenated cell tracers. A range of naphthalimide moieties containing two heterocyclic side chains of 2-nitroimidazole (**Fig 2.1**) and their reduction in hypoxic cells were investigated.<sup>11</sup> However, at the best of our knowledge, metronidazole has not been conjugated with any naphthalimides moiety.

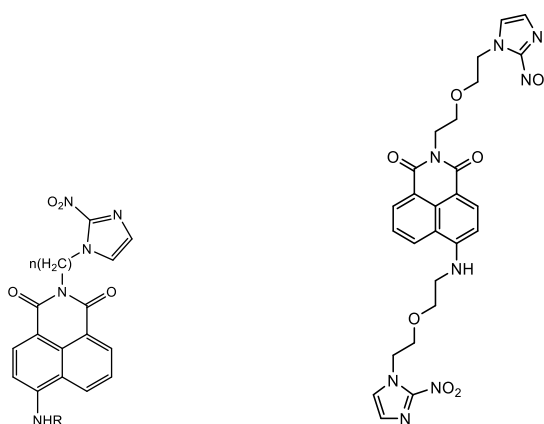


**Figure 2.1: Naphthalimides moiety containing one or two side chain of 2-nitroimidazole<sup>11</sup>**

On the other hand, Schiff bases are produced from a condensation process of primary amines with carbonyl compounds and were first reported in 1864.<sup>12</sup> The shared structure of Schiff bases is the imine group. These compounds are also known as anils or azomethines. These compounds are of considerable chemical and biological importance because of the existence of a lone pair electrons in a  $sp^2$  hybridized orbital of nitrogen atom of the imine group. Schiff Bases support in the mechanism of transamination and rasemination reaction in biological reactions.<sup>13,14</sup> Antibacterial, antifungal, antitumor, anticancer and antimicrobial activities of Schiff bases have been reported.<sup>15,16,17</sup>

A number of Schiff bases derived from metronidazole were synthesised and their biological properties evaluated *in vitro* for their anti-giardial, anti-trichomonal, antibacterial, and antifungal activities. Some of these compounds were found to be more active than the reference drug metronidazole.<sup>18</sup>

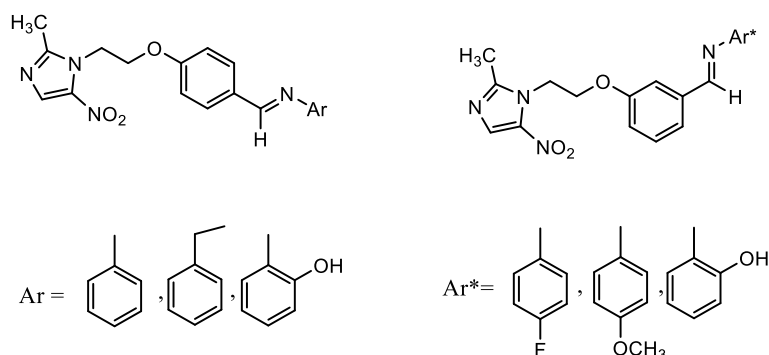


**Figure 2.2: Representation of some metronidazole -Based Schiff Base compounds**

Because of the low cost of metronidazole and its desirable properties and applications in hypoxia, it was decided to investigate whether it could be used as a bioreductive moiety to create hypoxia-imaging agents. By combing the properties of nitroimidazoles, naphthalimides and Schiff base, we sought to develop a new synthetic route to synthesise fluorescently labelled metronidazole to potentially investigate them in hypoxia *in vitro*. Thus, novel hypoxic- tracing agents were produced with different naphthalimide derivatives.

In addition, fluorescently labelled azomycin have been synthesised and their optical properties have been investigated and compared to that of metronidazole.

## 2.2 Aims

Based on the principle that nitro group can quench fluorescence and can be reduced under hypoxic conditions, fluorescently labelled nitroimidazoles were successfully prepared. To achieve this, we aimed to develop a new synthetic pathway to conjugate fluorescent naphthalimides to active redox nitroimidazoles moieties. To accomplish this, the following steps were investigated as shown in **Fig 2.3**.

- 1- 1,8-Naphthalic anhydride and its derivatives were synthesised with a terminal primary amine functional group. (**Step 1, Fig 2.3**)
- 2- Activating metronidazole and azomycin with a good leaving group was required in this study for potential nucleophilic substitution reactions. (**Step 2, Fig 2.3**)
- 3- Direct / multistep alkylation of primary amine with the activated nitroimidazoles was not successful. (**Step 3, Fig 2.3**)
- 4- Alternatively, functionalise the nitroimidazoles with aldehyde group. Consequently, condensation process of primary amines of naphthalimide with carbonyl tethered nitroimidazoles was successfully done to produce a range of nitroimidazole Schiff Bases compounds. (**Step 4, Fig 2.3**)

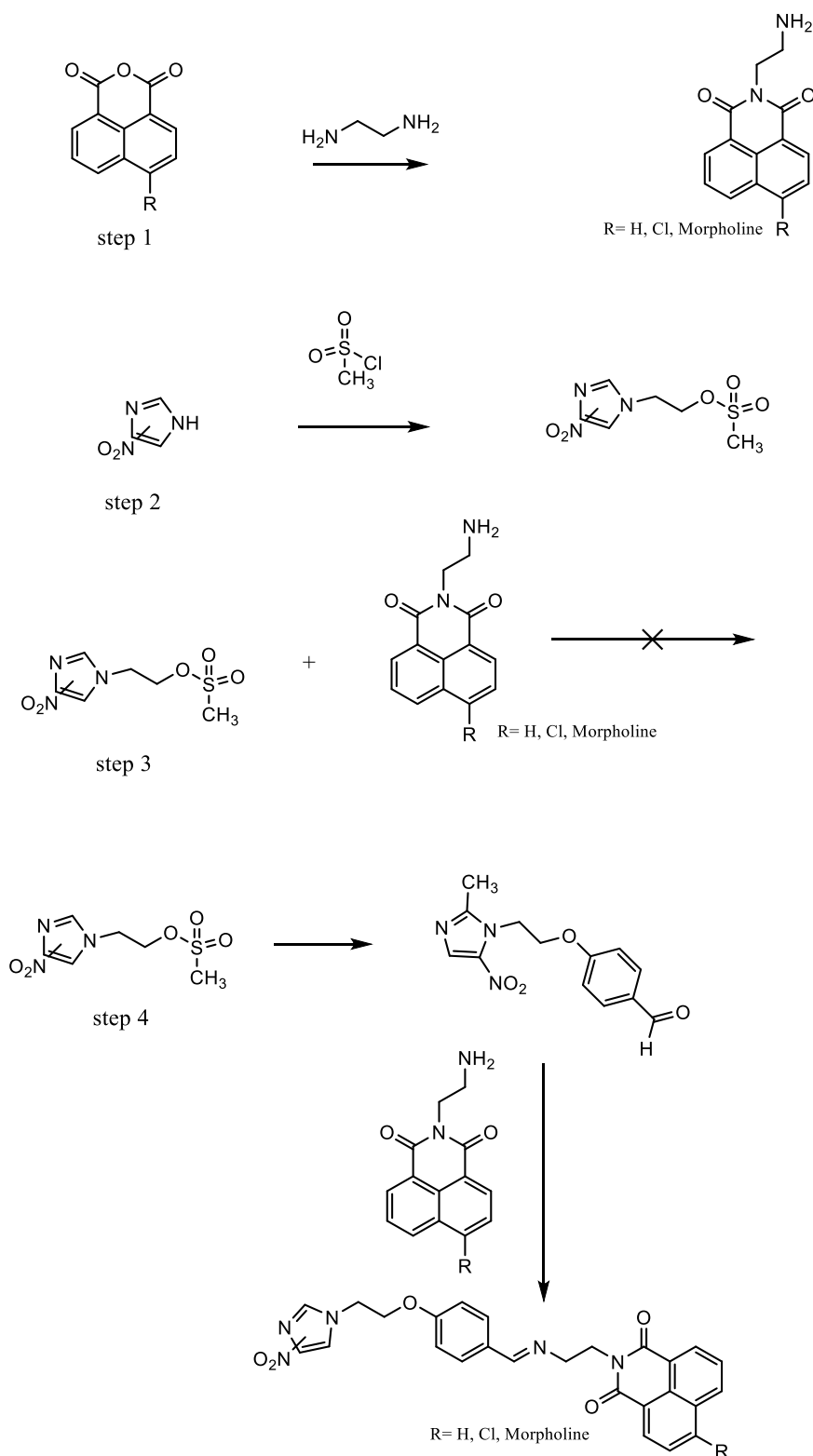


**Figure 2.3: Synthetic route for producing fluorescently labelled nitroimidazoles**

The detail of synthetic procedures and characterisations of all above reactions and compounds will be described in following section:

## 2.3 Result and discussions:

### 2.3.1 Synthesis and characterisation of fluorophores (naphthalimide derivatives):

The naphthalimide derivatives (**Fig 2.4**) were synthesised and purified according to previously reported literatures with some modifications as stated in the experimental procedure. Their  $^1\text{H}$  NMR and  $^{13}\text{C}$  NMR spectra matched data previously reported for these compounds. Through this modification, nitroimidazoles can be conjugated to the 1,8-naphthalic anhydride and its derivatives.

**2.1** was prepared according to a literature procedure described by M. Licchelli *et al.*<sup>19</sup> 2-(2-aminoethyl)-6-chloro-1H-benzo[de]isoquinoline-1,3(2H)-dione **2.1** was synthesised and modified according to previously reported procedure.<sup>20</sup> The procedure for producing **2.3** was reported by L. Song *et al.*<sup>21</sup> The synthesis of **2.3** according to the literature consisted of two separate steps. In the modification of first step, 4-chloro-1,8-naphthalic anhydride was used instead of 4-bromo-1,8-naphthalic anhydride. The replacement reaction of the chlorine in 4-chloro-1,8-naphthalic anhydride with morpholine was first tried using a ratio of 1:4. Although, the increasing of time duration of the reaction, TLC still showed the presence of 4-chloro-1,8-naphthalic anhydride. Thus, excess of morpholine was added to the reaction mixture which was refluxed for an additional day. Orange crystals were formed which were filtered off and washed with water to remove the solvent to give 6-morpholino-1H,3H-benzo[de]isochromene-1,3-dione. The next step was to terminate the obtained compound with a primary amine functional group, this method was exactly the same as reported in the literature.<sup>21</sup>

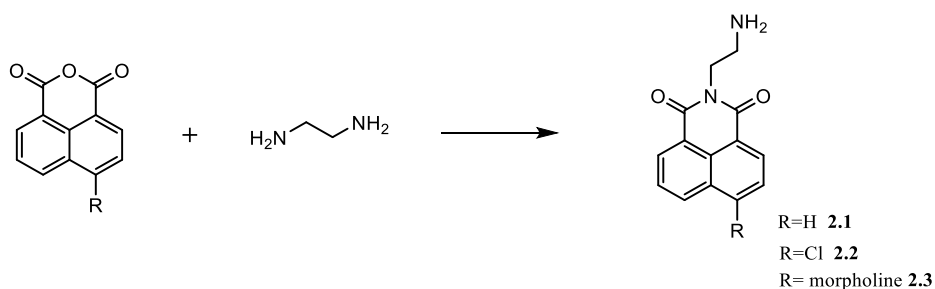


**Figure 2.4: Path way synthesis of n-(2-Aminoethyl)-1,8 naphthalimide 1 , 2-(2-aminoethyl)-6-chloro-1H-benzo[de]isoquinoline-1,3(2H)-dione 2.2 and 2-(2-aminoethyl)-6-morpholino-1H-benzo[de]isoquinoline-1,3(2H)-dione 2.3**

### 2.3.2 Fluorescently labelled Metronidazole

#### 2.3.2.1 Tosylation and mesylation process of metronidazole

Preparation of *2-(2-methyl-5-nitro-imidazol-1-yl)-ethyl ester toluene-4- sulfonate 2.4* is required in this study for potential nucleophilic substitution reactions onto metronidazole. It was prepared according to a method described by Z. Xiao and co-workers.<sup>22</sup> Compound **2.6** was synthesised according to a previously reported method<sup>23</sup> with some modification. The synthesis occurred over a long time period to ensure minimal starting material, which include increasing the time of reaction to 72 hours instead of 4 hours. This resulted in formation of **2.6** in high purity.

Tosylation of metronidazole using 4-methylbenzenesulfonyl chloride was successful and mesylation of metronidazole using methanesulfonyl chloride was also successful (**Fig 2.5**). However, it was found after the nucleophilic substitution reactions, removing methanesulfonic acid as by-product from the reaction mixture was much easier as it is water soluble. However, 4-methylbenzenesulfonic acid is more soluble in alcohols and other polar organic solvents which need more complicated purification methods to be eliminate from the reaction mixture. Accordingly, it was decided to use methanesulfonyl chloride to react with metronidazole because the product is easily purified.

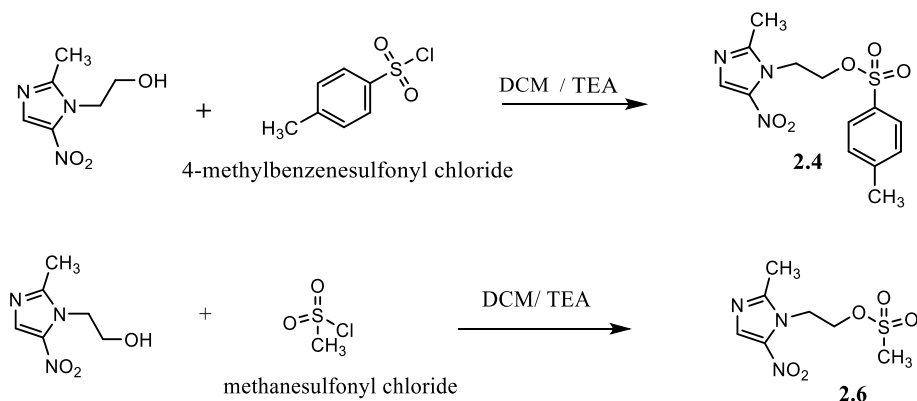


**Figure 2.5: Tosylation 2.4 and mesylation 2.6 of metronidazole.**

### 2.3.2.2 Attempted synthesis of 2-(2-((2-(2-methyl-5-nitro-1H-imidazol-1-yl)ethyl)amino)ethyl)-1H-benzo[de]isoquinoline-1,3(2H)-dione 2.5

Direct reaction of 2-(2-methyl-5-nitro-1H-imidazol-1-yl)ethyl 4-methylbenzenesulfonate **2.4** or 2-(2-methyl-5-nitro-imidazol-1-yl)-ethyl methanesulfonate **2.6** with (2-aminoethyl)-1,8-naphthalimide **2.1** under different conditions has been investigated (**Fig 2.6**). The factors that could affect alkylation of primary amine with electrophilic reagent were varied. Polar aprotic solvents such as DMF, DMSO, acetonitrile was examined with and without mild bases, such as  $K_2CO_3$  and  $Et_3N$  in this reaction. Polar protic solvents and strong nucleophilic bases such as NaOH were avoided in order to prevent the conversion of **2.4** or **2.6** to its alcoholic analogue. This reaction was also screened using  $H_2O$  and sodium dodecyl sulfate in the presence of  $NaHCO_3$  by adapting a reported procedure.<sup>24</sup> However, in this reaction TLC showed only the starting material. Refluxing the starting material in toluene with NaI,  $K_2CO_3$  was also not successful.<sup>25</sup> Although all reactions were monitored by TLC,  $^1H$  NMR spectra showed the presence of starting material along with other products which could not be separated by TLC, despite a range of solvent systems being used.

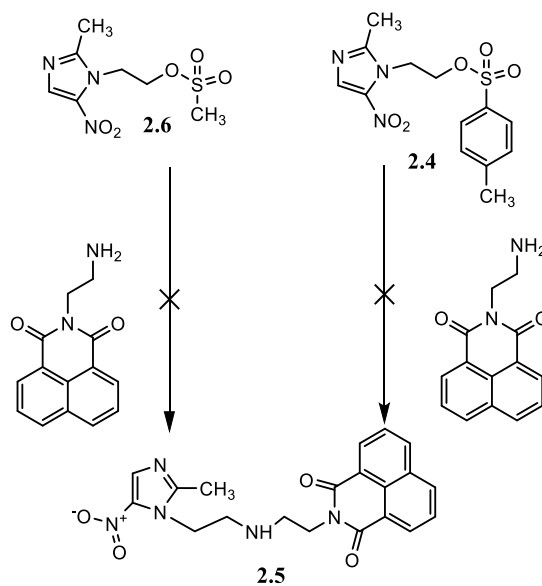


**Figure 2.6: Attempted synthesis of 2-(2-((2-(2-methyl-5-nitro-1H-imidazol-1-yl)ethyl)amino)ethyl)-1H-benzo[de]isoquinoline-1,3(2H)-dione 2.5**

Conversion of primary amines to the equivalent secondary amines proved to be unreliable and difficult to obtain pure product. Alkylation of primary amines with alkyl sulfonates usually end up with the production of the undesired tertiary amines, quaternary ammonium salts or mixture of both. Using the 2-nitrobenzenesulfonamide protecting group in such reaction can be useful to the synthesis of a wide range of secondary amines.<sup>26</sup> This method see **Fig 2.7** was described and reported previously by W. Kurosawa.<sup>26</sup> The idea behind the use of 2-nitrobenzenesulfonyl chloride is to protect the primary amines in the presence of a base to give N-monosubstituted 2-nitrobenzenesulfonamides. The next step is the alkylation of N-monosubstituted 2-nitrobenzenesulfonamide by reacting it with alkyl sulfonate to give N,N-disubstituted 2-nitrobenzenesulfonamide. Removing 2-nitrobenzenesulfonyl with a thiolate nucleophile giving the favourite secondary amines. However, the failure in producing N-monosubstituted 2-nitrobenzenesulfonamides prevented us to achieve the next steps in the proposal plan of this reaction.

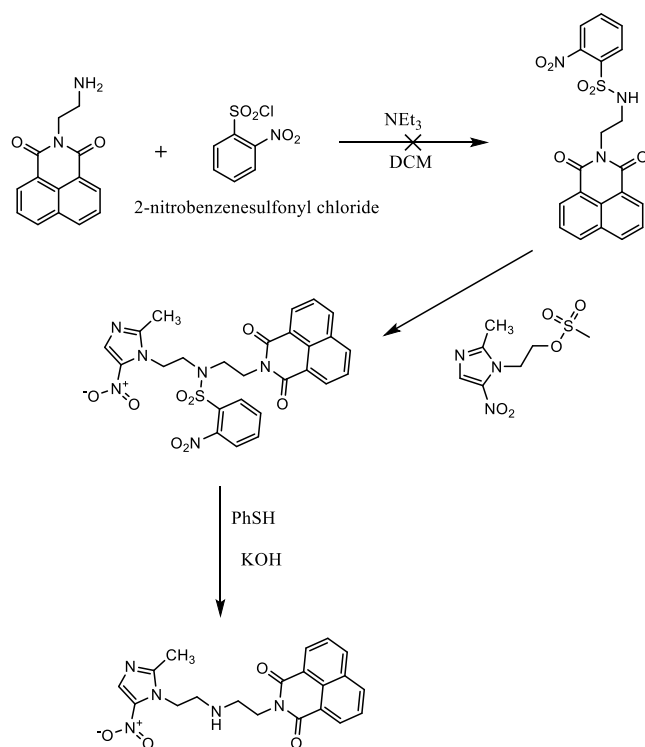


**Figure 2.7: Multi steps attempted synthesis of 2-(2-((2-(2-methyl-5-nitro-1H-imidazol-1-yl)ethyl)amino)ethyl)-1H-benzo[de]isoquinoline-1,3(2H)-dione**

### 2.3.2.3 Synthesis and characterisation of 2.7, 2.8, 2.9 and 2.10

#### 2.3.2.3.1 Synthesis and characterisation of 4-(2-(2-methyl-5-nitro-1H-imidazol-1-yl)ethoxy)benzaldehyde, 2.7

Due to the failure of directly conjugating metronidazole to naphthalimide moieties, an alternative strategy was investigated. 4-Hydroxybenzaldehyde was used to link these moieties together. Aldehyde tethered metronidazole was produced which was then reacted straightforwardly with a range of naphthalimide derivatives to produce a range of newly produced fluorescently labelled Schiff base tethered metronidazole (**Fig 2.8**).

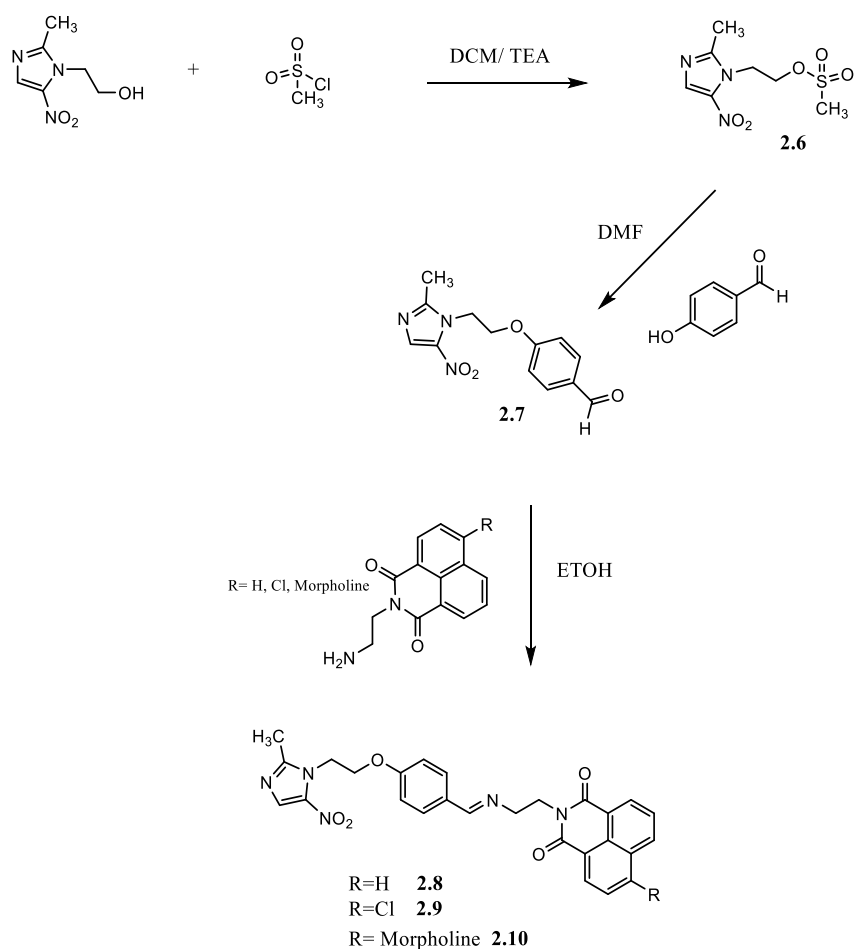


**Figure 2.8: Synthesis of compounds: 2.8, 2.9 and 2.10**

The first attempted to prepare **2.7**, was by reacting 2-(2-methyl-5-nitroimidazol-1-yl)-ethyl ester toluene-4-sulfonate **2.4** (Fig 2.5) with 4-hydroxybenzaldehyde in the presence of mild base K<sub>2</sub>CO<sub>3</sub>. However, this reaction produced the desired product in low yield (21%). That was due to the loss of the desired product during the purification of the crude product by column chromatography on silica gel (DCM: MeOH = 70: 1).

Due to the low yield of the product in previous reaction and the process of purification, 2-(2-methyl-5-nitroimidazol-1-yl)-ethyl methanesulfonate **2.6** was reacted with 4-hydroxybenzaldehyde to produce **2.7** with good yield (69%) (Fig 2.8). This proved to be an improvement to the synthesis of this compound compared to the use of 2-(2-methyl-5-nitroimidazol-1-yl)-ethyl ester toluene-4-sulfonate.<sup>18</sup> The product provided satisfactory analytical and spectroscopic data, which were in full agreement with its proposed structure. In <sup>1</sup>H NMR

spectra, as seen in **Fig 2.10**, the appearance of an extra two peaks at 7.79 and 7.91 in the aromatic region, which corresponds to the protons of 4-hydroxybenzaldehyde shifted when compared to the  $^1\text{H}$  NMR spectra of **2.6**, proof of producing **2.7**. An additional peak with an integral of one proton at 9.82 ppm was assigned to the aldehyde proton, also confirmed the formation of **2.7**. The appearance of the additional peaks in  $^{13}\text{C}$  NMR spectra upfield at 115, 132, 139, 163 and 190 ppm, were attributed to the benzene ring and aldehyde carbons atoms, further evidence of the formation of this compound. The infrared spectrum of this compound showed all the absorption peaks corresponding to metronidazole and an additional strong peak at  $1674\text{ cm}^{-1}$  that was attributed to the C=O (aldehyde) stretching.

#### 2.3.2.3.2 Synthesis and characterisation of (E)-2-(2-((4-(2-(2-methyl-5-nitro-1H-imidazol-1-yl)ethoxy)benzylidene)amino)ethyl)-1H-benzo[de]isoquinoline-1,3(2H)-dione, **2.8**

This was achieved according to the general procedure of producing a Schiff base which includes the mixing of aldehyde group with primary amine in the presence of suitable solvent, in this case ethanol, at room temperature for 17 hours. The desired product was obtained as a beige powder after filtration with a yield of 67%. This novel compound was fully characterised and data, detailed in the experimental part, are consistent with the suggested structure. In the  $^1\text{H}$  NMR spectrum, as seen in **Fig 2.10**, the proton signal corresponding to the aldehyde group in **2.7** disappeared and further peaks were seen at 3.85, 4.75, 6.89, 7.91 and 8.54 ppm which were assigned to n-(2-aminoethyl)-1,8 naphthalimide fragment. One additional peak with an integral of one proton also appeared at 8.35 ppm and was assigned to the proton of the imine bond of **2.8**.  $^{13}\text{C}$  NMR spectra displayed 19 peaks which were assigned to the carbons in the structure. Four peaks were found downfield representing

aliphatic carbons and the others were found at high field for the aromatic carbons and imine carbon.

In the FT-IR spectrum, compared to compound **2.7**, there was a new medium peak at  $1697\text{ cm}^{-1}$  corresponding to the formation of the imine bond (C=N stretching). Extra absorption peaks at  $1608\text{ cm}^{-1}$  and  $1647\text{ cm}^{-1}$  correspond to C=O (amide group) stretching of n-(2-Aminoethyl)-1,8 naphthalimide are also observed. The disappearance of the strong peak at  $1674\text{ cm}^{-1}$  that was attributed to C=O (aldehyde) stretching is further evidence of the formation of **2.8**. Mass spectrometry showed the expected  $[M+H]^+$  ion peak (498.1768, 100%) for the desired product. The success of this reaction was also confirmed by the UV-vis spectrum. It presented an absorbance maximum at 350 nm. The absorption detected in the spectrum of naphthalimide starting moieties displays exactly the same wavelength. which is close to values reported for similar fluorescent, naphthalic anhydride-derived imides.<sup>27</sup>

#### 2.3.2.3.3 Synthesis characterisation of (E)-6-chloro-2-(2-((4-(2-(2-methyl-5-nitro-1H-imidazol-1-yl)ethoxy)benzylidene)amino)ethyl)-1H-benzo[de]isoquinoline-1,3(2H)-dione, **2.9**

Another novel compound **2.9** was also produced, (**Fig 2.8**) as a result of condensation of **2.7** with 2-(2-aminoethyl)-6-chloro-1H-benzo[de]isoquinoline-1,3(2H)-dione **2.2** at room temperature for 17 hours. The desired compound was obtained as a bright yellow powder with a yield of; 38%. Compared to  $^1\text{H}$  NMR spectra of **2.7**, additional peaks at 3.85, 4.75, 7.97, 7.98, 8.42, 8.53 ppm appeared due to the chloro- naphthalimide moiety and its side chain. Moreover, the absence of the aldehyde group's proton and the existence of the imide group proton at 8.35 ppm are additional indication of the successful preparation of **2.9** (**Fig 2.10**). In the  $^{13}\text{C}$  NMR spectrum, the absence of the aldehyde group's carbon at 190 ppm and the

presence of extra peaks in aromatic and aliphatic field are also evidence of the effective preparation of **2.9**. Because of the similarity between **2.8** and **2.9** in the molecular structure, the infrared spectrum of **2.9** has very similar absorption peaks. As seen in **Fig 2.9**, The mass spectrometry analysis gave the exact theoretical mass (532.1379, 100%) with the correct Cl isotopic pattern. The product was soluble in acetone, DCM and chloroform.

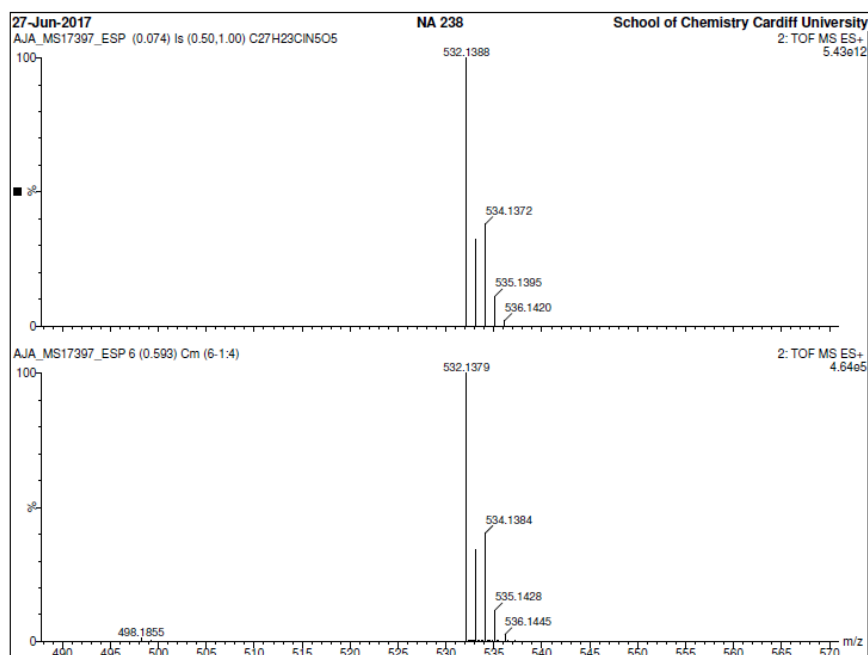


Figure 2.9: High resolution mass spectrometry of **2.9**

#### 2.3.2.3.4 Synthesis characterisation of (E)-2-(2-((4-(2-(2-methyl-5-nitro-1H-imidazol-1-yl)ethoxy)benzylidene)amino)ethyl)-6-morpholino-1H-benzo[de]isoquinoline-1,3(2H)-dione, **2.10**

This was synthesised by using the same procedure as that for **2.8** and **2.9**. However, the crude product was purified by column chromatography on silica gel (acetonitrile) to afford the desired product as a dark yellow powder with yield of; 35%. In the  $^1\text{H}$  NMR spectrum, as seen in **Fig 2.10**, there were extra four resonance peaks downfield and five more peaks in the aromatic region compared to that in **2.7**. These peaks are corresponding to the protons of the

naphthalimide moiety. Again, the disappearance of the aldehyde proton of **2.7** and the presence of a new peak with integral of one proton at 8.31 ppm were noticeable in the  $^1\text{H}$  NMR analysis. It was observed in the  $^{13}\text{C}$  NMR spectrum, compare to that of **2.7**, that there were extra peaks in both high and low field corresponding to carbons of naphthalimide fragment. Moreover, the disappearance of the distinguished aldehyde peak of **2.7** at 190 ppm and the appearance of imine carbon are a good proof of the formation of the compound. IR analysis gave similar results to that seen for **2.8** and **2.9**. Mass spectrometry showed the expected peak (583.2311, 100%) for the desired product. In term of solubility, the product was soluble in acetone and chloroform.

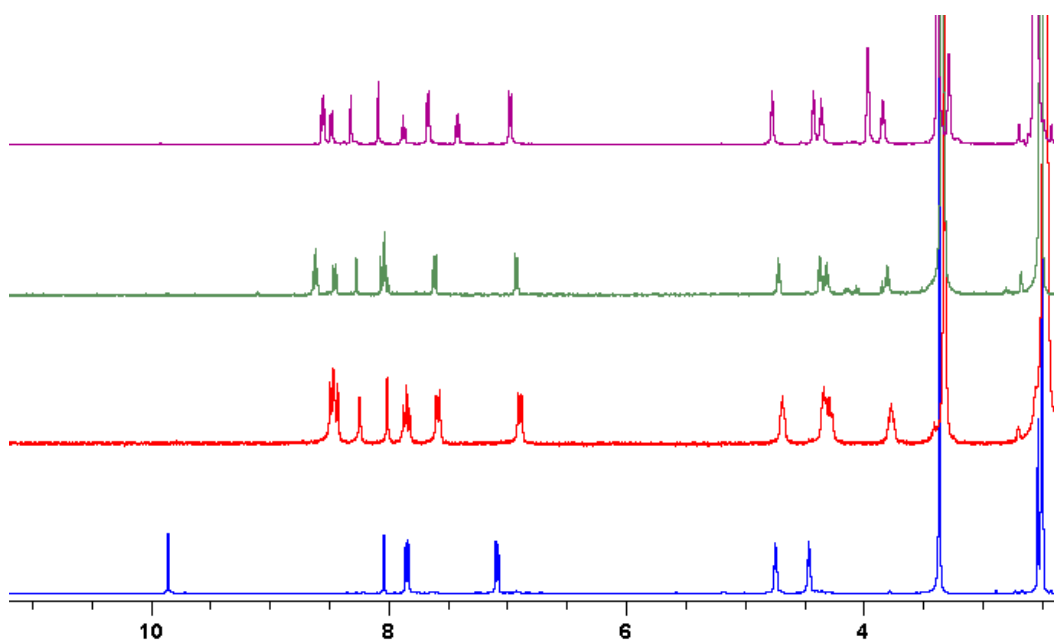
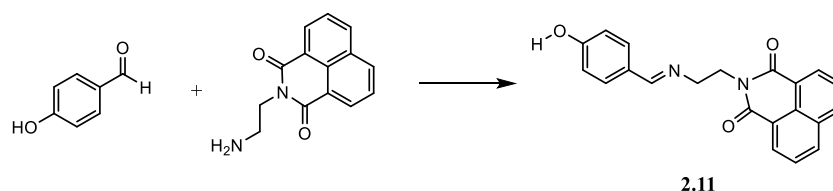


Figure 2.10:  $^1\text{H}$  NMR analysis for **2.7** (blue), **2.8** (red), **2.9** (green) and **2.10** (purple)

### 2.3.3 Synthesis and characterisation of (E)-2-(2-((4-hydroxybenzylidene)amino)ethyl)-1H-benzo[de]isoquinoline-1,3(2H)-dione **2.11**

The synthesis of **2.11**, (Fig 2.11) was carried out and the compound was used as fluorescence reference for **2.8**. The synthesis was carried out by reacting 4-hydroxybenzaldehyde with **2.1**. The desired product was obtained as a white powder (yield: 69%). To the best of our

knowledge (E)-2-(2-((4-hydroxybenzylidene) amino)ethyl)-1H-benzo[de]isoquinoline-1,3(2H)-dione **2.11**, which was fully characterised, is a novel fluorescent Schiff base compound. The success of producing this compound was supported by  $^1\text{H}$  NMR spectroscopy, as there were two additional doublet peaks at 6.7 and 7.5 ppm with integrals of two protons in aromatic region compared to **2.1**. These peaks correspond to the para substituted benzene ring. The presence of one further signal peak with integral of one proton at 8.22 ppm assigned for the proton of imine bond is an evidence of formation of Schiff base. There are 13 carbon peaks in the  $^{13}\text{C}$  NMR spectrum as expected for **2.11**. The analysis of mass spectrometry of the sample in acetone showed an ion peak for  $[\text{M}+\text{H}]^+$  at (345.12, 100%) in the agreement of the theoretical calculation.



**Figure 2.11: Synthesis of (E)-2-(2-((4-hydroxybenzylidene)amino)ethyl)-1H-benzo[de]isoquinoline-1,3(2H)-dione **2.11****

### 2.3.4 Synthesis and characterisation of fluorescently labelled 2-nitroimidazole

#### 2.3.4.1 Synthesis and characterisation of 2-nitromidazole

Because of the high cost of azomycin, we produced 2-aminoimidazole by reacting 2-aminoacetaldehydedimethylacetal and the *O*-methyl-isourea (**Fig 2.12**). Both starting materials are relatively cheap and therefore this reaction pathway has economic advantages. 2-

Aminoimidazole then was oxidised and converted to 2-nitroimidazole. This reaction was successful according to  $^1\text{H}$  NMR spectra analysis which appears as a singlet at around 7.4 ppm, this peak comes from the two identical protons of the imidazole ring. These protons are identical because of the resonance in imidazole ring and proton transfer, a singlet is observed.

There were two reaction procedures for preparing 2-nitroimidazole (**Fig 2.10**) which were followed,<sup>28,29</sup> however, the yield of the product was very low (~5-7%). After several attempts to optimise the yield by increasing the time of the reaction and repeating the extraction process many times, we decided to use commercially available 2-nitroimidazole for the preparation of fluorescently labelled 2-nitroimidazole.

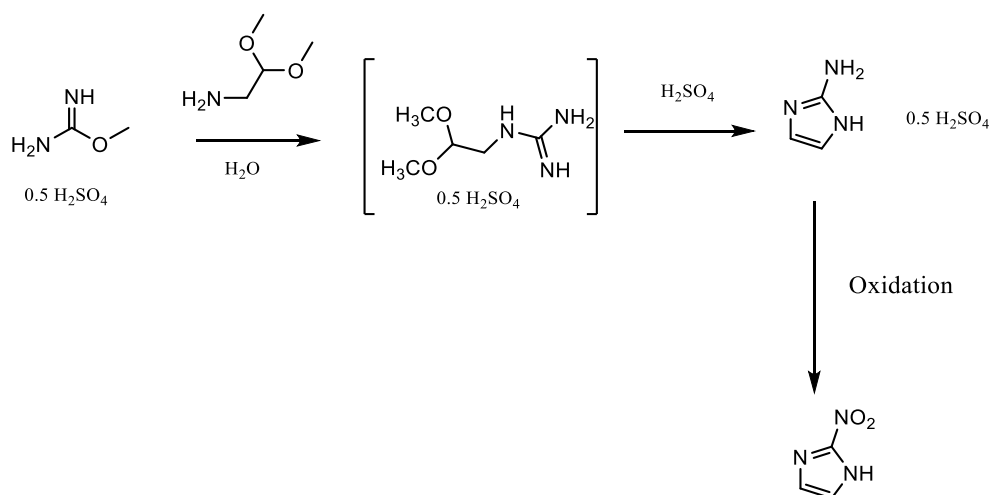


**Figure 2.12: Synthesis of 2-aminoimidazole and 2-nitroimidazole.**

#### 2.3.4.2 Attempted synthesis of 6-(2-nitro-1H-imidazol-1-yl)-1H,3H-benzo[de]isochromene-1,3-dione

This experiment was carried out in order to obtain fluorescently labelled azomycin that is able to be attached to a variety of diamines. This experiment was attempted by using a one-step synthesis starting from 4-chloro-1,8-naphthalic anhydride in the presence of  $K_2CO_3$  as seen in **Fig 2.13**. This reaction is an aromatic nucleophilic substitution reaction such a reaction is only observed when the aromatic ring is electron deficient. The mechanism of this reaction is described below:

The chlorine atom attached to the naphthalic anhydride ring is more electronegative than the carbon atom bonded to it. This produces a partial positive charge on the carbon and makes it

susceptible to be attacked by nucleophiles. The lone pair of electrons of the 2-nitroimidazole nitrogen atom are then capable to attack this carbon atom. The carbonyl groups of the anhydride moiety (which are electron withdrawing) and the conjugated system of aromatic ring may distribute the negative charge across the whole molecule. This may stabilise the intermediate and make this step more favourable for promoting the reaction. The chloride ion will pick up a proton and leave as hydrochloric acid.

However, after screening this reaction under different conditions, no product was observed according to  $^1\text{H}$  NMR spectra analysis as only the peaks of the starting material were seen. Strangely, the reactions were monitored by TLC which showed that there is a new polar product while 2-nitroimidazole disappeared. The possible explanation of this observation is that the potassium salt of 2-nitroimidazole formed making it more polar and soluble in water. However, while this reaction is theoretically possible, it is less likely to occur due to steric hindrance of the reaction. The anhydride moiety is held in a planar geometry as it is attached to the naphthalene aromatic system. It would therefore be difficult for the 2-nitroimidazole nitrogen  $\text{sp}^2$  orbital, containing the lone pair, to have enough access the carbon. This is because this lone pair are part of a five-membered ring also they are adjacent to nitro group that make the access to the positively charged carbon even more difficult. If the overlap of these two orbitals is prevented, then no nucleophilic attack can happen.

Another possible explanation for this is the lone pairs on the nitrogen of imidazole need to displace the chloride, having a nitro group (which is electron withdrawing group) may make this lone pair less basic and consequently less available.

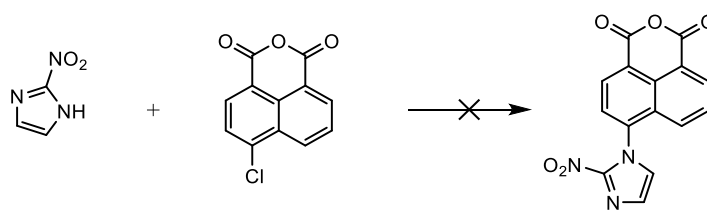


**Figure 2.13: Attempted synthesis of 6-(2-nitro-1H-imidazol-1-yl)-1H,3H-benzo[de]isochromene-1,3-dione**

We wished to extend the synthesis of metronidazole with naphthalamide to analogous 2-nitroimidazoles in order to fairly compare the potential reduction abilities of these compounds in hypoxic tissues. The prodrugs were synthesized according to the process outlined in **Fig 2.14**. The following synthetic approaches were carried out and the details for these steps are given below;

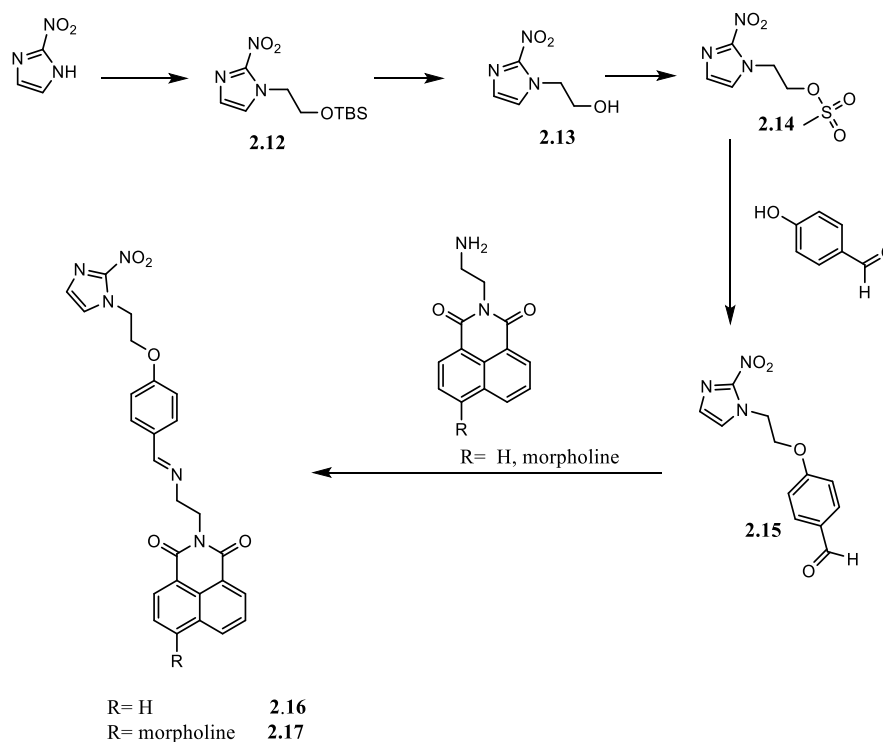


**Figure 2.14: Synthetic pathway of 2.15, 2.16 and 2.17**

#### 2.3.4.3 Synthesis and characterisation of 1-(2-((*tert*-butyldimethylsilyl)oxy)ethyl)-2-nitro-1H-imidazole, **2.12**

In the first step of this synthesis, it was important to have a side chain that have two carbon atoms to mimic the structure of metronidazole. Thus, (2-bromoethoxy)(*tert*-butyl)dimethylsilane was reacted with 2-nitroimidazole in the presence of potassium carbonate. This reaction was carried out according to the previously reported method described by Chen Jin *et al.*<sup>30</sup> Previous attempts to react 2-chloroethanol with 2-nitroimidazole to produce 2-(2-nitro-1H-imidazol-1-yl)ethanol **2.13** directly were not successful. By the increasing the reaction time for more than 72 hours, TLC showed the presence of starting material alongside with some of new products. <sup>1</sup>H NMR spectrum data presents obvious peaks of the starting materials and some very small peaks of other products on the baseline. This is probably due to the potential polymerisation of chloroethanol under these conditions. Failure of this attempt diverted our attention towards an alternate approach involving the use of (2-bromoethoxy)(*tert*-butyl)dimethylsilane as the alcohol is protected by the bulky *tert*-butyl dimethylsilane group. This promotes the nucleophilic attack only on the carbon atom adjacent to bromine atom. The success of this reaction can be simply detected by <sup>1</sup>H NMR spectroscopy. There are two doublets peaks for imidazole moiety. These are seen at 7.0 ppm and 7.2 ppm, in place of the original singlet resonance. In addition, the proton peaks of ethoxy *tert*-butyl dimethylsilane moiety were also observed.

#### 2.3.4.4 Synthesis and characterisation of 2-(2-nitro-1H-imidazol-1-yl)ethan-1-ol, **2.13**

The next step of this synthesis was to deprotect *tert*-butyl dimethylsilane from 1-(2-((*tert*-butyldimethylsilyl)oxy)ethyl)-2-nitro-1H-imidazole **12** to yield the alcoholic analogue **2.13**, (**Fig 2.14**). The attempt of deprotection with HCl and MeOH followed a method used by Chen

Jin *et al.*<sup>30</sup> In the <sup>1</sup>H NMR spectrum analysis of **2.13**, the distinguishing tert-butyl dimethylsilane peaks present in the <sup>1</sup>H NMR spectrum of **2.12** was not detected suggesting the removal of the protecting group had been successfully carried out.

#### 2.3.4.5 Synthesis and characterisation of 2-(2-nitro-1H-imidazol-1-yl)ethyl methanesulfonate, **2.14**

2-(2-Nitro-1H-imidazol-1-yl)ethyl methanesulfonate **2.14** was prepared according to a procedure described by J. Cao and co-workers (Li *et al.*, 2008) with some modification.<sup>31</sup> This entails reacting 2-(2-nitro-1H-imidazol-1-yl)ethanol **2.13** and methanesulfonyl chloride in the presence of triethylamine. DMAP was used as a catalyst in this procedure, however, we avoided using this reagent as it would be difficult to eliminate in the purification step, as it would remain in organic layer during the extraction process and then require further purification steps causing loss of the product.

The success of this reaction was confirmed by <sup>1</sup>H NMR spectroscopy which showed five resonances. Two of these resonances appeared in the aromatic region; two doublets characteristic of a 2-nitroimidazole moiety each with an integral of one proton. Two triplet resonances were seen between 4 and 5 ppm indicating the presence of the two CH<sub>2</sub> environments. One more singlet peak with an integral of three was observed at 3 ppm indicated the presence of the -CH<sub>3</sub> environment.

#### 2.3.4.6 Synthesis and characterisation of 4-(2-(2-nitro-1H-imidazol-1-yl)ethoxy)benzaldehyde, **2.15**

Synthesis of a novel azomycin derivative; 4-(2-(2-methyl-2-nitro-1H-imidazol-1-yl)ethoxy)benzaldehyde **2.15**, was carried out by the reaction of **2.14** with 4-

hydroxybenzaldehyde in the presence of a base. The product was obtained as a beige powder (yield 66%). The success of this compound was confirmed by  $^1\text{H}$  NMR spectrum which showed seven resonances as seen in Fig 2.15. Four of these resonances appeared in the aromatic region; four doublets characteristic of a 2-nitroimidazole moiety and para-substituted benzene with integrals of one and two protons. Two triplet resonances were seen between 4 and 5 ppm indicating the presence of the two  $\text{CH}_2$  environments. One more singlet peak with integral of one was observed at 9.82 ppm indicating the present of an aldehyde proton in this compound. The absence of the singlet peak for methyl group that was present in **2.14** is an additional evidence of the formation of this compound.  $^{13}\text{C}$  NMR spectrum resonances expected for the structure of **2.15** is 10 peaks. Although the carbons peaks in the correct place and carbon spectrum looks sensible, only nine peaks were observed instead of 10 peaks (Fig2.16). The missing carbon peak could be either the one corresponding for C- $\text{NO}_2$  or O-C-aromatic ring. That is because both are quaternary signals, which are often weak due to slow relaxation.

The infra-red analysis of this compound showed the distinguished carbonyl stretch  $\text{C}=\text{O}$  of aldehyde at  $1683\text{ cm}^{-1}$ , there are also two bands of moderate intensity in the region  $2758\text{ cm}^{-1}$  corresponding to  $\text{O}=\text{C}-\text{H}$  stretch. The absorbance corresponding to the azomycin moiety were observed such as  $\text{N}=\text{O}$  symmetric at  $1307\text{ cm}^{-1}$ ,  $1357\text{ cm}^{-1}$  and  $\text{N}=\text{O}$  asymmetric at  $1527\text{ cm}^{-1}$ . The mass spectrometry of **2.15** in chloroform found an ion peak for  $[\text{M}+\text{H}]^+$  at (262.0834, 100%) which was equivalent to the hypothetical calculation.

The Schiff bases **2.16** and **2.17** were prepared by reacting of 4-(2-(2-methyl-2-nitro-1H-imidazol-1-yl)ethoxy) benzaldehyde **2.15** with different aromatic amines **2.1** and **2.3** in ethanolic solution as depicted in Fig 2.14.

#### 2.3.4.7 Synthesis and characterisation of (E)-2-(2-((4-(2-(2-nitro-1H-imidazol-1-yl)ethoxy)benzylidene)amino)ethyl)-1H-benzo[de]isoquinoline-1,3(2H)-dione **2.16**

It was prepared according to the general method of producing a Schiff base. A mixture of **2.15** and n-(2-aminoethyl)-1,8 naphthalimide in ethanol was stirred for 24 hours in room temperature. The precipitate was filtered, and the product was obtained as a beige powder, (yield 44%). This novel compound was fully characterised and data, detailed in the experimental part, are consistent with the suggested structure. In the  $^1\text{H}$  NMR spectrum, as seen in **Fig 2.15**, the proton corresponding to the aldehyde group in **2.15** at 9.87 ppm disappeared and a resonance associated with the imine was seen at 8.35 ppm. Compared to **2.15**, Further peaks were seen at 3.85 4.75 6.89 7.91, and 8.54 ppm which were assigned to the naphthalimide moiety. Moreover, the success of this reaction was also confirmed by  $^{13}\text{C}$  NMR spectrum, with the absence of the aldehyde carbon peak and presence of the imine carbon peak (**Fig 2.16**). In the FT-IR spectrum, compared to **2.15**, there was a new medium absorbance at  $1697\text{ cm}^{-1}$  corresponding to the imine bond. There are additional absorption peaks at  $1662\text{ cm}^{-1}$  and  $1604\text{ cm}^{-1}$  which correspond to the amide group stretching. The presence of the methyl groups was confirmed by C–H stretching vibrations that appeared at  $2930$  and  $2862\text{ cm}^{-1}$ . The disappearance of the strong peak at  $1683\text{ cm}^{-1}$  that was attributed to carbonyl group of aldehyde stretching is further evidence of formation of **2.16**. High resolution mass spectrometry showed  $[\text{M}+\text{H}]^+$  ion peak at (484.1624, 100%) which matches the theoretical calculation of structure of **2.16**.

#### Synthesis and characterisation of (E)-6-morpholino-2-(2-((4-(2-(2-nitro-1H-imidazol-1-yl)ethoxy)benzylidene)amino)ethyl)-1H-benzo[de]isoquinoline-1,3(2H)-dione **2.17**:

It was prepared by the reaction of **2.15** and **2.3** (**Fig 2.14**). This newly prepared compound was successfully prepared in significantly low (yield 17%). That maybe due to the loss of the product during the purification step by using a chromatography separation method. The success of this compound was easily detected by  $^1\text{H}$  NMR spectrum, which showed the disappearance of the proton corresponding to the aldehyde group. In addition, triplet resonances were seen between 3.25 and 3.95 ppm with integral of 4 protons indicating the presence of the two  $\text{CH}_2$  environments of morpholine. Two more triple peaks with integral of two protons were also detected at 3.7 and 4.3 ppm and five characteristic peaks with integral of one were seen in the aromatic region corresponding to naphthalimide moiety. One more singlet peak with an integral of one proton was observed at 8.5 ppm representing the proton of the imine bond (**Fig 2.15**). As seen in **Fig 2.16**, the  $^{13}\text{C}$  NMR spectrum also confirmed the successful preparation of this product as there are 25 peaks were seen that match the proposal structure of **2.17**. As explained previously in **2.16**, the disappearance of the aldehyde group's carbon at 191 ppm and appearance of the imine carbon are also an indication of the successful preparation of **2.17**. Because of the similarity of the structure between **2.16** and **2.17**, the FT-IR spectrum of **2.17** was similar to that of **2.16**. The High Resolution Mass spectrometry showed the expected ion peak of  $[\text{M} + \text{H}]^+$  at (569.2159, 100%).

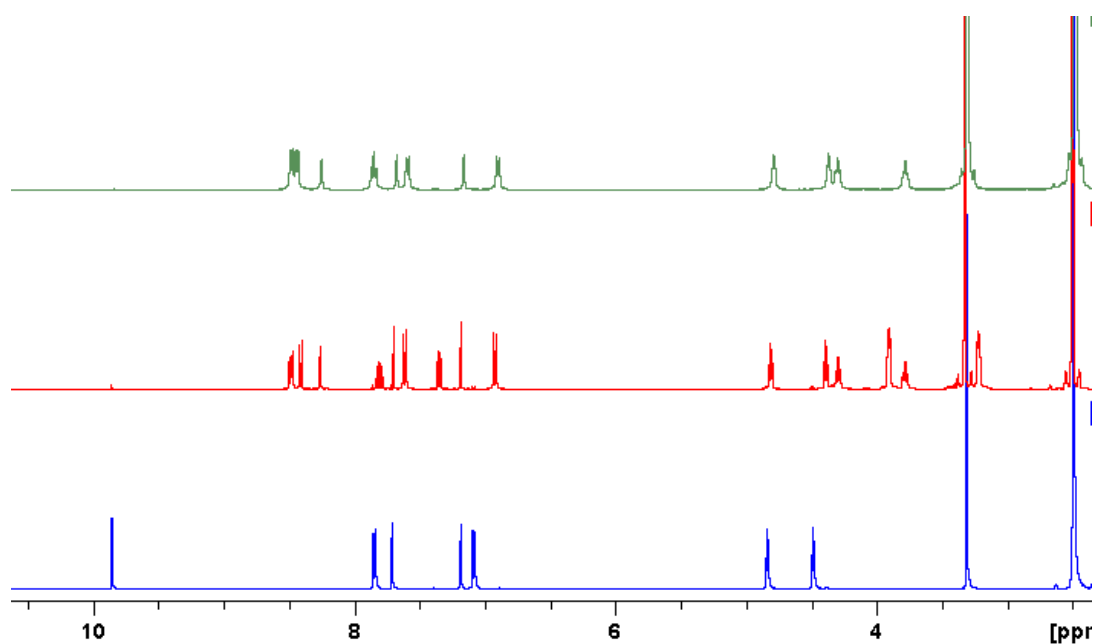


Figure 2.15:  $^1\text{H}$  NMR analysis for 2.15 (blue), 2.16(green) and 2.17(red)

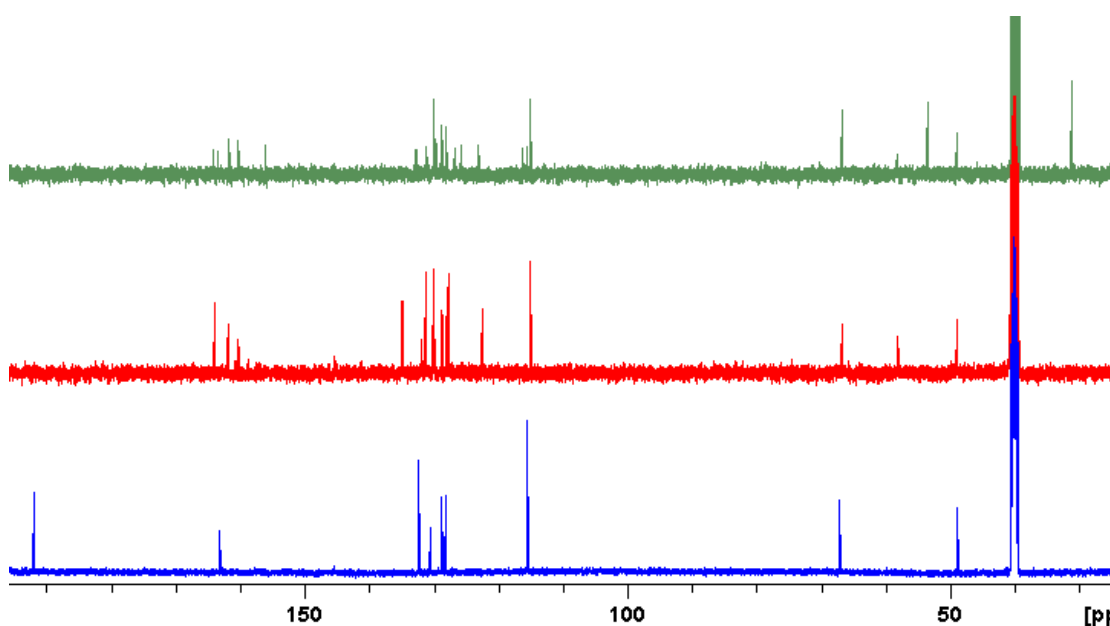
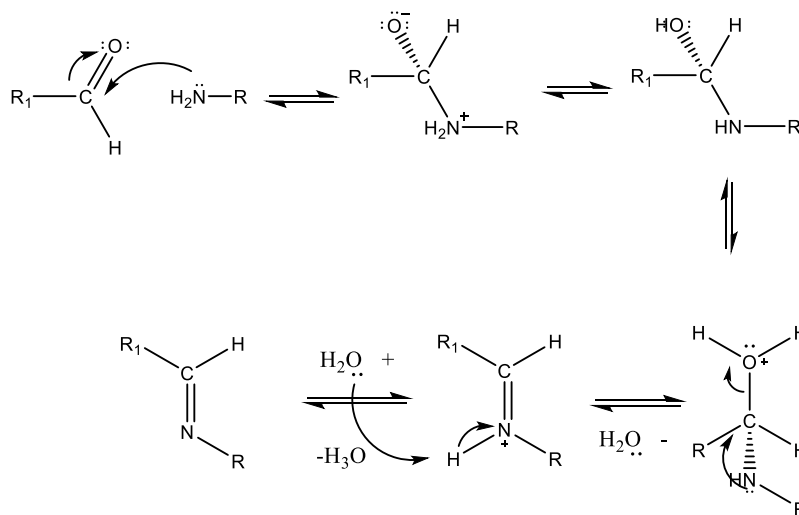


Figure 2.16:  $^{13}\text{C}$  NMR analysis for 2.15 (blue), 2.16(red) and 2.17(green)

The formation of the imine bond in both Schiff base compounds **2.16** and **2.17** proceeds via a nucleophilic addition mechanism. Due to differences in electronegativities, the carbonyl group in **2.15** is polarized. The carbon atom has a partial positive charge, and the oxygen atom has a partially negative charge. A lone pair of electrons on the nitrogen of the primary amine in **2.1** and **2.3** is attracted to the partial-positive carbon of the carbonyl group in **2.15**. Then

one of the protons transferred from the nitrogen of primary amine to the oxygen anion. Follow by protonation of the hydroxy group to yield an oxonium ion, which easily leaves as a water molecule. Then a proton from the positively charged nitrogen immigrated to water, to form an imine bond (**Fig 2.17**). The reaction is reversible, so in the aqueous condition the reaction may be potentially revert to the starting material.



**Figure 2.17: General mechanism of formation Schiff base compounds**

### 2.3.5 Synthesis and characterisation of N-(2-(1,3-dioxo-1H-benzo[de]isoquinolin-2(3H)-yl) ethyl)-2-(2-nitro-1H-imidazol-1-yl) acetamide **2.19**

Compound **2.19** was synthesised in order to obtain another fluorescently labelled azomycin which binds via amid bond. This could be more stable compound in water solution than that of **2.16** and **2.17** which have easily hydrolysed imine bond.

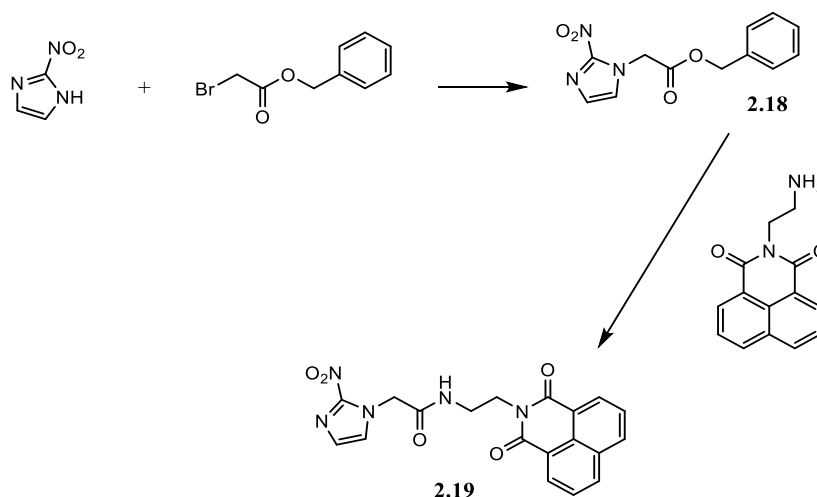


**Figure 2.18: Synthetic scheme for producing 2.19**

Benzyl 2-(2-nitro-1H-imidazol-1-yl) acetate **2.18**, (Fig 2.18) was a novel compound which was produced in order to be reacted with naphthalimide or naphthalimide derivatives. It was synthesised by reacting 2-nitroimidazole with benzyl 2-bromoacetate in the presence of potassium carbonate to deprotonate 2-nitroimidazole. The reaction mixture was refluxed in acetonitrile for 17 hours to yield a brown sticky residue (yield:44%). The success of producing this compound was confirmed by <sup>1</sup>H NMR and <sup>13</sup>C NMR spectrum, mass spectrometry and IR spectroscopy. In the <sup>1</sup>H NMR spectrum, compared to 2-nitroimidazole, there are two doublets peaks seen at 7.3 ppm and 7.8 ppm, rather than the singlet resonance. In addition, the peaks with an integral of 5 protons appeared in the aromatic region between 7.3 and 7.5 ppm indicated the presence of the benzyl group. There are also two singlet peaks between 4.6 and 5.20 ppm representing the two protons adjacent to the carbonyl group and the benzene ring respectively. <sup>13</sup>C NMR spectroscopy also presented the nine peaks expected for the structure of this compound. In the FT-IR spectrum, compared to 2-nitroimidazole, there was a new medium absorbance at 1739 cm<sup>-1</sup> assigned to the ester group (C=O stretching). Additional absorption peaks at 3109, 3124 cm<sup>-1</sup> correspond to stretching (unsaturated C-H bond of benzyl group). The mass spectrometry showed the expected [M+H]<sup>+</sup> ion peak (261.24, 100%) for the desired product.

The next step was to react n-(2-Aminoethyl)-1,8 naphthalimide with **2.18** (Fig 2.18) in acetonitrile. The reaction mixture was refluxed under N<sub>2</sub> for 27 hours. The solvent was evaporated in a vacuum. The residue was washed initially with diethyl ether then with acetone to remove the by-product (benzyl alcohol). The crude product was then purified by column chromatography on silica gel (Methanol: DCM) to afford the desired product was obtained as a pale-yellow powder (yield 25%). The <sup>1</sup>H NMR spectroscopy showed peaks expected for the structure. The distinguishing benzyl peaks present in the <sup>1</sup>H NMR spectrum of **2.18** was not detected suggesting the removal of the benzyl group had been successfully done. Moreover, additional peaks corresponding to the naphthalimide moiety appeared. The same observations were seen in the <sup>13</sup>C NMR data, disappearance of peaks of the benzyl group and the presence of the carbon's peaks of naphthalimide moiety were confirmed the synthesis of this compound. The mass spectrometry illustrated the expected [M+H]<sup>+</sup> ion peak (394.12,100%) for the suggested product.

The reaction of **2.18** with 2-(2-aminoethyl)-6-morpholino-1H-benzo[de]isoquinoline-1,3(2H)-dione, **2.3**, was also attempted, however the residue cannot be purified. The product separation by using TLC was not successful, despite the examination of many solvent systems. This prevent the further use of chromatographic technique.

#### 2.4 Stability of the new compounds

All these novel compounds **2.8**, **2.9**, **2.10**, **2.16** and **2.17** were air stable. The compounds were left in water for 12 hours, 24 hours, 27 hours and 5 days to investigate the stability of these compound in water and the effect of the time on this stability. All compounds were water stable after 27 hours and did not show any starting material according to TLC and NMR spectra. However, the imine bond proton has disappeared in <sup>1</sup>H NMR analysis and the peak of

aldehyde carbon was observed in  $^{13}\text{C}$  NMR spectrum after 5 days. This was an evidence of hydrolysis of these compounds in aqueous solution. Although, the NMR analysis of this compounds showed no changes when it left in aprotic solvents for the same duration of time.

## 2.5 Optical properties

### 2.5.1 UV-vis analysis

#### 2.5.1.1 UV-vis analysis of 2.8, 2.9 and 2.10

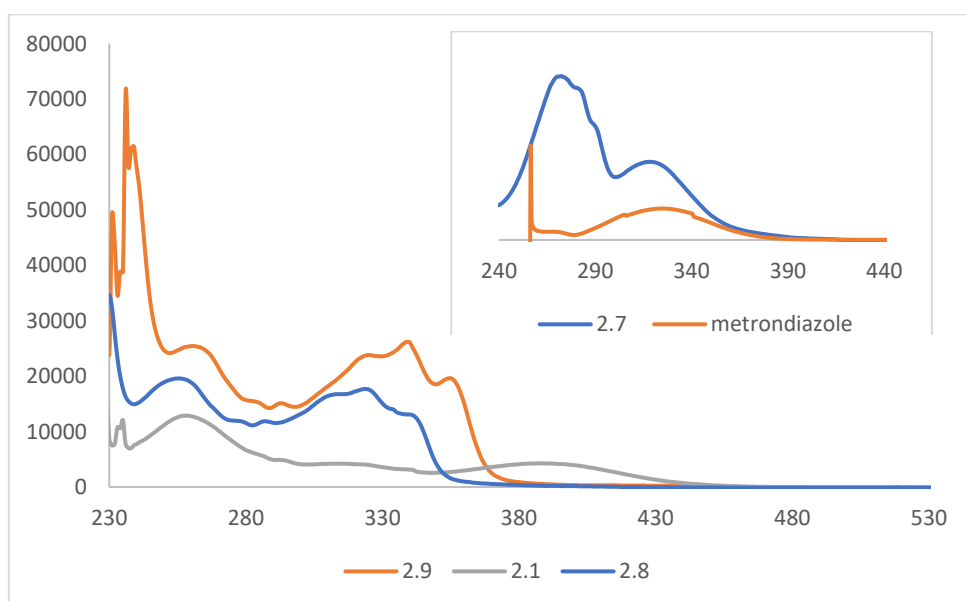


**Figure 2.19:** UV-vis absorption profiles of 2.8 ( $2.4 \times 10^{-5} \text{ mol dm}^{-3}$ ), 2.9 ( $2.6 \times 10^{-5} \text{ mol dm}^{-3}$ ) and 2.10 ( $2.9 \times 10^{-5} \text{ mol dm}^{-3}$ ) in chloroform. Inset shows the UV-vis absorption spectrum of metronidazole in DMSO at  $8.5 \times 10^{-6} \text{ M}$  and 2.7 in DCM at  $1.3 \times 10^{-5} \text{ M}$

Effect of substituent in position 4 of naphthalene ring on the absorption spectra is shown in **Fig 2.19**. Spectra of unsubstituted 1,8-naphthalimide of metronidazole **2.8** and 4-chloro-1,8-naphthalimide of metronidazole **2.9** are very similar. Only very small bathochromic shift of quite a few nanometres can be observed in the case of chloro-analogue in comparison with

unsubstituted 1,8-naphthalimide of metronidazole. However, considerable changes can be noted by introduction of morpholine group to naphthalene ring.

In the UV-Vis spectrum recorded for **2.8**, there is a broad absorption was seen between 289 and 354 nm. Within the spectrum an internal charge transfer (ICT) state arises from the  $\pi$ - $\pi^*$  electron transfer occurring with  $\lambda$  maximum at 348 nm. The values are in good agreement with those values reported in the literature.<sup>32</sup>

The molar extinction coefficient  $\mathcal{E}$  at the absorption maxima is  $12,652 \text{ M}^{-1}\text{cm}^{-1}$  for **2.8**. The observed value is closely comparable to related literature example that are based on the naphthalimide chromophore.<sup>33</sup>

The replacement of the hydrogen atom with chlorine in the naphthalene ring have a little effect on the absorption properties as shows in **Fig 2.19**. The same observation was seen in UV-Vis spectrum of **2.9**, there is a broad absorption was seen between 323nm and 358 nm due to the internal charge transfer (ICT) state whit  $\lambda$  maximum at 358 nm. The molar extinction coefficient  $\mathcal{E}$  at the absorption maxima is  $18,692 \text{ M}^{-1}\text{cm}^{-1}$ . The chloro substituents in **2.9** causes a further red shift of approximately 10 nm. The values are in close agreement with those values reported in the literature of bromo substituent 1,8-naphthalimide.<sup>33,34</sup>

Substitution by morpholine group in the naphthalene ring drastically alters the absorption of 1,8-naphthalimide. The compounds become yellow due to the presence of an absorption band in the region of  $\sim 400 \text{ nm}$ .<sup>33</sup>

Compound **2.10** was absorbed at 395 nm. which is the good range since the expected value is eight-fold larger than those of analogous substituents 1,8-naphthalimide.<sup>21</sup> The molar extinction coefficient  $\mathcal{E}$  at the absorption maxima for **2.10** is  $4,034 \text{ M}^{-1}\text{cm}^{-1}$ .

All three reagents **2.8**, **2.9** and **2.10** exhibit an absorption at approximately 325 nm which are corresponding to metronidazole as seen in **Fig 2.19**, inset. Whereas the peak at  $\sim 265$  is

expected to be corresponded to benzaldehyde moiety of **2.7** due to the internal charge transfer (ICT) arises from the  $\pi$ - $\pi^*$  and  $n$ - $\pi^*$  electron transfer of this group.

### 2.5.1.2 UV-vis analysis of **2.16** and **2.17**

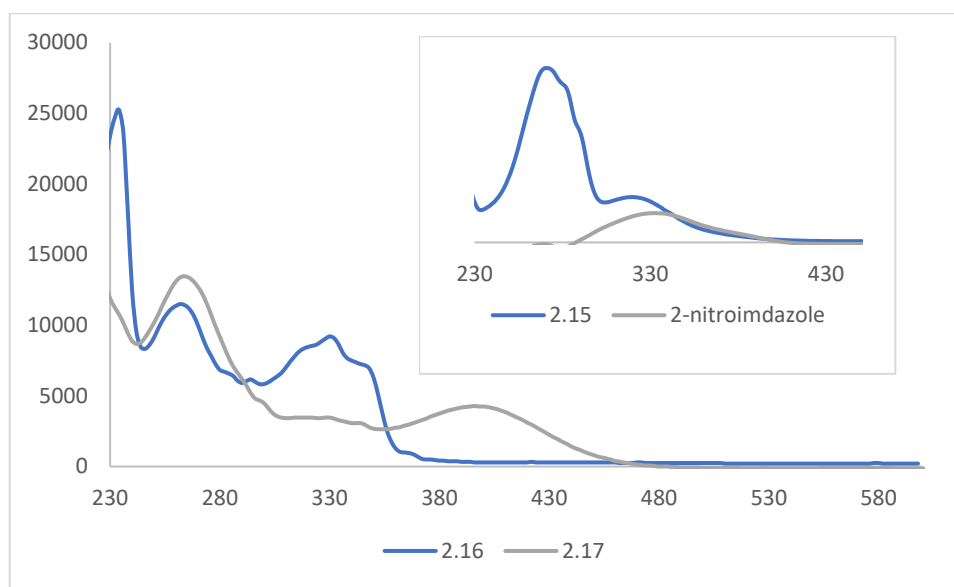


**Figure 2.20:** UV-vis absorption profiles of **2.16** ( $2.4 \times 10^{-5} \text{ mol dm}^{-3}$ ) and **2.17** ( $2.8 \times 10^{-5} \text{ mol dm}^{-3}$ ) in chloroform. Inset shows the UV-vis absorption spectrum of 2-nitroimidazole in DMSO at  $5.6 \times 10^{-6} \text{ M}$  and **2.15** in DCM at  $1.3 \times 10^{-5} \text{ M}$

The absorption spectra of **2.16** is very similar to that of **2.8** in exhibiting a peak at approximately 348 nm with an extinction coefficient in the region of  $6,958 \text{ M}^{-1} \text{ cm}^{-1}$  structure in the spectra as **Fig 2.20** shows.

Also, the absorption spectra of **2.17** is similar to that of **2.10** in displaying a peak at about 402 nm which is in the good agreement with that of morpholine substituents 1,8-naphthalimide.<sup>21</sup> The molar extinction coefficient  $\mathcal{E}$  at the absorption maxima for **2.17** is  $4,250 \text{ M}^{-1} \text{ cm}^{-1}$ . This value is similar to that of **2.10**.

Both **2.16** and **2.17** show an absorption at  $\sim 325 \text{ nm}$  corresponded to nitroimidazole moiety. This value is consistent with the UV-vis for 2-nitroimidazole and **2.15** (**Fig 2.20, inset**).

## 2.5.2 Luminescence analysis

### 2.5.2.1 Luminescence analysis of 2.8, 2.9 and 2.10

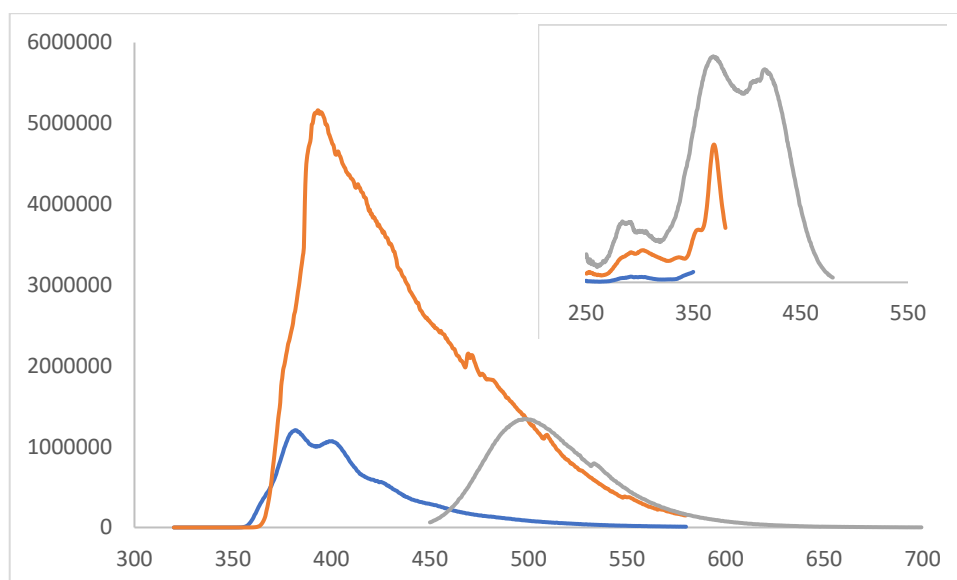


**Figure 2.21: luminescence analysis of 2.8 (blue), 2.9 (red) and 2.10 (grey). Inset: excitation spectra**

In photophysical studies, the solutions of **2.8**, **2.9** in  $\text{CH}_3\text{Cl}$  was found to be emissive (**Fig 2.21**; **Table 1**). Following excitation at 345 nm, **2.8** showed a visible peak at 375 nm, with a lower energy shoulder at 401 nm (**Fig 2.21**), corresponding to the 1,8 naphthalimide fluorophore.<sup>35</sup> The emitting state of **2.8** is ascribed to  $\pi-\pi^*$  character.<sup>35</sup> With excitation of 345 nm and detection at 401 nm respectively, time-resolved lifetime measurements in chloroform detected <0.5 ns.

Although the absorption properties of **2.8** and **2.9** are relatively similar, for **2.9** a slight bathochromic shift in emission maxima ca. 33 nm were observed with respect to that of **2.8** and an increase in emission lifetime was also noted, indicating an effect given likely by the withdrawing chlorine atom. Similar to that in **2.8**, the emitting of **2.9**, is ascribed to  $\pi-\pi^*$  character. Time life for **2.9** was 3.6 ns measured in chloroform and was higher than that in **2.8**.

The solutions of **2.10** in CH<sub>3</sub>Cl was found to be highly emissive, (**Fig 2.21; Table 1**). By using the excitation of 416 nm, a single visible peak was noted at 500 nm which is assigned to morpholine substituents 1,8-naphthalimide. The values are in close agreement with those values reported in the literature of morpholine substituent 1,8-naphthalimide.<sup>36</sup> The lifetime of **2.10** was found to be single component and significantly higher than that in **2.8** and **2.9** display (7.1 ns). The emitting state of **2.10** is ascribed not only to  $\pi-\pi^*$  character but also to charge transfer (CT) character and this is due to the presence of the nitrogen atom of morpholine located at the back of the naphthalimide. This results in large Stoke shift (4038 cm<sup>-1</sup>).

#### 2.5.2.2 Luminescence analysis of 2.16

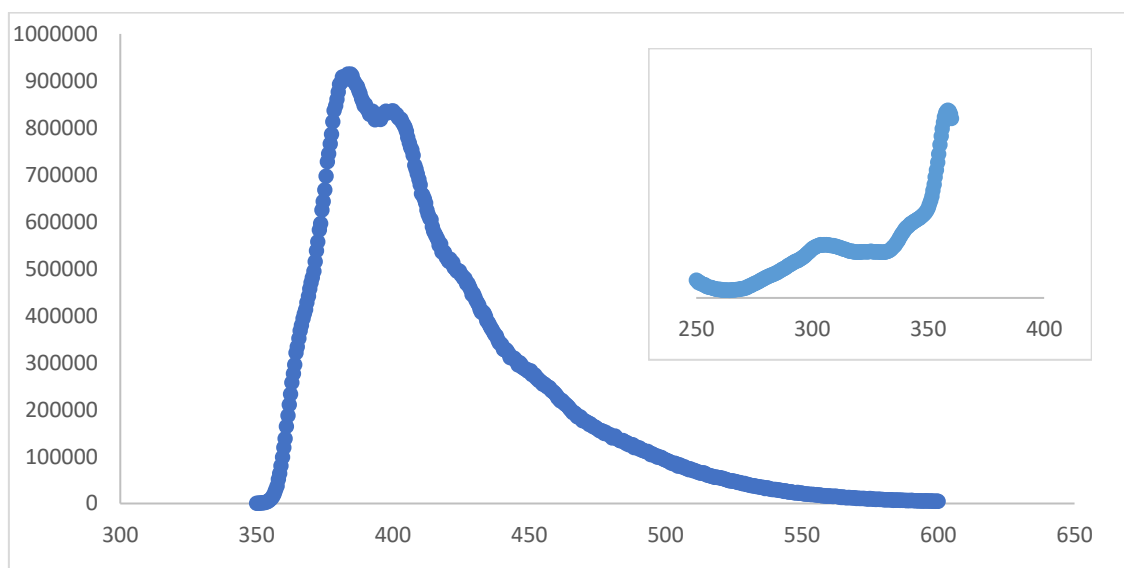


**Figure 2.22: luminescence analysis of 2.16. Inset: excitation spectra at  $\lambda_{\text{exc}}=358$**

At an excitation wavelength of 345 nm, **2.16** showed a visible peak at 385 nm, with a lower energy shoulder at 401 nm (**Fig 2.22; Table 1**), which are corresponding to the naphthalimide fluorophore. These values were similar to **2.8**. The corresponding excitation spectra exhibit a

band between 307 and 342 nm (**Fig 2.22; inset**). This is in close agreement with the data observed from the UV-vis spectrum. The emitting state of **2.16** is ascribed to  $\pi$ - $\pi^*$  character.

### 2.5.2.3 Luminescence analysis of 2.17

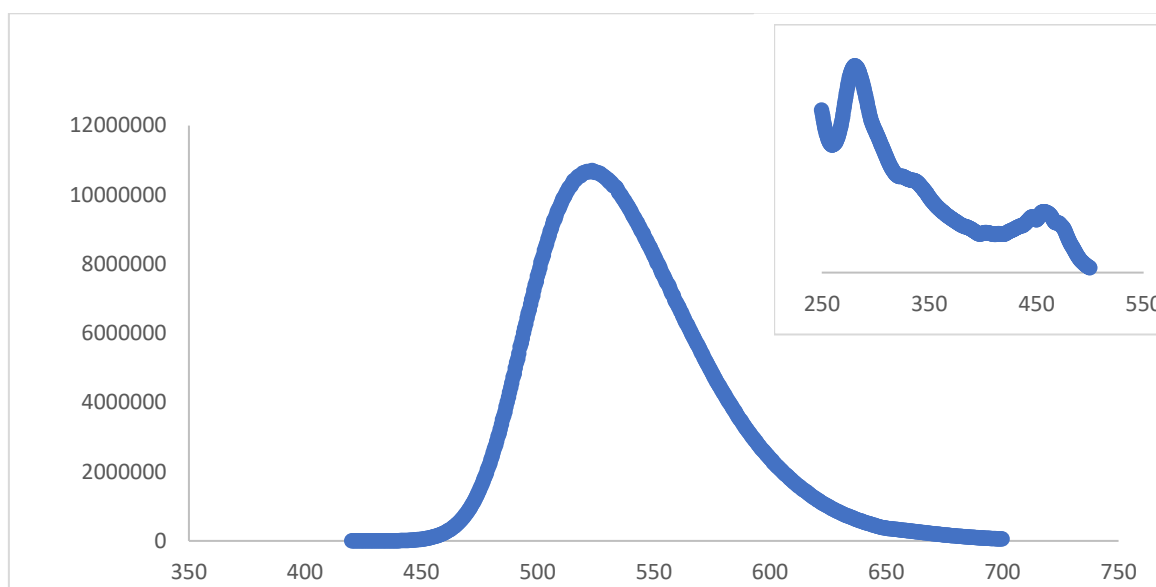


**Figure 2.23: luminescence analysis of 2.17. Inset: excitation spectra at  $\lambda_{exc}=436$**

Similar to that of **2.10**, solution of **2.17** in  $\text{CH}_3\text{Cl}$  was highly emissive and by using the excitation of 400 nm, a single visible peak was noted at 526 nm which is assigned to morpholine substituents 1,8-naphthalimide (**Fig 2.23; Table 1**). This value is 26 time higher than that in **2.10** and in a good agreement with those values reported in the literature of morpholine substituent 1,8-naphthalimide.<sup>36</sup> The corresponding excitation spectra exhibit a band between 345 and 462nm (**Fig 2.23; inset**) which are relatively comparative to the observations from the UV-vis studies.

The corresponding Time-resolved luminescence data of **2.16** and **2.17** were also recorded showing lifetimes of <20 ns (Table 1), consistent with fluorescence ( $\pi$ - $\pi^*$ ). The data for **2.16** best fit to a bi-exponential decay, with approximately two equal quenched species (0.5 ns, 48

%) and, longer component (2.9 ns). However, the lifetime of **2.17** was revealed to be single component and fairly extended compared to **2.16** show (3.7 ns).

The presence of two lifetimes means that two lumophores are present, typically suggesting the presence of two species, one of which could be an impurity. However, according to TLC and the spectroscopic analysis of this compound, it was pure and so this phenomenon may be a result of an equilibrium process meaning two species exist in solution.

**Table 1: Luminescence properties of 8, 9, 10, 16 and 17**

Compound	$\lambda_{\text{exc}}/ \text{nm}$	$\lambda_{\text{em}}/ \text{nm}$	Stokes shift ( $\text{cm}^{-1}$ )	t/ns
2.8	345	401	4048	0.5
2.9	371	475	5902	3.6
2.10	416	500	4038	7.1
2.16	358	401	2995	0.5, 2.9
2.17	457	525	2834	3.7

## 2.6 Confocal Microscopy

Aqueous stock solutions of the reagents were prepared by first dissolving the compound in a small amount of DMSO and then making up to volume in water. For each compound 5.0 mg was dissolved in 1 ml of DMSO and made up to 25.0 ml using distilled water. It was immediately clear that in these conditions, (i) the morpholine complexes were more soluble than the parent naphthalimide or the chloro derivative and (ii) the 2-nitroimidazole species

were more soluble than the 2-methyl-5-nitroimidazole. All subsequent experiments utilised the morpholine derivatives as they were more soluble, and their fluorescence was more red shifted.

For the labelling experiment, the imaging agent (1.0  $\mu\text{L}$ ) was added to a suspension of yeast (50.0  $\mu\text{L}$ ) along with PBS buffer (0.50 ml). The solution was left to stand for 10 minutes and then placed in a centrifuge and the yeast cells were spun down into a pellet. The solution was discarded, and the cells were resuspended in PBS (0.50 ml) and then spun down again and the solution was discarded. The cells were finally resuspended (0.50 ml) and a sample (50.0  $\mu\text{L}$ ) placed on a slide (with cover slip) to be imaged.

Three types of yeast samples were utilised: *Schizosaccharomyces Pombe*, *Candida Utilis* and *Saccharomyces Cerevisiae*.

*S Pombe* is a unicellular eukaryote, with a rod-shaped. It has a 7-14  $\mu\text{m}$  length and a 3-4  $\mu\text{m}$  diameter. The cell grows entirely by elongation at its ends. Division occurs through formation of a cell plate that cleaves the cell at its midpoint. Within a cell there are extensive and largely continuous mitochondrial reticulum which forms two large separate parts centred at opposite ends of the cell. In addition, there are two smaller mitochondria. Vacuoles formed two multi-lobed complexes, one at each end of the cell.

*C. Utilis* is slightly smaller than *S. Pombe* and has a slightly different internal structure. There is only one mitochondrion per cell, and the mitochondrion forms a peripherally placed reticulum.

Even in a budding cell, only one mitochondrion is present, and it extends from the mother to the daughter cell. Images also show a vacuole cluster suggesting a single continuous multi-lobed structure.

*S. Cerevisiae* is a round/oval cell, 5-10  $\mu\text{m}$  in diameter. Like *C. Utilis* and unlike *S. Pombe* it reproduces by a process known as budding.

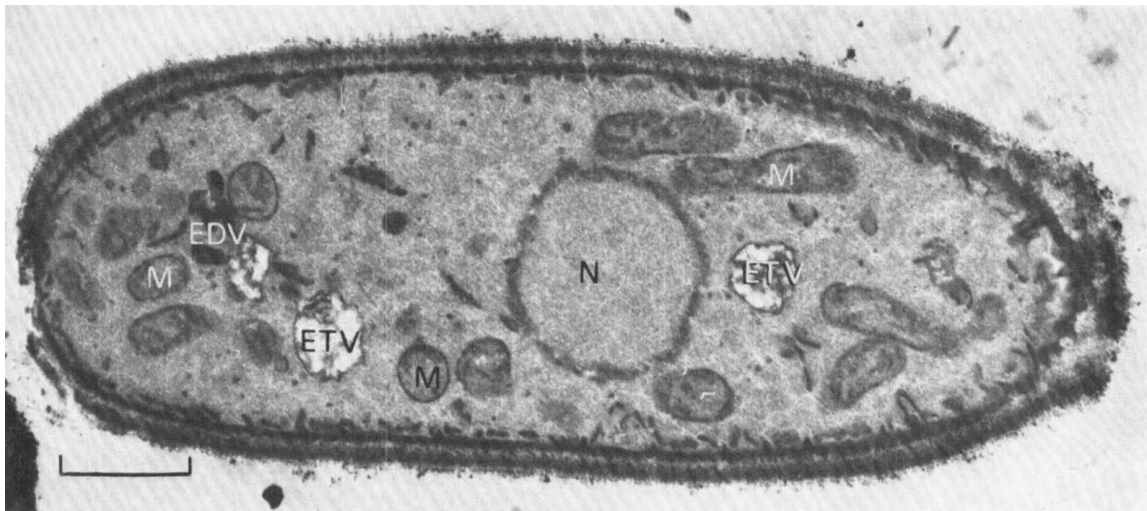


Figure 2.24: A thin slice electron micrograph of *S. pombe*. N = nucleus, M= mitochondria, EDV/ETV = electron dense/transparent vacuoles; bar = 1 $\mu$ m.<sup>37</sup>

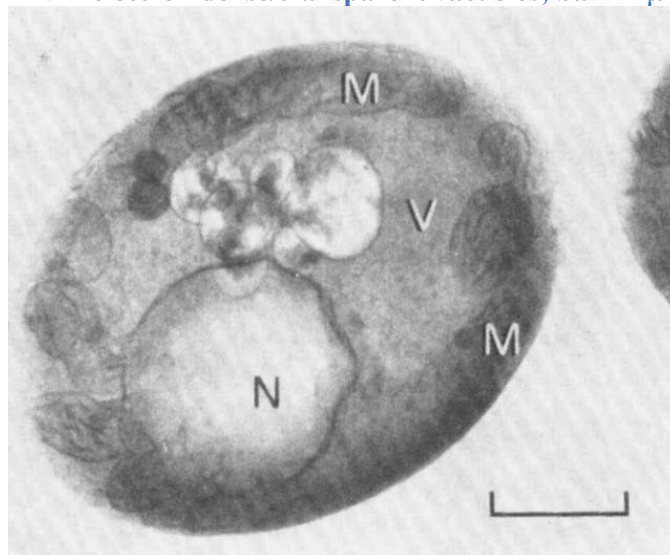
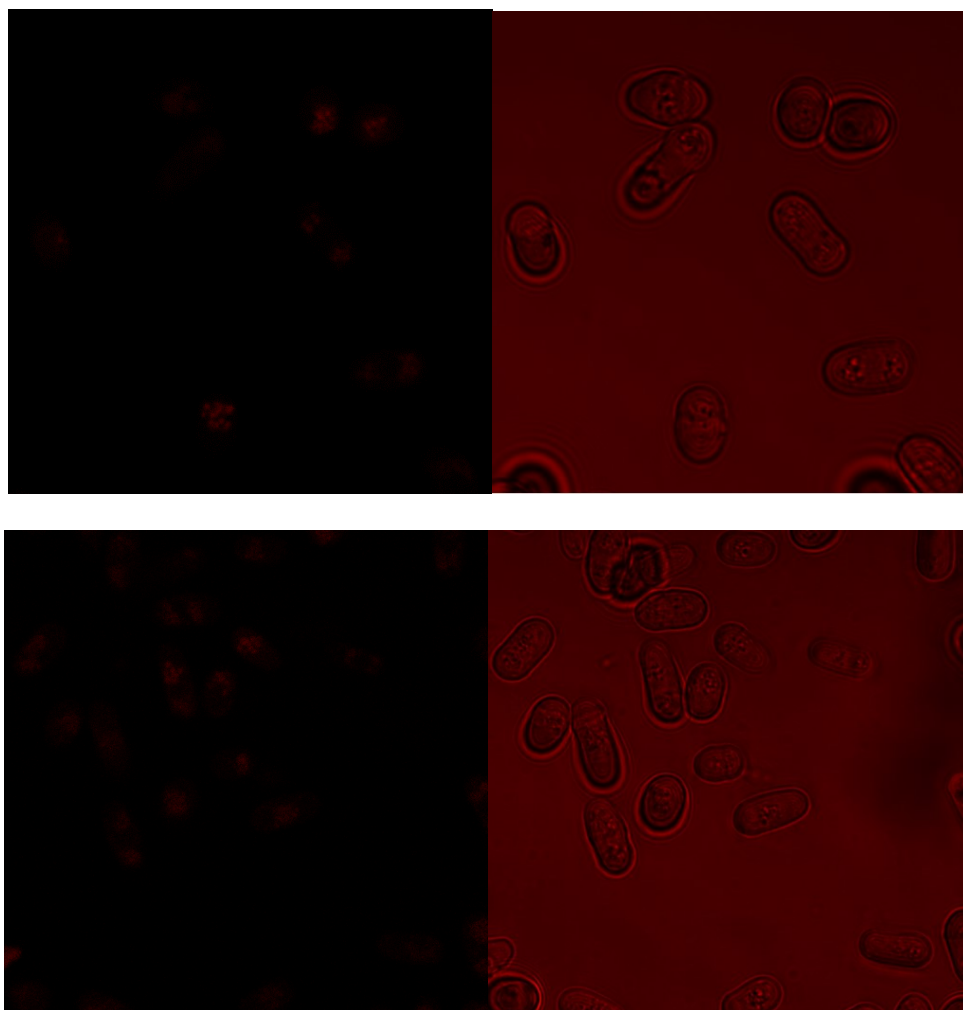


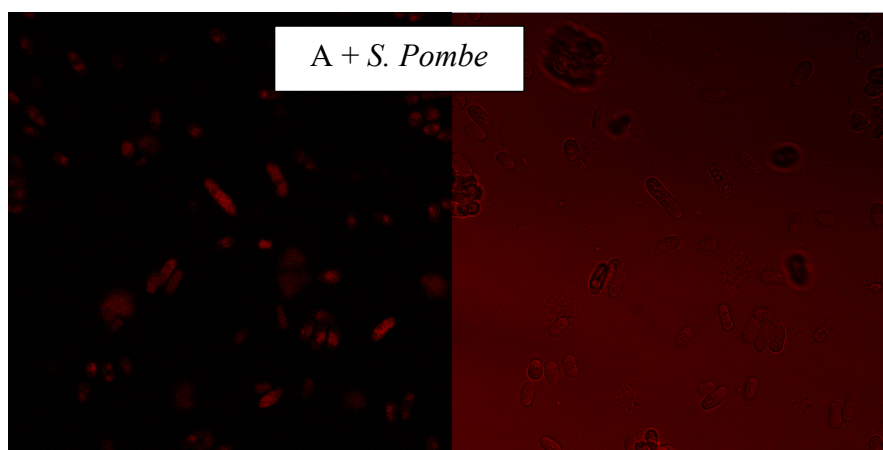
Figure 2.25: *C. Utilis* N = nucleus, M= mitochondria, V = vacuole ; bar = 1 $\mu$ m.<sup>37</sup>

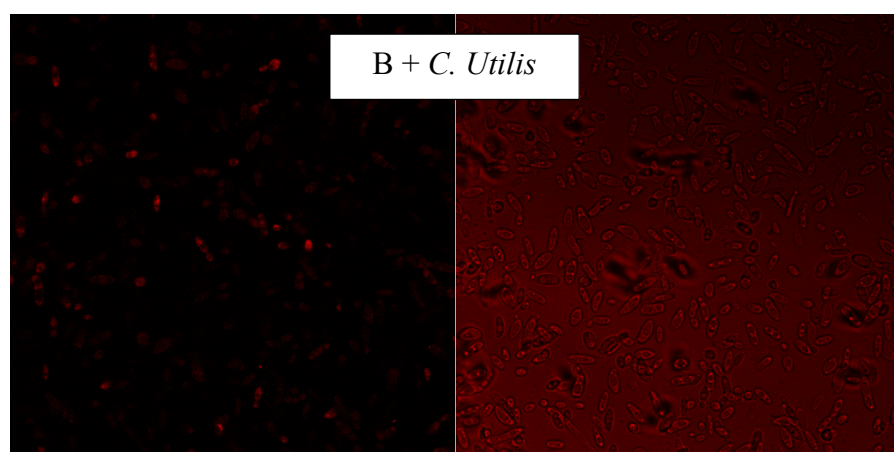
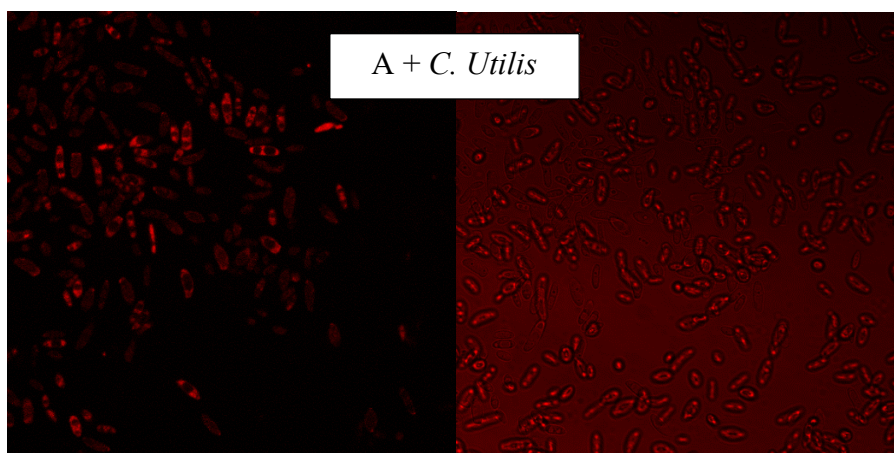
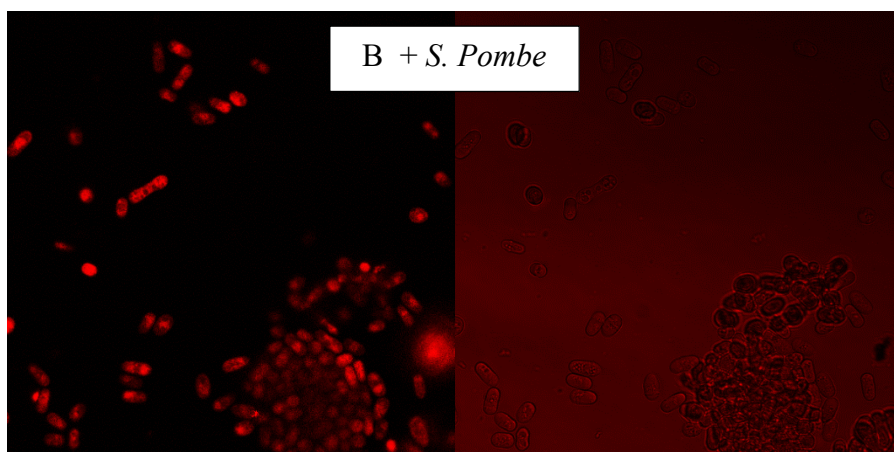
Confocal images were obtained for *S. Pombe* by exciting at 405 nm and detecting between 410-580nm. Images were compared to a control without the addition of dye A (**2-Nitroimidazole**), to assess the degree of autofluorescence present. In both cases, with and without the dye, a small degree of luminescence within the cells was observed. From this it was assumed that little, if any, dye had entered into the cells. Repeating the experiment, but additionally adding glucose to the starved cells, made no difference to the observed results. From these it was decided to investigate whether a longer exposure to the imaging agent was required to observe reagent uptake.



**Figure 2.26: Top left: autofluorescence of *S. Pombe*. Bottom left fluorescence image of *S. Pombe* exposed to A and B for 10 minutes. Images to the right are the brightfield images of each fluorescent image.**

At this point, A and B were used with all three cell lines using the same conditions as in the previous experiment except that the cells were now left with the reagent overnight (18 hours).





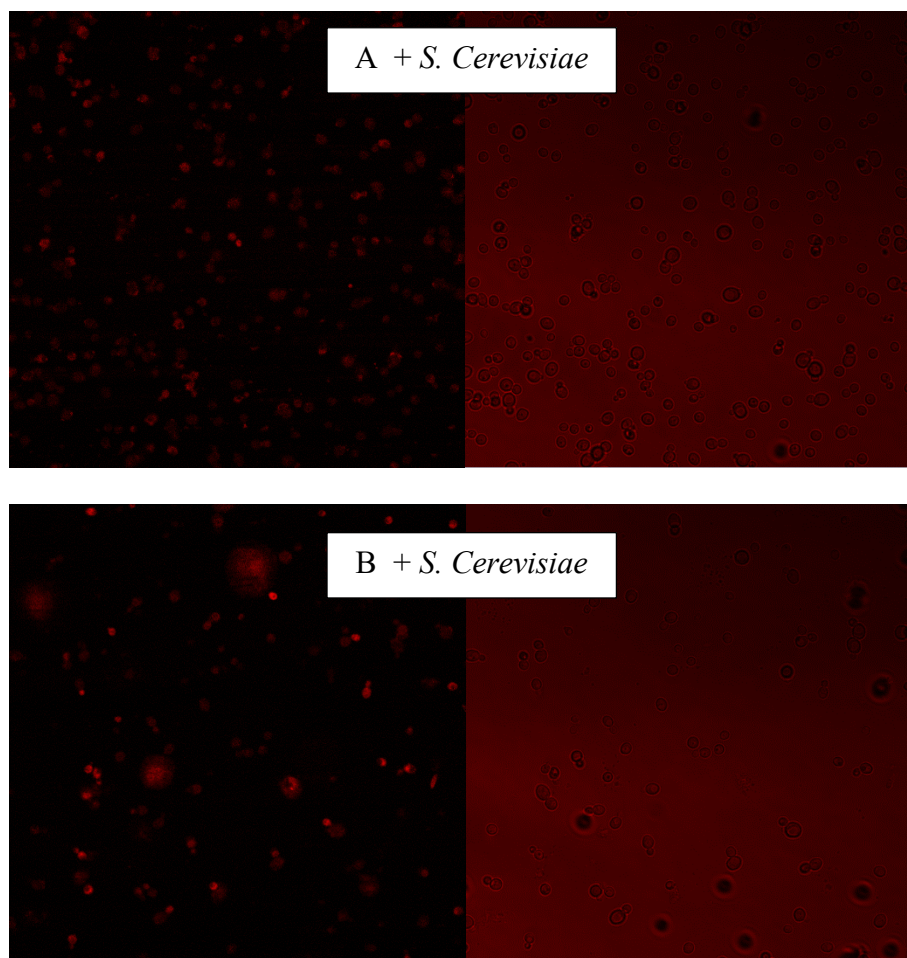


**Figure 2.27: Top left: autofluorescence of *S. Pombe*. Bottom left: fluorescence image of *S. Pombe* exposed to A and B for 18 hours. Images to the right are the brightfield images of each fluorescent image**

In addition, control experiments were carried out for the cells of *C. Utiis* and *S. Cerevisiae*, which demonstrated negligible auto-fluorescence when compared to the labelled cells. From the images it is clear that significant reagent has occurred over the prolonged period. In additions, for *S. Pombe* and *S. Cerevisiae*, there appears to be greater uptake when using the less soluble 2-methyl -5-nitroimidazole reagent, **B**. In all images, no selectivity of the reagent for a specific part of the cell was observed. That is, fluorescent reagent did not appear to localise in the nucleus, mitochondria or vacuoles. However, when *S. Cerevisiae* was imaged with **B**, it did appear that the budding daughter cells were brighter than the mother cell, perhaps suggested that (i) either the young cell wall was more permeable to the reagent or (ii)

that in the process of budding the interface between mother and daughter allowed the reagent to enter the cells, though why this would result in preferential localisation in the daughter cell is unclear.

## 2.7 Experimental section

### 2.7.1 Materials

All organic solvents were reagent grade and used as received unless stated otherwise.

Distilled water was used throughout the experiments. NMR studies were measured on a Bruker AM-400 or Bruker Av-500 or Ultrashield (300, 400 and 500 MHz). Infrared spectra were recorded on a FT/IR-660 Plus Fourier Transform infrared spectrometer (JASCO). Mass spectra were produced using a Waters LCT Premier XE spectrometer. UV–visible spectra recorded on a Lambda 20 (Perkin Elmer); measurements were performed at 25 °C.

Luminescence spectra were obtained on a HORIBA Scientific Jobin Yvon Fluorolog 3 spectrophotometer using quartz cuvettes with a path length of 1cm.

#### **N-(2-Aminoethyl)-1,8 naphthalimide, 2.1**

It was prepared according to a modified literature procedure<sup>19</sup>. 1,8-naphthalic anhydride (5 g, 25 mmol) was dispersed in H<sub>2</sub>O (50 ml) and added dropwise for 30 minutes to a solution of ethylenediamine (11.1 ml, 0.17 mmol). The reaction mixture was stirred and heated at 70 °C. Then the precipitate formed was heated at 80 °C for additional 15min, a light brown precipitate was filtered. The filtered solution was remained at room temperature overnight. yellow crystals were obtained yield (4.65 g, 77%). <sup>1</sup>H NMR (300 MHz, CDCl<sub>3</sub>) δ 8.63 (d, *J* = 7.2 Hz, 2H), 8.24 (d, *J* = 8.3 Hz, 2H), 7.78 (t, *J* = 7.8 Hz, 2H), 4.31 (t, *J* = 6.6 Hz, 2H), 3.09

(t,  $J = 6.6$  Hz, 2H); IR: 3350(s), 3289(s), 1698(s), 1654(s), 1625(s), 1589(s)  $\text{cm}^{-1}$ ; MS ES<sup>+</sup> [M+H]<sup>+</sup> calcd for[C<sub>14</sub>H<sub>12</sub>N<sub>2</sub>O<sub>2</sub>]: 241.26; found: 241.9; UV (chloroform, nm)= 345.

## **2 (2-Aminoethyl)-6-chloro-1H-benzo[de]isoquinoline-1,3(2H)-dione, 2.2**

It was prepared according to a modified literature procedure<sup>20</sup>. A suspension of 4-chloro-1,8-naphthalic anhydride (1 g, 5mmol) in H<sub>2</sub>O (5 ml) was added dropwise over 10 minutes to a solution of ethylenediamine (2.2 ml, 33mmol) in water 12ml. The reaction mixture was stirred and heated at 75 °C. Then the precipitate formed was heated at this temperature for 30 minutes. The precipitate was filtered and was recrystallised from chloroform. The desired product was yellow powder. <sup>1</sup>H NMR (400 MHz, CDCl<sub>3</sub>)  $\delta$  8.60 (d,  $J = 7.3$  Hz, 1H), 8.54 (d,  $J = 8.5$  Hz, 1H), 8.44 (d,  $J = 7.9$  Hz, 1H), 7.77 (t,  $J = 8.0$  Hz, 2H), 4.20 (t,  $J = 6.6$  Hz, 2H), 3.00 (t,  $J = 6.6$  Hz, 2H); <sup>13</sup>C NMR (126 MHz, CDCl<sub>3</sub>)  $\delta$  164.06, 163.81, 139.24, 132.17, 131.33, 130.77, 129.35, 129.15, 127.88, 127.41, 122.99, 121.49, 43.19, 40.45.

## **2-(2-Aminoethyl)-6-morpholino-1H-benzo[de]isoquinoline-1,3(2H)-dione, 2.3:**

The synthesis of this compound was prepared according to a modified literature procedure<sup>21</sup>.

This procedure includes two steps;

Synthesis of 6-morpholino-1H,3H-benzo[de]isochromene-1,3-dione. Morpholine (1.4g, 16mmol) was added dropwise to a suspension of 4-chloro-1,8-naphthalic anhydride (0.8 g, 4mmol) in ethylene monomethyl ether. The reaction mixture was refluxed for 2 days under N<sub>2</sub>. Then 3 drops of morpholine was added and the reaction mixture was refluxed in atmosphere for one more day. The reaction solution was remained in room temperature, orange crystals formed which was filtered and washed with water to give 6-morpholino-1H,3H-benzo[de]isochromene-1,3-dione as dark yellow crystals. Yield (71 %). <sup>1</sup>H NMR (300 MHz,

CDCl<sub>3</sub>): 8.60 (d, *J* = 7.2 Hz, 1H), 8.54 (d, *J* = 8.1 Hz, 1H), 8.48 (d, *J* = 8.5 Hz, 1H), 7.76 (t, *J* = 7.5 Hz, 1H), 7.26 (d, *J* = 8.0 Hz, 1H), 4.44 (t, *J* = 4.5 Hz, 4H), 4.04 (t, *J* = 4.1 Hz, 4H).

preparation of 2-(2-aminoethyl)-6-morpholino-1H-benzo[de]isoquinoline-1,3(2H)-dione:

A solution of (0.0566 g, 2 mmol) 6-morpholino-1H,3H-benzo[de]isochromene-1,3-dione in EtOH 20 ml was added dropwise to a solution of ethylenediamine (120 g, 2 mmol) in EtOH 20 ml. the mixture was refluxed for 16 hours. The solid was filtered and the solvent was evaporated from filtrate which was washed with water to give the product as dark yellow powder. Yield (60 %). <sup>1</sup>H NMR (300 MHz, CDCl<sub>3</sub>) δ 8.61 (d, *J* = 7.3 Hz, 1H), 8.55 (d, *J* = 8.0 Hz, 1H), 8.44 (d, *J* = 8.5 Hz, 1H), 7.73 (t, *J* = 7.9 Hz, 1H), 7.25 (d, *J* = 8.1 Hz, 1H), 4.29 (t, *J* = 6.5 Hz, 2H), 4.03 (t, *J* = 3.8 Hz, 4H), 3.28 (t, *J* = 4.0 Hz, 3.0, 4H), 7 (t, *J* = 6.5 Hz, 2H).

#### **2-(2-Methyl-5-nitroimidazole-1-ethyl 4- methylbenzene sulfonate, 2.4**

This synthesis was prepared according to a literature procedure<sup>22</sup>. <sup>1</sup>H NMR (300 MHz, DMSO) δ 7.92 (s, 1H), 7.59 (d, *J* = 8.2 Hz, 2H), 7.39 (d, *J* = 8.2 Hz, 2H), 4.54 (t, *J* = 4.8 Hz, 2H), 4.38 (t, *J* = 4.8 Hz, 2H), 2.48 (s, 6H); IR: 3132(w), 2976(w), 1597(s), 1523(s), 1462(m), 1390(m), 1355(s), 1167(s).

#### **2-(2-Methyl-5-nitro-imidazol-1-yl)-ethyl methanesulfonate, <sup>23</sup>2.6**

Metronidazole (5 g, 29.2 mmol), TEA (6.1 mL, 4.4 g, 43.9 mmol, 1.5 equiv.) were suspended in CH<sub>2</sub>Cl<sub>2</sub> (25 mL) and cooled to (~10°C). Then A solution of methanesulfonyl chloride (2.7mL, 4g, 34.9 mmol, 1.2 equiv.) in CH<sub>2</sub>Cl<sub>2</sub> (5 mL) was added dropwise to the previous suspension. The reaction mixture was stirred at room temperature for 3 days and the precipitate was remained in solution for 2 days. Then the solid was filtered and washed with H<sub>2</sub>O thoroughly to give white solid. (7.1 g, 97%). <sup>1</sup>H NMR (300 MHz, DMSO) δ 8.07 (s, 1H),

4.65 (t,  $J = 5.0$  Hz, 2H), 4.55 (t,  $J = 5.0$  Hz, 2H), 3.15 (s, 3H), 2.46 (s, 3H);  $^{13}\text{C}$  NMR (101 MHz, DMSO)  $\delta$  13.9, 36.6, 45, 68.4, 133, 138, 151.6

**4-(2-(2-Methyl-5-nitro-1H-imidazol-1-yl)ethoxy benzaldehyde, 2.7:**

It was prepared according to a literature procedure<sup>18</sup> which involves addition of 4-hydroxybenzaldehyde (0.366 g, 3.0 mmol) to a solution of 2-(2-methyl-5-nitro-imidazol-1-yl)-ethyl methanesulfonate (0.747 g, 3.0 mmol) in 2 mL DMF, potassium carbonate (0.828 g, 6.0 mmol). The suspension was heated to 85°C for 48 h (the reaction was monitored by TLC plate). After cooling, the solvent was removed by vacuum line then water (3 mL) was added to the residue. The solid was filtered and washed with water (3 time\*50 ml). The product was obtained as dark yellow powder. Yield: (0.58 g, 69%);  $^1\text{H}$  NMR (400 MHz, DMSO)  $\delta$  9.87 (s, 1H), 8.05 (s, 1H), 7.86 (d,  $J = 7.7$  Hz, 2H), 7.10 (d,  $J = 8.2$  Hz, 2H), 4.65 (t,  $J = 5.0$  Hz, 2H), 4.55 (t,  $J = 5.0$  Hz, 2H), 2.46 (s, 3H);  $^{13}\text{C}$  NMR (101 MHz, DMSO)  $\delta$  14, 45, 67, 115, 130, 132, 133, 139, 152, 163, 190; IR: 3133(w), 2960(w), 1674(s), 1577(s), 1531(s), 1508(s), 1432(m), 1377(s), 1361(s)  $\text{cm}^{-1}$ .

**(E)-2-(2-((4-(2-(2-methyl-5-nitro-1H-imidazol-1-yl)ethoxy)benzylidene)amino)ethyl)-1H-benzo[de]isoquinoline-1,3(2H)-dione, 2.8:**

A mixture of 4-(2-(2-methyl-5-nitro-1H-imidazol-1-yl)ethoxy benzaldehyde (0.275g, 1 mmol) and aminoethyl)-1,8 naphthalimide (240, 1mmol), in ethanol (20 mL) was stirred for 17 hours (the reaction was monitored by TLC). The solid obtained was filtered and wash with ethanol to give a beige powder yield (0.337g, 67%).  $^1\text{H}$  NMR (400 MHz, DMSO)  $\delta$  8.49 (dd,  $J = 16.2, 8.2$  Hz, 4H), 8.28 (s, 1H), 8.05 (s, 1H), 7.93 – 7.83 (m, 2H), 7.62 (d,  $J = 8.8$  Hz, 2H), 6.92 (d,  $J = 8.7$  Hz, 2H), 4.72 (t,  $J = 4.8$  Hz, 2H), 4.35 (dt,  $J = 14.5, 6.2$  Hz, 4H), 3.80 (t,  $J = 7.1$  Hz, 2H), 2.30 (s, 3H).  $^{13}\text{C}$  NMR (101 MHz, DMSO)  $\delta$  14.7, 30.1, 45.8, 58.0, 67.0, 115.0,

122.1, 129.3, 130.06, 131.2, 131.5, 133.07, 135.2, 152.7, 160.2, 162.5, 164.0; IR: 3124(w), 2956(w), 2845(w), 1695(s), 1625(s), 1608(s), 1514(s), 1436(m), 1450(m), 1379(s), 1338(s), 1105(vs)  $\text{cm}^{-1}$ ; HR MS ES<sup>+</sup> [M+H]<sup>+</sup> calcd for [C<sub>27</sub>H<sub>23</sub>N<sub>5</sub>O<sub>5</sub>]: 498.1777; found: 498.1768; UV-vis (CH<sub>3</sub>Cl):  $\lambda_{\text{max}}$  ( $\epsilon / \text{M}^{-1}\text{cm}^{-1}$ ) = 264(19,375), 311(20,000), 321(17375), 331(17,583), 348(12,250) nm.

**(E)-6-chloro-2-(2-((4-(2-(2-methyl-5-nitro-1H-imidazol-1-yl)ethoxy)benzylidene)amino)ethyl)-1H-benzo[de]isoquinoline-1,3(2H)-dione, 2.9:**

A mixture of 4-(2-(2-methyl-5-nitro-1H-imidazol-1-yl)ethoxy)benzaldehyde (0.68g, 187 mmol) and 2-(2-aminoethyl)-6-chloro-1H-benzo[de]isoquinoline-1,3(2H)-dione (0.68g, 186.3 mmol), in ethanol (20 mL) was stirred for 24 hours (the reaction was monitored by TLC). The solid obtained was filtered and washed with ethanol to give a yellow powder (0.50 g, 38%).

<sup>1</sup>H NMR (400 MHz, DMSO)  $\delta$  8.62 (t,  $J = 8.0$  Hz, 2H), 8.46 (d,  $J = 7.8$  Hz, 1H), 8.46 (d,  $J = 7.8$  Hz, 1H), 8.46 (d,  $J = 7.8$  Hz, 1H), 8.01 (s, 1H), 8.04 (t,  $J = 4.4$  Hz, 1H), 7.61 (d,  $J = 8.5$  Hz, 2H), 6.92 (d,  $J = 8.7$  Hz, 2H), 4.72 (t,  $J = 5.0$  Hz, 2H), 4.37 (t,  $J = 4.9$  Hz, 2H), 4.37 (t,  $J = 4.9$  Hz, 2H), 3.79 (d,  $J = 6.9$  Hz, 2H), 2.30 (s, 3H). <sup>13</sup>C NMR (126 MHz, CDCl<sub>3</sub>)  $\delta$  14.37, 40.92, 45.94, 58.45, 66.68, 108.75, 114.23, 121.58, 123.8, 124.88, 128.51, 129.37, 129.62, 129.64, 129.88, 130.07, 130.39, 139.30, 159.63, 162.54, 163.50, 163.54; IR: 3122(w), 2962(w), 1699(s), 1668(s), 1651(s), 1635(s), 1558(s), 1541(s), 1516(s), 1508(s), 1456(m), 1373(s), 1346(s), 1051(vs)  $\text{cm}^{-1}$ ; HR MS ES<sup>+</sup> [M+H]<sup>+</sup> calcd for [C<sub>27</sub>H<sub>22</sub>ClN<sub>5</sub>O<sub>5</sub>]: 532.1388; found: 532.1379; UV (chloroform, nm) = 377, 354, 323, 267 nm. UV-vis (CH<sub>3</sub>Cl):  $\lambda_{\text{max}}$  ( $\epsilon / \text{M}^{-1}\text{cm}^{-1}$ ) = 264(25,550), 327(23,807), 342(27,192), 358(18,692) nm.

**(E)-2-(2-((4-(2-(2-methyl-5-nitro-1H-imidazol-1-yl)ethoxy)benzylidene)amino)ethyl)-6-morpholino-1H-benzo[de]isoquinoline-1,3(2H)-dione, 2.10:**

A mixture of 4-(2-(2-methyl-5-nitro-1H-imidazol-1-yl)ethoxy benzaldehyde (0.137g, 0.5 mmol) and 2-(2-aminoethyl)-6-morpholino-1H-benzo[de]isoquinoline-1,3(2H)-dione (0.162g, 0.5 mmol), in ethanol (20 mL) was stirred for 24 hours (the reaction was monitored by TLC). The solid was filtered then it was purified by column chromatography on silica gel (acetonitrile) to afford compound 10 as dark yellow powder yield (0.103g, 35%);  $^1\text{H}$  NMR (400 MHz, DMSO)  $\delta$  8.62 (t,  $J = 8.0$  Hz, 2H), 8.46 (d,  $J = 7.8$  Hz, 1H), 8.46 (d,  $J = 7.8$  Hz, 1H), 8.46 (d,  $J = 7.8$  Hz, 1H), 8.01 (s, 1H), 8.04 (t,  $J = 4.4$  Hz, 1H), 7.61 (d,  $J = 8.5$  Hz, 2H), 6.92 (d,  $J = 8.7$  Hz, 2H), 4.72 (t,  $J = 5.0$  Hz, 2H), 4.37 (t,  $J = 4.9$  Hz, 2H), 4.37 (t,  $J = 4.9$  Hz, 2H), 4.01 (t, 4H), 3.79 (d,  $J = 6.9$  Hz, 2H), 3.27 (t, 4H), 2.30 (s, 3H).  $^{13}\text{C}$  NMR (126 MHz, CDCl<sub>3</sub>)  $\delta$  14.37, 40.92, 45.94, 53.25, 58.45, 65.33, 66.68, 114.05, 115.05, 118.76, 123.98, 125.05, 125.05, 129.88, 130.02, 132.54, 133.12, 134.43, 152.22, 156.45, 159.98, 162.22, 164.02, 165.01; IR: 3122(w), 2962(w), 1699(s), 1668(s), 1651(s), 1635(s), 1558(s), 1541(s), 1516(s), 1508(s), 1456(m), 1373(s), 1346(s), 1051(vs)  $\text{cm}^{-1}$ ; HR MS ES<sup>+</sup> [M+H]<sup>+</sup> calcd for [C<sub>27</sub>H<sub>23</sub>N<sub>5</sub>O<sub>5</sub>]: 583.2305; found: 583.2311; UV-vis (CH<sub>3</sub>Cl):  $\lambda_{\text{max}}$  ( $\epsilon / \text{M}^{-1}\text{cm}^{-1}$ ) = 259(9,862), 317(3,600), 323(4068), 339(2,693), 391(4,034) nm.

**(E)-2-(2-((4-hydroxybenzylidene)amino)ethyl)-1H-benzo[de]isoquinoline-1,3(2H)-dione,**

**2.11:**

Compounds **2.11** was synthesized and purified according to the following procedure: A mixture of 4-hydroxybenzaldehyde (0.122g, 1 mmol) and n-(2-Aminoethyl)-1,8 naphthalimide (0.240g, 1 mmol) in ethanol was stirred for 19 hours (the reaction was monitored by TLC). The solid obtained was filtered and washed with ethanol to give the desire product as a white powder yield (189g, 69%).  $^1\text{H}$  NMR (300 MHz, DMSO)  $\delta$  8.49 (dd,  $J = 13.2, 7.8$  Hz, 4H), 8.22 (s, 1H), 7.88 (t,  $J = 7.8$  Hz, 2H), 7.52 (d,  $J = 8.3$  Hz, 2H), 6.77 (d,  $J = 8.4$  Hz, 2H), 4.31 (t,  $J = 7.1$  Hz, 2H), 3.78 (t,  $J = 7.0$  Hz, 2H);  $^{13}\text{C}$  NMR (101 MHz, DMSO)  $\delta$  163.86, 162.09,

160.31, 134.83, 131.77, 131.22, 130.14, 127.83, 127.71, 122.49, 115.84, 58.09, 40.84; IR: 3037(w), 2877(w), 2786(w), 1701(vs), 1696(vs), 1436(m), 1063(vs)  $\text{cm}^{-1}$ ; MS  $\text{ES}^+$   $[\text{M}+\text{H}]^+$  calcd for 345.1227; found: 345.12; UV-vis (DMSO):  $\lambda_{\text{max}}$  ( $\epsilon / \text{M}^{-1}\text{cm}^{-1}$ ) = 269(9,705), 291(5,588), 300(4,764), 351 (6,758) nm.

### **2- Aminoimidazole:**

It was synthesised according to literature procedure.<sup>38</sup> Yield: 1.75 g brown powder:  $^1\text{H}$  NMR (400 MHz,  $\text{D}_2\text{O}$ ): 6.5 (s, 2H). IR: 3150(w), 3000(w), 2750(w), 1680(m)  $\text{cm}^{-1}$ .

### **2-Nitroimidazole:**

It was synthesised and purified according to previously reported method described by Agrawal *et. al*<sup>28</sup>

A mixture of 2-Aminoimidazolium sulfate (1.57 g, 5.94 mmol) and fluoboric acid was dissolved in water (10 mL). The solution was cooled to  $-20\text{ }^\circ\text{C}$  in an ice-salt bath. sodium nitrite (4.1 g, 59.4 mmol) was dissolved in water (10 mL) then was added to the cooled 2-aminoimidazolium sulfate solution. The reaction mixture was stirred at  $-10\text{ }^\circ\text{C}$  for 3 hours. This mixture was added to a solution of  $\text{CuSO}_4 \cdot 5\text{H}_2\text{O}$  (29.7 g, 119 mmol) in water 200 ml. 4.1 g of sodium nitrite was added to the reaction mixture and was stirred for 12 hours. Dilute  $\text{HNO}_3$  was added to the mixture in order to adjust the PH to 2. The mixture was reaction was the reaction was quenched with  $\text{H}_2\text{O}$  and extracted with EtOAc. The combined organic layers were dried over ( $\text{MgSO}_4$ ) then the solution was concentrated in vacuum a yellow-coloured residue was obtained. The residue was washed with 10 mL of  $\text{Et}_2\text{O}$  then it was recrystallized from EtOH to obtain small yellow crystals (0.120g ,5 %).  $^1\text{H}$  NMR (400 MHz, DMSO)  $\delta$ 6.62 (s, 2H); IR: 3163(w), 2970(w), 2846(w), 1541(s), 1517(s), 1361(s), 1338(s).

### **1(2-((*tert*-butyldimethylsilyl)oxy)ethyl)-2-nitro-1*H*-imidazole, 2.12**

2-nitroimidazole (1.2g, 10.62mmol) and  $K_2CO_3$  (7g, 21.24mmol) was stirred in DMF (10mL). (2-bromoethoxy)(*tert*-butyl)dimethylsilane (2.8g, 11.68mmol) was added dropwise to the mixture. The mixture was heated under  $N_2$  at 80°C for overnight. The reaction was quenched with  $H_2O$  and extracted with EtOAc. The combined organic layers were dried over  $Mg_2SO_4$ . The solvent was evaporated. The crude was then washed with  $H_2O$  to obtain yellow crystals.  $^1H$  NMR (400 MHz, DMSO)  $\delta$  7.72 (d,  $J = 1.0$  Hz, 1H), 7.29 (d,  $J = 1.0$  Hz, 1H), 4.65 (t,  $J = 5.2$  Hz, 2H), 4.00 (t,  $J = 5.2$  Hz, 2H), 0.88 (s, 9H), 0.01 (s, 6H); IR: 3115(w), 2927(w), 2854(w), 1527(s), 1498(m), 1479(m), 1361, 1338(m), 1325(m)  $cm^{-1}$ .

### **2-(2-Nitro-1H-imidazol-1-yl)ethanol, 2.13**

1(2-((*tert*-butyldimethylsilyl)oxy)ethyl)-2-nitro-1H-imidazole (1g, 3.69mmol) was dispersed in MeOH (50mL) then HCl 37% (3 ml) was added dropwise. The reaction mixture was stirred at room temperature for 48 hours (the completion of reaction was monitored with TLC). The solution was concentrated in vacuum and purified by column chromatography on silica gel (DCM: MeOH = 80: 1) to obtained compound 3 (1.8g, 70%) as yellow powder.  $^1H$  NMR (300 MHz, DMSO) 7.66 (d,  $J = 1.0$  Hz, 1H), 7.18 (d,  $J = 1.0$  Hz, 1H), 4.72 (s, 1H), 4.47 (t,  $J = 5.3$  Hz, 2H), 3.71 (t,  $J = 5.3$  Hz, 2H); IR: 3213(w), 3099(w), 2848(w), 1539(s), 1533(s), 1506(s), 1489(m), 1363(s), 1072(vs)  $cm^{-1}$ .

### **2-(2-Nitro-1H-imidazol-1-yl)ethyl hydrogen sulfate, 2.14**

2-(2-nitro-1H-imidazol-1-yl)ethanol (5 g, 29.2 mmol), TEA (6.1 mL, 4.4 g, 43.9 mmol, 1.5 equiv.) were dissolved in  $CH_2Cl_2$  (25 mL) and cooled to ( $\sim 10^\circ C$ ). Then A solution of methanesulfonyl chloride (2.7mL, 4g, 34.9 mmol, 1.2 equiv.) in  $CH_2Cl_2$  (5 mL) was added dropwise for one hour to the previous suspension. The reaction mixture was stirred at r.t. for 3 days. Then it was extracted with ethyl acetate (20 ml\*5 times). Ethyl acetate layers were

combined and dried with MgSO<sub>2</sub>. The solvent was evaporated to obtain the product as yellow solid. <sup>1</sup>H NMR (300 MHz, CDCl<sub>3</sub>) δ 7.24 (d, *J* = 6.4 Hz, 1H), 7.21 (d, *J* = 11.6 Hz, 1H), 4.47 (t, *J* = 5.3 Hz, 2H), 3.71 (t, *J* = 5.3 Hz, 2H), 3.00 (s, 20H); <sup>13</sup>C NMR (101 MHz, DMSO) δ 155.232, 128.87, 128.22, 68.74, 48.93, 37.19; IR: 3115(w), 3095(w), 2964(w), 1539(s), 1506(s), 1487(m), 1340(s), 1364(s), 1172(vs) cm<sup>-1</sup>.

#### **4-(2-(2-Nitro-1H-imidazol-1-yl)ethoxy)benzaldehyde, 2.15**

4-Hydroxybenzaldehyde (0.329g, 2.7 mmol) was added to a solution of 2-(2-nitro-1H-imidazol-1-yl)ethyl methanesulfonate (0.534g, 2.7 mmol) in 2 mL DMF, potassium carbonate (0.745g, 5.4 mmol). The suspension was heated to 85<sup>0</sup>C for 48 h (the reaction was monitored by TLC plate. After cooling, the solvent was removed by vacuum line then water (3 mL) was added to the residue. The solid was filtered and washed with water (15ml). The desired product was obtained as a beige powder yield (0.395g, 66%). <sup>1</sup>H NMR (500 MHz, DMSO) δ 9.87 (s, 1H), 7.86 (d, *J* = 8.1 Hz, 2H), 7.73 (s, 1H), 7.20 (s, 1H), 7.10 (d, *J* = 8.1 Hz, 2H), 4.85 (t, *J* = 5.0 Hz, 2H), 4.50 (t, *J* = 5.0 Hz, 2H); <sup>13</sup>C NMR (126 MHz, DMSO) δ 191.90, 163.20, 132.28, 130.54, 128.78, 127.92, 115.24, 67.08, 48.86; IR: 3147(w), 3035(w), 2864(w), 2758(w), 1683(s), 1589(s), 1558(s), 1525(s), 1508(s), 1475(m), 1355(s), 1340(s), 1305(s) cm<sup>-1</sup>; HR MS ES+ [M+H]<sup>+</sup> calcd for [C<sub>12</sub>H<sub>11</sub>N<sub>3</sub>O<sub>4</sub>]; 262.0828; found 262.0834. UV-vis (CH<sub>3</sub>Cl): λ<sub>max</sub> (ε /M<sup>-1</sup>cm<sup>-1</sup>) = 272(97,538), 323(10,516) nm.

#### **(E)-2-(2-((4-(2-(2-nitro-1H-imidazol-1-yl)ethoxy)benzylidene)amino)ethyl)-1H-benzo[de]isoquinoline-1,3(2H)-dione, 2.16**

Compound **16** was synthesized and purified according to the following procedure: A mixture of 4-(2-(2-nitro-1H-imidazol-1-yl)ethoxy)benzaldehyde (0.065, 0.25 mmol) and *n*-(2-Aminoethyl)-1,8 naphthalimide (0.060, 0.25 mmol), in ethanol (20 mL) was stirred for 24

hours (the reaction was monitored by TLC). The solid obtained was filtered to give the product as a beige powder, yield (0.053g, 44%).  $^1\text{H}$  NMR (400 MHz, DMF)  $\delta$  8.91 (dd,  $J$  = 16.8, 7.6 Hz, 4H), 8.70 (s, 1H), 8.30 (t,  $J$  = 6.6 Hz, 2H), 8.12 (s, 1H), 8.04 (d,  $J$  = 7.9 Hz, 2H), 7.61 (s, 1H), 7.35 (d,  $J$  = 8.3 Hz, 2H), 5.23 (t,  $J$  = 3.2 Hz, 2H), 4.81 (t,  $J$  = 4.4 Hz, 2H), 4.75 (t,  $J$  = 5.8 Hz, 2H), 4.23 (t,  $J$  = 6.0 Hz, 2H).  $^{13}\text{C}$  NMR (101 MHz, DMSO)  $\delta$  163.86, 161.83, 160.20, 134.82, 131.77, 131.22, 129.98, 129.77, 128.67, 128.07, 127.82, 127.70, 122.47, 115.00, 66.72, 58.10, 48.93, 40.75; IR: 3032(w), 2960(w), 2836(w), 1697(w), 1662(s), 1604(s), 1541(s), 1508(s), 1478(m), 1363(s), 1338(s), 1307(s)  $\text{cm}^{-1}$ ; HR MS ES+  $[\text{M}+\text{H}]^+$  calcd for  $[\text{C}_{26}\text{H}_{22}\text{N}_5\text{O}_5]$ ; 484.1621; found:484.1624. UV-vis ( $\text{CH}_3\text{Cl}$ ):  $\lambda_{\text{max}}$  ( $\epsilon/\text{M}^{-1}\text{cm}^{-1}$ ) = 266(11,166), 320(8,458), 332(9,083), 3489(6,958) nm.

**(E)-6-morpholino-2-(2-((4-(2-(2-nitro-1H-imidazol-1-yl)ethoxy)benzylidene)amino)ethyl)-1H-benzo[de]isoquinoline-1,3(2H)-dione, 2.17**

Compounds **17** was synthesized and purified according to the following procedure: A mixture of 4-(2-(2-nitro-1H-imidazol-1-yl)ethoxy)benzaldehyde (0.130g, 0.50 mmol) and 2-(2-aminoethyl)-6-morpholino-1H-benzo[de]isoquinoline-1,3(2H)-dione (162g, 0.50 mmol), in ethanol (20 mL) was stirred for 24 hours (the reaction was monitored by TLC). The solid obtained was filtered then it was purified by column chromatography on silica gel (acetonitrile) to give the product as a yellow powder yield (46g, 17%);  $^1\text{H}$  NMR (400 MHz, DMSO)  $\delta$  8.49 (dd,  $J$  = 8.3, 5.0 Hz, 2H), 8.42 (d,  $J$  = 8.1 Hz, 1H), 8.27 (s, 1H), 7.87 – 7.77 (m, 1H), 7.70 (s, 1H), 7.62 (d,  $J$  = 8.8 Hz, 2H), 7.36 (d,  $J$  = 8.2 Hz, 1H), 7.19 (s, 1H), 6.93 (d,  $J$  = 8.8 Hz, 2H), 4.82 (t,  $J$  = 5.1 Hz, 2H), 4.40 (t,  $J$  = 5.2 Hz, 2H), 4.30 (t,  $J$  = 7.1 Hz, 2H), 3.95 – 3.88 (m, 4H), 3.79 (t,  $J$  = 6.8 Hz, 2H), 3.25 – 3.20 (m, 4H);  $^{13}\text{C}$  NMR (101 MHz, DMSO)  $\delta$  164.01, 163.48, 161.77, 160.20, 155.94, 132.69, 131.18, 131.07, 129.99, 129.79, 129.61, 128.67, 128.07, 126.61, 125.76, 123.04, 116.29, 115.59, 115.00, 66.73, 66.66, 58.19,

53.50, 48.93, 31.17; IR: 3232(s), 1685(s), 165(s), 1597(w), 1539/9s), 1508(s), 1434(m), 1357(s), 1307(s), 1161(vs)  $\text{cm}^{-1}$ . HR MS ES+[M+H]<sup>+</sup> calcd for [C<sub>30</sub>H<sub>28</sub>N<sub>6</sub>O<sub>6</sub>]; 569.2149; found 569.2151; UV-vis (CH<sub>3</sub>Cl):  $\lambda_{\text{max}}$  ( $\epsilon / \text{M}^{-1} \text{cm}^{-1}$ ) = 268(1,278), 402(4250) nm.

### **Benzyl 2-(2-nitro-1H-imidazol-1-yl) acetate, 2.18**

Benzyl 2-bromoacetate (0.690g, 3mmol) was added to a solution of 2-nitroimidazole (0.339g, 3mmol) and K<sub>2</sub>CO<sub>3</sub> (414g, 3mmol) in acetonitrile 25ml. The suspension was refluxed under N<sub>2</sub> for 15 hours (the reaction was monitored by TLC). Precipitate was filtered then filtrate was reduced in a vacuum to yield brown sticky residue (0.442g, 56.44%); <sup>1</sup>H NMR (400 MHz, DMSO)  $\delta$  7.68 (d, J = 5.5 Hz, 1H), 7.55 – 7.27 (m, 5H), 7.23 (d, J = 14.0, 6.9 Hz, 1H), 5.40 (s, 2H), 5.09 (s, 2H); <sup>13</sup>C NMR (101 MHz, DMSO)  $\delta$  167.73, 135.78, 129.03, 128.99, 128.83, 128.56, 128.40, 67.28, 50.99. IR: 3124(w), 3109(w), 3030(w), 2956(w), 2895(w), 1739(vs), 16109s), 1541(s), 1504(s), 1489(m), 1454(m), 1359(s), 1386(s), 1200(vs)  $\text{cm}^{-1}$ ; MS ES+ [M+H]<sup>+</sup> calcd for [C<sub>12</sub>H<sub>11</sub>N<sub>3</sub>O<sub>4</sub>]: 262.24, found: 262.09.

### **N-(2-(1,3-dioxo-1H-benzo[de]isoquinolin-2(3H)-yl) ethyl)-2-(2-nitro-1H-imidazol-1-yl) acetamide, 2.19**

*N*-(2-Aminoethyl)-1,8 naphthalimide (0.120g, 0.5mmol) was added to a solution of benzyl 2-bromoacetate (0.130g, 0.5mmol) in acetonitrile 10ml. the suspension was refluxed under N<sub>2</sub> for 72 hours (the reaction was monitored by TLC). The solvent was evaporated in a vacuum. The residue was washed initially with diethyl ether then with acetone to remove the by-product (benzyl alcohol). Acetone was reduced in rotary evaporator. Yellow solid was washed again with acetone to yield pale yellow powder. Yield (0.050g, 25 %); <sup>1</sup>H NMR (300 MHz, DMSO)  $\delta$  8.51 (dd, J = 13.9, 7.4 Hz, 4H), 7.90 (t, J = 7.8 Hz, 2H), 7.57 (d, 1H), 7.15 (d, 1H), 5.00 (s, 2H), 4.17 (t, 2H), 3.46 (t, 2H); <sup>13</sup>C NMR (126 MHz, DMSO)  $\delta$  166.26, 164.15,

## Fluorescently Labelled Nitroimidazole

---

134.71, 131.77, 131.19, 129.17, 128.02, 127.82, 127.64, 122.71, 51.97, 39.49, 37.23;

IR:3280(w), 3128(w), 3113(w), 2960(w), 1668(s), 1660(s), 1622(s), 1587(s), 1537(s),

1487(m), 1377(s), 1340(s), 1184(vs)cm<sup>-1</sup>; MS ES+ [M+H]<sup>+</sup> calcd for [C<sub>19</sub>H<sub>15</sub>N<sub>5</sub>O<sub>5</sub>]: 394.36,

found 394.12.

## 2.8 References

- 1 J. Rao, A. Dragulescu-Andrasi and H. Yao, *Curr. Opin. Biotechnol.*, 2007, **18**, 17–25.
- 2 L. G. F. Patrick and A. Whiting, *Dye. Pigment.*, 2002, **52**, 137–143.
- 3 F. Karci, İ. Şener and H. Deligöz, *Dye. Pigment.*, 2003, **59**, 53–61.
- 4 M. Braña, J. Castellano, C. Roldán, A. Santos, D. Vázquez and A. Jiménez, *Cancer Chemother. Pharmacol.*, 1980, **4**, 61–66.
- 5 W. W. Stewart, *J. Am. Chem. Soc.*, 1981, **103**, 7615–7620.
- 6 W. Zhu, C. Hu, K. Chen and H. Tian, *Synth. Met.*, 1998, **96**, 151–154.
- 7 G. R. Bardajee, A. Y. Li, J. C. Haley and M. A. Winnik, *Dye. Pigment.*, 2008, **79**, 24–32.
- 8 L. Jia, Y. Zhang, X. Guo and X. Qian, *Tetrahedron Lett.*, 2004, **45**, 3969–3973.
- 9 H. Tian, J. Gan, K. Chen, J. He, Q. L. Song and X. Y. Hou, *J. Mater. Chem.*, 2002, **12**, 1262–1267.
- 10 E. Martin, R. Weigand and A. Pardo, *J. Lumin.*, 1996, **68**, 157–164.
- 11 Y. Liu, Y. Xu, X. Qian, J. Liu, L. Shen, J. Li and Y. Zhang, *Bioorg. Med. Chem.*, 2006, **14**, 2935–2941.
- 12 Z. Cimerman, S. Miljanic and N. Galic, *Croat. Chem. Acta*, 2000, **73**, 81–95.
- 13 K. Y. Lau, A. Mayr and K.-K. Cheung, *Inorganica Chim. Acta*, 1999, **285**, 223–232.
- 14 A. S. Shawali, N. M. S. Harb and K. O. Badahdah, *J. Heterocycl. Chem.*, 1985, **22**, 1397–1403.
- 15 H. Chabane, Y. Adjeroud and M. Liacha, *Org. Commun.*, 2017, **10**, 24–31.
- 16 K. Meenakshi, N. Gopal and M. Sarangapani, *Int. J. Pharm. Pharm. Sci.*, 2014, **6**, 318–322.
- 17 R. M. Ramadan, A. K. Abu Al-Nasr and O. A. M. Ali, *J. Mol. Struct.*, 2018, **1161**, 100–107.
- 18 N. E. Kassar, H. A. Saadeh, W. H. Talib, A. M. Mahasneh, H. Kaur, K. Goyal, R. Sehgal and M. S. Mubarak, *Med. Chem. Res.*, 2014, **23**, 4872–4882.
- 19 M. Licchelli, A. O. Biroli, A. Poggi, D. Sacchi, C. Sangermani and M. Zema, *Dalt. Trans.*, 2003, 4537–4545.
- 20 U. Samanta, SUVA and Pain, ANINDITA and Dutta, SUSANTA and Sanyal, *Acta Pol. Pharm.*, 2001, **58**, 351–356.
- 21 L. Song, X.-D. Sun, Y. Ge, Y.-H. Yao, J. Shen, W.-B. Zhang and J.-H. Qian, *Chinese Chem. Lett.*, 2016, **27**, 1776–1780.
- 22 H.-Q. Li, Z.-P. Xiao, R.-Q. Fang and H.-L. Zhu, *J. Chem. Crystallogr.*, 2008, **38**, 461–466.
- 23 E. L. Miyamoto Y1, Kalisiak J, Korthals K, Lauwaet T, Cheung DY, Lozano R, Cobo ER, Upercroft P, Upercroft JA, Berg DE, Gillin FD, Fokin VV, Sharpless KB, *PNAS*, 2013, **110**, 17564–17569.
- 24 C. B. Singh, V. Kavala, A. K. Samal and B. K. Patel, *European J. Org. Chem.*, 2007, **2007**, 1369–1377.
- 25 D. Alawadi, H. Saadeh, H. Kaur, K. Goyal, R. Sehgal, T. Ben Hadda, N. ElSawy and M. Mubarak, *Med. Chem. Res.*, 2015, **24**, 1196–1209.

- 26 W. Kurosawa, T. Kan and T. Fukuyama, in *Organic Syntheses*, American Cancer Society, 2003, **125**, 8112-8113.
- 27 J. Wang, L. Yang, C. Hou and H. Cao, *Org. Biomol. Chem.*, 2012, **10**, 6271-6274.
- 28 K. C. Agrawal, K. B. Bears, R. K. Sehgal, J. N. Brown, P. E. Rist and W. D. Rupp, *J. Med. Chem.*, 1979, **22**, 583-586.
- 29 B. Cavalleri, G. Volpe, V. Arioli, F. Pizzocheri and A. Diena, *J. Med. Chem.*, 1978, **21**, 781-784.
- 30 C. Jin, S. A. Wen, Q. Zhang, Q. Zhu, J. Yu and W. Lu, *Acs Med. Chem. Lett.*, 2017, **8**, 762-765.
- 31 J. Cao, Y. Liu, L. Zhang, F. Du, Y. Ci, Y. Zhang, H. Xiao, X. Yao, S. Shi, L. Zhu, H. Kung and J. Qiao, *J. Radioanal. Nucl. Chem.*, 2017, **312**, 263-276.
- 32 J.-M. Chovelon and I. Grabchev, *Spectrochim. Acta Part A Mol. Biomol. Spectrosc.*, 2007, **67**, 87-91.
- 33 M. S. Alexiou, V. Tychopoulos, S. Ghorbanian, J. H. P. Tyman, R. G. Brown and P. I. Brittain, *J. Chem. Soc., Perkin Trans. 2*, 1990, 837-842.
- 34 J. Kollár, P. Hrdlovič, Š. Chmela, M. Sarakha and G. Guyot, *J. Photochem. Photobiol. A Chem.*, 2005, **170**, 151-159.
- 35 B. Ventura, A. Bertocco, D. Braga, L. Catalano, S. D'Agostino, F. Grepioni and P. Taddei, *J. Phys. Chem. C*, 2014, **118**, 18646-18658.
- 36 C. L. Fleming, T. D. Ashton and F. M. Pfeffer, *Dye. Pigment.*, 2014, **109**, 135-143.
- 37 M. T. Davison and P. B. Garland, *Microbiology*, 1977, **98**, 147-153.
- 38 H. Weinmann, M. Harre, K. Koenig, E. Merten and U. Tilstam, *Tetrahedron Lett.*, 2002, **43**, 593-595.

---

## **CHAPTER 3**

# **Design and Synthesis of Metal Complexes based on the Terpyridine Ligand and Nitroimidazoles**

## CHAPTER 3      Design and Synthesis of Metal Complexes based on the Terpyridine Ligand and Nitroimidazoles

### 3.1      Introduction

Metal complexes have been intensively studied as potential reagents for chemotherapy.<sup>1,2</sup> There are many examples of metal complexes that have been used as anti-tumor reagents.<sup>3</sup> *Cisplatin* is one of the most active treatments of several type of cancer.<sup>4</sup> However there are many disadvantages, including efficiency against only a small range of tumours and drug resistance.<sup>5</sup> These difficulties encourage researchers to find new metal-based anticancer drugs. Palladium (II) complexes have been stated to have an antitumor effect with reduced toxicity compared to cisplatin.<sup>6</sup> Pd(II) complexes based on terpyridine also showed a more influential antigrowth effect than the Pt(II) analogue and cisplatin against some cancer cells.<sup>7</sup> Copper(II) has a significant role in many biological reactions beside its part in increasing anticancer efficiency of organic molecules.<sup>8,9</sup> Copper (II) complexes with terpyridyl exhibited cytotoxicity against tumour cells.<sup>10</sup> Czerwinska *et al.*<sup>11</sup> Synthesised copper(II) complexes with terpyridine which revealed cytotoxic activity against tumour cells . Zinc (II) also plays an important role in cellular processes and metabolism and it has been chelated by the terpy ligand. Zn-terpy conjugated to adenine (**Fig 3.1**) has been produced and its properties were investigated by Qin *et al.* The resulting complex showed effective *in vitro* cytotoxicity against several human tumor cell lines. Their cytotoxicity was approximately 10 times higher than the anticancer drug cisplatin.<sup>12</sup>

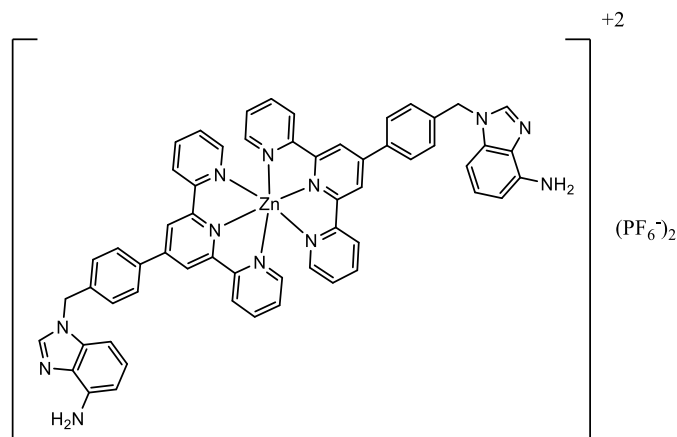


**Figure 3.1: Zn-terpy with adenine complex**

Several complexes with 4'-substituted terpy have been synthesized by Wang *et al.* All the complexes showed high cytotoxicity against four human cell lines. The Cu complex, shown in **Figure 3.2**, in this study display higher cytotoxicity than cisplatin.<sup>13</sup>

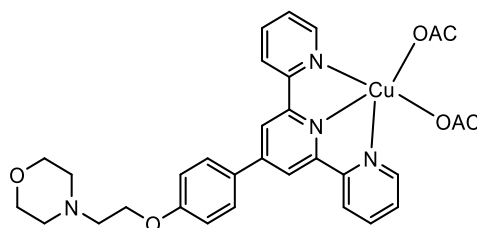


**Figure 3.2: Cu-terpy with conjugated morpholine**

Coordination chemistry of a terpyridine-based ligand is a developing research topic because of their application in biochemical chemistry.<sup>14</sup> Complexes of this ligand can be effectively introduced into nucleic acids to act as potential anticancer agents. They also showed excellent antibacterial properties.<sup>15</sup>

In addition, there are a number of studies reported on the metal complexes of metronidazole; for example Callaghan, four decades ago, reported Pt and Cu complexes of 2-methyl-5-nitrobenzimidazole.<sup>16</sup> Some transition metals were directly bound to metronidazole were reported by Obaleye *et al.*,<sup>17</sup> This study showed all the complexes had greater inhibitory activity on the organism compared to its free metronidazole. Silver (I) complexes of

metronidazole were also synthesised and the antimicrobial activities of the complexes were evaluated and compared with antibacterial properties of the parent silver salts. While there are several reports of metal complexes conjugated to pendant nitroimidazoles,<sup>18, 17</sup> to the best of our knowledge, metronidazole has not been used as a terminal group of terpy. Therefore, that an interesting objective was the synthesis of transition metal complexes of terpy-metronidazole. Such complexes may have improved or different antimicrobe and anticancer activities. Similarly, 2-nitroimidazole has not been attached to terpy in any previous research. Thus, the synthesis and characterisation of this ligand and its complexes was achieved in this report. It is hoped that the novel terpyridine ligands and their complexes will have promising biological potential differing from the original metronidazole or azomycin. These metal-nitroimidazoles complexes have two reducible sites; metronidazole/azomycin and transition metal core. Both have distinctive redox activities and subsequently, exceptional interactions with target hypoxic and normoxic cells. Theoretically, these type of complexes with two reducible sites provide better selectivity and sensitivity for targeting hypoxic cell than either transition metal-complexes only or the nitroimidazole compounds alone.<sup>18</sup> To further discover the configuration–activity associations and study new metal-based anticancer drugs, the synthesis and characterization of new Fe(II), Co(II), Ni(II), Pd(II), Cu(II) and Zn(II) complexes with ligands based on the terpyridine ligand and nitroimidazoles are described in this work for the first time.

## 3.2 Introduction to terpyridines

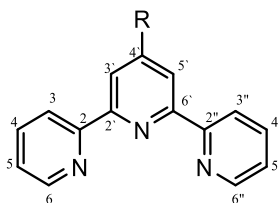


**Figure 3.3: Zn-terpy with adenine complex**

Terpyridine (terpy) (**Fig 3.3**), is a useful ligand first isolated over 85 years ago, as a product of the reaction of pyridine with iron (III) chloride.<sup>19</sup> Terpy is widely used as a building block in supramolecular chemistry because of its desired properties such as  $\pi$ -stacking ability, directional H-bonding and the ability to produce stable complexes of well-defined geometry.<sup>20</sup> The physical properties can be easily varied by adding different functional groups to any site of the terpy backbone. For instance, the addition of *p*-hydroxyphenyl group at the 4- position decreases the ligand's solubility, while biphenyl groups in the 4' position greatly increases the  $\pi$ -stacking properties.<sup>21</sup> Redox and photophysical properties can also be tuned by changing electron donor or withdrawing substituents.<sup>22,23</sup>

### 3.2.1 Synthesis of pyridine

The synthesis of pyridine rings is central to the synthesis of terpyridine. Most synthesis of terpyridine involve the synthesis of a pyridine with two pyridyl substituents! The most common procedures for the making of pyridine include: conversion from another ring, and by heterocyclic cyclization.<sup>24</sup> 2,4,6 Substituted pyridines were synthesized using several synthetic methods, often by the reaction of N-phenacyl pyridinium salts with unsaturated ketones and  $\text{NH}_4\text{OAc}$ .<sup>25,26</sup> However, these starting materials have to be initially produced therefore this process is rather expensive. Recently some original procedures for pyridine

preparation have been improved. For example, synthesis of pyridine was carried out by Potts *et al* by mixing ketoketene dithioacetals with methyl ketones in the presence of  $\text{NH}_4\text{OAc}$ .<sup>27</sup> Pyridine and its derivatives can be also produced by reacting N phosphinyloethanimines with aldehydes,<sup>28</sup> Addition of lithiated enaminophosphonates to chalcones is also another method for pyridine production,<sup>29</sup> while the reaction of acetophenones with benzaldehydes in the present of amino acetate without solvent is yet another procedure.<sup>20</sup> This latter reaction has also been reported without catalyst under microwave irradiation.<sup>30</sup>

### 3.2.2 Synthesis of terpyridine

#### The *Kohnke* method for the synthesis of terpyridines of type 2, 2': 6'2''terpyridine

(terpy):

According to this method, terpy can obtained by the reaction between (2-pyridacyl)-pyridinium halide and unsaturated ketone by a Michael addition to produce **a**. By adding ammonium acetate central pyridine ring is constructed to form 2,2':6'2'' terpyridine (**Fig 3.4**). However, by using this method the yield was low commonly about to 30–50% because of multistep purification.<sup>31,32</sup>

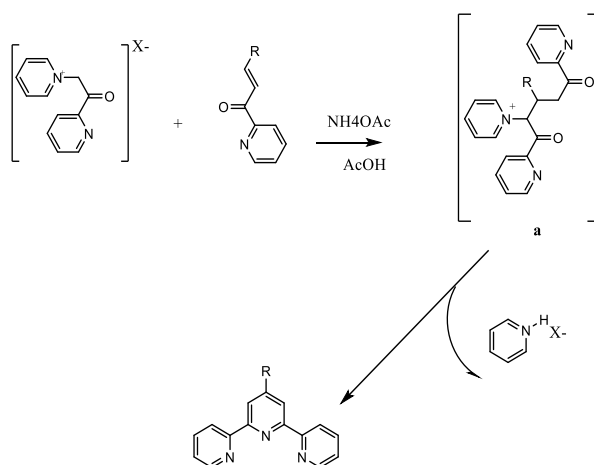


**Figure 3.4: Kohnke's synthetic pathway for terpyridine production**

### Potts Method:

This procedure is used to synthesise of 2,2' : 6',2''-terpyridine and its 4'-substituted derivatives. It depends on using accessible reagents and solvents and it consists of two steps.

Potts condensation obtained 4'-methylsulfonyl-2,2' : 6',2''-terpyridine, and the following replacement of the methyl sulfonyl group produce 2,2' : 6',2''-terpyridine or its derivatives.

The yield of the desired product in this procedure is usually about 30% (**Fig 3.5**).<sup>33</sup> The yield of final product can be improved slightly by using an improved procedure reported by Jameson *et al.*<sup>34</sup> The yield obtained by using this two-step method up was to 47%. N,N-dimethylformamide dimethyl acetal in toluene was used in this procedure instead of carbon disulphide used in the original Pott method.

Jameson's method (**Fig 3.6**) has become the preferred way for produce terpy; yet, some issues make it not ideal. For example, issues exist with the production and isolation of the desired pyridyl-enaminone leading to variations in the yield of the reaction due to the use of potassium t-butoxide.<sup>35</sup>

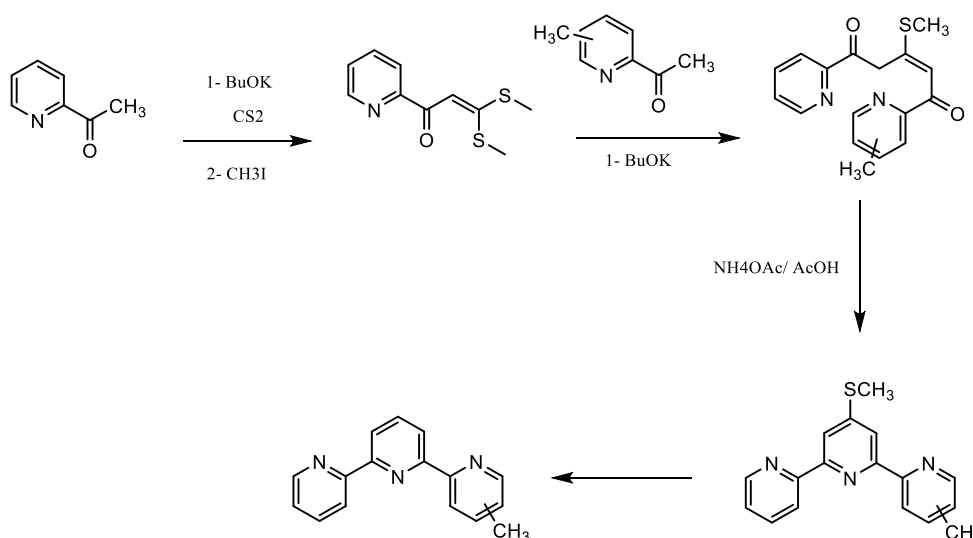


**Figure 3.5: Pott's synthetic pathway for terpyridine production**

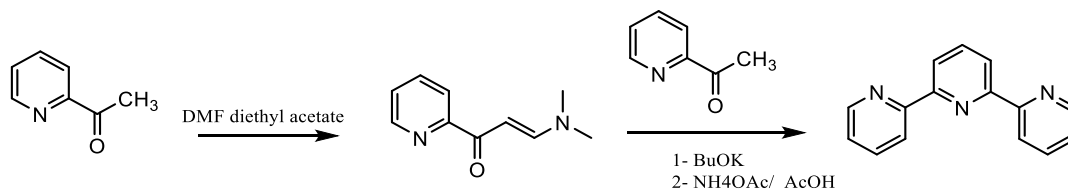


Figure 3.6: Jameson's synthetic pathway for terpy formation

### Raston's method: Green Synthesis of Terpyridine

The Raston method (Fig 3.7) for the synthesis of 2,2': 6'2''terpyridine (terpy) is mechanistically the same as the Kronhke synthesis but producing terpy by this approach is much easier to carried out and purify. It was carried out without solvent. This technique has made a dramatic progress in the yield.<sup>20</sup>

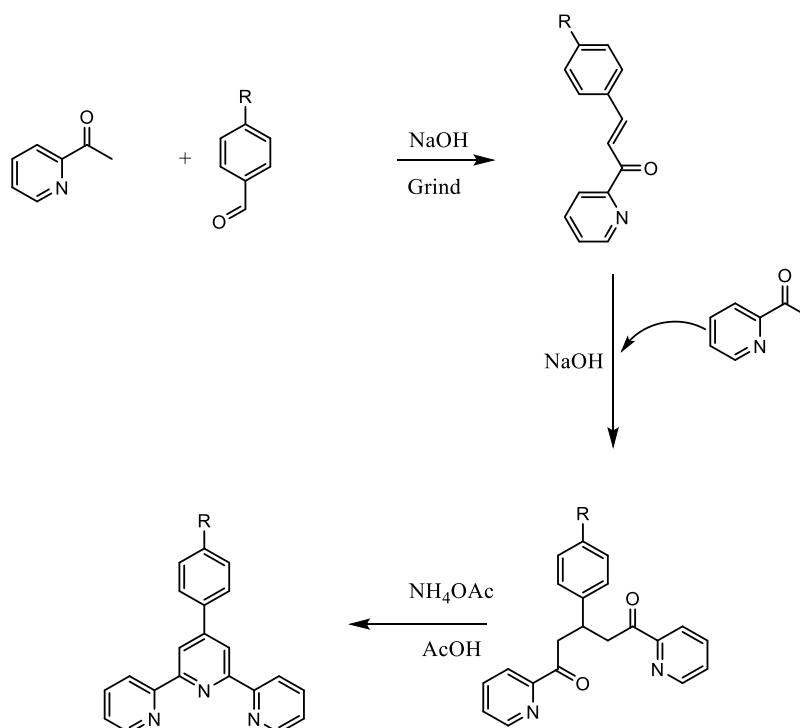
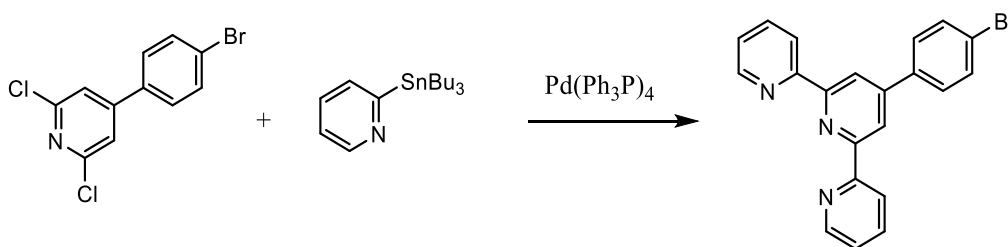


Figure 3.7: Synthetic scheme of Raston reaction for terpyridine synthesis

### Other Methods

Several 2,2' : 6',2''-terpyridines can be synthesised by using Stille cross-coupling.<sup>36,37</sup> This procedure includes the use of trialkylstannylpyridines and the overall yields of the 2,2' : 6',2''-terpyridines was up to 70% (**Fig 3.8**). Although the yield of terpy was high the experimental technique is difficult owing to special conditions essential for dealing with organotin compounds. Moreover, using expensive solvents and catalysts are other disadvantage of this method.<sup>38, 39</sup>



**Figure 3.8: Synthetic scheme of Stille cross-coupling for terpyridine synthesis**

### 3.2.3 Coordination Chemistry of Terpy

Terpyridine is a chelating ligand with three coordination sites. The typical ratio of transition metal: ligand in terpy complexes is either 1:1 or 1:2. Typically the 1:2 terpy complexes are based on octahedral geometry and show D<sub>2d</sub> central symmetry. Terpyridine undergoes many changes when coordinated. The most noticeable of these is the alteration in configuration of the terminal pyridine rings. Free terpy ligand normally exhibits a trans, trans-equilibrium structure. However, upon the addition of the metal centre, a cis, cis structure occurs, as shown in (**Fig 3.9**).

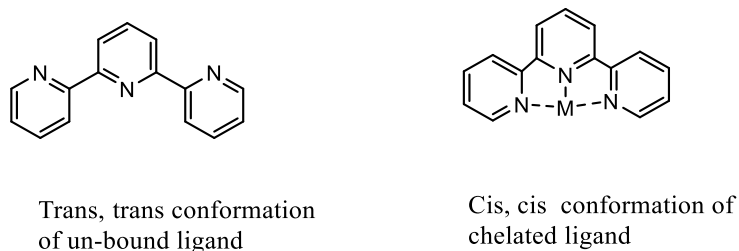


**Figure 3.9: Alteration in configuration of free and bound ligand**

To perform efficiently as a tridentate ligand, it is essential for the ligand to twist and decrease the interannular angle between the central and terminal pyridine rings. Upon complexation the dihedral angle between the terminal and central rings increases and the C-C-N angles decrease.<sup>40</sup> (Fig 3.10).

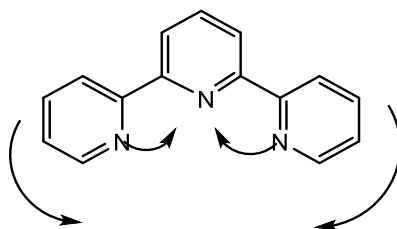


**Figure 3.10: Distortion in the bond angles of ligand due to complexation**

### 3.2.4 Survey of the Co-ordination of Terpyridine to First Row Late Transition Metals

The co-ordination chemistry of terpyridine with the first-row late transition metals (Fe-Cu) has been extensively covered. The well-defined geometry of the products has led to numerous further spectroscopic studies. For example, the addition of two equivalents of terpyridine to Fe(II) produces low spin six co-ordinate  $[\text{Fe}(\text{terpy})_2]^{2+}$ . The electrochemistry of this complex has been studied and contrasted to Ru(II).<sup>41</sup> Five redox steps were observed for both complexes, four where at negative potential and the reversible Fe(II)/Fe(III) couple was observed at positive potential (+1.09V vs SCE for Fe compared to +1.27V vs SCE for  $[\text{Ru}(\text{terpy})_2]^{2+/3+}$ ). The first three reductive processes were reversible but the reduction at

most negative potential lead to an ECE mechanism and the loss of the compound from solution. Considerable attention has been paid to the photophysical properties of these due to their potential use in light harvesting photodevices.<sup>42</sup> Particular focus was given to the excited state properties of  $[\text{Fe}(\text{terpy})_2]^{2+}$ . The octahedral complex has a low spin  $d^6$  ground state ( $^1A_{1g}$ ), with  $^3,5\text{MC}$  (metal centred) and  $^1,3\text{MLCT}$  (metal-ligand charge transfer) excited states and the relative ordering of these states were presented. The relative energies of these states is fundamental to their potential as chromophores in dye-sensitised solar cells and the rocking of the terpyridine was found to heavily affect the relative energies.<sup>43</sup> Related to this, Canton *et al*<sup>44</sup> investigated the dynamic Jahn-Teller distortion of the photo-induced HS state of  $[\text{Fe}(\text{terpy})_2]^{2+}$ .

The Co(II) complex of terpyridine is well established<sup>45</sup> and  $[\text{Co}(\text{terpy})_2]\text{X}_2$  ( $\text{X} = \text{Cl}^-, \text{Br}^-, \text{NO}_3^-$  and  $\text{ClO}_4^-$ ) was found to display temperature dependant spin-crossover between the high-spin  $^4T_1$  and low-spin  $^2E$  states. Nevertheless, UV-vis spectra displayed doublet-doublet transitions irrespective of the ratio, although the low temperature EPR of  $[\text{Co}(\text{terpy})_2](\text{ClO}_4)_2$  shows both spin states. This equilibrium was further explored by Kilner and Halcrow<sup>46</sup> who showed in the solid state,  $[\text{Co}(\text{terpy})_2](\text{BF}_4)_2$  was low spin below 100K and 87% high spin at room temperature. A study on the varying oxidation state in  $[\text{Co}(\text{terpy})_2]^{3+/2+/+}$  was carried out by Wieghardt *et al* who showed that the Co(III) was diamagnetic (LS  $d^6$ ), Co(II) contained high spin and by studying intraligand bond distances, they showed that  $[\text{Co}(\text{terpy})_2]^+$  contained a Co(I) centre and not  $[\text{Co}(\text{II})(\text{terpy}^0)(\text{terpy}^*)]^+$ . Accordingly, the UV-vis spectrum show intense MLCT bands.<sup>47</sup>

The structure of  $[\text{Ni}(\text{terpy})_2]^{2+}$  with  $(\text{PF}_6)^{-2}$  or  $\text{ClO}_4^-$  has been reported.<sup>48,49</sup> The cation has approximate  $D_{2d}$  symmetry, with the main distortion from octahedral symmetry being an axial compression. There are significant examples where a mono-terpyridine complex has been formed with the two or three least sterically demanding ligands making the complex 5 or

six co-ordinate.<sup>50</sup> However, heavier metals such as Pd and Pt produce square plane diamagnetic complexes with terpy. In such cases, the terpy has a bite angle not suited to square planar coordination and this results in some distortions in central ring bond and the square plane. In both octahedral and square plane complexes, the inter-ring bond is shorter than the bonds of the terminal rings.<sup>51</sup> (Fig 3.11).

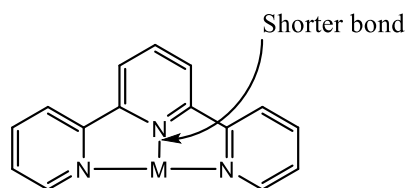


**Figure 3.11: Illustration presenting the length of central nitrogen-metal bond compared to the terminal bonds**

Similarly, Cu(II) also show a tendency to form both bis terpy  $[\text{Cu}(\text{terpy})_2]^{2+}$  and mono-terpy  $[\text{Cu}(\text{terpy})\text{X}_n]^{2+}$  complexes. A thorough description of the Jahn Teller distortion shown by  $[\text{Cu}(\text{terpy})_2]^{2+}$  was reported by Schiemann<sup>52</sup> while non-Jahn Teller active, five co-ordinate mono-terpyridine species have been reported by Reinen.<sup>53</sup>

### 3.3 Result and Discussion

In this section the following aspects will be covered:

- 1- Synthesis and characterisation of two new ligands based on the terpyridine and nitroimidazoles.
- 2- Synthesis and characterization new Fe(II), Co(II), Ni(II), Pd(II), Cu(II) and Zn(II) complexes of metronidazole containing ligand 1.

- 3- Synthesis and characterization new Fe(II),Co(II), Ni(II), Pd(II), Cu(II) and Zn(II) complexes of azomycin containing ligand 2.
- 4- Electronic Absorption Spectroscopy of both ligands and their complexes.
- 5- Electrochemical studies for the ligands and the complexes.

## Ligands Synthesis

### 3.3.1 Synthesis and characterisation of Ligand 1 (L<sup>1</sup>)

Two pathways were attempted to obtain 4'-(4-(2-(2-methyl-5-nitro-1H-imidazol-1-yl)ethoxy)phenyl)-2,2':6',2''-terpyridine, **L<sup>1</sup>**. The first attempt which was not successful included using 5-nitroimidazole conjugating with aldehyde to be reacted with 2-acetyl pyridine as shown in **Fig 3.12**. The other successful method involved 4'-(4-Hydroxyphenyl)-2,2',6',2''-terpyridine **E** being directly reacted with a 5-nitroimidazol moiety terminated with a good leaving group as shown in **Fig 3.13**. The description of both synthetic pathways will be described in detail as the following:

In the first experiment 2-acetyl pyridine **A** was reacted directly with 4-(2-(2-methyl-5-nitro-1H-imidazol-1-yl)ethoxy)benzaldehyde **B** in the present of strong base KOH and ammonium acetate as shown in **Fig 3.12**. The mixture was stirred in EtOH in room temperature for 24 hours. Analysis by TLC did not show any sign of the product. The reaction time and the temperature were increased in order to force the reaction however there was no evidence of any product.

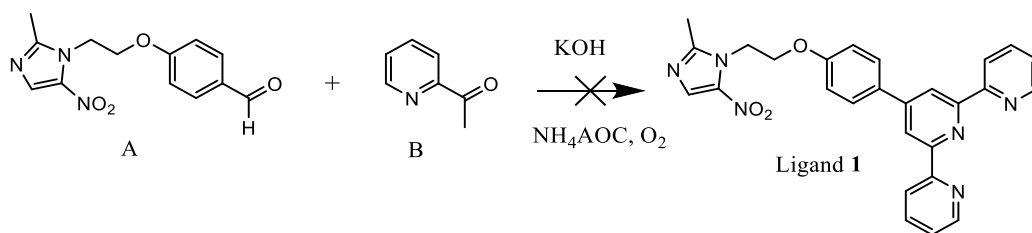


**Figure 3.12: Illustration presenting attempted synthesis of 4'-(4-(2-(2-methyl-5-nitro-1H-imidazol-1-yl)ethoxy)phenyl)-2,2':6',2''-terpyridine L<sup>1</sup>**

An alternative attempt was carried out using the same starting material as shown in **Fig 3.12** with potassium tert-butoxide as base and anhydrous THF as solvent, adapted from previously reported procedure.<sup>54</sup> It was successful in making the reaction go to completion (the reaction was monitored with TLC), however, the reaction ended up with a mixture of products rather than the expected pure desired product according to TLC and <sup>1</sup>H NMR. Purification through recrystallisation in ethanol, THF, and DCM also failed. Further, thin layer chromatography was unsuccessful in fully separating the mixture in spite of the usage of various solvent systems of DCM/Methanol, acetonitrile and hexane/ethyl acetate preventing the possibility of purification by column chromatography.

Thereafter the successful reaction was carried out by reacting 2-acetyl pyridine **B** with 4-hydroxy benzaldehyde **C** instead of 4-(2-(2-methyl-5-nitro-1H-imidazol-1-yl)ethoxy)benzaldehyde (**Fig 3.13**). This route was considered in order to facilitate a Michael addition with less steric hindrance. This reaction was achieved following literature precedent.<sup>13</sup> This reaction produced 3-(4-hydroxyphenyl)-1,5-di(pyridin-2-yl)pentane-1,5-dione **D** as an intermediate product which was then cyclised with ammonium acetate in ethanol. The final product of this reaction was 4'-(4-Hydroxyphenyl)-2,2',6',2''-terpyridine **E** which was subsequently reacted with 2-(2-methyl-5-nitro-1H-imidazol-1-yl)ethyl methanesulfonate **F** to obtain the desired product ligand **1** as a green crystals.

Recrystallisation of **L**<sup>1</sup> involved the diffusion of acetonitrile into DCM solution (23%).

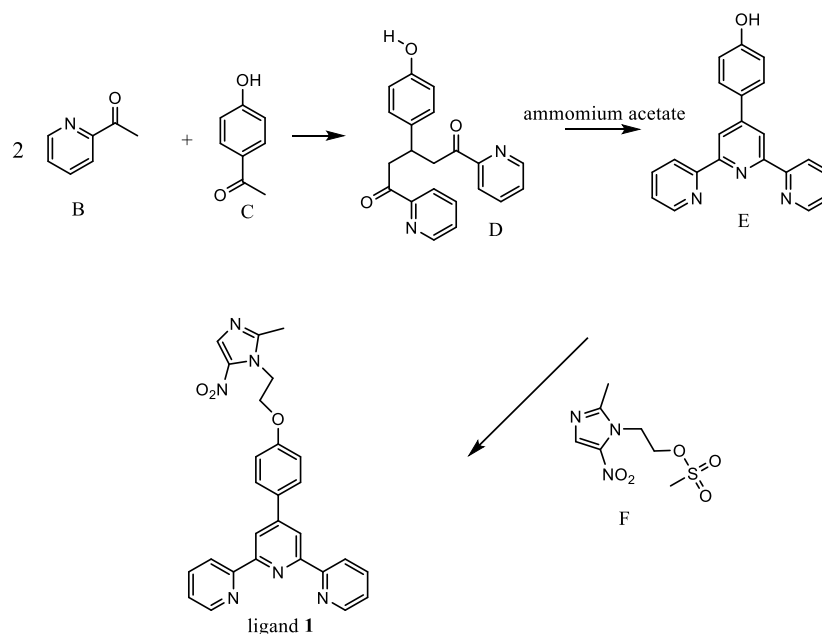


**Figure 3.13: The synthetic pathway of 4'-(4-(2-(2-methyl-5-nitro-1H-imidazol-1-yl)ethoxy)phenyl)-2,2':6',2''-terpyridine L<sup>1</sup>**

4'-(4-(2-(2-methyl-5-nitro-1H-imidazol-1-yl)ethoxy)phenyl)-2,2':6',2''-terpyridine is a novel compound was fully characterised and data, detailed in the experimental part, are consistent with the suggested structure as depicted in **Fig 3.13**.

<sup>1</sup>H NMR spectrum shown in **Fig 3.14**, produced all relevant peaks corresponding to metronidazole group. A singlet at 2.46 ppm corresponding to the methyl group of the Me in **F** disappeared and further peaks were seen at 8.77, 8.68, 8.61, 8.15, and 7.65 which were assigned to the terpyridine moiety. <sup>13</sup>C NMR spectra indicated 18 peaks which were assigned to the carbons in the structure. Three peaks were found in down field representing aliphatic carbons and the other were found in the high field for the aromatic carbons. 11 signals in <sup>13</sup>C have high intensity because they have bonds with the hydrogen atoms compared to these with no bonds with hydrogen.

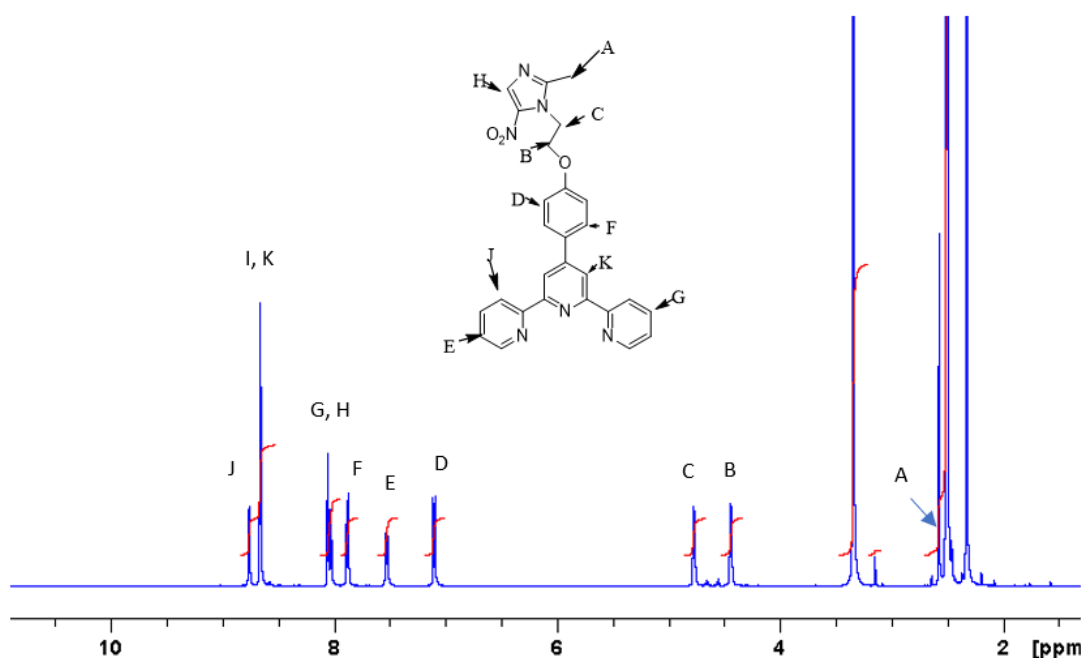
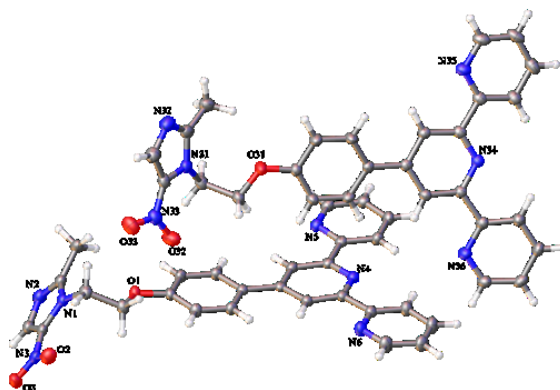


Figure 3.14:  $^1\text{H}$  NMR analysis of  $\text{L}^1$  in  $\text{DMSO-d}_6$

FT-IR spectrum of the resulting product presented vibrational peak at  $1590\text{ cm}^{-1}$  that was corresponded to  $\text{C}=\text{N}$  stretching peaks of terpy moiety. Vibrational peaks at  $1521$  and  $1455\text{ cm}^{-1}$  were attributed to  $\text{N}=\text{O}$  asymmetric stretching and  $\text{CH}_2$  bending. The absorption at  $1342$  and  $1365\text{ cm}^{-1}$  were assigned to  $\text{N}=\text{O}$  symmetric stretching.<sup>55,56</sup> Further characterization by high resolution mass spectrometry corroborated the result which showed the expected  $[\text{M}+\text{H}]^+$  ion peak ( $479.1833$ , 100%) for the desired product.

Single pale brown cut block-shaped crystals were recrystallised from a mixture of DCM and MeCN by slow evaporation. X-ray represented the exact configuration of  $\text{L}^1$ , (Fig 3.15). The bonds and angles were as expected, and the connectivity is in the agreement with spectroscopic data. It also exhibits a trans, trans configuration structure.



**Figure 3.15:** Crystal structure of 4'-(4-(2-(2-methyl-5-nitro-1H-imidazol-1-yl)ethoxy)phenyl)-2,2':6',2''-terpyridine **L**<sup>1</sup>

A number of metal complexes of **L1** were then synthesised and their redox activity were tested. The redox activity was measure as describe in electrochemistry section.

### 3.3.2 Synthesis and characterization of ligand 2 (**L**<sup>2</sup>)

We wished to extend the synthesis of the metronidazole terpy ligand to the analogous 2-nitroimidazoles to compare the potential reduction abilities and other properties of these two ligands and their complexes.

As represent in **Fig 3.16**, to react 4'-(4-Hydroxyphenyl)-2,2',6',2''-terpyridine, **E**, with a 2-nitroimidazole moiety, the latter has to be terminated with a good leaving group. Thus, **G** and **H** were synthesised as intermediate steps to facilitate the potential nucleophilic substitution reactions on 2-nitroimidazole. The alcohol terminated of 2-nitroimidazole **G**, was synthesised according to the procedure reported previously.<sup>57</sup> 3-(2-Nitro-1H-imidazol-1-yl)propyl methanesulfonate **H** was a novel compound which was synthesised by the addition of methanesulfonyl chloride to a mixture of **H** and triethylamine in DCM. Ligand **2** was produced by adding 4'-(4-Hydroxyphenyl)-2,2',6',2''-terpyridine **E** to a solution of **H** in

acetonitrile in the presence of base ( $K_2CO_3$ ). The desired product was purified by recrystallising the crude product in acetonitrile. The pure desired product was attained as yellow crystals (14%). However, these crystals were too small for analysis by single crystal X-ray diffraction.

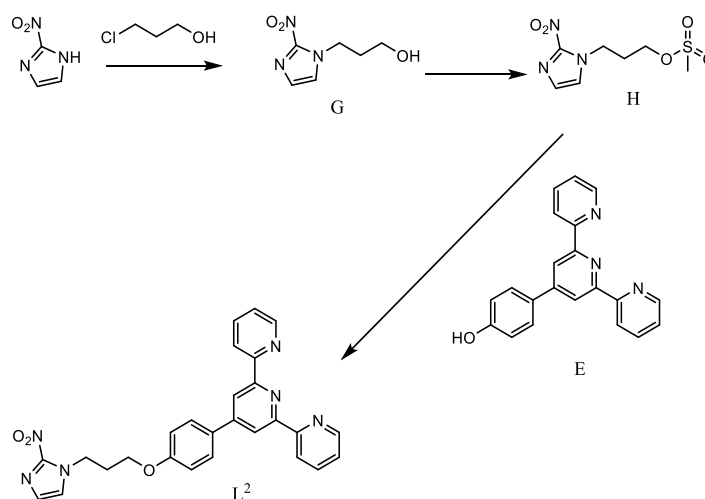


**Figure 3.16: The synthetic pathway of 4'-(4-(3-(2-nitro-1H-imidazol-1-yl)propoxy)phenyl)-2,2':6',2''-terpyridien  $L^2$**

$L^2$  is a newly produced compound and was fully characterised and data is detailed in the experimental section. The data is consistent with the suggested structure as shown in **Fig 3.16**. The successful synthesis of this compound was easily detected by  $^1H$  NMR spectrum, with the disappearance of a singlet at 3.2 ppm assigned for the methyl group of **H** and the presence of all relevant peaks corresponding to 2-nitroimidazole. The disappearance of one singlet peak at 10.22 ppm assigned to -OH proton of **E** is also a good proof of the formation of  $L^2$  (**Fig 3.17**).  $^{13}C$  NMR spectra indicated 18 peaks which were assigned to the carbons in the structure. Three peaks were found in down field and the rest located in the up field. The infra-red data for the FT-IR spectrum of  $L^2$  shows medium band at  $1583\text{ cm}^{-1}$  that were attributed to C=N stretching peaks. Vibrational peaks are similar to those of  $L^1$  with peaks at 1516 and 1361 was corresponding to N=O asymmetric stretching and N=O symmetric stretching, respectively.<sup>56</sup> Stretching peak of C-H saturated bond were observed at 2937 and

there is a weak band at  $3035\text{ cm}^{-1}$  which ascribed to C-H unsaturated bond of the pyridine groups in this ligand. The high-resolution mass spectrum produced the required parent ion peak at 479.1832, (100%).

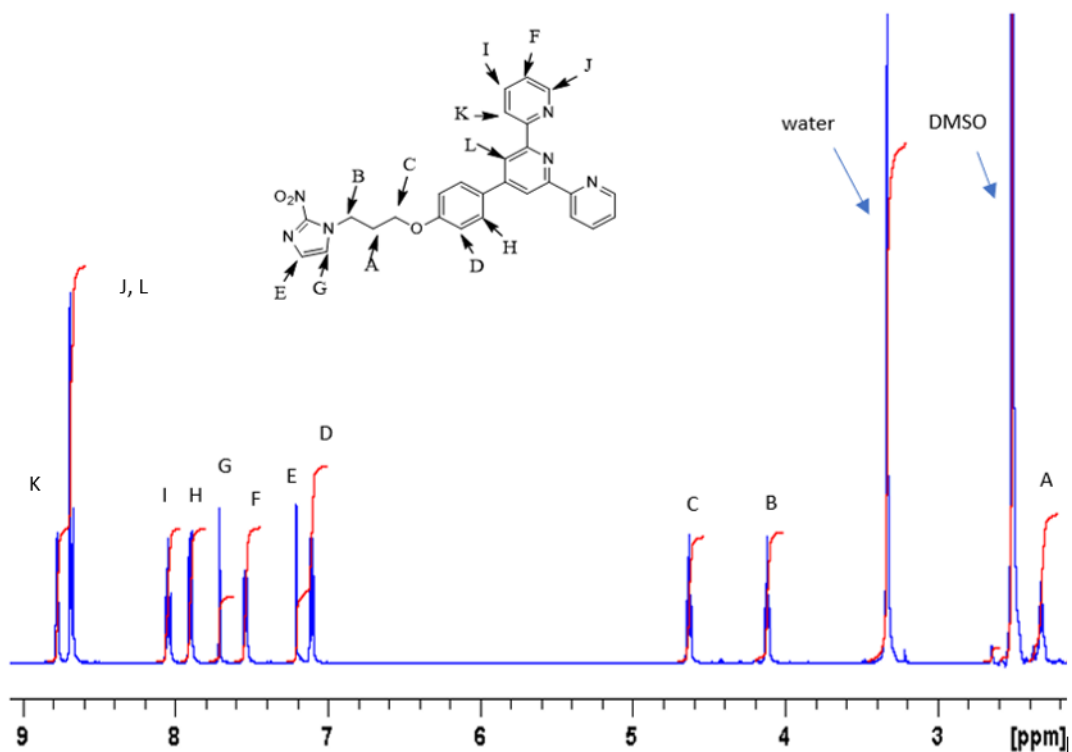


Figure 3.17:  $^1\text{H}$  NMR analysis of  $\text{L}^2$  in  $\text{DMSO-d}_6$

### 3.3.3 Complexes of $\text{L}^1$

All metal complexes of the terpyridine- metronidazole ligands were synthesized as stated in the Experimental Section. Treatment of the free metronidazole-substituted terpy ligands with corresponding salts in an ethanol or ethanol/ DCM mixture at room temperature afforded complexes in modest yields (29% -50%). One exception is the palladium complex of this ligand which was prepared in  $\text{H}_2\text{O}$ . All of these complexes are air-stable powders at room temperature. They are soluble in in acetonitrile, acetone and DMSO. Attempts to obtain a single crystal suitable for X-ray analysis were not successful. The structures of the

synthesized complexes were confirmed with the support of IR, UV spectroscopy, and HRMS. Only the diamagnetic complexes **1**, **4**, and **6** were analysed by  $^1\text{H}$  NMR spectroscopy.

### **Octahedral complexes of $\text{L}^1$**

The octahedral complexes of  $\text{L}^1$  were found to include the complexes of iron (II) cobalt (II), nickel (II), Cu (II) and zinc (II). These metal complexes were produced by a similar procedure. Two equivalents of  $\text{L}^1$  with one equivalent of the corresponding salts in an ethanol or ethanol/ DCM mixture at room temperatures afforded complexes in modest yields.

#### **3.3.3.1 Bis( 4'-(4-(2-(2-methyl-5-nitro-1H-imidazol-1-yl)ethoxy)phenyl)-2,2':6',2''-terpyridine) iron (II)tetra fluoroborate (1)**

The iron complex, **1**, was synthesised by adding  $\text{Fe}(\text{BF}_4)_2$  to two equivalents of  $\text{L}^1$ . A purple colour was observed directly, and a purple precipitate was formed after 15 minutes. This colour is in the agreement with that observed for similar octahedral complexes of iron (II) with terpy.<sup>58</sup>  $^1\text{H}$  NMR were recorded in DMSO- $d_6$ . The  $^1\text{H}$  NMR spectra showed up-field shift compared to the  $\text{L}^1$ . The chemical shifts of the protons adjacent to the pyridyl rings were shifted up field. The results indicate the coordination of the ligands with the metal ions. The  $^1\text{H}$  NMR spectra was very comparable to that of  $\text{L}^1$  showed 18 carbon peaks shifted up-field. The mass spectrometry analysis data of the complexes agree with the theoretical values. High resolution mass spectrometry confirmed the formulation of the complex, showing  $[\text{M}]^+$  with the correct isotopic pattern. The producing of complex was further supported by negative mode ESI-HRMS spectrometry, which documented a peak at 1098.3002 corresponding to  $[(\text{L}^1)_2\text{-Fe-BF}_4]^-$  ion. The UV/vis spectrum was carried out in acetonitrile and a band was observed at 569(9074) nm which was in good agreement with the UV/ vis recorded by Martin and Lissfl<sup>59</sup> assigned as metal-to-ligand charge transfer (MLCT) transition. Peaks of Fe (II)

complex at 257(17154), 285(22676), 324(30185) nm were assigned to the  $\pi$ - $\pi^*$  of the ligand transition. The IR spectra indicated the presence of 5-nitroimidazole and the terpy backbone. Comparison to the IR spectra of free **L**<sup>1</sup>, the band of C=N at 1590 cm<sup>-1</sup> of free ligands shifted to higher frequency by 14 cm<sup>-1</sup> after coordination. That is perhaps suggesting the more rigid the complex, the more energy is required for the bond to vibrate. Complex **1** was soluble in acetonitrile, acetone and DCM.

### 3.3.3.2 Bis( 4'-(4-(2-(2-methyl-5-nitro-1H-imidazol-1-yl)ethoxy)phenyl)-2,2':6',2''-terpyridine) nickel (II) tetra fluoroborate (**2**)

Terpy-nickel(II) complexes [Ni(tpy)<sub>2</sub>]X<sub>2</sub>·H<sub>2</sub>O (X = Br or I) were synthesised as the first time by Morgan and Burstall in the 1930s<sup>60</sup> and were found to show octahedral coordination.<sup>61</sup> The nickel (II) complex, **2**, was prepared using a similar method to **1** and the product was deep orange in colour. Attempts to obtain <sup>1</sup>H NMR was done. This reveal only the solvent peaks though the use of wide range proton mode confirming the paramagnetic species of this complex. The UV/vis present a peak at 250nm, 324nm and 400nm. High resolution negative mode ESI-HRMS spectrometry, which documented a peak at 1100.2917 corresponding to [(L<sup>1</sup>)<sub>2</sub>Ni-BF<sub>4</sub>]<sup>+</sup> ion. IR spectra were similar to that in **2**. The  $\nu$ (C=N) underwent a shift in frequency and intensity, caused by complexation. In UV/vis, peaks of this complex at 278 (40581), and 324 (53145) were assigned to the  $\pi$ - $\pi^*$  of the ligand transition and the 344 (49272) nm absorptions were assigned to MLCT transition which was in good agreement with the UV/ vis recorded by Ratone et al. of m/z [Ni-terpy Cl<sub>2</sub> H<sub>2</sub>O]<sup>+2</sup>.<sup>62,63</sup>

### 3.3.3.3 Bis(4'-(4-(2-(2-methyl-5-nitro-1H-imidazol-1-yl)ethoxy)phenyl)-2,2':6',2''-terpyridine) cobalt (II) tetra fluoroborate (3)

The cobalt (II) complex **3** appeared as red powder. The IR spectrum was similar to that of **1** and **3**, presenting the common features of **L**<sup>1</sup> and the band of C=N at 1590 cm<sup>-1</sup> of free ligands shifted to higher frequency. In the UV/vis, the bands of Co(II) complex at 297(1500), 337(1900) were corresponding to the  $\pi$ - $\pi^*$  of the ligand transition and 523(78.18) absorption band was assigned to MLCT transition. These values agree with the UV/vis spectrum recorded for [Co-(terpy)<sub>2</sub>].<sup>64,65</sup> As shown in **Fig 3.18**, the obtained mass spectrometry, the experimental data of **3** perfectly matches the theoretical expectations, therefore confirming the chemical structure. Attempts to obtain H<sup>1</sup> NMR spectrum were unsuccessful given features broadened peaks as might be expected for the para magnetic complex.

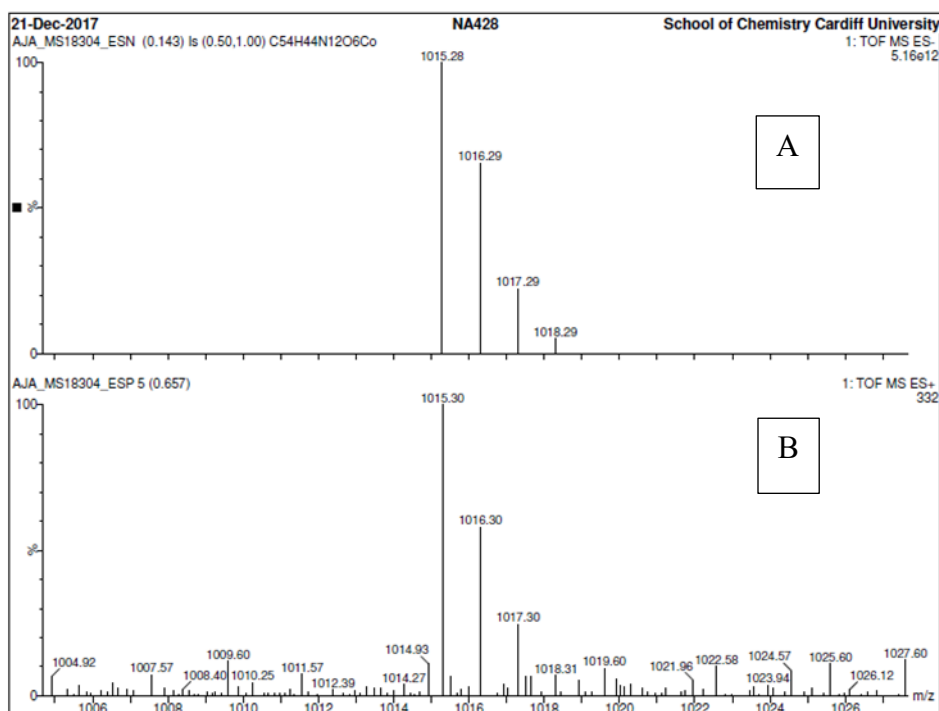


**Figure 3.18: Experimental and theoretical mass spectra of 3: (A) theoretical spectrum, (B) experimental spectrum**

#### 3.3.3.4 Bis( 4'-(4-(2-(2-methyl-5-nitro-1H-imidazol-1-yl)ethoxy)phenyl)-2,2':6',2''-terpyridine) zinc (II)chloride(4)

The zinc (II) complex (4) was synthesised using a method similar to that for **1** and **2**. A white precipitate was formed after 3 hours of stirring with yield of (59%). The <sup>1</sup>H NMR spectra of the complexes showed up-field shift for the 6,6''-tpyHs compared to the **L**<sup>1</sup>. Despite considerable effort to obtain the <sup>13</sup>C NMR spectrum for **4**, all attempts failed due to the poor solubility of the sample, as the sample solution became cloudy when the concentration increases. The IR spectra was similar to the previous complexes **1-3**. However, in the mass spectrum there are two high mass peaks. One of these peaks was at 510.14 (98%) and exactly matches the theoretical expectation of the complex  $m/z [Zn(L^1)_2]^{+2}$ , 1020/2. The other peak at 587.10 (15%) could possibly be  $[Zn(L^1)_2(HCO_2)]^{+2}$ , with the inclusion of formic acid occurring due to its use in the matrix of electrospray. The UV/vis spectrum produced three absorbance peaks at 283(32181), 295 (35309) and 327(29981) were assigned to the  $\pi-\pi^*$  of the ligand transition and the 341(26945) absorptions were allocated for MLCT transition and is in agreement with similar complexes reported in the literature<sup>66</sup>.

#### 3.3.3.5 Bis( 4'-(4-(2-(2-methyl-5-nitro-1H-imidazol-1-yl)ethoxy)phenyl)-2,2':6',2''-terpyridine) copper (II)chloride (5)

The copper(II) complex of **L**<sup>1</sup> was green powder which is in agreement with that reported for similar octahedral complexes in the literature.<sup>58, 10</sup> In the UV/vis spectrum, the bands of at 278(21000), 301(23000) and 337(26000) were assigned to the  $\pi-\pi^*$  of the **L**<sup>1</sup> and the band at 350(9120) were assigned to a MLCT transition which is in agreement with data reported in previously.<sup>13,58</sup> The IR spectra of the complexes are rather similar and exhibit common

features due to the related chelating N-donor polypyridyl ligands. The identification of **5** was also supported by high resolution positive mode ESI-HRMS spectrometry, which presented a peak corresponding to  $[(L^1)_2-Cu]^+$  at 1019.2807 (100%) confirming the ligand metal ratio 2:1. In addition, the isotope distribution for the complex spectrum is in perfect agreement to the theoretical prediction (**Fig 3.19**).

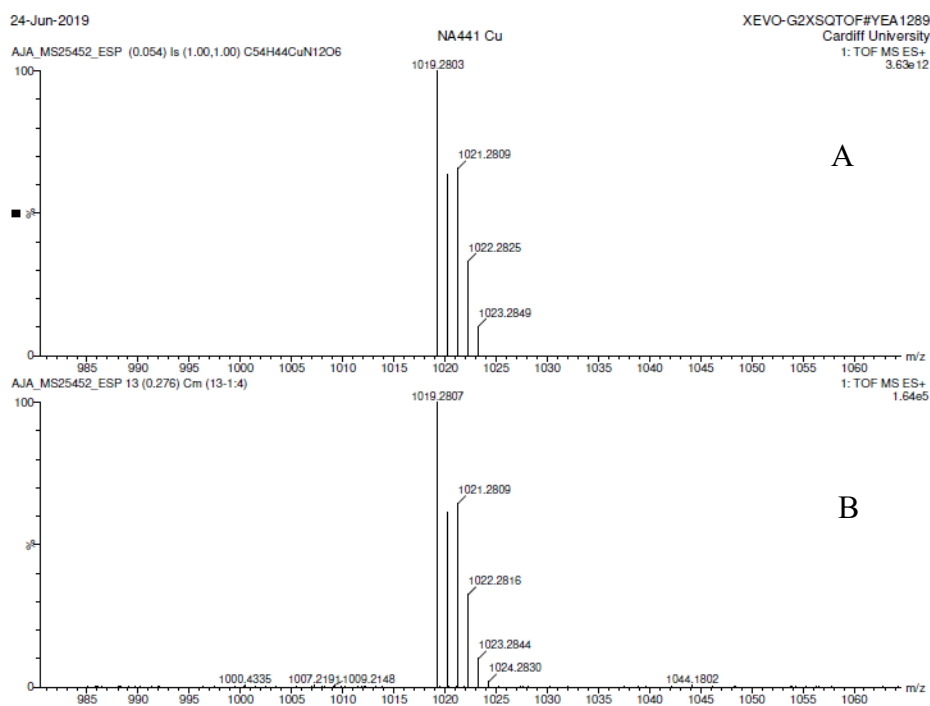


**Figure 3.19: Experimental and theoretical mass spectra of 5: (A) theoretical spectrum, (B) experimental spectrum**

### Square planar group complexes of L<sup>1</sup>

#### 3.3.3.6 ( 4'-(4-(2-(2-Methyl-5-nitro-1H-imidazol-1-yl)ethoxy)phenyl)-2,2':6',2''-terpyridine) palladium (II)acetate (6)

The palladium acetate complex **6** was synthesis by stirring 1 equivalent of ligand **1** in DCM with 1 equivalent of Pd(CH<sub>3</sub>COO)<sub>2</sub> in water for 17 hours at room temperature. The complex was obtained as a grey powder. In the <sup>1</sup>H NMR spectra, the chemical shift corresponding to the proton of the pyridyl rings, shifting up-field. The <sup>1</sup>H NMR spectra of **7** provided information about the bonding mode of acetate in Pd (II) complexes. The acetate anion in this complex can act as a monodentate or bidentate ligand. This type of complex may select a six-coordinate geometry one tridentate terpy, and two acetate ligand one of them is monodentate and the other is bidentate. The other possible configuration of this complex is a square planar four-coordinate geometry one tridentate terpy and one monodentate acetate ligands. In the six-coordinate geometry two peaks of methyl will appear in <sup>1</sup>H NMR owing to bidentate and monodentate acetate ligands for six-coordinate geometry. Though, only a single peak (s, 3H) was found at 2.07 ppm for this complex, suggesting the four-coordinate around Pd(II) ion or rapid exchange of anions in the NMR timescale. Despite the effort of increasing the concentration of the sample solution of this complex to obtain <sup>13</sup>C NMR spectrum, all attempts have failed. However Pd(II) has a d<sup>8</sup> configuration, and due to 4d metal typically giving complexes with a strong ligand field, the four coordinate square planer is heavily favoured. The IR spectrum show common features of the ligand **1** shifting due to the related chelating N-donor polypyridyl ligands. The peaks of Pt(II) complex **6** at were 278(22197),305(19872) and 352(14299), attributed to a π-π\* intraligand L<sup>1</sup> transition of terpy<sup>64</sup>, whereas the peak at 368(14363) was assigned to metal-to-ligand charge transfer

(MLCT) transition.<sup>67</sup> The mass spectrometry analysis data of the complexes are in agreement with theoretical values with a peak corresponding to the  $[\text{L}^1\text{-Pd-CH}_3\text{CO}_2]^+$  at 629.08 suggesting the ligand metal ratio of 1:1.  $[\text{Pd(II)(Terpy)Cl}]\text{Cl}$  was reported previously and cytotoxicity against some cell lines was studied.<sup>13</sup>

### 3.3.4 Spectroscopic Properties of $\text{L}^1$ complexes

#### 3.3.4.1 Vibrational Spectroscopy

An unequivocal interpretation of IR spectra is always problematic, however by comparison of related spectra it is possible to try to assign peaks and draw some conclusion. Key stretches for all compounds have been tabulated in table 2. As that in  $\text{L}^1$ , FT-IR spectrum of the resulting complexes of  $\text{L}^1$  presented vibrational peaks of C=C (imidazole ring) stretching and C=N (imidazole ring) stretching peaks. Vibrational peaks attributed to symmetric N=O stretching and N=O asymmetric stretching were also observed. The shift of pyridine ring vibration at around  $1550\text{ cm}^{-1}$  in all complexes indicated co-ordination from the pyridine rings. The band of C=N at  $1590\text{ cm}^{-1}$  of the terpyridine moiety of  $\text{L}^1$  show a slight increase in value on comparison with the free ligand upon metalation.<sup>41</sup> That is because after coordination with metal, the compound became heavier and need more energy for the bonds to be vibrated. As the energy is directly proportional to frequency. Complex **1**, **2** and **3** reveal one characteristic band at indicative of ionic tetrafluoroborate at  $1052\text{ cm}^{-1}$ .<sup>68</sup> However, this value seem to be slightly higher in **3** than the previously reported value as shown in table 2.

**Table 2: IR stretching frequencies of L<sup>1</sup> and its complexes**

Compound	BF <sub>4</sub>	N=O <sub>asym</sub>	N=O <sub>sym</sub>	C=N	C-H	C=C-H	
Metronidazole	–	1531	1354-1367		2848	3099	
L <sup>1</sup>	–	1521	1342- 1325	1590	2981-2953	3122-3024	
[Fe(L <sup>1</sup> ) <sub>2</sub> ](BF <sub>4</sub> ) <sub>2</sub>	1	1052	1521-1541	1382 -1365	1604	2881	3124
[Ni(L <sup>1</sup> ) <sub>2</sub> ](BF <sub>4</sub> ) <sub>2</sub>	2	1052	1554 ,1521	1379 1363	1602	2885	3115
[Co(L <sup>1</sup> ) <sub>2</sub> ](BF <sub>4</sub> ) <sub>2</sub>	3	1169	1506, 1523	1367, 1344	1598	2971	3024
[Zn(L <sup>1</sup> ) <sub>2</sub> ] Cl <sub>2</sub>	4	–	1576, 1521	1361- 1342	1576	2980	3075
[Cu(L <sup>1</sup> ) <sub>2</sub> ] Cl <sub>2</sub>	5	–	1523	1384-1365	1598	2881	3091
[Pd L <sup>1</sup> (OAc)]OAc	6	–	1521, 1543	1361, 1331	1593	2989	3062

### 3.3.4.2 <sup>1</sup>H and <sup>13</sup>C NMR of Fe, Pd and Zn complexes of L<sup>1</sup>

The <sup>1</sup>H NMR spectra of the iron, palladium and zinc complexes of L<sup>1</sup> are highly comparable to each other and to their ligand, the slight differences arising in the respective chemical shifts. All proton in the iron, palladium and zinc complexes of L<sup>1</sup> are more deshielded compared to the free ligand L<sup>1</sup> with exception of the three resonance peaks in the aliphatic region which are assigned to methyl groups of 5-mitroimidazole moiety. This shift is because the great decrease in electron density around the protons adjacent to pyridyl rings as a result of the coordination of nitrogen donors to metal centre.

The <sup>1</sup>H NMR spectra of L<sup>1</sup> and its Fe, Pd and Zn complexes were shown in **Fig 3.20**. In general, the peak of methyl group of the complexes stays in the same place after coordination as it is remote from the nitrogen atoms of polypyridine which are responsible for chelating the metals. Similarly, the peaks of B and C remain in the same position for the same reason. There is a slight shift was observed for D and H. However, the noticeable shifts were observed for the peaks near terpy moiety.

As shown in **Fig 3.21**, the most sifted protons in case of  $\text{Fe}(\text{L}^1)$  are E, F, K and J compared to the free  $\text{L}^1$  ligand.

The chemical shift for **4** and **6** almost has the same shifting pattern. As the peaks of E, F and G underwent slight movement in the position with  $\text{ca} \sim 0.35$  ppm compared to the free  $\text{L}^1$ .

However, the most shifted peaks in case of  $\text{Pd}(\text{II})$  and  $\text{Zn}(\text{II})$  complexes was noticed for I and K with about 0.5 ppm with comparison of  $\text{L}^1$  (**Fig 3.21**), (**Table 3**).

The shifts occur due to a combination i) the electron withdrawing nature of the coordinated metal centre ii) the magnetic anisotropy caused by the aromatic rings rigidly held in space, such effects are not easy to predict.

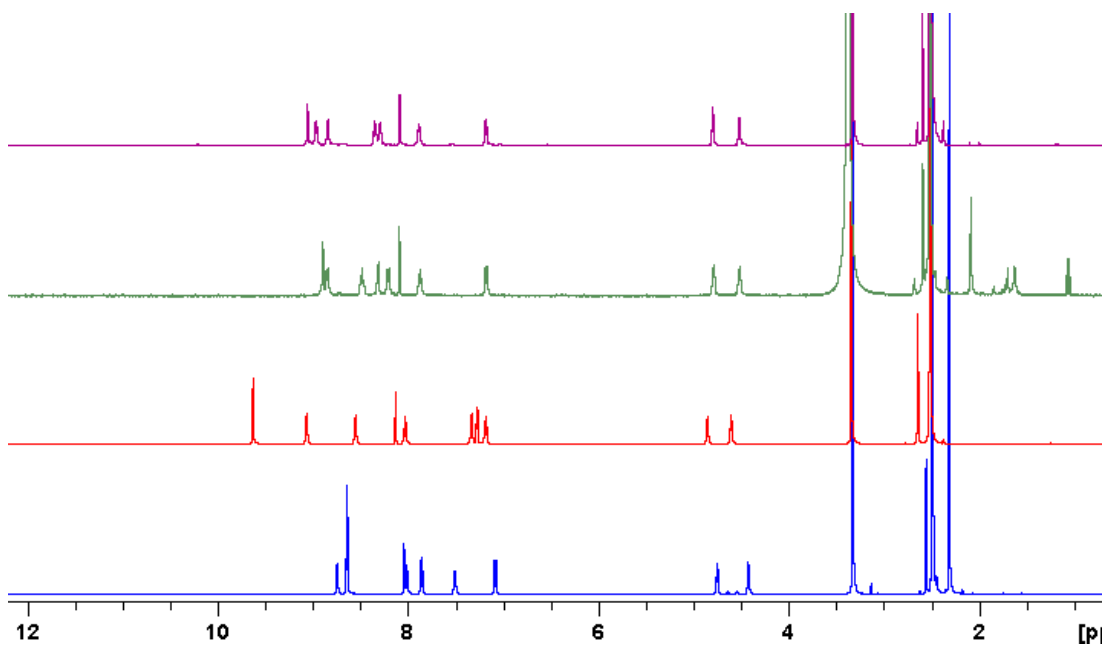


**Figure 3.20:**  $^1\text{H}$  NMR spectra of free  $\text{L}^1$  (blue), Fe (red), Pd (green), and Zn (purple) complexes in  $\text{d}_6$ -DMSO

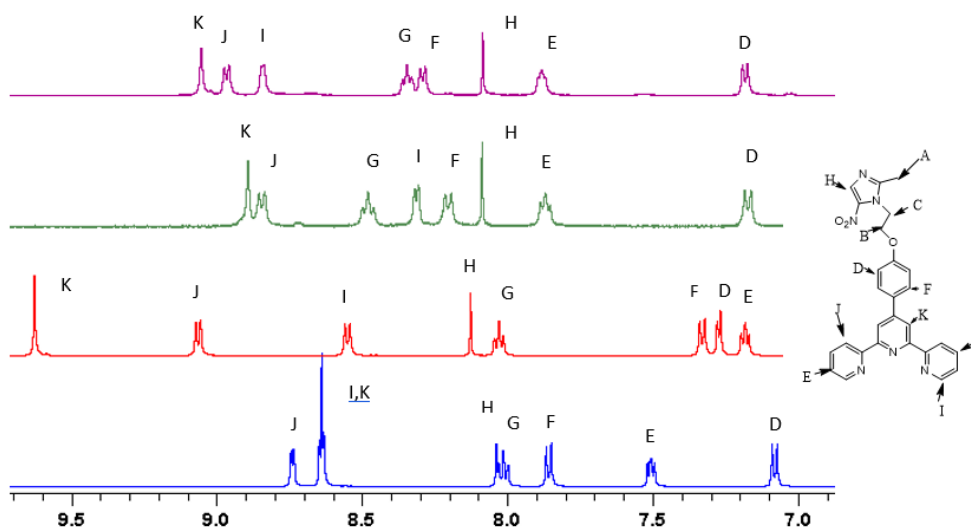


Figure 3.21: Aromatic region of  $^1\text{H}$  NMR spectra of free  $\text{L}^1$  (blue), Fe (red), Pd (green), and Zn (purple) complexes in  $\text{d}^6$  DMSO

Table 3:  $^1\text{H}$  NMR spectra of free  $\text{L}^1$ , Fe, Pd, and Zn complexes

compound	D	E	F	G	H	I	J	K
$\text{L}^1$	7.09	7.52	7.87	8.02	8.06	8.65	8.75	8.65
$[\text{Fe}(\text{L}^1)_2](\text{BF}_4)_2$	7.27	7.17	7.33	8.02	8.13	8.55	9.07	9.64
$[\text{Pd} \text{L}^1(\text{OAc})]\text{OAc}$	7.17	7.87	8.20	8.48	8.08	8.31	8.85	8.89
$[\text{Zn}(\text{L}^1)_2]^{+2}\text{Cl}^-$	7.17	7.88	8.28	8.34	8.08	8.84	8.97	9.05

The  $^{13}\text{C}$  NMR spectra of  $\text{L}^1$  is shown in **Fig 3.22** with its  $\text{Fe}^{\text{II}}$  complex. Despite considerable effort to increase the samples concentrations to obtain the  $^{13}\text{C}$  NMR spectrum of Pd and Zn complexes of  $\text{L}^1$ , all attempts failed. While the Zn complex shows solubility in  $\text{DMSO-d}^6$ , once the concentration increases the solution become cloudy. As a result of this, the  $^{13}\text{C}$  NMR

data is of poor quality and unsuitable for comparison to the free ligand and  $[\text{Fe}(\text{L}^1)_2](\text{BF}_4)_2$  spectra, which are highly soluble in  $\text{DMSO-d}^6$ .

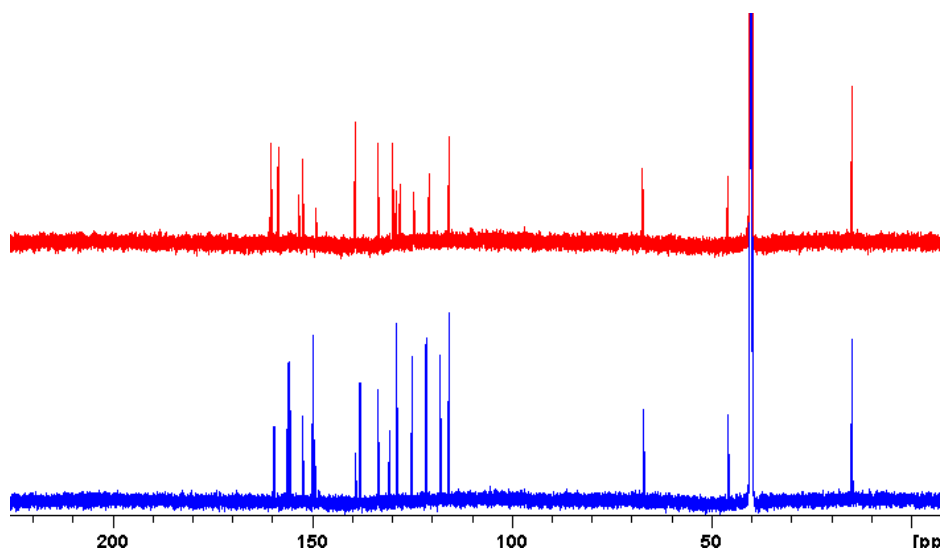


Figure 3.22:  $^{13}\text{C}$  NMR spectra of  $\text{L}^1$  (blue) and its iron complex (red)

### 3.3.4.3 Electronic Absorption Spectroscopy

The electronic spectrum of  $\text{L}^1$  and its complexes have been measured in solution and the significant absorption bands are given in table 4. The electronic absorption spectra of free ligand  $\text{L}^1$  and all complexes present absorption at high energy  $\sim 300\text{-}320$  which are attributed to triimine-centred  $\pi\text{-}\pi^*$  and  $n\text{-}\pi^*$  excitations characteristic of intra-ligand terpy transition.<sup>13</sup> The essential absorption of the prepared complexes appeared red shifted compared to free ligand  $\text{L}^1$  as seen in **Fig 3.23** and **Fig 3.24**. The electronic reflectance spectra of **5** are characterized by a broad band at  $731(10)$  typical for overlapping  $d_{xy} \rightarrow d_{x^2-y^2}$ ,  $d_{yz}$ ,  $d_{xz} \rightarrow d_{x^2-y^2}$  and  $d_{z^2} \rightarrow d_{x^2-y^2}$  transitions between d orbitals of the coordinated copper(II) ion.<sup>11,69</sup> Despite the incredible efforts to obtain d-d transitions for the rest of the complexes, all attempted failed. The concentration of the solution of the complexes have been increased from  $10^{-6}$  to  $10^{-1}$  M, however d-d transition cannot be observed.

**Table 4: Electronic spectral assignments for L<sup>1</sup> and complexes**

Compound <sup>a</sup>	$\pi-\pi^*$ transition/ $\lambda$ (nm)	MLCT/ $\lambda$ (nm)	References (for MLCT)
<b>L<sup>1</sup></b>	298(44435), 279(33891), 324(55564)	–	
[Fe(L <sup>1</sup> ) <sub>2</sub> ](BF <sub>4</sub> ) <sub>2</sub> <b>1</b>	257(17154), 285(22676), 324(30185)	569(9074)	59
[Ni(L <sup>1</sup> ) <sub>2</sub> ](BF <sub>4</sub> ) <sub>2</sub> <b>2</b>	278 (40581), 324 (53145)	344(49272)	62, 63
[Co(L <sup>1</sup> ) <sub>2</sub> ](BF <sub>4</sub> ) <sub>2</sub> <b>3</b>	297(1900), 330(1500)	523(78)	65
[Zn(L <sup>1</sup> ) <sub>2</sub> ] Cl <sub>2</sub> <b>4</b>	268(1700), 291(28000), 327(27000)	346(29000)	66
[Cu(L <sup>1</sup> ) <sub>2</sub> ] Cl <sub>2</sub> <b>5</b>	278(21000), 301(23000),337(26000)	350(9120)	58,13
[Pd L <sup>1</sup> (OAc)]OAc <b>6</b>	278(22197),305(19872), 352(14299)	368(14363)	67, 13

<sup>a</sup> Perform at room temperature (**1, 2, 3**) in CH<sub>3</sub>CN solution, (**4, 5**) in DMSO, (**6**) in H<sub>2</sub>O and L<sup>1</sup> in DCM solution; Number in the parentheses indicates molar absorption coefficient  $\epsilon$  (M<sup>-1</sup>cm<sup>-1</sup>).

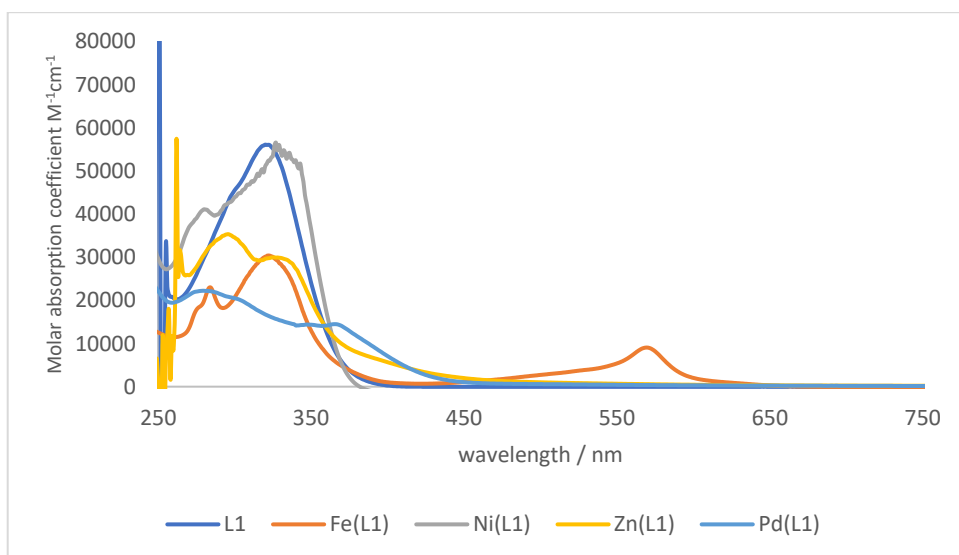


**Figure 3.23: UV-vis absorption profiles of L<sup>1</sup> and its complexes**

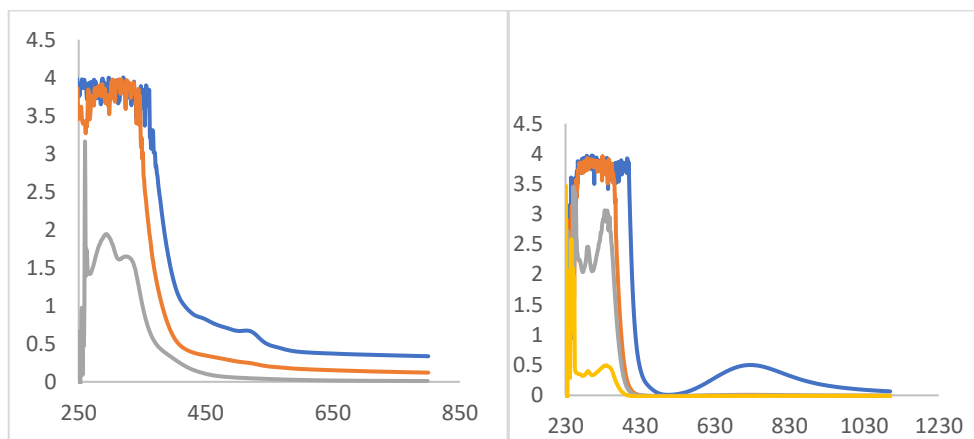


Figure 3.24: UV-vis absorption profiles 3 (left) and 5 (right)

### 3.3.5 Complexes of $L^2$

The general synthetic route for the synthesis of the complexes of  $L^2$ , consists of the addition of a solution of 4'-(4-(3-(2-nitro-1H-imidazol-1-yl)propoxy)phenyl)-2,2':6',2''-terpyridine in DCM to a solution of the metal salt in ethanol. In octahedral complexes, two equivalents of the  $L^2$  with one equivalent of the corresponding salts in an ethanol or ethanol/ DCM mixture at room temperatures afforded complexes in ~ 50 % yields. However, the square planer complexes were prepared by adding one equivalents of the  $L^2$  with one equivalent of the corresponding salts in ethanol/ DCM mixture at room temperature. All reactions occur almost instantaneously with immediate colour change occur upon mixing, with the exception being the reaction with Pd(II) which required prolonged timing over 12 hours.

#### Octahedral complexes of $L^2$

Complexes of iron (II) zinc (II), cobalt (II), copper (II) and nickel (II) with  $L^2$  were prepared using method analogue to those for  $L^1$ .

### 3.3.5.1 Bis (4'-(4-(3-(2-nitro-1H-imidazol-1-yl)propoxy)phenyl)-2,2':6',2''- terpyridine) iron(II) tetra fluoroborate (7)

Upon the addition of 1 equivalent of metal ion solution to 2 equivalents of  $L^2$ , the colour has changed immediately to purple. After several minutes a purple precipitate formed the octahedral structure complex similar this reported in the literature.<sup>58</sup> In the  $^1H$  NMR spectra, the chemical shifts of the protons adjacent to the pyridyl rings were shifted up field because of the coordination to the metal ion. The  $^{13}C$  NMR spectrum showed 18 carbon peaks. The UV-vis consistent with the proposed structure. This indicates absorbance of Fe (II) complex at 232(250000), 285(130000) and 328(170000) nm were assigned to the  $\pi-\pi^*$  of the ligand transition and the 572(50000) nm absorption was assigned to MLCT transition.<sup>59</sup> Positive mode ESI-HRMS gave a peak at 506.1414, (100 %) corresponding to the dicationic  $[Fe(L^2)]^{+2}$  m/z ion. High resolution  $ES^+$  spectrum for  $[Fe(L^2)_2BF_4]^+$  found to be 1099.2924 which matches the theoretical calculation. Comparison of the IR spectra of 7 to free  $L^2$ , show the band for C=N at  $1583\text{ cm}^{-1}$  for free  $L^2$  shifted to higher frequency of  $1600\text{ cm}^{-1}$  after coordination.

### 3.3.5.2 Bis (4'-(4-(3-(2-nitro-1H-imidazol-1-yl)propoxy)phenyl)-2,2':6',2''- terpyridine) Ni (II)tetra fluoroborate (8)

The nickel (II) complex, 8, was produce by following the procedure used to prepare 7. Beige colour precipitate was obtained after 3 hours. High resolution positive mode ESI-HRMS spectrometry, showed a peak at 1101.2926, (100%) corresponding to the  $[(L^2)_2- Ni-BF_4]^+$  ion with the correct isotope pattern. Positive mode ESI-HRMS gave a peak at 507.1399, (100%) corresponding to the  $[Ni(L^2)]^+$  m/z ion. Because of the great similarity between 7 and 8, they

have almost the same absorbance in the infra-red spectra. The electronic absorption spectra of **8** show typical  $\pi$ - $\pi^*$  transitions at high energy at 235(36000), 286(53000) and 317(61000) nm and MLCT transition at 343(71000) nm. The spectrum is in good agreement with the UV/vis spectrum recorded by Ratone *et al.*<sup>62</sup> of  $m/z$   $[\text{Ni-terpy Cl}_2 \text{ H}_2\text{O}]^{+2}$ .

#### 3.3.5.3 Bis (4'-(4-(3-(2-nitro-1H-imidazol-1-yl)propoxy)phenyl)-2,2':6',2''- terpyridine) cobalt (II)tetra fluoroborate (**9**)

The cobalt (II) complex, **9**, was isolated as deep red powder. High resolution mass spectrometry suggested the formulation of the complex, showing  $[\text{M}+\text{H}]^+$  at 507.6309, (100%) corresponding to  $m/z$   $[\text{Co}(\text{L}^2)_2]^{+2}$  ion with the correct isotopic pattern. IR analysis was similar to that in **7** and **8**. The UV/vis spectrum was carried out in acetonitrile and a band was observed at 518(2100) nm which was in good agreement with the UV-vis spectrum recorded by Cameron *et al.*<sup>65</sup> assigned as metal-to-ligand charge transfer (MLCT) transition. Moreover, in the UV-vis spectrum, the peaks at 225(80000), 286(79000) and 317(90000) nm were assigned to the  $\pi$ - $\pi^*$  transition of the ligand.

#### 3.3.5.4 Synthesis of bis (4'-(4-(3-(2-nitro-1H-imidazol-1-yl)propoxy)phenyl)-2,2':6',2''- terpyridine) copper(II)chloride (**10**)

The copper (II) complex of  $\text{L}^2$ , **10**, was synthesised by stirring 2 equivalents of  $\text{L}^2$  with 1 equivalent of copper chloride in EtOH for 4 hours at room temperature. The complex was a green powder similar to analogous complexes.<sup>58, 10</sup> As that in copper complex of  $\text{L}^1$ , the paramagnetic nature of octahedral copper(II) was also confirmed by the presence of very broad peaks in the  $^1\text{H}$  NMR spectrum. Again, the infra-red spectrum of **10** was similar to that

of **7**, **8** and **9**. The high resolution mass spectrum gave a peak at (1019.2822, 100%) corresponding to the  $[\text{Cu}(\text{L}^2)_2]^{+2}$  ion (**Fig 3.25**). This value agrees with the theoretical value, as seen in **Fig 3.25**, showing the correct isotopic pattern. In the UV-vis spectrum, the peaks of Cu(II) complex **10** at 285(18673) and 321(15057) were attributed to a  $\pi-\pi^*$  intraligand  $\text{L}^2$  transition of terpy, whereas the peak at 369 (3181) was assigned to metal-to-ligand charge transfer (MLCT) transition, again in the agreement with data in the literature.<sup>13,58</sup>

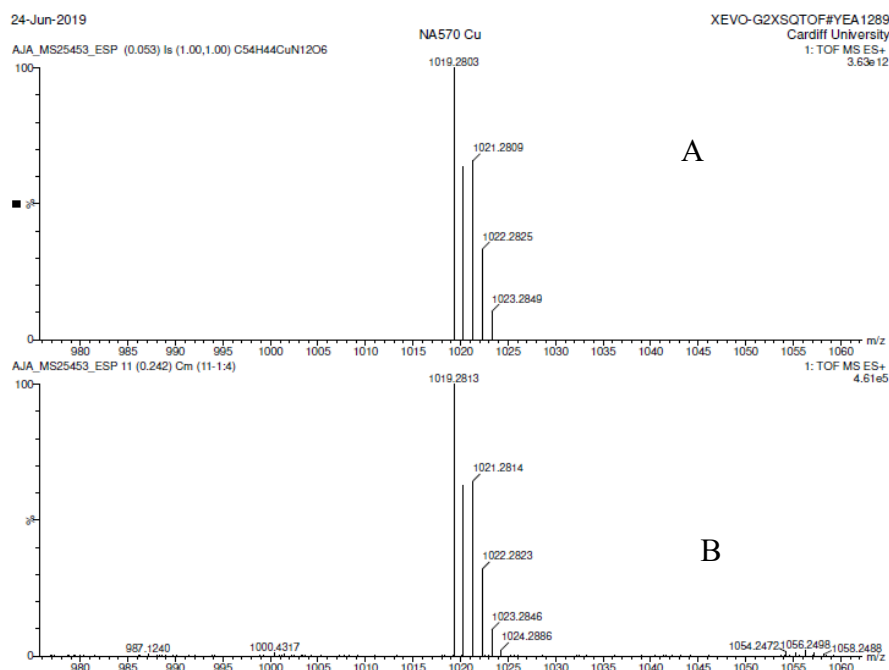


**Figure 3.25: Experimental and theoretical mass spectra of 10: (A) theoretical spectrum, (B) experimental spectrum**

### 3.3.5.5 Synthesis of 4'-(4-(3-(2-nitro-1H-imidazol-1-yl)propoxy)phenyl)-2,2':6',2''-terpyridine zinc (II) chloride (**11**)

The Zn complex of  $\text{L}^2$  was prepared using method analogous to that for  $\text{L}^1$ . The desired product was obtained as a white powder with 46 % yield. The  $^1\text{H}$  NMR spectra of the complex showed down-field shift for the 6,6''-tpyHs compared to the free  $\text{L}^2$  due to related coordinating N-donor polypyridyl ligands. Again, the  $^{13}\text{C}$  NMR spectrum was of poor quality,

due to the low solubility of  $[\text{Zn}(\text{L}^2)_2]^{+2}$ . Similar to that of  $[\text{Zn}(\text{L}^1)_2]^{+2}$ , positive mode mass spectrometry reveals two peaks, one of these peaks was at 510.14 that exactly matches the theoretical expectation of the complex  $m/z$   $[\text{Zn}(\text{L}^2)_2]^{+2}$ . The other peak at 587.10 could probably be corresponded to  $m/z$ :  $[\text{C}_{45}\text{H}_{44}\text{N}_{12}\text{O}_6\text{Zn} \cdot \text{Formic acid}]$ .  $[\text{Zn}(\text{L}^2)_2]^{+2}$  and  $[\text{Zn}(\text{L}^1)_2]^{+2}$  have very similar features in the electronic spectra, showing typical  $\pi$ - $\pi^*$  transitions at high energy at 288(19313), 323(11745) and 340(10036) which are corresponding to intra-ligand terpy and absorption of the MLCT transition is observed at higher wavelength 340(10036) and 385(4098). That is in agreement with similar complexes reported in the literature.<sup>66</sup>

### Square planar group complexes of $\text{L}^1$

#### 3.3.5.6 Synthesis of 4'-(4-(3-(2-nitro-1H-imidazol-1-yl)propoxy)phenyl)-2,2':6',2''-terpyridine palladium (II) acetate (**12**)

Complex **12** was prepared by mixing one equivalent of  $\text{L}^2$  with one equivalent of palladium acetate to yield a yellow powder. Positive mode ESI-HRMS spectrometry, showed a peak corresponding to the  $[\text{L}^2\text{-Pd-CH}_3\text{CO}_2]^+$  at 629.0773 suggesting the ligand metal ratio of 1:1. In the  $^1\text{H}$  NMR spectrum, one set of signals for  $\text{L}^2$  and again these have shifted relative to the starting ligand. The  $^{13}\text{C}$  NMR spectra of  $\text{L}^2\text{-Pd-CH}_3\text{CO}_2$  displayed 19 peaks consistent with the carbons in the structure. The IR spectrum shows common features of the  $\text{L}^2$  shifting due to the related chelating N-donor polypyridyl ligands. In the UV-vis, the peaks of Pt(II) complex **12** at nm281(20127), 307(16242) and 320(14327) were attributed to a  $\pi$ - $\pi^*$  intraligand  $\text{L}^2$  transition of terpy, whereas the peak at 375(13057), 393(12489) was assigned to metal-to-ligand charge transfer (MLCT) transitions.<sup>67</sup> The red shift of **12** indicated that the metal coordinated with the ligand through nitrogen atoms.

### 3.3.6 Spectroscopic Properties of L<sup>2</sup> complexes

#### 3.3.6.1 Vibrational Spectroscopy

Comparing of the IR spectra of the free L<sup>2</sup> to the complexes shows, the band of C=N at 1583 cm<sup>-1</sup> shifted to higher frequency after coordination, which suggested the coordination of the metal ion with the nitrogen atom of pyridyl. FT-IR spectrum of the resulting complexes of L<sup>2</sup> presented all the absorption peaks of (imidazole ring) such as N=O asymmetric and symmetric. As with the complexes of L<sup>1</sup>, the [Fe(L<sup>2</sup>)<sub>2</sub>](BF<sub>4</sub>)<sub>2</sub>, [Co(L<sup>2</sup>)<sub>2</sub>](BF<sub>4</sub>)<sub>2</sub> and [Ni(L<sup>2</sup>)<sub>2</sub>](BF<sub>4</sub>)<sub>2</sub> complexes exhibit one characteristic band indicative of ionic tetrafluoroborate at 1052 cm<sup>-1</sup>. L<sup>2</sup> complexes have similar behaviour to L<sup>1</sup> complexes in the infra-red spectrum when coordinate with the metal ions.

**Table 5: IR stretching frequencies of L<sup>2</sup> and its complexes**

Compound		BF <sub>4</sub>	N=O <sub>asym</sub>	N=O <sub>sym</sub>	C=N	C-H	C=C-H
2-nitroimidazole		–	1541, 1519	1359, 1338		2950	–
Terpy-OH		–	–	–	1581, 1560	–	3064
L <sup>2</sup>		–	1533, 1516	1361- 1300	1583	2973	3111-3053
[Fe(L <sup>2</sup> ) <sub>2</sub> ](BF <sub>4</sub> ) <sub>2</sub>	7	1053	1539, 1521	1361 -1300	1600	2873	3116, 3086
[Ni(L <sup>2</sup> ) <sub>2</sub> ](BF <sub>4</sub> ) <sub>2</sub>	8	1050	1539 ,1521	1363, 1307	1600	2954, 2873	3134, 3116
[Co(L <sup>2</sup> ) <sub>2</sub> ](BF <sub>4</sub> ) <sub>2</sub>	9	1051	1541, 1521	1363	1600	2872	3122
[Zn(L <sup>2</sup> ) <sub>2</sub> ]Cl <sub>2</sub>	10	–	1541, 1521	1361, 1355	1598	2912, 2826	3079, 3055

$[\text{Cu}(\text{L}^2)_2] \text{Cl}_2$	11	_	1521	1355	1597	2959, 2879	3064
$[\text{Pd} \text{L}^2(\text{OAc})] \text{OAc}$	12	_	1539, 1521	1351, 1309	1591	2989	3101, 3072

### 3.3.6.2 $^1\text{H}$ and $^{13}\text{C}$ NMR of Fe, Pd and Zn complexes of $\text{L}^2$

All protons in the iron, palladium and zinc complexes of  $\text{L}^2$  are shifted compared to the free ligand  $\text{L}^2$ . As that in  $\text{L}^1$ , this shift occurs as a result of the great decrease in electron density around the protons next to the polypyridine moiety because of the coordination of nitrogen donors to metal centre.

As seen in **figure 3.26**, it is clear from  $^1\text{H}$  NMR spectra of Fe, Pd and Zn complexes of  $\text{L}^2$  that the peaks at aliphatic regions remain in their position after coordination. This is because these protons are remote from the chelating sites and the coordination does not have effect on these protons. However, the position of the peaks in aromatic region underwent noticeable changes (**Fig 3.27**), due to the coordination of the ligand to the metal ions as explained previously in  $\text{L}^1$  complexes.

Although, the peaks of E, D and G of **11** and **12** are in the aromatic region, they remain the same upon metalation. The peaks of H and K slightly shifted after coordination with approximately 0.32 ppm. However, the most shifted protons in case of **11** are I with ca~ 76 ppm and about 40 ppm in case of **12** (**Fig 3.27**) (**Table 6**).

The peak of E and G of **7** remained almost the same after coordination, whereas L was the most shifted peak with ca~ 94 ppm compared to free  $\text{L}^2$  (**Table 6**).

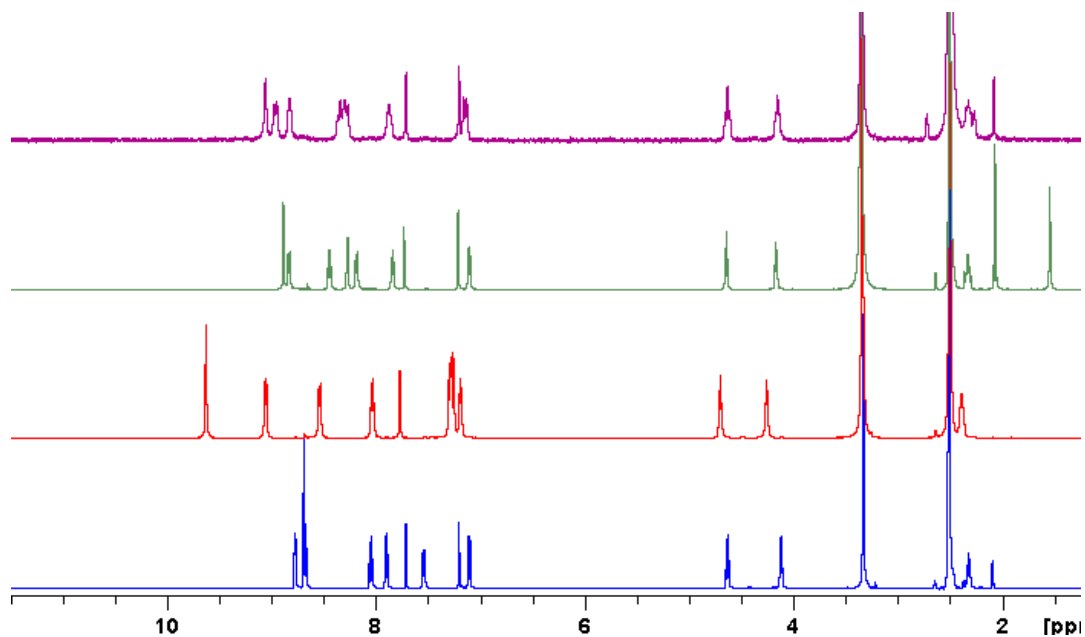


Figure 3.26:  $^1\text{H}$  NMR spectra of free  $L^2$  (blue), 7 (red), 12 (green), and 11 (purple) complexes in  $d_6$  DMSO

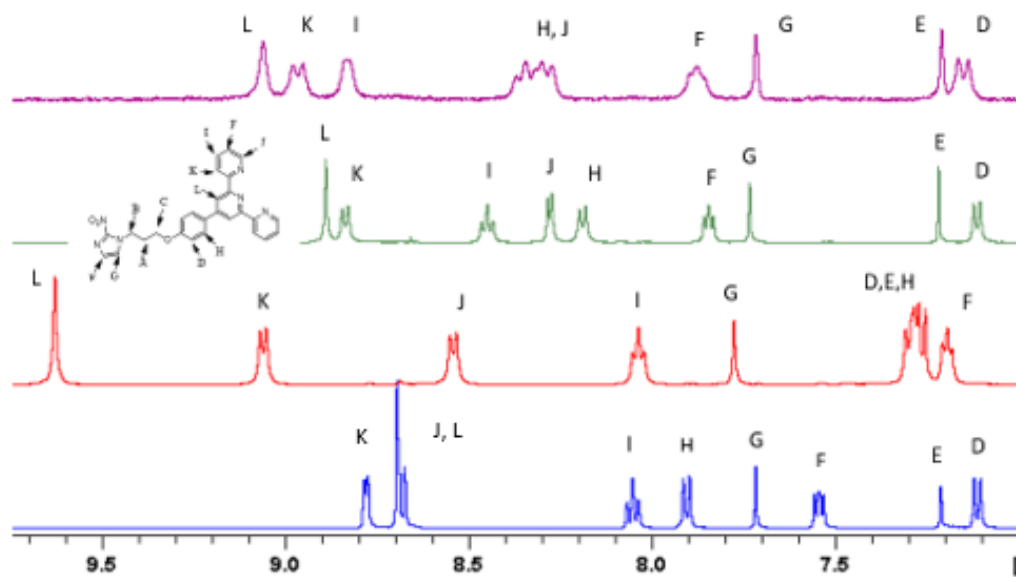


Figure 3.27: The aromatic region  $^1\text{H}$  NMR spectra of free  $L^2$  (blue), Fe (red), Pd (green), and Zn (purple) complexes in  $d_6$  DMSO

**Table 6: <sup>1</sup>H NMR spectra of free L<sup>2</sup>, Fe, Pd, and Zn complexes**

compound		D	E	F	G	H	I	J	K	L
L <sup>2</sup>		7.11	7.2	7.54	7.72	7.91	8.07	8.67	8.77	8.69
[Fe(L <sup>2</sup> ) <sub>2</sub> ](BF <sub>4</sub> ) <sub>2</sub>	7	7.18	7.24	7.27	7.77	7.31	8.03	8.53	9.09	9.63
[Pd L <sup>2</sup> (OAc)]OAc		7.14	7.21	8.20	7.72	8.20	8.49	8.33	8.87	8.92
12										
[Zn(L <sup>2</sup> ) <sub>2</sub> ] Cl <sub>2</sub>		7.14	7.21	7.87	7.72	8.28	8.83	8.34	8.97	9.09
11										

The <sup>13</sup>C NMR spectra of **7** was compared with <sup>13</sup>C NMR spectrum of the free ligand as shown in **Fig 3.28**, exhibit the expected eighteen carbon atoms and this confirm the symmetry of Fe complexes with two equivalent terpy-nitroimidazole ligands. While the intensity of <sup>13</sup>C NMR signals of **12** were very weak and the spectrum is little noisy compared to that in **7**, it shows the expected peaks for this complex. In addition, two extra carbon peaks were observed, one of them in the aliphatic region at 23 ppm assigned to the methyl group of acetate ligand. The other carbon peak was found at 176 ppm corresponding to the carbonyl carbon of the acetate ligand (**Fig 3.29**).

Again, despite considerable effort to increase the samples concentrations to obtain the <sup>13</sup>C NMR spectrum of **11**, all attempts failed using range of solvents from CD<sub>3</sub>CN to DMSO.

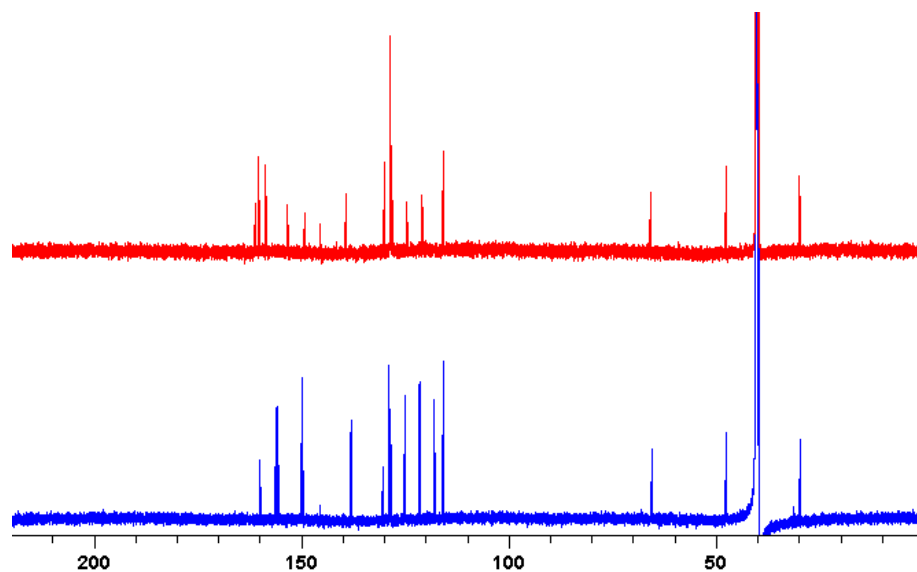


Figure 3.28:  $^{13}\text{C}$  NMR spectra of  $\text{L}^2$  (blue) and 7 (red)

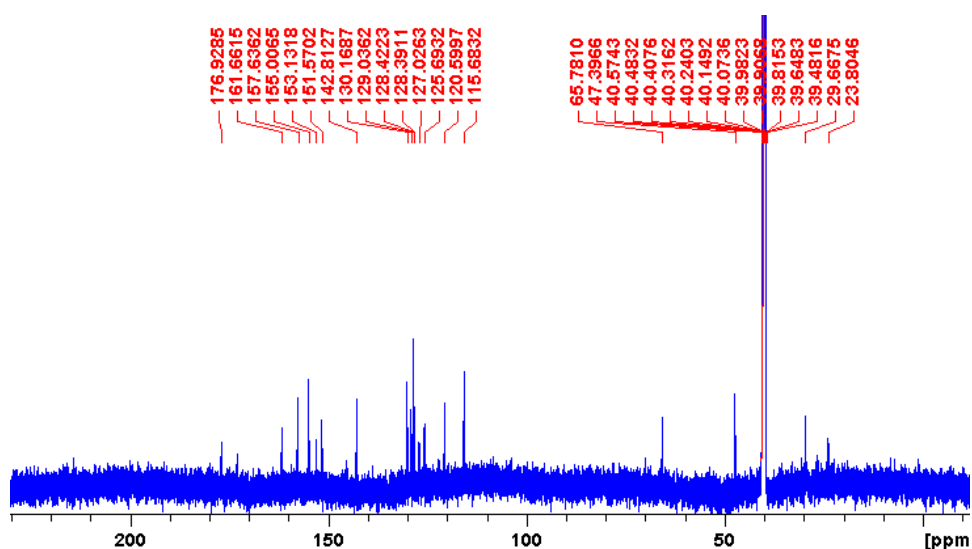


Figure 3.29:  $^{13}\text{C}$  NMR spectrum of 12

The NMR spectra of Fe, Pd and Zn complexes of  $\text{L}^2$  are highly comparable to their counterparts of  $\text{L}^1$  complexes with exception of the peaks of nitroimidazole moieties. For instance, when the  $^1\text{H}$  NMR spectra of the  $[\text{Fe}(\text{L}^1)_2](\text{BF}_4)_2$  compared with that of  $[\text{Fe}(\text{L}^2)_2](\text{BF}_4)_2$ , the proton in the aromatic region have the same pattern of shift (Fig 3.30).

The same phenomenon occurs with the  $^{13}\text{C}$  NMR spectra as seen in Fig 3.31.

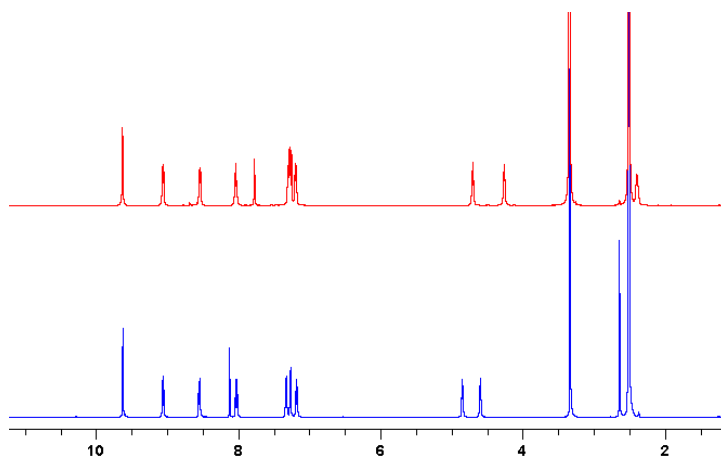


Figure 3.30:  $^1\text{H}$  NMR spectra of 1 (blue) and 7 (red)

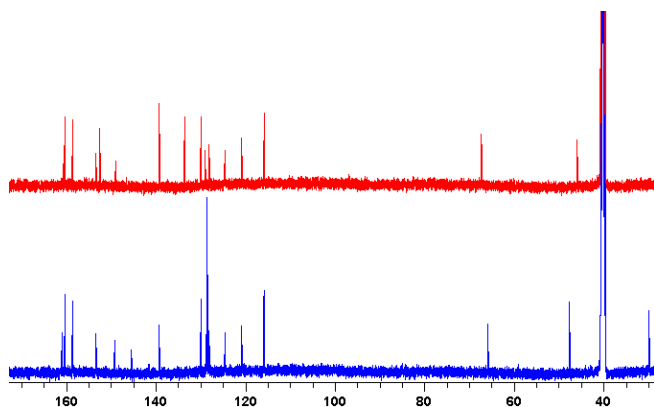


Figure 3.31:  $^{13}\text{C}$  NMR spectra of 1 (blue) and 7 (red)

### 3.3.6.3 Electronic Absorption Spectroscopy

Similar to that in  $\text{L}^1$  complexes, the electronic absorption spectra of  $\text{L}^2$  complexes show typical  $\pi\text{-}\pi^*$  transitions at high energy  $\sim 300\text{-}320$  and absorption of MLCT transitions observed at higher wavelength as presented in **Fig 3.32** and **Fig 3.33**. All the values have been tabulated in table 7. Copper complex of  $\text{L}^2$ , **10**, exhibit a broad band at 741(99) representing d-d transitions between d orbitals of the coordinated  $\text{Cu}^{+2}$ .<sup>11,69</sup> Again, as that in  $\text{L}^1$  complexes, d-

d transition of the other complexes cannot be obtained, despite running the spectra at significantly higher concentrations.

**Table 7: Electronic spectral assignments for L<sup>2</sup> and complexes**

Compound <sup>a</sup>	$\pi-\pi^*$ transition/ $\lambda$ (nm)	MLCT/ $\lambda$ (nm)	References (MLCT)
L <sup>2</sup>	257(21000),286(34000) ,320(13000)	—	
[Fe(L <sup>2</sup> ) <sub>2</sub> ](BF <sub>4</sub> ) <sub>2</sub>	7 232(250000), 285(130000), 328(170000).	572(50000)	59
[Ni(L <sup>2</sup> ) <sub>2</sub> ](BF <sub>4</sub> ) <sub>2</sub>	8 235(36000), 286(53000), 317(61000).	343(71000)	62, 63
[Co(L <sup>2</sup> ) <sub>2</sub> ](BF <sub>4</sub> ) <sub>2</sub>	9 225(80000), 286(79000),317(90000).	518(2100)	65
[Cu(L <sup>2</sup> ) <sub>2</sub> ] Cl <sub>2</sub>	10 285(18673), 321(15057).	369(3181)	13,58
[Zn(L <sup>2</sup> ) <sub>2</sub> ] Cl <sub>2</sub>	11 288(19313), 323(11745), 340(10036).	385(4098)	66
[Pd L <sup>2</sup> OAc]OAc	12 281(20127), 307(16242), 320(14327).	375(13057),393(12489)	13, 67

Electronic spectral assignments for L<sup>2</sup> and complexes.<sup>a</sup> Perform at room temperature (7, 8, 9) in CH<sub>3</sub>CN, (10) in DMSO, (L<sup>2</sup>, 11, 12) in CH<sub>3</sub>Cl; Number in the parentheses indicates molar absorption coefficient  $\epsilon$  (M<sup>-1</sup>cm<sup>-1</sup>).

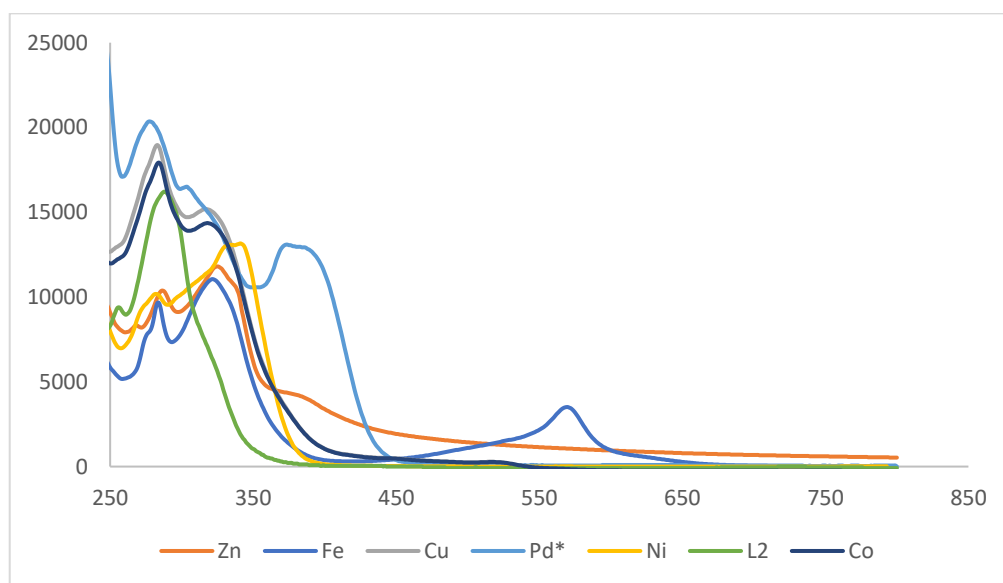


**Figure 3.32: UV-vis absorption profiles of L<sup>2</sup> and its complexes**

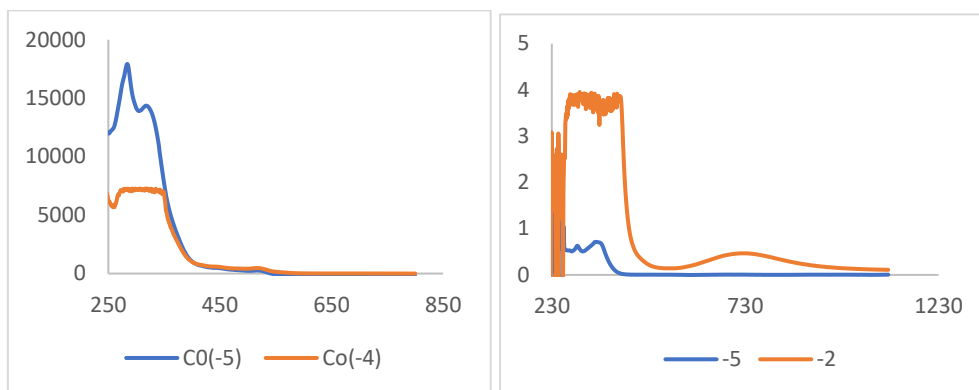


**Figure 3.33: UV-vis absorption profiles of 9 (left) and 10 (right)**

### 3.4 Electrochemistry

The cyclic voltammetry experiments were carried out with an PARSTAT 2273 (Advanced Electrochemical System from Princeton Applied Research) in conjunction with General Purpose Electrochemical System software (GPES version 4.7 for Windows) in a three-electrode glass cell with Teflon cap. A platinum working electrode a silver reference electrode and a platinum counter electrode were used for all experiments. The working electrode was washed with acetone and dried for 15 minutes prior to each use. In some compounds, a 0.1 M [Bu<sub>4</sub>N][PF<sub>6</sub>] solution in anhydrous dichloromethane (DCM) was used as supporting electrolyte. Ferrocene was used as internal reference. DCM was degassed with nitrogen and all experiments were carried out in an inert atmosphere. A background measurement was recorded in each experiment. Approximately 5mg of each compound were added to the solution and the redox potential of each sample then was recorded. All the data that has been recorded has been manipulated according to ferrocene in non-aqueous solution as a reference, at 298.5K and corresponds to 0.2V s<sup>-1</sup> scan rate unless otherwise stated.

The cyclic voltammogram of  $L^1$  reveals one reversible reduction in the cathodic region at -1.71 V referenced against ferrocenium/ferrocene (Fc<sup>+</sup>/Fc). Inspection of isolated feature reveals a single reversible wave process at cathodic potential of -1.71 V vs (Fc<sup>+</sup>/Fc), which is reversible over the scan rate range 200- 800 V s<sup>-1</sup> (Fig 3.34). This was demonstrated by plotting the square root of the scan rate against the peak current (Fig 3.34; inset). The profile, ratio of cathodic to anodic peak current, and peak to peak separation would suggest that this is one-electron transfer process. In the previously reported literatures, the redox behaviour of terpyridine typically revealed three redox couples referenced to the Ag/Ag<sup>+</sup> electrode. One reversible couple with a half-wave potential of -2.047 V, quasi reversible wave at -2.507 V and an irreversible cathodic wave at -2.99 V.<sup>70</sup> Those values do not much the value obtained in this study, the possible explanation for this could refer the presence of nitroimidazole moiety with terpy in  $L^1$ . Nitroimidazoles such as metronidazole and azomycin have distinctive redox activities, therefor reversible couple with a half-wave potential of -1.71 V could be assigned to nitroimidazole moiety.

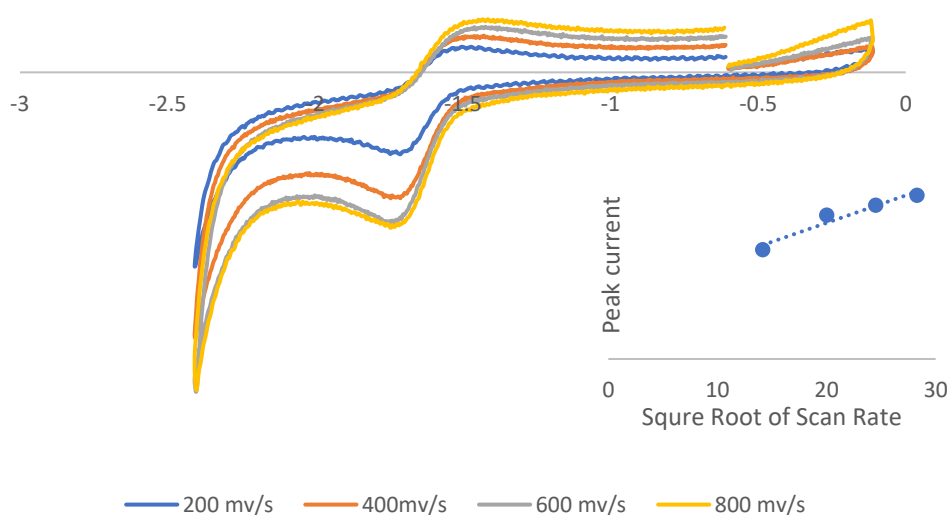
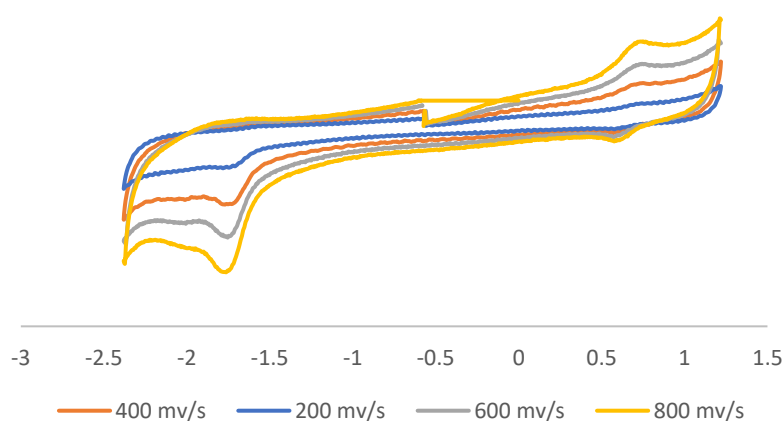


Figure 3.34: Cyclic voltammogram for  $L^1$  vs (Fc<sup>+</sup>/Fc)

The cyclic voltammogram of the Fe (II) complex of **L**<sup>1</sup> reveals a quasi-reversible redox process in the anodic region at +0.73 V referenced against ferrocenium/ferrocene (Fc<sup>+</sup>/Fc). This process is most likely attributed to Fe(II)/Fe(III) redox couple. There is one irreversible reduction in the cathodic region at -1.76 V referenced against ferrocenium/ferrocene which could be ligand-based process (**Fig 3.35**).

However, The structure of [Fe(terpy)<sub>2</sub>]<sup>2+</sup> with (PF<sub>6</sub>)<sup>2-</sup> or ClO<sub>4</sub><sup>-</sup> has been reported and its electrochemistry revealed five redox steps where observed, four where at negative potential and the reversible Fe(II)/Fe(III) couple was observed at positive potential at +1.09V vs. SSCE.<sup>41</sup> Another study of electrochemistry of [Fe(terpy)<sub>2</sub>](BF<sub>4</sub>)<sub>2</sub> presented The electrochemical response of the complex [Fe(terpy)<sub>2</sub>](BF<sub>4</sub>)<sub>2</sub> in MeCN solution + 0.1 M TBAPF<sub>6</sub>, using a carbon electrode, presented three reversible redox processes at -1.75, -1.6 V and +0.75 V, attributed to the reduction of terpyridine ligands and to oxidation of the metal centre. A third irreversible electrochemical reduction, at -2.420 V vs Fc<sup>-</sup>/Fc<sup>+</sup> with higher peak current is observed.<sup>71</sup>



**Figure 3.35: Cyclic voltammogram for complex 1 vs (Fc<sup>+</sup>/Fc)**

The cyclic voltammogram of the Nickel complex **2**, reveals one irreversible reduction process in the cathodic region at -2.17 V vs. (Fc<sup>+</sup>/Fc), which is irreversible over the scan rate range 200- 800 V s<sup>-1</sup> (**Fig 3.36**). In the previously reported Ni-terpy, there were two reversible and electrochemical features at -1.62 and -1.88 V vs. Fc<sup>+</sup>/Fc. Both features were assigned to ligand-based electrochemical processes.<sup>72</sup>

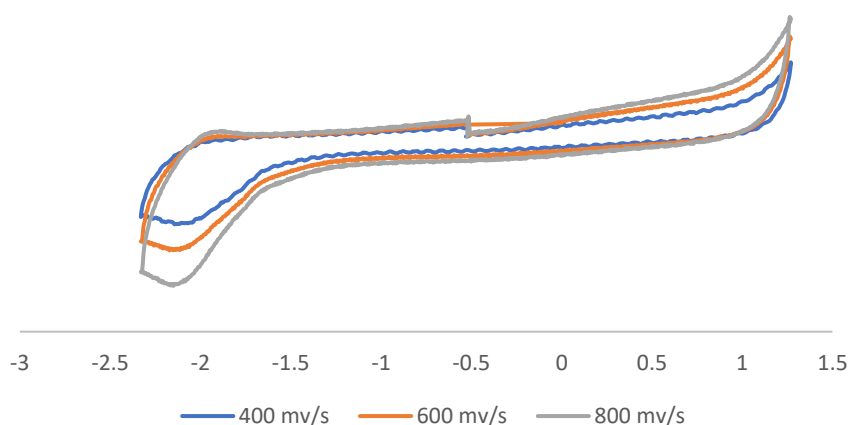


**Figure 3.36: Cyclic voltammogram for complex 2 vs (Fc<sup>+</sup>/Fc)**

The voltammogram of the Co (II) complex **3**, has quite similar electrochemical behaviour to the analogue Ni(II) complex **3** showing a similar irreversible reduction at -1.6 V (vs Fc<sup>+</sup>/Fc), (**Fig 3.37**). Without further investigation it is difficult to assign the exact origins of this feature. However, similarities of the voltammograms of complex **3** and complex **4**, may suggest that the observed processes are largely ligand based. The electrochemistry of [Co(terpy)<sub>2</sub>]<sup>+2</sup> has been studied before and the cyclic voltammogram for this complex displayed two reversible one-electron electrochemical features one at -2.03 V vs. Fc<sup>+</sup>/Fc, attributed to a one-electron ligand-based reduction. The other reversible reduction present at -1.17 V vs. Fc<sup>+</sup>/Fc, is a reversible metal-based process, assigned to a Co<sup>II</sup>/Co<sup>I</sup> reduction.<sup>72</sup>

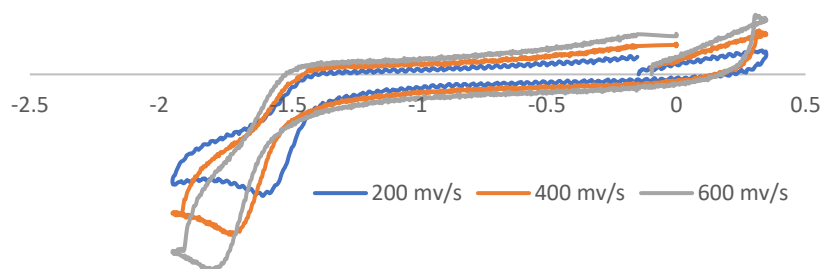


**Figure 3.37: Cyclic voltammogram for complex 3 vs (Fc<sup>+</sup>/Fc)**

The cyclic voltammogram of **L<sup>2</sup>**, exhibits a quasi-reversible wave at -1.7 mV referenced against (vs Fc<sup>+</sup>/Fc) (**Fig 3.38**). The separation between the anodic and cathodic peaks, Ep<sup>c</sup> – Ep<sup>a</sup>, is 34 mV which is significantly lower than the 59 mv theoretically expected for a one-electron Nerstian process. Compared to **L<sup>1</sup>**, both ligands show electrochemical features at -1.7 V. This may be assigned to NO<sub>2</sub> electrochemical processes of the nitroimidazole ligands or terpy ligand.

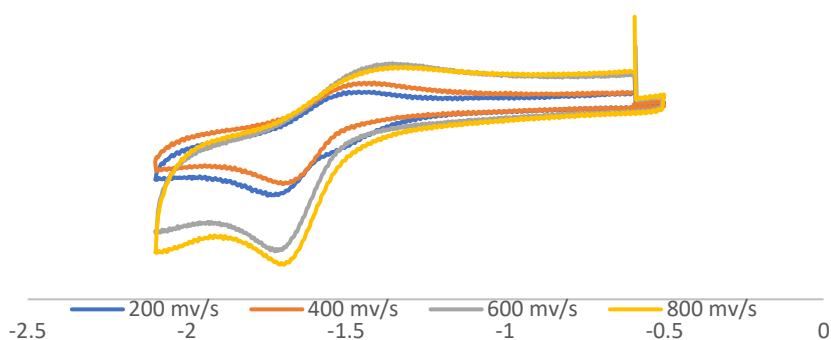


**Figure 3.38: Cyclic voltammogram for L2 vs (Fc<sup>+</sup>/Fc)**

The iron complex **7**, contains a single reversible wave process at cathodic potential of -2.02 V (vs Fc<sup>+</sup>/Fc), which has been ascribed to ligand-based process. This was reversible over the scan of 200 – 800 V s<sup>-1</sup> (**Fig 3.39**) and was demonstrated by plotting the square root of the scan rate against the peak current (**Fig 3.39; inset**). The separating between the anodic and cathodic peaks, E<sub>p</sub><sup>c</sup> - E<sub>p</sub><sup>a</sup> is 120 mv which is significantly higher than the 59 mv theoretically expected for a one- electron Nerstian process perhaps suggesting a two electron process. However, the plots of i<sub>pc</sub> and i<sub>pa</sub> vs. V<sup>1/2</sup> are linear and the i<sub>pa</sub>/i<sub>pc</sub> ratio is close to unity in the 20–80 mV s<sup>-1</sup> scan rate range. In contrast to voltammogram of **1** and previously reported [Fe(terpy)<sub>2</sub>(BF<sub>4</sub>)<sub>2</sub>]<sup>71</sup>, the voltammogram of **7** does not reveal any reversible couple corresponding Fe(II)/Fe(III) which expected to be seen at positive potential at about 0.75 V vs (Fc<sup>+</sup>/Fc). Both voltammogram of **L**<sup>2</sup> and **7** revealed electrochemical process at negative potential.

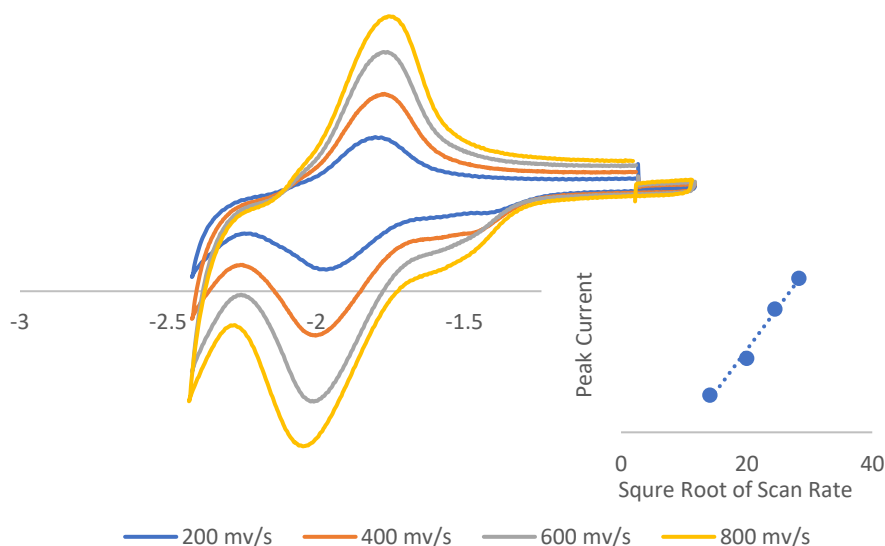


**Figure 3.39: Cyclic voltammogram for complex 7 vs (Fc<sup>+</sup>/Fc)**

Cobalt complex, **9**, contains of sequence of small and ill-defined waves in the cathodic and anodic region indicating rapid decomposition of oxidized or reduced species formed (**Fig3.40**). The voltammogram did not change over the scan rate of 200 – 800  $\text{Vs}^{-1}$ .

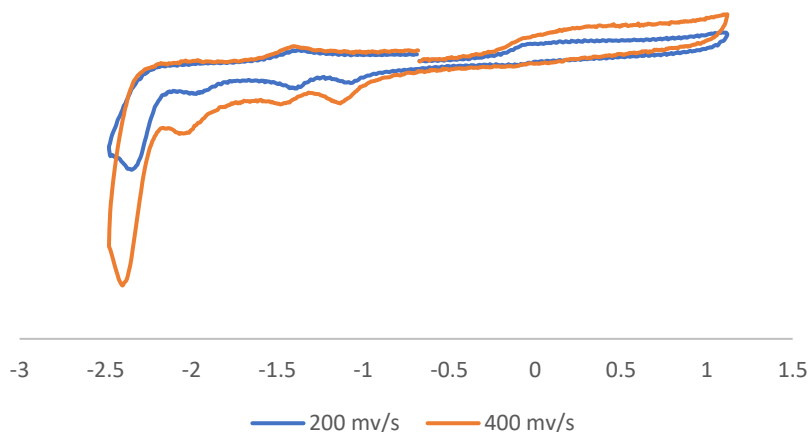


**Figure 3.40: Cyclic voltammogram for complex 9 vs (Fc+/Fc)**

The cyclic voltammogram of complex **12**,  $[\text{Pd L}^2(\text{OAc})]\text{OAc}$  reveals two irreversible reduction within the cathodic region at -1.342 V and -1.551 V referenced against (vs Fc+/Fc) (**Fig 3.41**). As these processes not in the free ligand, it is tentatively assumed these reductive processes are associated with Pd-terpy fragment not to the nitroimidazole.

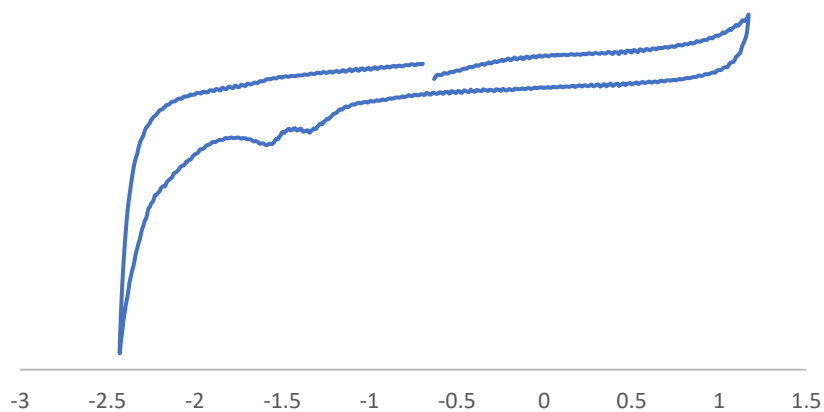


**Figure 3.41: Cyclic voltammogram for complex 12 vs (Fc+/Fc)**

The cyclic voltammogram of **11**, Zn complex of  $L^2$ , shows one irreversible reduction within the cathodic region at -1.956 V referenced against (vs  $Fc^+/Fc$ ) (**Fig 3.42**). The typical voltammogram of Zn-tpy exhibits two reversible electrochemical features, at -1.68 and -1.81 V vs.  $Fc^+/Fc$ . Since the reduction of  $Zn^{II}$  to  $Zn^I$  is unlikely to happen under these conditions, the two waves are allocated to ligand-based reduction processes.<sup>72</sup>

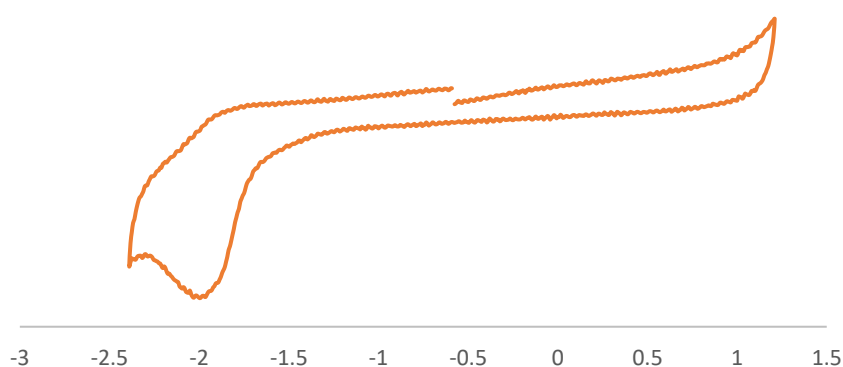


**Figure 3.42: Cyclic voltammogram for complex 11 vs ( $Fc^+/Fc$ )**

### 3.4.1 Summary of electrochemistry

The electrochemical behaviour of all these ligands and their complexes are listed in table 8. Typically, these ligands and complexes are reduced between -1.6 and -2.0 volt vs ( $Fc^+/Fc$ ). It is difficult to determine whether this is the reduction of nitroimidazole or terpy ligand however as the addition of metal ions greatly affects the potential, this would be unexpected for the more remote nitroimidazole moiety. Looking at the free ligands, one would expect that 2-nitroimidazole are more readily reduced than 5-nitroimidazole and as such, if the reduction process in  $L^1$  and  $L^2$  where imidazole based,  $L^2$  would be reduce at a more positive potential. As this is not the case it seems likely that the processes are associated with the terpy ligand.

**Table 8: Electrochemical parameter for the redox processes exhibited by L1, L2 and their complexes in anhydrous DCM solution (supporting electrolyte: [Bu4N][PF6](0.1 mol dm<sup>-3</sup>); T:20 0C. Measured at 0.1 Vs<sup>-1</sup>**

compound		E <sub>p</sub> /V (ΔE, mV) <sup>a,b</sup>
L <sup>1</sup>		-1.71
[Fe(L <sup>1</sup> ) <sub>2</sub> ](BF <sub>4</sub> ) <sub>2</sub>	1	+0.73, -1.76
[Ni(L <sup>1</sup> ) <sub>2</sub> ](BF <sub>4</sub> ) <sub>2</sub>	2	-2.17
[Co(L <sup>1</sup> ) <sub>2</sub> ](BF <sub>4</sub> ) <sub>2</sub>	3	-1.6
L <sup>2</sup>		-1.7 (43)
[Fe(L <sup>2</sup> ) <sub>2</sub> ](BF <sub>4</sub> ) <sub>2</sub>	7	-2.02 (120) (reversible)
[Zn(L <sup>2</sup> ) <sub>2</sub> ] Cl <sub>2</sub>	11	-1.956
[Pd(L <sup>2</sup> )OAc]OAc	12	-1.34, -1.55

<sup>a</sup> The potential at which reversible process occur are calculated as the average of the oxidative and reductive peak potentials (E<sub>p</sub><sup>ox</sup> + E<sub>p</sub><sup>red</sup>)/2. <sup>b</sup> for irreversible process, the anodic or cathodic peak potentials are given. Potentials are given in volts vs (Fc<sup>+</sup>/Fc).

### 3.5 Experimental Section

#### 4'-(4-Hydroxyphenyl)-2,2',6',2''-terpyridine E

The compound was synthesised and purified according to a modified literature procedure.<sup>13</sup> 4-Hydroxybenzaldehyde (2.44 g, 20 mmol) was dissolved in ethanol (100) ml. 2-Acetylpyridine (4.84 g, 40 mmol) and KOH (4.2 g) were added. After stirring for a few minutes, NH<sub>4</sub>OH (50 ml, 25%) was added to the solution. The reaction mixture was stirred at 50°C for 16 hours (the reaction was monitored by TLC). The reaction mixture was adjusted to pH 5 by adding 15 ml acetic acid. The precipitate was filtered and washed with ethanol (3 \* 10 ml). Brown crystals were obtained after drying. Yield (2.23 g, 34%). <sup>1</sup>H NMR (DMSO, 400 MHz) δ 9.08 (m, 4H), 8.91 (s, 2H), 8.72 (td, 2H, J = 7.8, 1.2 Hz), 8.14 (td, 2H, J = 7.8, 1.2 Hz), 8.02 (d, 2H, J = 9.0

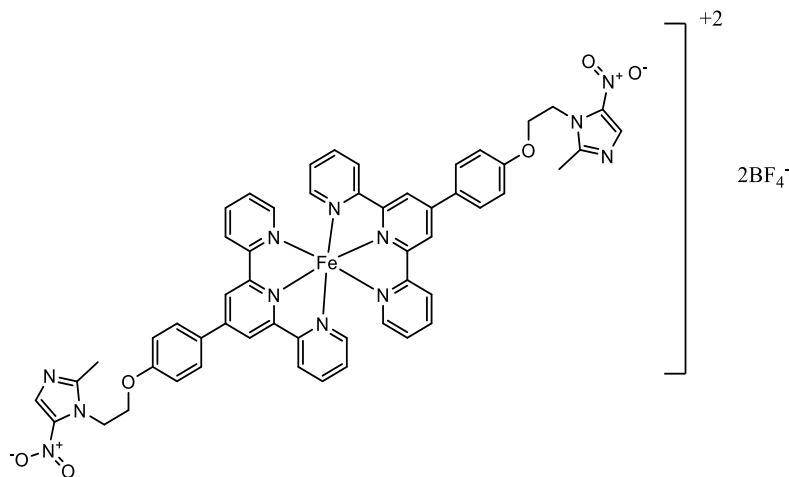
Hz), 7.05 (d, 2H,  $J = 9.0$  Hz);  $^{13}\text{C}$  NMR (DMSO, 100 MHz)  $\delta$ : 160.5, 156.3, 155.9, 149.8, 149.1, 136.8, 131.7, 129.4, 123.7, 121.2, 118.4, 116.5.

**4'-(4-(2-(2-Methyl-5-nitro-1H-imidazol-1-yl)ethoxy)phenyl)-2,2':6',2''-terpyridine (L<sup>1</sup>):**

4'-(4-Hydroxyphenyl)-2,2',6',2''-terpyridine (0.815g, 0.5 mmol) was added to a solution of 2-(2-methyl-5-nitro-1H-imidazol-1-yl)ethyl methanesulfonate (0.124g, 0.5 mmol) in DMF (20 mL), with potassium carbonate (0.69g, 0.5 mmol). The suspension was heated to 85°C for 72h (the reaction was monitored by TLC). After cooling, the solid was filtered then it was sonicated for 5 minutes in DCM (100 ml). The solid was filtered and solvent was evaporated from filtrate. The product was recrystallised from DCM and ETOH and it was obtained as light green crystals. Yield: 0.322g (23%);  $^1\text{H}$  NMR (300 MHz, DMSO)  $\delta$  8.77 (d,  $J = 4.0$  Hz, 2H), 8.68 (d,  $J = 3.5$  Hz, 2H), 8.61 (s, 2H), 8.15 – 8.01 (m, 3H), 7.90 (d,  $J = 8.6$  Hz, 2H), 7.65 (t, 2H), 7.11 (d,  $J = 8.7$  Hz, 3H), 4.78 (t,  $J = 4.9$  Hz, 2H), 4.46 (t,  $J = 4.7$  Hz, 2H) 2.55 (s, 3H);  $^{13}\text{C}$  NMR (101 MHz, DMSO)  $\delta$  159.52, 156.09, 156.09, 155.50, 152.32, 149.81, 137.94, 133.40, 130.59, 128.76, 124.98, 121.40, 117.80, 115.73, 67.04, 46.20, 14.68; IR: 3122 (w), 3024 (w), 2981 (w), 2935 (w), 1590 (m), 1521 (s), 1425 (m), 1458, 1356 (s), 1342 (s), 1325 (s), 1156 (vs); UV-Vis (DCM):  $\lambda$  max ( $\epsilon/\text{M}^{-1}\text{cm}^{-1}$ ): 296(104000), 323(130000); HR MS ES+ calcd for  $[\text{C}_{27}\text{H}_{22}\text{N}_6\text{O}_3]$ : 478.1832; found 479.1833. Single pale brown cut block-shaped crystals were recrystallised from a mixture of DCM and MeCN by slow evaporation. X-ray:  $\text{C}_{27}\text{H}_{22}\text{N}_6\text{O}_3$ ,  $M_r = 478.50$ , A pale brown cut block-shaped crystal with dimensions 0.160 × 0.120 × 0.090, triclinic,  $P-1$  (No. 2),  $a = 9.4656(2)$  Å,  $b = 11.4449(2)$  Å,  $c = 21.6596(5)$  Å,  $\alpha = 84.804(2)^\circ$ ,  $\beta = 81.640(2)^\circ$ ,  $\gamma = 83.234(2)^\circ$ ,  $v = 2298.90(8)$  Å<sup>3</sup>,  $T = 100(2)$  K,  $Z = 4$ ,  $Z' = 2$ ,  $\mu(\text{MoK}\alpha) = 0.094$ , 47667 reflections measured, 10513 unique ( $R_{int} = 0.0328$ ) which were used in all calculations. The final  $wR_2$  was 0.1195 (all data) and  $R_1$  was 0.0436 ( $I > 2(I)$ ).

**Bis( 4'-(4-(2-(2-methyl-5-nitro-1H-imidazol-1-yl)ethoxy)phenyl)-2,2':6',2''-terpyridine)**

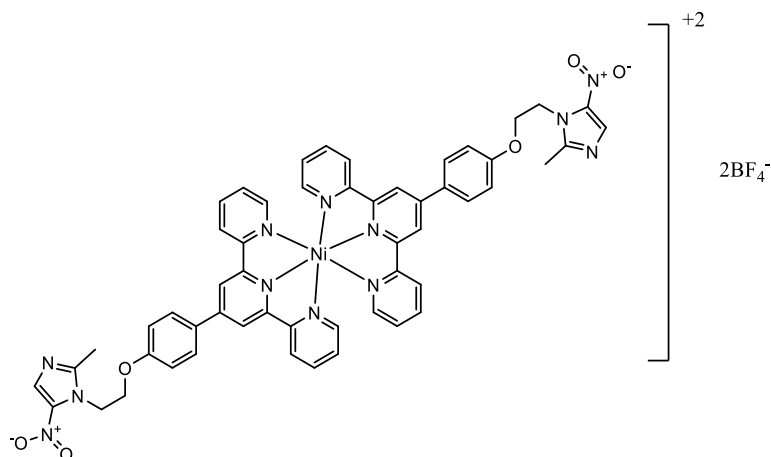
**iron (II)tetra fluoroborate (1):**



A solution of 4'-(4-(2-(2-methyl-5-nitro-1H-imidazol-1-yl)ethoxy)phenyl)-2,2':6',2''-terpyridine (0.059g, 0.125mmol) in DCM (5 ml) was added to a solution of Fe(BF<sub>4</sub>)<sub>2</sub>·6H<sub>2</sub>O (0.023g, 0.065 mmol) dissolved in ethanol (5 ml). On addition, a dark purple precipitate formed, washed with EtOH and DCM. yield (0.053g, 39%) <sup>1</sup>H NMR (300 MHz, DMSO) δ 9.64 (s, 4H), 9.07 (d, *J* = 7.2 Hz, 4H), 8.55 (d, *J* = 8.3 Hz, 4H), 8.13 (s, 2H), 8.03 (t, *J* = 7.5 Hz, 4H), 7.33 (d, *J* = 8.4 Hz, 4H), 7.27 (d, *J* = 5.2 Hz, 4H), 7.19 (d, *J* = 6.4 Hz, 4H), 4.85 (t, *J* = 6.0 Hz, 4H), 4.60 (t, *J* = 3.9 Hz, 4H), 2.64 (s, 6H); <sup>13</sup>C NMR (126 MHz, DMSO) δ 160.43, 160.24, 158.45, 153.27, 152.40, 148.90, 139.12, 133.51, 129.83, 128.91, 127.99, 124.49, 120.71, 115.73, 67.16, 45.77, 14.75; IR: 3124 (w), 2881(w), 1604 (m), 1541(s), 1521(s), 1458 (m), 1382 (s), 1365(s), 1052 (vs); UV-Vis (CH<sub>3</sub>CN): λ<sub>max</sub> (ε/M<sup>-1</sup>cm<sup>-1</sup>): 257(17154), 285(22676), 324(30185), 569(9074); MS ES<sup>+</sup> [M-BF<sub>4</sub>]<sup>+</sup> calcd for [C<sub>54</sub>H<sub>44</sub>N<sub>12</sub>O<sub>6</sub>FeBF<sub>4</sub>]; 1099.67 found 1099.29. HR MS ES<sup>+</sup> [(L<sup>1</sup>)<sub>2</sub>-Fe-BF<sub>4</sub>]<sup>+</sup> calcd for [C<sub>54</sub>H<sub>44</sub>N<sub>12</sub>O<sub>6</sub>FeBF<sub>4</sub>]; 1098.2978; found 1098.3002.

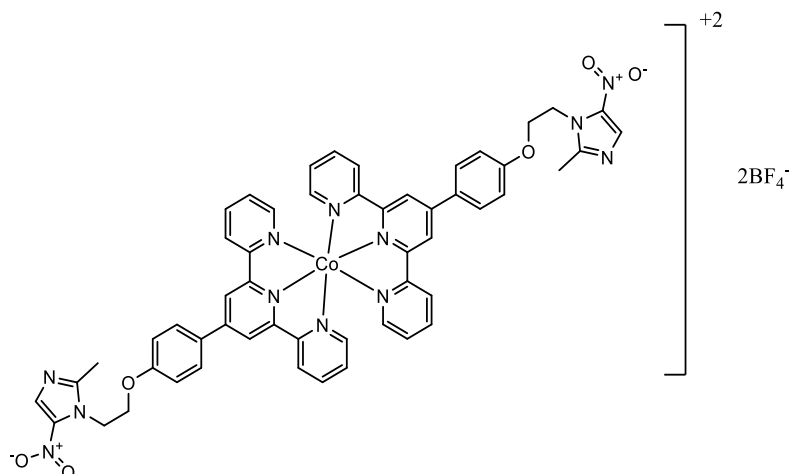
**Bis( 4'-(4-(2-(2-methyl-5-nitro-1H-imidazol-1-yl)ethoxy)phenyl)-2,2':6',2''-terpyridine)**

**nickel (II)tetra fluoroborate (2):**



To Ni(BF<sub>4</sub>)<sub>2</sub>·6H<sub>2</sub>O (0.010g, 0.0312 mmol) dissolved in ethanol (5 ml), 4'-(4-(2-(2-methyl-5-nitro-1H-imidazol-1-yl)ethoxy)phenyl)-2,2':6',2''-terpyridine (0.029g, 0.06mmol) in DCM (5 ml) was added and the mixture was stirred at room temperature for 3 h before filtering, (yield 0.010g, 15 %); IR ; 3115(w), 2885(w), 1602(m), 1554(s), 1521(s), 1473(m), 1379(s), 1363(s), 1052(vs).; MS ES<sup>+</sup> [M-BF<sub>4</sub>]<sup>+</sup> calcd for [C<sub>54</sub>H<sub>44</sub>N<sub>12</sub>O<sub>6</sub>NiBF<sub>4</sub>]: 1101.29; found: 1101.30; HRMS ES<sup>+</sup> [(L<sup>1</sup>)<sub>2</sub>- Ni-BF<sub>4</sub>]<sup>+</sup> calcd for [C<sub>54</sub>H<sub>44</sub>N<sub>12</sub>O<sub>6</sub>NiBF<sub>4</sub>]: 1101.2926; found: 1101.2917; UV/vis (DMSO, nm): 278 (40581), 324 (53145), 344(49272).

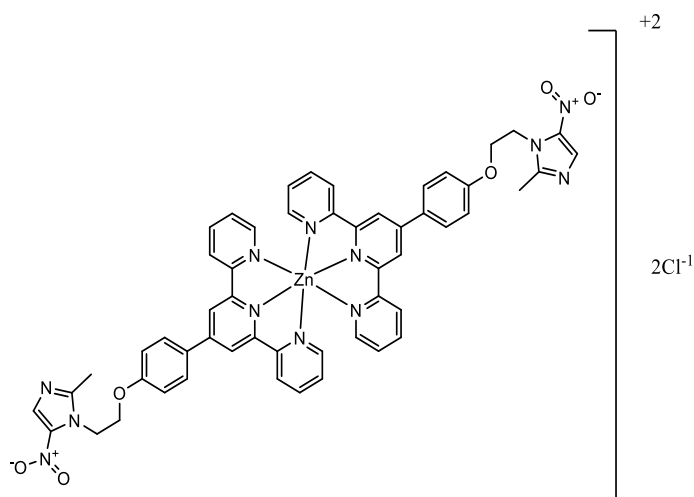
**Bis(4'-(4-(2-(2-methyl-5-nitro-1H-imidazol-1-yl)ethoxy)phenyl)-2,2':6',2''-terpyridine) cobalt (II)tetra fluoroborate (3):**



A solution of 4'-(4-(2-(2-methyl-5-nitro-1H-imidazol-1-yl)ethoxy)phenyl)-2,2':6',2''-terpyridine (0.059g, 0.125mmol) in 5 ml of DCM was added to a solution of  $\text{Co}(\text{BF}_4)_2 \cdot 6\text{H}_2\text{O}$  (0.021g, 0.065 mmol) dissolved in ethanol (5 ml). The reaction mixture was stirred at room temperature for 5 hours. The precipitate was filtered and washed with DCM and EtOH to obtain the complex as a red powder, yield (0.050 g, 40%); IR: 3122(w), 3024(w), 9871(w), 1598(m), 1506(s), 1523(s), 1458(m), 1427(m), 1367(s), 1344(s), 1169(vs); UV-Vis ( $\text{CH}_3\text{CN}$ ):  $\lambda_{\text{max}}$  ( $\epsilon/\text{M}^{-1} \text{cm}^{-1}$ ): 297(1500), 337(1900), 523(78.18); MS  $\text{ES}^+$  calcd for  $[\text{C}_{45}\text{H}_{44}\text{N}_{12}\text{O}_6\text{Co}]$  1015.28; found: 1015.30; HRMS  $\text{ES}^+$   $[(\text{L}^1)_2\text{-Co-BF}_4]^{+}$  calcd for  $[\text{C}_{54}\text{H}_{44}\text{BF}_4\text{CoN}_{12}\text{O}_6]$ : 1102.2903; found: 1102.2904.

### Bis( 4'-(4-(2-(2-methyl-5-nitro-1H-imidazol-1-yl)ethoxy)phenyl)-2,2':6',2''-terpyridine)

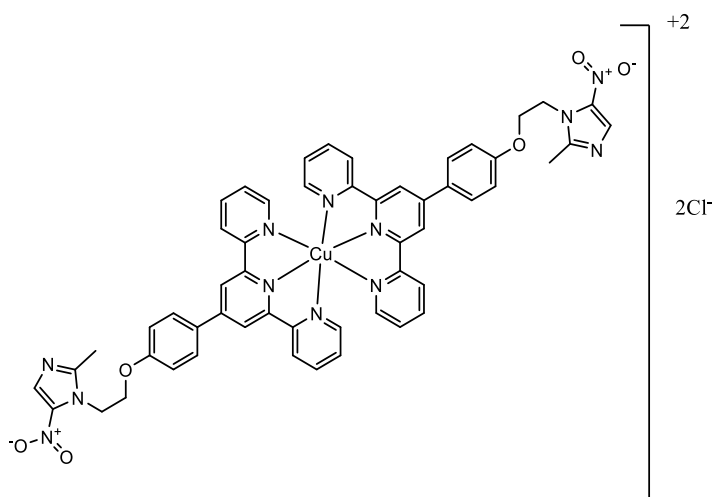
#### Zinc (II)chloride (4)



A solution of 4'-(4-(2-(2-methyl-5-nitro-1H-imidazol-1-yl)ethoxy)phenyl)-2,2':6',2''-terpyridine (0.059g, 0.125mmol) in DCM (5 ml) was added to a solution of  $\text{ZnCl}_2$  (0.010g, 0.065 mmol) dissolved in ethanol (5 ml). The reaction mixture was stirred at room temperature for 5 hours. The precipitate was filtered and washed with DCM and EtOH. Yield: (0.037g, 59%);  $^1\text{H}$  NMR (500 MHz, DMSO)  $\delta$  9.05 (s, 4H), 8.96 (d,  $J = 8.0$  Hz, 4H), 8.84 (d,

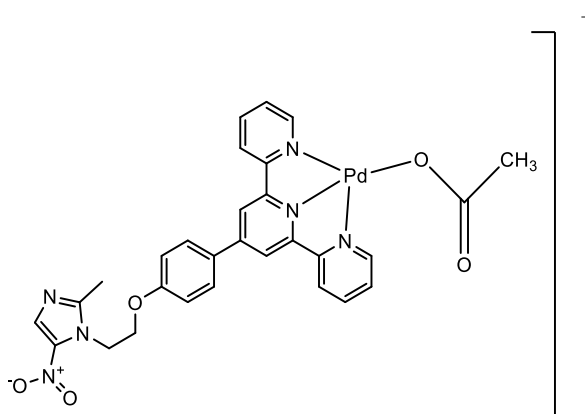
$J = 2.9$  Hz, 4H), 8.34 (t,  $J = 7.0$  Hz, 4H), 8.29 (d,  $J = 8.7$  Hz, 4H), 8.08 (s, 2H), 7.91 – 7.84 (m, 4H), 7.18 (d,  $J = 8.5$  Hz, 4H), 4.79 (t,  $J = 4.9$  Hz, 4H), 4.51 (t,  $J = 5.0$  Hz, 4H), 2.59 (s, 6H); IR: 3075 (w), 2980 (w), 1576 (s), 1521 (s), 1473 (m), 1361 (s), 1188 (s), 408; MS ES+  $m/z$   $[M]^+$  calcd for  $[C_{45}H_{44}N_{12}O_6Zn]$ : 510.13 found 510.14; UV–Vis (DMSO):  $\lambda_{max}$  ( $\epsilon/M^{-1} cm^{-1}$ ): 268(1700), 299(28000), 327(27000), 346(29000) nm.

**4'-(4-(2-(2-Methyl-5-nitro-1H-imidazol-1-yl)ethoxy)phenyl)-2,2':6',2''-terpyridine copper (II)chloride (5):**



A solution of 4'-(4-(2-(2-methyl-5-nitro-1H-imidazol-1-yl)ethoxy)phenyl)-2,2':6',2''-terpyridine (0.029g, 0.065mmol) in DCM 5ml was added to a solution of  $CuCl_2$  (0.010g, 0.065 mmol) dissolved in ethanol 5ml. The reaction mixture was stirred at room temperature for 5 hours. Green precipitate was filtered and washed with DCM and EtOH; Yield: (0.019g, 55.8%) IR: 3397(b), 3091(w), 3010 (w), 2881(w), 1598 (s), 1523(s), 1473(m), 1436 (m), 1384 (s), 1365 (s), 1186, 418; UV–Vis (DMSO):  $\lambda_{max}$  ( $\epsilon/M^{-1} cm^{-1}$ ): 278(21000), 301(23000), 337(26000), 350(9120), 731(100); HRMS ES+  $[(L^1)_2-Cu]^+$  calcd for  $[C_{54}H_{44}CuN_{12}O_6]$ : 1019.2803; found: 1019.2807.

**4'-(4-(2-(2-Methyl-5-nitro-1H-imidazol-1-yl)ethoxy)phenyl)-2,2':6',2''-terpyridine palladium (II)acetate (6):**



A solution of  $\text{Pd}(\text{CH}_3\text{COO})_2$  (0.029g, 0.06mmol) dissolved in 5 ml  $\text{H}_2\text{O}$  was added to a solution of 4'-(4-(2-(2-methyl-5-nitro-1H-imidazol-1-yl)ethoxy)phenyl)-2,2':6',2''-terpyridine (0.029g, 0.06mmol) dissolved in DCM (5ml). The reaction mixture was stirred at room temperature for 17 hours. The solvent was removed by vacuum line then it was washed with DCM. The desired product was obtained as yellow powder yield (0.012, 29%);  $^1\text{H}$  NMR (400 MHz, DMSO)  $\delta$  8.89 (s, 2H), 8.84 (d,  $J = 8.4$  Hz, 2H), 8.48 (t,  $J = 8.4$  Hz, 2H), 8.31 (d,  $J = 5.4$  Hz, 2H), 8.20 (d,  $J = 9.2$  Hz, 2H), 8.08 (s, 1H), 7.87 (t,  $J = 5.3$  Hz, 2H), 7.17 (d,  $J = 9.0$  Hz, 2H), 4.78 (t,  $J = 4.1$  Hz, 2H), 4.51 (t,  $J = 3.2$  Hz, 2H), 2.58 (s, 3H), 2.08 (s, 3H); IR: 3062 (w), 2989 (w), 1593 (s), 1558 (s), 1541(s), 1521 (s), 1473 (m), 1361(s), 1313 (m), 480; UV-Vis ( $\text{H}_2\text{O}$ ):  $\lambda_{\text{max}}$  ( $\epsilon/\text{M}^{-1}\text{cm}^{-1}$ ): 278(22197),305(19872), 352(14299), 368(14363); MS ES+  $[\text{M}-\text{OAc}]^+$  calcd for  $[\text{C}_{29}\text{H}_{25}\text{N}_6\text{O}_5\text{Pd}]$ : 643.09; found: 629.08.

**3-(2-Nitro-1H-imidazol-1-yl)propan-1-ol:**

3-Choloropropan-1-ol (1.4g,9.73mmol) was added dropwise to a mixture of 2-nitroimidazole (1g, 8.85mmol) and  $\text{K}_2\text{CO}_3$ (5.8g, 17.70mmol) in DMF (10mL). The reaction mixture was stirred and heated at  $100^\circ\text{C}$  for 40 h. The reaction mixture was diluted with  $\text{H}_2\text{O}$  (10ml) and

extracted with EtOAc. The organic layers were combined and dried over MgSO<sub>4</sub>. The crude product was purified by column chromatography on silica gel (DCM: MeOH = 80: 1) to obtain the desired product as yellow powder (1.3g, 88%). <sup>1</sup>H NMR (400 MHz, DMSO) δ 7.77 (d, *J* = 0.9 Hz, 1H), 7.29 (d, *J* = 1.0 Hz, 1H), 4.76 (t, *J* = 5.0 Hz, 1H), 4.52 (t, 5.0 Hz, 2H), 3.53 (dd, *J* = 11.1, 5.9 Hz, 2H), 2.07 – 1.99 (m, 2H).

**(2-Nitro-1H-imidazol-1-yl)propyl methanesulfonate:**

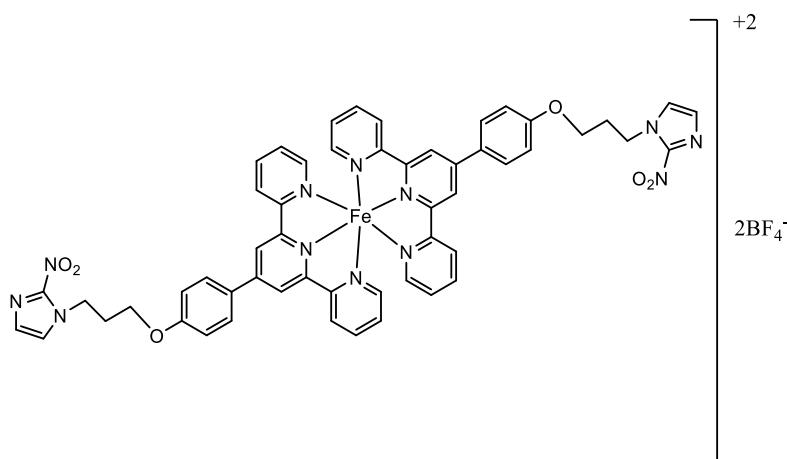
3-(2-nitro-1H-imidazol-1-yl)propan-1-ol (0.836 g, 4.8 mmol), TEA (0.727g mL, 7.2 mmol, 1.5 equiv.) were dissolved in CH<sub>2</sub>Cl<sub>2</sub> (25 mL) and cooled to (~10°C). Then A solution of methanesulfonyl chloride (0.656g ,5.7 mmol, 1.2 equiv.) in CH<sub>2</sub>Cl<sub>2</sub> (5 mL) was added dropwise for one hour to the previous suspension. The reaction mixture was stirred at room temperature for 3 days. Then it was extracted with ethyl acetate (20 ml\*5). Ethyl acetate layers were combined and dried over MgSO<sub>4</sub>. The solvent was evaporated in rotary evaporator to obtain the product as yellow liquid (0.709g, 58 %). <sup>1</sup>H NMR (300 MHz, DMSO) δ 7.68 (d, *J* = 4.5 Hz, 2H), 7.20 (d, *J* = 6.8 Hz, 2H), 4.50 (t, *J* = 7.1 Hz, 2H), 4.25 (t, *J* = 6.0 Hz, 2H), 3.20 (s, 3H), 2.43 – 2.16 (m, 2H).

**4'-(4-(3-(2-Nitro-1H-imidazol-1-yl)propoxy)phenyl)-2,2':6',2''-terpyridine(L<sup>2</sup>):**

4'-(4-Hydroxyphenyl)-2,2',6',2''-terpyridine (1.5g, 4.6 mmol) to a solution of 3-(2-nitro-1H-imidazol-1-yl)propyl methanesulfonate (2.00 g, 8 mmol) in 20 mL DMF, *potassium carbonate* (3.6g, 26 mmol). The suspension was heated to 85<sup>0</sup>C for 72h (the reaction was monitored by TLC plate). The solid was filtered and solvent was evaporated from filtrate. Crude product was recrystallised from acetonitrile. The product was obtained as yellow crystals. Yield (0.479g, 14%); <sup>1</sup>H NMR (500 MHz, DMSO) δ 8.77 (d, *J* = 4.6 Hz, 2H), 8.68 (d, *J* = 10.2 Hz, 4H), 8.04 (t, *J* = 7.7 Hz, 2H), 7.90 (d, *J* = 8.4 Hz, 2H), 7.71 (s, 1H), 7.57 –

7.50 (m, 2H), 7.20 (s, 1H), 7.10 (d,  $J = 8.5$  Hz, 2H), 4.63 (t,  $J = 6.8$  Hz, 2H), 4.12 (t,  $J = 5.8$  Hz, 2H), 2.40 – 2.20 (m, 2H);  $^{13}\text{C}$  NMR (126 MHz, DMSO)  $\delta$  159.95, 156.09, 155.54, 149.82, 149.48, 137.94, 130.24, 128.72, 128.43, 128.36, 124.98, 121.40, 117.79, 115.74, 65.43, 47.44, 31.17; IR: 3111(w), 3053(w), 2937(w), 1583(s), 1566(s), 1533(s), 1516(s), 1487(m), 1469(m), 1361(s), 1316(s); HRMS ES+ calcd for  $[\text{C}_{27}\text{H}_{23}\text{N}_6\text{O}_3]$ : 479.1831; found: 479.1832; UV-Vis ( $\text{CH}_3\text{CN}$ ):  $\lambda$  max ( $\epsilon/\text{M}^{-1}\text{cm}^{-1}$ ): 257(21000), 286(34000), 320(13000)nm.

**Bis (4'-(4-(3-(2-nitro-1H-imidazol-1-yl)propoxy)phenyl)-2,2':6',2''- terpyridine) iron (II) tetra fluoroborate (7):**



A solution of 4'-(4-(3-(2-nitro-1H-imidazol-1-yl)propoxy)phenyl)-2,2':6',2''-terpyridine (0.059g, 0.125mmol) in DCM (5 ml) was added to a solution of  $\text{Fe}(\text{BF}_4)_2 \cdot 6\text{H}_2\text{O}$  (0.023g, 0.065 mmol) dissolved in EtOH (5 ml). On addition, a dark purple precipitate formed, which was collected and washed with EtOH (5 ml) and DCM (5ml). The product was obtained as a dark purple solid soluble in acetonitrile, yield (0.053g, 83%).  $^1\text{H}$  NMR (400 MHz,  $\text{CD}_3\text{CN}$ )  $\delta$  9.16 (s, 4H), 8.62 (d,  $J = 7.6$  Hz, 4H), 8.31 (d,  $J = 8.8$  Hz, 4H), 7.93 (td,  $J = 7.9, 1.4$  Hz, 4H), 7.43 (d,  $J = 1.1$  Hz, 2H), 7.29 (d,  $J = 8.9$  Hz, 4H), 7.21 (d,  $J = 4.9$  Hz, 4H), 7.18 (d,  $J = 1.1$  Hz, 2H), 7.13 – 7.06 (m, 4H), 4.74 (t,  $J = 6.8$  Hz, 4H), 4.25 (t,  $J = 5.8$  Hz, 4H), 2.50 – 2.40 (m, 4H);  $^{13}\text{C}$  NMR (126 MHz, DMSO)  $\delta$  160.89, 160.23, 158.47, 153.26, 149.13, 145.34,

139.15, 129.83, 128.64, 128.42, 128.00, 124.46, 120.76, 115.75, 65.76, 47.49, 29.77;

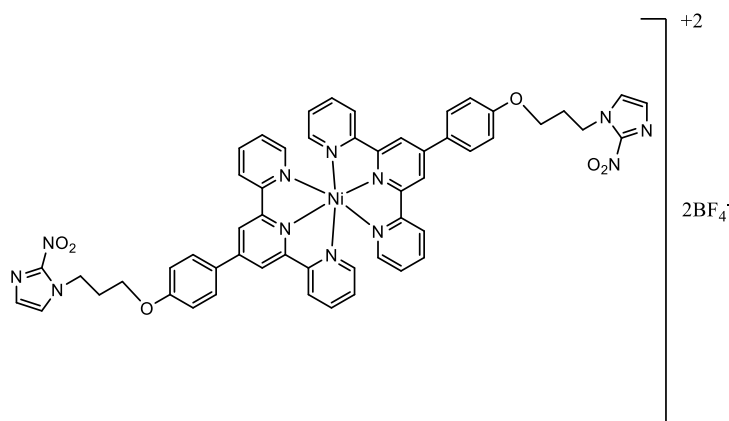
IR:3116(w), 3086(w), 2873(w), 2873(w), 1600(m), 1539(m), 1521(m), 1483(m), 1465(m),

1361(s), 1300(s), 1053 (vs); HRMS ES<sup>+</sup> [(L<sup>2</sup>)<sub>2</sub>-Fe-BF<sub>4</sub><sup>-</sup>]<sup>+</sup> calcd for [C<sub>54</sub>H<sub>44</sub>BF<sub>4</sub>FeN<sub>12</sub>O<sub>6</sub>]:

1099.2885; found: 1099.2924; UV-Vis (CH<sub>3</sub>CN): λ max (ε/M<sup>-1</sup>cm<sup>-1</sup>): 232(250000),

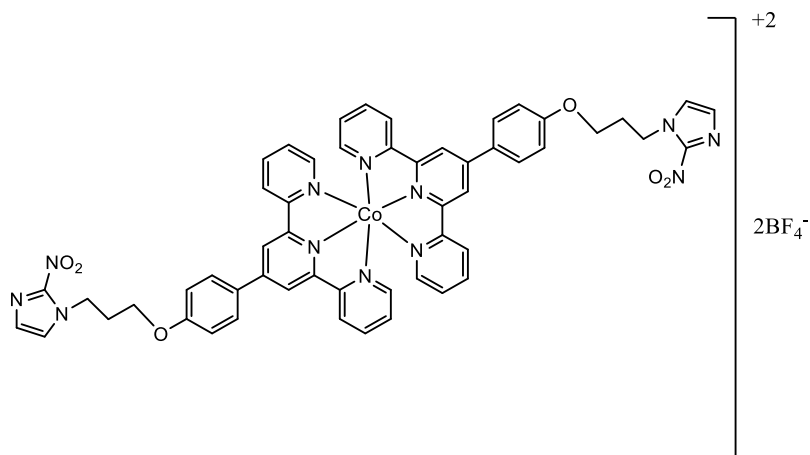
285(130000), 328(170000), 572(50000).

**Bis (4'-(4-(3-(2-nitro-1H-imidazol-1-yl)propoxy)phenyl)-2,2':6',2''- terpyridine) nickel (II)tetra fluoroborate (8):**



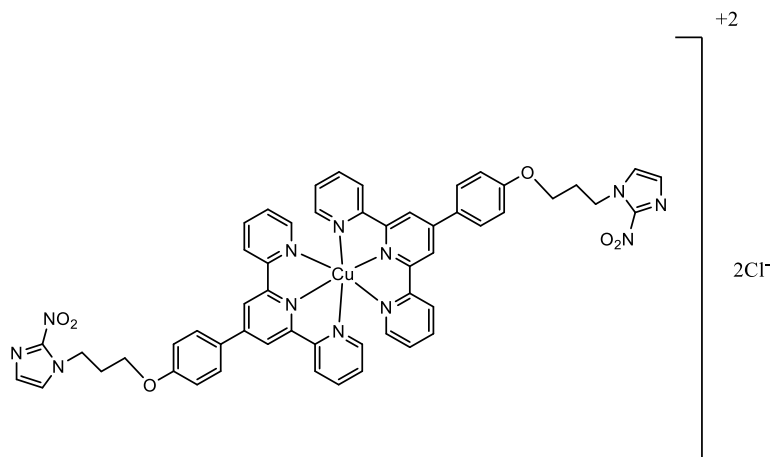
To Ni(BF<sub>4</sub>)<sub>2</sub>·6H<sub>2</sub>O (0.010g, 0.0312 mmol) dissolved in ethanol 5 ml, (4'-(4-(3-(2-nitro-1H-imidazol-1-yl)propoxy)phenyl)-2,2':6',2''-terpyridine 0.029g, 0.065mmol) in DCM 5ml was added, the mixture was stirred at room temperature for 3 h before filtering, yield (0.023g, 68.8%); IR; 3134(w), 3116(w), 2954(w), 2873(w), 1600(m), 1558(m), 1539(s), 1521(s), 1473(m), 1458(m), 1363(s), 1307(m), 1048(vs); HRMS ES<sup>+</sup> calcd for [C<sub>54</sub>H<sub>44</sub>BF<sub>4</sub>NiN<sub>12</sub>O<sub>6</sub>]: 1101.2889; found: 1101.2926; HRMS ES<sup>+</sup> m/z calcd for [C<sub>54</sub>H<sub>44</sub>NiN<sub>12</sub>O<sub>6</sub>]: 507.1398; found 507.1399; UV-Vis (CH<sub>3</sub>CN): λ max (ε/M<sup>-1</sup>cm<sup>-1</sup>): 235(36000), 286(53000),317(61000), 343(71000) nm.

**Bis (4'-(4-(3-(2-nitro-1H-imidazol-1-yl)propoxy)phenyl)-2,2':6',2''- terpyridine) cobalt (II)tetra fluoroborate (9):**



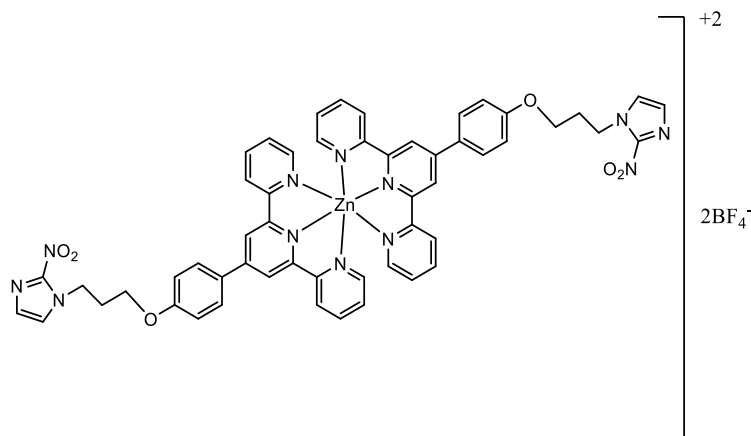
To an ethanolic solution (5ml)  $\text{Co}(\text{BF}_4)_2 \cdot 6\text{H}_2\text{O}$  (0.010g, 0.03mmol), 4'--(4-(3-(2-nitro-1H-imidazol-1-yl)propoxy)phenyl)-2,2':6',2''-terpyridine (0.029g, 0.06 mmol) in DCM (5 ml) was added and stirred for 3 hours. Upon the addition of co salt the solution turned to dark red and precipitate was formed. The precipitate was filtered to obtain the product as red powder yield (0.026g, 77.8%); IR;3122(w), 2872(w), 1600(s), 1541(s), 1521(s), 1471(m), 1363(s), 1051(vs); HRMS ES+ $[(\text{L}^2)_2\text{-Co-BF}_4]^{+}$  calcd for  $[\text{C}_{54}\text{H}_{44}\text{BF}_4\text{CoN}_{12}\text{O}_6]$ : 1102.2868; found: 1102.2875. HRMS ES+ m/z calcd for  $[\text{C}_{54}\text{H}_{44}\text{CoN}_{12}\text{O}_6]$ : 507.6309; found 507.6309. UV-Vis ( $\text{CH}_3\text{CN}$ ):  $\lambda_{\text{max}}$  ( $\epsilon/\text{M}^{-1}\text{cm}^{-1}$ ): 225(80000), 286(79000), 317(90000), 518(2100).

**4'--(4-(3-(2-Nitro-1H-imidazol-1-yl)propoxy)phenyl)-2,2':6',2''- terpyridine copper (II) chloride (10):**



To CuCl<sub>2</sub> · 2H<sub>2</sub>O (0.005g, 0.0312 mmol) dissolved in ethanol 5 ml, (4'-(4-(3-(2-nitro-1H-imidazol-1-yl)propoxy)phenyl)-2,2':6',2''-terpyridine 0.029g, 0.06mmol) in DCM 5 ml was added, the mixture was stirred at room temperature for 3 hours. Green precipitate was formed which was filtered and washed initially with DCM (5 ML) then ETOH. The desired product was obtained as green powder, yield (0.007g, 22.6%); IR: 3450(b), 3064(s), 2956(s), 2879(s), 1595(s), 1521(s), 1471(s), 1435(m), 1355(s); HRMS ES<sup>-</sup> [(L<sup>1</sup>)<sub>2</sub>- Cu<sup>+</sup>] calcd for [C<sub>54</sub>H<sub>44</sub>CuN<sub>12</sub>O<sub>6</sub>]: 1019.2803; found: 1019. 2822. UV-Vis (DMSO): λ max (ε/M<sup>-1</sup>cm<sup>-1</sup>): 285(18673), 321(15057), 369(3181), 741(91) nm.

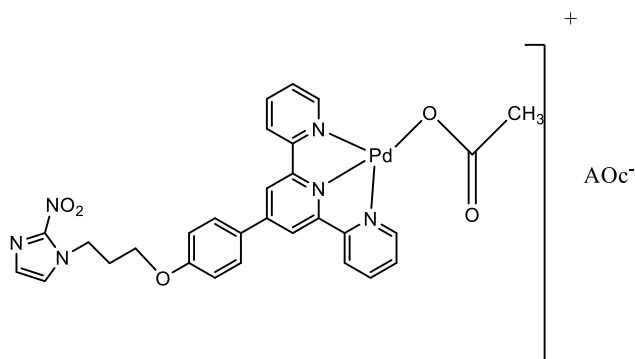
**4'-(4-(3-(2-Nitro-1H-imidazol-1-yl)propoxy)phenyl)-2,2':6',2''- terpyridine zinc (II) chloride (11):**



To  $\text{Zn}(\text{Cl})_2$  (0.007g, 0.03 mmol) dissolved in ethanol (5 ml), (4'-(4-(3-(2-nitro-1H-imidazol-1-yl)propoxy)phenyl)-2,2':6',2''-terpyridine (0.029g, 0.06mmol) in DCM 5 ml was added and the mixture was stirred at room temperature for 3 hours. White precipitate was filtered and washed with deionised water (5 ml) and DCM (5ml). Yield:(0.014, 46%);  $^1\text{H}$  NMR (300 MHz, DMSO)  $\delta$  9.06 (s, 4H), 8.97 (d,  $J = 6.5$  Hz, 4H), 8.84 (s, 4H), 8.42 – 8.25 (m, 8H), 7.92 – 7.84 (m, 4H), 7.71 (s, 2H), 7.21 (s, 2H), 7.15 (d,  $J = 7.3$  Hz, 4H), 4.62 (d,  $J = 6.8$  Hz, 4H), 4.15 (d,  $J = 4.9$  Hz, 4H), 2,33 (m,4H). IR: 3079(w), 3055(w), 2912(w), 2868(w), 1598(s), 1541(s), 1521(s), 1477(m), 1436(m), 1361(s),1355(s), 780, 518. MS ES+ m/z calcd for  $[\text{C}_{54}\text{H}_{44}\text{ZnN}_{12}\text{O}_6]$ : 510.14. found: 510.14: UV-Vis ( $\text{CH}_3\text{CN}$ ):  $\lambda$  max ( $\epsilon/\text{M}^{-1}\text{cm}^{-1}$ ): 288(19313), 323(11745), 340(10036), 385(4098) nm.

#### 4'-(4-(3-(2-Nitro-1H-imidazol-1-yl)propoxy)phenyl)-2,2':6',2''- terpyridine palladium

##### (II) acetate (12):



To  $\text{Pd}(\text{AOC})_2$  (0.014g, 0.06 mmol) dissolved in ethanol (5 ml), (4'-(4-(3-(2-nitro-1H-imidazol-1-yl)propoxy)phenyl)-2,2':6',2''-terpyridine (0.029g, 0.06mmol) in DCM (5 ml) was added and the mixture was stirred at room temperature for 12 hours. The solvent was evaporated from filtrate. The crude product was dispersed in chloroform. The solid was filtered and washed with chloroform (5 ml). The product was obtained as yellow solid, yield (0.015g, 38%).  $^1\text{H}$  NMR (500 MHz, DMSO)  $\delta$  8.92 (s, 2H), 8.86 (d,  $J = 7.9$  Hz, 2H), 8.49 (t,  $J$

= 8.5 Hz, 2H), 8.33 (d,  $J = 5.5$  Hz, 2H), 8.21 (d,  $J = 8.8$  Hz, 2H), 7.93 – 7.82 (m, 2H), 7.72 (s, 1H), 7.21 (s, 1H), 7.15 (d,  $J = 8.8$  Hz, 2H), 4.64 (t,  $J = 6.9$  Hz, 2H), 4.18 (t,  $J = 5.8$  Hz, 2H), 2.33 (dt,  $J = 12.8, 6.3$  Hz, 2H);  $^{13}\text{C}$  NMR (126 MHz, DMSO)  $\delta$ 176.93, 161.61, 157.64, 155.01, 153.13, 151.57, 142.81, 130.17, 129.04, 128.48, 128.39, 127.03, 125.69, 120.60, 115.68, 65.78, 47.40, 29.67, 23.80; IR; 3411(b), 3101(w), 3072(w), 1591(s), 1539(s), 1521(s), 1475(m), 1351(s), 1309(s); HRMS ES<sup>+</sup> [M-OAc]<sup>+</sup> calcd for [C<sub>29</sub>H<sub>25</sub>N<sub>6</sub>O<sub>5</sub>Pd]: 643.09; found: 629.0773; UV-Vis (CH<sub>3</sub>CN):  $\lambda$  max ( $\epsilon/\text{M}^{-1}\text{cm}^{-1}$ ): 281(20127), 307(16242), 320(14327), 375(13057), 393(12489) nm.

### 3.6 References

- 1 C. Marzano, M. Pellei, F. Tisato and C. Santini, *Anticancer. Agents Med. Chem.*, 2009, **9**, 185–211.
- 2 C. Acilan, B. Cevatemre, Z. Adiguzel, D. Karakas, E. Ulukaya, N. Arda, N. Ribeiro, I. Correia and J. Pessoa, *Eur. J. Cancer*, 2016, **61**, S137--S138.
- 3 N. B. Behrens, G. M. Diaz and D. M. L. Goodgame, *Inorganica Chim. Acta*, 1986, **125**, 21–26.
- 4 Y.-P. Ho, S. C. F. Au-Yeung and K. K. W. To, *Med. Res. Rev.*, 2003, **23**, 633–655.
- 5 H. Khan, A. Badshah, G. Murtaz, M. Said, Z.- Rehman, C. Neuhausen, M. Todorova, B. J. Jean-Claude and I. S. Butler, *Eur. J. Med. Chem.*, 2011, **46**, 4071–4077.
- 6 F. V Rocha, C. V Barra, A. V. G. Netto, A. E. Mauro, I. Z. Carlos, R. C. G. Frem, S. R. Ananias, M. B. Quilles, A. Stevanato and M. C. da Rocha, *Eur. J. Med. Chem.*, 2010, **45**, 1698–1702.
- 7 E. Ulukaya, F. Ari, K. Dimas, M. Sarimahmut, E. Guney, N. Sakellaridis and V. T. Yilmaz, *J. Cancer Res. Clin. Oncol.*, 2011, **137**, 1425.
- 8 H. Kozłowski, T. Kowalik-Jankowska and M. Jezowska-Bojczuk, *Coord. Chem. Rev.*, 2005, **249**, 2323–2334.
- 9 H. A. El-Boraey, S. M. Emam, D. A. Tolan and A. M. El-Nahas, *Spectrochim. Acta Part A Mol. Biomol. Spectrosc.*, 2011, **78**, 360–370.
- 10 S. Roy, S. Saha, R. Majumdar, R. R. Dighe and A. R. Chakravarty, *Polyhedron*, 2010, **29**, 2787–2794.
- 11 K. Czerwiska, B. Machura, S. Kula, S. Krompiec, K. Erfurt, C. Roma-Rodrigues, A. R. Fernandes, L. S. Shul’Pina, N. S. Ikonnikov and G. B. Shul’Pin, *Dalt. Trans.*, 2017, **46**, 9591–9604.
- 12 Q. Jiang, J. Zhu, Y. Zhang, N. Xiao and Z. Guo, *BioMetals*, 2009, **22**, 297–305.
- 13 S. Wang, W. Chu, Y. Wang, S. Liu, J. Zhang, S. Li, H. Wei, G. Zhou and X. Qin, *Appl. Organomet. Chem.*, 2013, **27**, 373–379.
- 14 L.-X. Zhao, J. Sherchan, J. K. Park, Y. Jahng, B.-S. Jeong, T. C. Jeong, C.-S. Lee and E.-S. Lee, *Arch. Pharm. Res.*, 2006, **29**, 1091–1095.
- 15 Z. Naseri, A. N. Kharat, A. Banavand, A. Bakhoda and S. Foroutannejad, *Polyhedron*, 2012, **33**, 396–403.
- 16 V. Callaghan, D. M. L. Goodgame and R. P. Tooze, *Inorganica Chim. Acta*, 1983, **78**, L1–L4.
- 17 J. A. Obaleye and A. Lawal, *J. Appl. Sci. Environ. Manag.*
- 18 C. Ricardo, P. Kumar and L. Wiebe, *J. Diagnostic Imaging Ther.*, 2015, **2**, 103–158.
- 19 G. T. Morgan and F. H. Burstall, *J. Chem. Soc.*, 1932, 20–30.
- 20 G. W. V Cave and C. L. Raston, *J. Chem. Soc. D Chem. Commun.*, 2000, 2199–2200.
- 21 N. W. Alcock, P. R. Barker, J. M. Haider, M. J. Hannon, C. L. Painting, Z. Pikramenou, E. A. Plummer, K. Rissanen and P. Saarenketo, *Dalt. Trans.*, 2000, 1447–1462.
- 22 J.-P. Collin, S. Guillerez and J.-P. Sauvage, *J. Chem. Soc.*, 1989, 776–778.

- 23 J. P. Collin, S. Guillerez, J. P. Sauvage, F. Barigelletti, L. De Cola, L. Flamigni and V. Balzani, *Inorg. Chem.*, 1991, **30**, 4230–4238.
- 24 A. R. Katritzky, *Synthesis (Stuttg.)*, 1999, **1999**, 2114–2118.
- 25 F. Kröhnke, W. Zecher, J. Curtze, D. Drechsler, K. Pfléghar, K. E. Schnalke and W. Weis, *Angew. Chemie Int. Ed. English*, **1**, 626–632.
- 26 F. Kröhnke, *Synthesis*, 1976, **1976**, 1–24.
- 27 K. T. Potts, M. J. Cipullo, P. Ralli and G. Theodoridis, *J. Am. Chem. Soc.*, 1981, **103**, 3585–3586.
- 28 T. Kobayashi, H. Kakiuchi and H. Kato, *Bull. Chem. Soc. Jpn.*, 1991, **64**, 392–395.
- 29 F. Palacios, A. M. O. de Retana and J. Oyarzabal, *Tetrahedron Lett.*, 1996, **37**, 4577–4580.
- 30 G. Yin, Q. Liu, J. Ma and N. She, *Green Chem.*, 2012, **14**, 1796–1798.
- 31 E. C. Constable, *Macromol. Symp.*, 1995, **98**, 503–524.
- 32 A. Winter, D. A. M. Egbe and U. S. Schubert, *Org. Lett.*, 2007, **9**, 2345–2348.
- 33 K. T. Potts, D. A. Usifer, A. Guadalupe and H. D. Abruna, *J. Am. Chem. Soc.*, 1987, **109**, 3961–3967.
- 34 D. L. Jameson and L. E. Guise, *Tetrahedron Lett.*, 1991, **32**, 1999–2002.
- 35 M. W. Cooke, J. Wang, I. Theobald and G. S. Hanan, *Synth. Commun.*, 2006, **36**, 1721–1726.
- 36 H.-J. Park and Y. K. Chung, *Dalt. Trans.*, 2012, **41**, 5678–5686.
- 37 A. R. Stefankiewicz, M. Wasa-chorab, J. Harrowfield, M. Kubicki, Z. Hnatejko, M. Korabik and V. Patroniak, *Dalt. Trans.*, 2013, **42**, 1743–1751.
- 38 Y.-W. Zhong, C.-J. Yao and H.-J. Nie, *Coord. Chem. Rev.*, 2013, **257**, 1357–1372.
- 39 L. Santos, G. B. Rosso, R. Pilli and M. Eberlin, *J. Org. Chem.*, 2007, **72**, 5809–5812.
- 40 E. C. Constable, ed. H. J. Emeléus, Academic Press, 1986, vol. 30, pp. 69–121.
- 41 D. E. Morris, K. W. Hanck and M. K. DeArmond, *J. Electroanal. Chem. Interfacial Electrochem.*, 1983, **149**, 115–130.
- 42 D. Saccone, C. Magistris, N. Barbero, P. Quagliotto, C. Barolo and G. Viscardi, *Materials (Basel)*.
- 43 J. Nance, D. N. Bowman, S. Mukherjee, C. T. Kelley and E. Jakubikova, *Inorg. Chem.*, 2015, **54**, 11259–11268.
- 44 X. Zhang, M. L. Lawson Daku, J. Zhang, K. Suarez-Alcantara, G. Jennings, C. A. Kurtz and S. E. Canton, *J. Phys. Chem. C*, 2015, **119**, 3312–3321.
- 45 S. Kremer, W. Henke and D. Reinen, *Inorg. Chem.*, 1982, **21**, 3013–3022.
- 46 C. A. Kilner and M. A. Halcrow, *Dalton Trans.*, 2010, **39**, 9008–9012.
- 47 J. England, E. Bill, T. Weyhermüller, F. Neese, M. Atanasov and K. Wieghardt, *Inorg. Chem.*, 2015, **54**, 12002–12018.
- 48 M. I. Arriortua, T. Rojo, J. M. Amigó, G. Germain and J. P. Declercq, *Bull. des Sociétés Chim. Belges*, 1982, **91**, 337–338.
- 49 A. T. Baker, D. C. Craig and A. D. Rae, *Aust. J. Chem.*, 1995, **48**, 1373–1378.
- 50 R.-A. Fallahpour, M. Neuburger and M. Zehnder, *Polyhedron*, 1999, **18**, 2445–2454.
- 51 T. K. Aldridge, E. M. Stacy and D. R. McMillin, *Inorg. Chem.*, 1994, **33**, 722–727.
- 52 A. Meyer, G. Schnakenburg and O. Schiemann, *Acta Crystallogr. Sect. E, Crystallogr.*

- Commun.*, 2015, **71**, 1245–1249.
- 53 M. I. Arriortua, J. L. Mesa, T. Rojo, T. Debaerdemaeker, D. Beltran-Porter, H. Stratemeier and D. Reinen, *Inorg. Chem.*, 1988, **27**, 2976–2981.
- 54 F. Tessore, D. Roberto, R. Ugo, M. Pizzotti, S. Quici, M. Cavazzini, S. Bruni and F. De Angelis, *Inorg. Chem.*, 2005, **44**, 8967–8978.
- 55 K. Czerwinska, B. Machura, S. Kula, S. Krompiec, K. Erfurt, C. Rodrigues, A. Fernandes, L. Shulpina, N. S. Ikonnikov and G. Shul'pin, *Dalt. Trans.*
- 56 D. V. Kumar, V. A. Babu, G. R. Rao and G. C. Pandey, *Vib. Spectrosc.*, 1992, **4**, 39–57.
- 57 C. Jin, S. A. Wen, Q. Zhang, Q. Zhu, J. Yu and W. Lu, *Acs Med. Chem. Lett.*, 2017, **8**, 762–765.
- 58 R. Hogg and R. G. Wilkins, *J. Chem. Soc.*, 1962, **0**, 341–350.
- 59 R. B. Martin and J. Ann Lissfelt, *J. Am. Chem. Soc.*, 1956, **78**, 938–940.
- 60 G. Morgan and F. H. Burstall, *J. Chem. Soc.*, 1937, **0**, 1649–1655.
- 61 E. C. Constable, J. Lewis, M. C. Liptrot and P. R. Raithby, *Inorganica Chim. Acta*, 1990, **178**, 47–54.
- 62 G. Barone, G. Gennaro, A. M. Giuliani and M. Giustini, *RSC Adv.*, 2016, **6**, 4936–4945.
- 63 S. K. Padhi, R. Sahu and V. Manivannan, *Polyhedron*, 2008, **27**, 2221–2225.
- 64 R. Indumathy, M. Kanthimathi, T. Weyhermuller and B. U. Nair, *Polyhedron*, 2008, **27**, 3443–3450.
- 65 C. C. Collins, S. Regalado-Love, R. I. Portillo, D. J. Boston, M. P. Shores and I. Bhowmick, *Adv. Mater. Technol.*, 2019, **4**, 1800406.
- 66 G. Albano, V. Balzani, E. C. Constable, M. Maestri and D. R. Smith, *Inorganica Chim. Acta*, 1998, **277**, 225–231.
- 67 I. Eryazici, C. N. Moorefield and G. R. Newkome, *Chem. Rev.*, 2008, **108**, 1834–1895.
- 68 C. Preti and G. Tosi, *Can. J. Chem.*, 1975, **53**, 177–185.
- 69 *Comprehensive coordination chemistry : the synthesis, reactions, properties and applications of coordination compounds. Vol.3, Main group and early transition elements*, Pergamon, Oxford, 1987.
- 70 L. Persaud and G. Barbiero, *Can. J. Chem.*, 1991, **69**, 315–321.
- 71 J. P. F. Rebolledo-Chávez, M. Cruz-Ramírez, R. Patakfalvi, F. J. T. Rangel and L. Ortiz-Frade, *Electrochim. Acta*, 2017, **247**, 241–251.
- 72 N. Elgrishi, M. B. Chambers, V. Artero and M. Fontecave, *Phys. Chem. Chem. Phys.*, 2014, **16**, 13635–13644.

---

## **CHAPTER 4**

**Fluorescently Labelled SPION-coated**

**Silica Nanoparticles for Cell**

**Multifunctional Imaging Probe**

## CHAPTER 4      **Fluorescently Labelled SPION-coated Silica Nanoparticles for Cell Multifunctional Imaging Probe**

### 4.1      **Introduction**

Molecular imaging has developed rapidly over the last decade and involves a mixture of *in vivo* imaging and the application of molecular biology targeting by recognising living biological processes at a cellular and molecular level without invasive biopsies or surgical procedures. It is particularly useful for exposing defects in cells and molecules which cause illness.<sup>1</sup> Molecular imaging also aids researchers to visualise the uptake and toxicity of novel drugs in the initial stages of drug development. Many imaging technologies have been widely used to assist clinicians and researchers, including optical imaging (fluorescence, bioluminescence),<sup>2</sup> computed tomography (CT),<sup>3</sup> magnetic resonance imaging (MRI),<sup>4</sup> positron emission tomography (PET)<sup>5</sup> and single-photon emission computed tomography (SPECT)<sup>6</sup>. Each of these modalities has its own benefits and limitations, such as spatial, resolution and sensitivity. Although many molecular imaging techniques now exist, no single modality can offer perfect images that provide all the essential information. For example, optical fluorescence imaging can only be used in tissue with limited depth (millimetres). Positron emission tomography (PET) has high sensitivity, providing clear anatomical information, but inadequate temporal and spacial resolution. Magnetic resonance imaging (MRI) offers excellent special resolution but low sensitivity.<sup>7</sup> Therefore, dual imaging agents are used to improve the quality of the images in order to attain an appropriate picture of the organs and a superior reliability of the obtained information.<sup>8</sup> A range of combinations of different diagnostic instruments including PET/near-infrared optical fluorescence (NIRF),

MRI/optical and PET/CT have been described.<sup>9,10</sup> Recently, the development of a multi-modality analytical technique for PET/MR imaging has been reported.<sup>11</sup>

MRI offers excellent spatial resolution but low sensitivity. It is used for visualising soft tissue and provides reliable information about anatomic structures. While positron emission tomography (PET), which is based on the detection of  $\gamma$ -photons that arise through nuclear decay, provides very sensitive images, it is usually used to image biochemical processes, and consequently track tumours where metabolism rapidly occurs.<sup>12</sup>

Obtaining precise and reliable information may be difficult when working under the limitations of a single technique. To compensate for the disadvantages of a method, some reports show how data from two instrumentation may be complimentary.<sup>13</sup> **Fig 4.1** illustrates how the combination of these two scans from MRI and PET provide better and more comprehensive information. Though this approach may be useful, the use of dual MRI/PET scan for clinical use has only become available in the last decade,<sup>14</sup> meaning that much more research in this area is required.

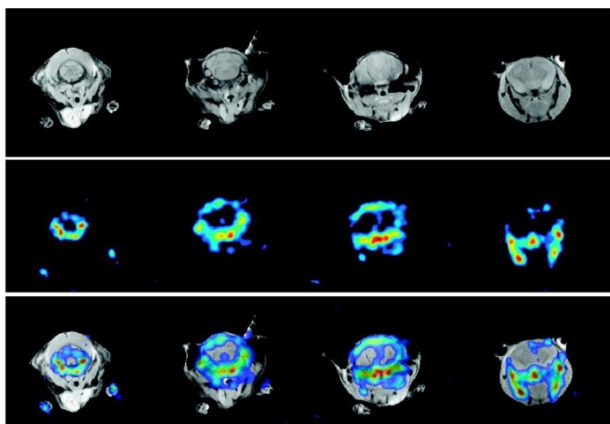


**Figure 4.1:** MRI scans (a), PET images(b), dual MRI/PET images

## 4.2 Theory

### 4.2.1 Nuclear Magnetic Resonance

Nuclear magnetic resonance (NMR) is used by chemists to characterise the structure of the chemical compounds and is based on the MRI technique, which is used to image soft tissue in the human body, thereby assisting clinicians in diagnosing disease. In this section, a brief discussion of the physical concept of NMR is provided.<sup>15</sup>

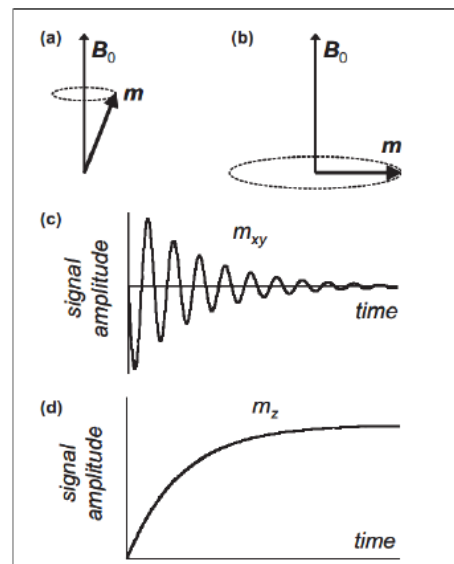


**Figure 4.2: (a) Precession of the net magnetisation of the proton around z-axis, (b) the effect of the radio frequency pulse on the net magnetisation, (c) the alteration of transverse resonance over time, and (d) longitudinal signal amplitude over time<sup>15</sup>**

When a group of nuclei is placed in a magnetic field ( $B_0$ ), each spin aligns their magnetic dipoles in one of the two possible orientations. A small proportion align against the applied magnetic field (high energy configuration) and the majority of these orientations align with the axis of the applied magnetic field (low energy configuration). Anti-parallel and parallel protons can cancel out each other's forces. However, as there are slightly more parallel protons on the lower energy level left, the magnetic dipoles add together their moments in the direction of the external magnetic field. This generates a net magnetisation ( $M$ ) aligned with

the z-axis and precession occurs around this axis (**Fig 4.2**) according to the Larmor frequency, as given by Equation 1. The magnetisation of these protons cannot be measured because it is longitudinal to the applied magnetic field. Upon applying a radiofrequency pulse, this net magnetic moment is tipped from the z-axis to the xy-plane. This motion induces an electrical current in the receiver coil. The electrical current is then detected as the NMR signal. Each signal is distinguished by a specific nucleus in a specific environment.

$$\text{Equation 1} \quad \omega_0 = \gamma B_0$$

$$\text{Equation 2} \quad \nu_0 = \gamma B_0 / 2\pi$$

$\omega_0$  is the precession frequency,  $B_0$  is the strength of externally applied field,  $\gamma$ : gyromagnetic ratio.

When, the net magnetisation returns to the equilibrium state this phenomenon is called relaxation. This can occur by exchanging energy between the higher energy state nuclei and their surroundings ( $T_1$  relaxation) or energy transfer between nuclei ( $T_2$  relaxation).  $T_1$  relaxation is known as spin lattice relaxation and it is the time required for the longitudinal magnetisation to reach two thirds of its value, and this is the basis of  $T_1$  weighted images. However,  $T_2$  relaxation time (spin-spin relaxation) is the time required for the transverse magnetic field to decay to 37% of its value. As a result of the differences between  $T_1$  and  $T_2$  relaxation of various  $^1\text{H}$  nuclei, different tissues may be distinguished.<sup>15</sup>

#### 4.2.2 Magnetic Resonance Imaging (MRI)

The physical principle of this technique is based on the theory of NMR spectroscopy.

However, data acquisition by MRI reveals three-dimensional images. This is because the NMR frequency of the nucleus is proportional to the strength of the magnetic field according to the Larmor equation (Equation 2). Therefore, by applying a gradient field, the Larmor

frequency of the slice water nuclei will be dependent upon its position within this field's gradient. Hence, we can relate the signal to its position. In MRI, field gradients are applied to the  $x$ -,  $y$ - and  $z$ -axes in order to place the proton in a three-dimensional manner. Relaxation information are accumulated by a computer with a two-dimensional Fourier transformation to provide the NMR signals and ultimately produce a 3-D image. Owing to biological parameters, for example the repetition time  $T_R$  (time between two following radio frequency pulses) and the echo time  $T_E$  (time between the radio frequency pulse and the measurement of the first signal), the operator may weigh the image and acquire the correct kind of image contrast. Fundamentally, a long repetition time,  $T_R$ , permits the protons within the tissues to complete longitudinal magnetisation to the  $z$ -axis and consequently this decreases the influence of  $T_1$ . However, long  $T_E$  permit the loss of transverse magnetisation and increasing  $T_2$  effects. Conversely,  $T_1$ -weighted imaging is acquired by using a rapid  $T_R$  and a rapid  $T_E$ , allowing full recovery of the short  $T_1$  proton within the tissues (for instance fat) whereas only partial recovery of tissues with long  $T_1$  (for instance cerebrospinal fluid). In contrast,  $T_2$ -weighted imaging is obtained by using long  $T_R$  and long  $T_E$ . Protons in the fluids possess a long  $T_2$  and are commonly linked with pathologies, therefore  $T_2$ -weighted images are usually chosen for such diagnostics.

The contrast between different types of soft tissue is usually noticeable, and the information acquired by MRI scans in such cases does not require imaging agents. However, the enhancement of contrast can be increased by the presence of paramagnetic molecules *in vivo*. The capacity of such molecules to enhance the relaxation times of protons in a certain area is called relaxivity, which is known as  $R_1 = 1/T_1$  or  $R_2 = 1/T_2$ . Hence, for example, the presence of endogenous haemoglobin is utilised for mapping brain function. As oxyhaemoglobin is diamagnetic, it has low  $R_1$  relaxivity. While the deoxygenated counterpart, deoxyhaemoglobin, is paramagnetic and has high relaxivity. The presence and the absence of

oxygen in the brain haemoglobin determines the brain areas and measure blood flow variations. However, this does not usually deliver a clear anatomic description. If the contrast between tissues is inadequate, paramagnetic chemical species, known as contrast agents, are usually employed to provide a contrast enhancement. Contrast agents increase contrast by their impact on the relaxation time of proton nuclei. Moreover, contrast agents can affect the behaviour of water protons located nearby and increase their relaxation rates in the tissue in which the agent accumulates.<sup>16</sup>

Nowadays, there are two categories of MRI contrast agents:  $T_1$  agents and  $T_2$  agents. In general,  $T_1$ -agents (for instance, gadolinium chelates) increase the longitudinal relaxation rates ( $1/T_1$ ) of protons in human tissue. However,  $T_2$  contrast agents (such as superparamagnetic iron oxide nanoparticles, SPIONs) are responsible for increasing the transverse relaxation rates ( $1/T_2$ ), which are relaxation effects resulting from the induced local field inhomogeneities leading to a negative contrast.<sup>17</sup>

Most of the clinically used  $T_1$  contrast agents are based on gadolinium-containing azamacrocycles (**Fig 4.3**).<sup>18</sup> Even with the common use of these contrast agents containing gadolinium, free gadolinium ions are very toxic.<sup>19</sup> For this reason, the development of less toxic contrast agents was required.

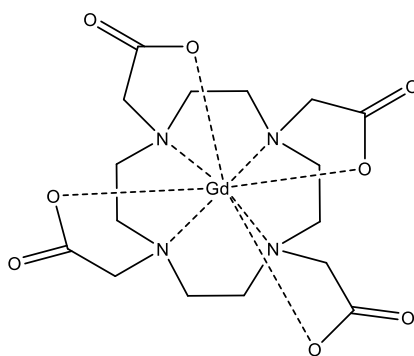


**Figure 4.3: Gd<sup>3+</sup> bound by 1,4,7,10-tetraazacyclododecane-1,4,7,10-tetraacetic acid (DOTA)**

However, in addition there are a number of clinically used T<sub>2</sub> contrast agents based on SPIONs, which are super-paramagnetic iron oxide nanoparticles. Typically, these contain Fe<sub>3</sub>O<sub>4</sub>, although some contain Fe<sub>2</sub>O<sub>3</sub>. These particles range in size from 5-100 nm. The contrast agents will be discussed in more detail in later sections.

#### 4.2.3 Physical Principles of Magnetism

As contrast agents are based on molecular species that perturb the local magnetic environment in a sample, it is appropriate to consider the magnetic properties of molecules. All materials exhibit magnetic properties to some extent, and this depends on their atomic construction and the temperature. These features appear in any materials due to the rotation of the electrons around atomic nuclei. Positively charged atomic nuclei and electrons spinning around their axes cause magnetic moments. Overall, these effects might cancel out, which is why some atoms have no magnetic dipole. Yet, other atoms are permanent magnetic dipoles because the magnetic moments are not totally cancelled out. A magnetic dipole moment is defined as the force of a magnetic dipole and the ability of the dipole to align parallel with an applied external magnetic field (H). The magnetisation (M) is considered as the quantity of the magnetic moment per unit volume and its value is given by the following equation:

$$M = \chi H \quad (3)$$

Where  $\chi$  = the volumetric magnetic susceptibility

Magnetic materials can be categorised according to their  $\chi$ .<sup>20</sup> As long as the materials show poor repulsion, they are classified as diamagnets. When the materials demonstrate small positive susceptibility, they are paramagnets; however, the materials are termed as ferromagnetic substances if they display a large positive susceptibility. In the absence of an external magnetic field, ferromagnetic material continue to hold their magnetic properties but paramagnets and diamagnets lose these features in this case.<sup>21</sup>

There are a number of significant factors that affect the magnetic susceptibility of SPIONs, such as the size, shape and crystallinity of the SPIONs and surfactant groups coating the particles.<sup>20</sup>

#### 4.2.4 Superparamagnetism

SPIONs that display exceptional magnetic properties are different from their bulk counterparts (ferromagnetic material). they exhibit a zero magnetic state in the absence of an external magnetic field. That is because of their particles' dimensions.<sup>22</sup> In the crystal arrangement of magnetite, iron ions are located in two different lattices in an inverse spinel structure (Fig 4.4). The net spontaneous magnetisation of the iron nanoparticles is responsible for the crystal construction of ferrite. Every unit cell in this arrangement consists of two  $\text{Fe}^{2+}$  and four  $\text{Fe}^{3+}$  centres. Both ions have high spin and they possess unpaired d-electrons. Thus, they hold paramagnetic properties. Magnetic dipoles on the metal centre increase as a consequence of the motion of these unpaired electrons.<sup>23</sup>

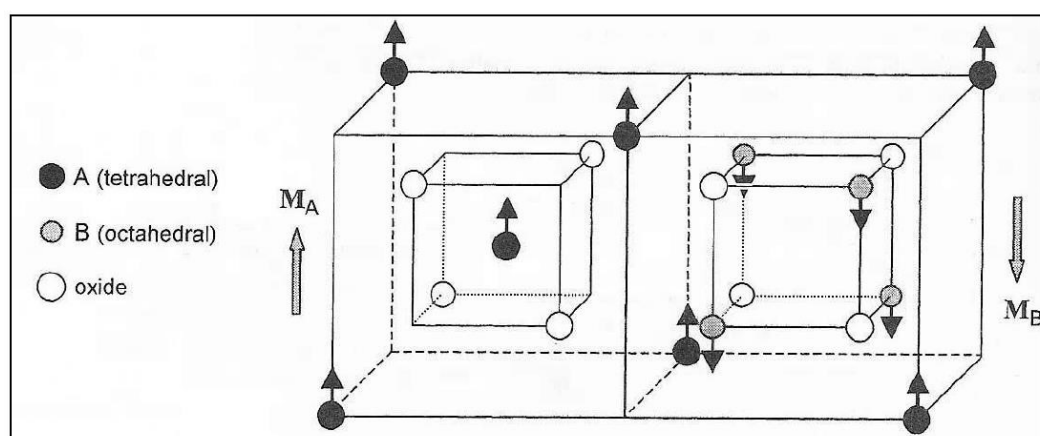


Figure 4.4: Inverse spinel unit cell of magnetite<sup>23</sup>

The properties of SPIONs were predicted in 1930.<sup>24</sup> It was also hypothesised that particles below 15 nm comprise of a single magnetic domain and exhibit superparamagnetic properties.

This domain acts as the unpaired electrons in a paramagnetic material, meaning that in the existence of an external magnetic field, the magnetic moment of the crystallite aligns itself with the field. However, it shows zero magnetic properties when the applied magnet is removed. That is because the thermal energy, in the absence of applied magnet, is adequate to distract the magnetic moments and cancel the net magnetisation of a given material.

Superparamagnetic material shows greater magnetic susceptibilities than typical paramagnetic materials. This is because the magnetic moments of individual particle domains are larger than the magnetic moments of unpaired electrons in paramagnetic materials. Moreover, instead of each separate atom being individually affected by the applied magnetic field, the magnetic moment of the domain aligns entirely with the magnetic field.<sup>25</sup>

#### 4.2.5 Positron Emission Tomography (PET)

A PET scan is a medical imaging technique used to obtain images of the body by injecting a radioactive tracer into the body. A camera is then used to monitor the distribution of the substance into the body tissue. The physical principle behind this modality has been detailed extensively in the literature.<sup>26,27</sup> The theory of PET is based on the emission of positrons and subsequent detection of  $\gamma$ -photons upon annihilation. The most common radionuclides used are  $^{18}\text{F}$ ,  $^{15}\text{O}$  and  $^{13}\text{N}$ , with  $^{11}\text{C}$ ,  $^{64}\text{Cu}$  and  $^{68}\text{Ga}$  among others of interest in previously reported research. These isotope emitters undergo a decay process when a proton is changed to a neutron and it emits a positron. A positron is the antimatter counterpart of an electron and when it collides with an electron in the tissue, a process called annihilation occurs, which converts mass to energy ( $E = mc^2$ ) in the form of two photons. The annihilation procedure produces two 511 keV  $\gamma$ -photons that move in opposite directions (**Fig 4.5**). These photons are detected and used to identify the point of annihilation.

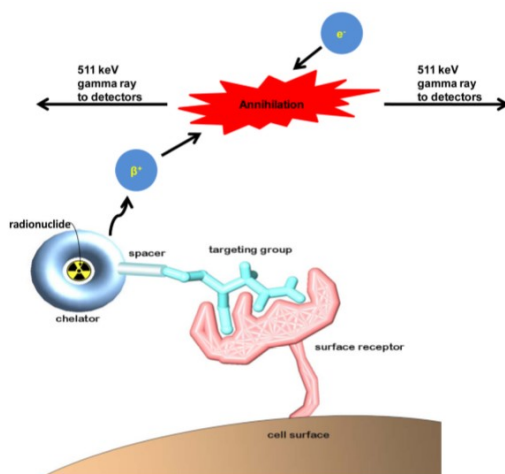


**Figure 4.5: Illustration of the physical principle of Positron Emission Tomography (PET)<sup>27</sup>**

The PET camera uses scintillation crystals placed around the subject to detect these photons. This converts  $\gamma$ -photons into visible photons by absorbing these photons and then emitting photons at a longer wavelength. The visible photons are then converted into an electrical signal. X-ray computed tomography (CT) medical imaging is usually employed at the same time as using PET in order to visualise the skeletal structure to deliver a reference for the imaging agent site.

PET radioisotope based on  $^{18}\text{F}$ , particularly 18-fluorodeoxyglucose (FDG) (a glycolysis marker), shown in **Fig 4.6**, has been widely used in the clinic. PET is used to evaluate the consumption rate and metabolism of glucose within tissues in different parts of the body. The irreversible accumulation of the radiolabelled glucose analogue (FDG) permits measurement of the consumption rate of glucose in cells within the body tissues that are undergoing metabolism. This agent is used clinically to distinguish between benign and malignant tumours, as the metabolic rate, and hence consumption of glucose, is quicker in malignant

cancerous tissues. This aids clinicians to screen and investigate the changes occurring in a tumour during a chemotherapy course.<sup>12</sup>

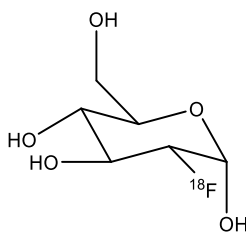
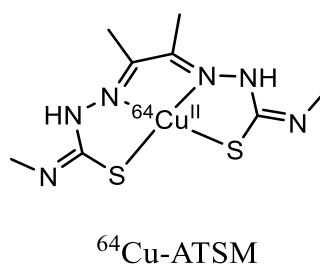


**Figure 4.6: 18-Fluorodeoxyglucose (FDG)**

Many radiolabelled agents are under investigation, though currently their production is usually restricted by their short half-lives. The half-life of  $^{18}\text{F}$  is 109.8 minutes; therefore, the synthesis of the positron emitters, production of the imaging agent and the following clinical scan are dictated by this timescale.<sup>12</sup>

The synthesis of radiolabelled agents of radiometals such as Zr, Y, In, Ga and Cu have been studied as radionuclides.<sup>28</sup> In terms of reasonable aqueous reduction procedures related to metal-based radiopharmaceuticals, only Cu(II) and its complexes are prone to redox processes.<sup>27</sup>

The principle of bioreduction efficiency in copper radiolabelled agent was investigated in thiosemicarbazone complexes, particularly Cu-ATSM (**Fig 4.7**).<sup>29</sup> The selective retention/decomplexation of Cu(I) from Cu(II) in hypoxic cells was proposed for this complex.<sup>29</sup> Furthermore, bis(thiosemicarbazonato) complexes of the radiometal Cu(II) have been extensively studied for the imaging of hypoxia.<sup>29</sup>



$^{64}\text{Cu}$ -ATSM

**Figure 4.7: Structure of  $^{64}\text{Cu}$ -ATSM**

### 4.3 SPIONs synthesis

SPIONS are nanoparticles that have been shown to be effective T2 MRI contrast agents. In addition, it has been shown that metal ions may be doped into the SPION framework, meaning they can be labelled with PET isotopes. As such, they are potential bimodal PET-MRI agents. Furthermore, they may be coated with fluorescent surfactants, allowing the use of further imaging modalities. This chapter explores the synthesis of multimodal SPION imaging agents.

Superparamagnetic iron oxide consists of three different iron oxides: Magnetite ( $\text{Fe}_3\text{O}_4$ ), maghemite ( $\gamma\text{-Fe}_2\text{O}_3$ ) and hematite ( $\alpha\text{-Fe}_2\text{O}_3$ ). There is also another type of SPIONs called ferrites. These comprise of iron oxides and other transition metal ions such as Cu, Co, Mn and Ni, which have also been classified as superparamagnetic species.<sup>30</sup> However, the present review focuses only on pure iron oxide nanoparticles that possess superparamagnetic properties. **Figure 4.8** illustrates the three most significant published approaches aimed at the synthesis of SPIONs.<sup>31</sup> Only chemical methods of producing SPIONs will be highlighted in this report. There are many chemical approaches that can be used for SPION synthesis such as: microemulsions<sup>32</sup>, sol-gel syntheses<sup>33</sup>, sonochemical reactions<sup>34</sup>, hydrothermal reactions<sup>35</sup>, hydrolysis and thermolysis of precursors<sup>36</sup>, flow injection syntheses<sup>37</sup> and electrospray syntheses.<sup>38</sup> A coprecipitation method is the most common technique for SPION synthesis.<sup>39</sup>

However, the synthesis of SPIONS is a challenging procedure because of their colloidal nature. It requires a reproducible industrial process that produces a monodisperse population with a high degree of crystallinity and magnetisation. Usually, further complex steps of purifications are needed to achieve these requirements. For example, size-exclusion chromatography<sup>40</sup>, magnetic filtration<sup>41</sup> or flow field gradient.<sup>42</sup>

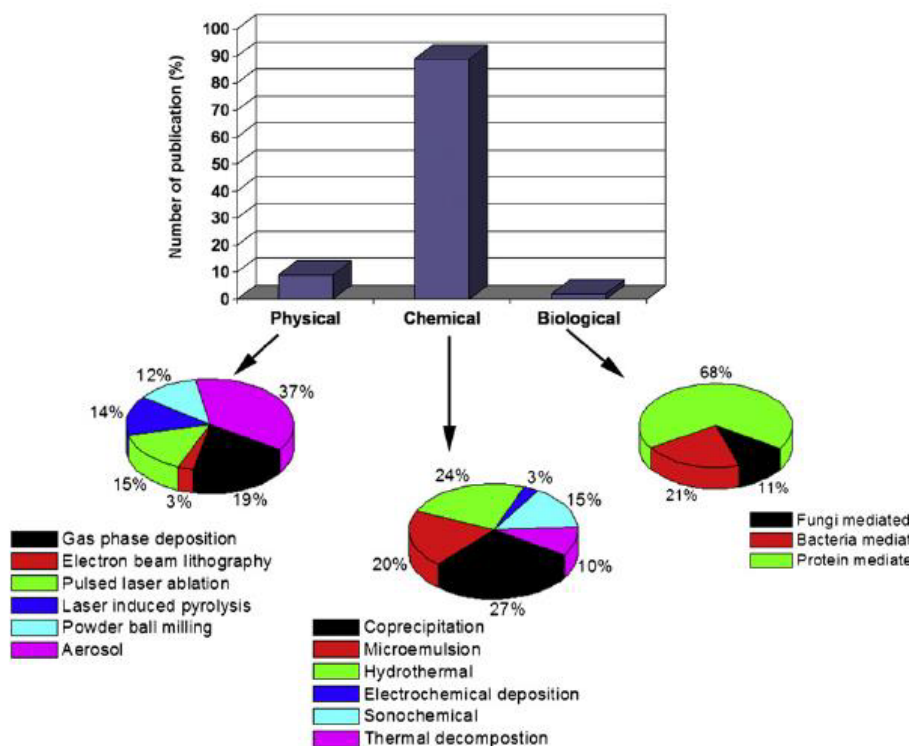


**Figure 4.8: Published work on SPION synthesis by three different pathways up until 2011.**  
 Source: Institute of Science and Technology

However, this project will focus only on the coprecipitation process, which was developed by Massart,<sup>43</sup> as it is the simplest and most efficient approach for SPION synthesis<sup>44</sup>. Although, large quantities of SPIONs can be produced by this procedure, the management of nanoparticle size distribution is limited. In this process, iron oxides (either  $\text{Fe}_3\text{O}_4$  or  $\gamma\text{Fe}_2\text{O}_3$ ) are prepared by adding a base to an aqueous mixture of  $\text{Fe}^{2+}$  and  $\text{Fe}^{3+}$  salt at a 1:2 molar ratio in an oxygen-free environment by passing  $\text{N}_2$  gas through the solution. By applying  $\text{N}_2$  throughout the solution, magnetite will be protected from oxidation and the dimension of the particles will be minimised.<sup>45</sup> The precipitated nanoparticles are black in colour and have an average diameter of 10 nm.<sup>46</sup> This reaction includes two different steps; nucleation and particle growth, which must be separated to obtain the optimum conditions for producing monodisperse nanoparticles.<sup>47</sup>

#### 4.4 Stabilization of Magnetic Particles

The stabilisation of SPIONs in suspension is a significant step in order to avoid oxidation and aggregation. Magnetite can be easily oxidised to maghemite. The presence of maghemite is undesirable as it is less stable and lower in magnetic moments than magnetite.<sup>48</sup> Several forces control the stabilisation of iron oxide, such as: hydrophobic–hydrophilic, magnetic dipole force, the electrostatic repulsive forces and van der Waals. SPIONs tend to aggregate and cluster in suspension. This is due to hydrophobic connections between the particles. Moreover, magnetic dipole-dipole forces increase the aggregation.<sup>49</sup> In the existence of an applied magnetic field, additional magnetisation of these clusters can happen, causing their aggregation.<sup>50</sup> This aggregation can hinder the effectiveness of SPIONs in drug delivery because of their low surface area and larger sizes. Therefore, the stabilisation of SPIONs in suspension made by adjusting their surface is vital especially in terms of drug delivery. The modification of SPIONs' surfaces can be achieved either during their preparation or after the process of SPION synthesis. Numerous approaches have been investigated, including both monomeric and polymeric stabilisers.<sup>31</sup>

##### 4.4.1 Polymer stabilisers

Many polymers are used for coating SPIONs, resulting in dextran-, carboxydextran-<sup>51</sup> and polyethylene glycol (PEG)-coated SPIONs,<sup>52</sup> which are commercially available as Feridex®, Resovist® and PEG-Ferron®, correspondingly.<sup>53</sup> (**Fig 4.9**) These are T<sub>2</sub> MRI contrast agents. The coating capability results from hydrophobic interactions and non-covalent bonding between these polymers and the nanoparticles.<sup>54</sup>

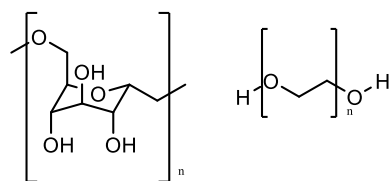


**Figure 4.9: Dextran and polyethylene glycol**

Although coating SPION nanoparticles with polymer species was successful, large SPIONS were obtained. Thus, nonpolymeric coating species have been studied.<sup>55</sup>

#### 4.4.2 Organic Stabilisers

Organic stabilisers have been successfully linked to the surface of magnetite.<sup>56</sup> This included carboxylate, sulphonate, phosphate and phosphonate with disulphonic esters. Oleic acid,<sup>57</sup> lauric acid, dodecyl phosphonate, hexadecyl phosphonate and dihexadecyl phosphonate (**Fig4.10**) are monomeric SPION stabilisers.<sup>58</sup>

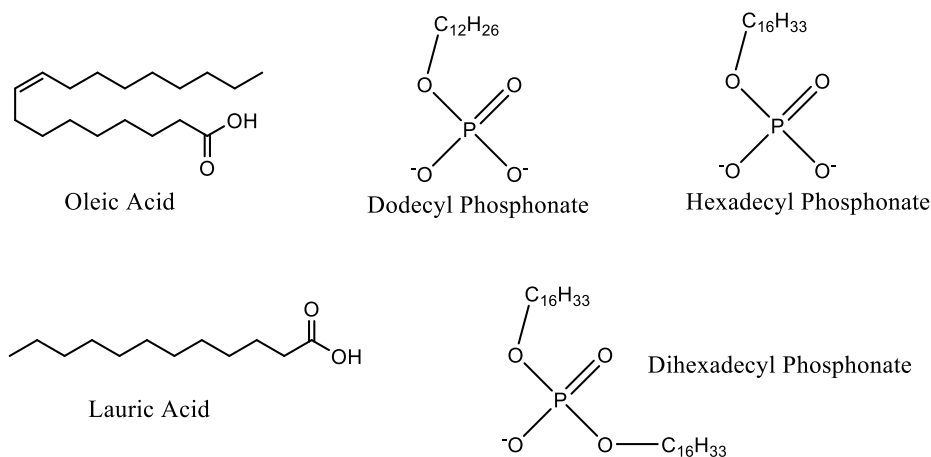


**Figure 4.10: Some examples of monomeric species used for coating iron oxide nanoparticles**

#### 4.4.3 Inorganic Material

The example for the inorganic coating substance that has been used as an inorganic stabiliser of iron oxide nanoparticles is silica.

##### 4.4.3.1 Silica coating

This project will focus on silica protective coatings, particularly (3-aminopropyl) triethoxysilane (APTES) (**Fig 4.11**). Silica shells are suitable for use as a stabiliser owing to their stability under aqueous conditions and simplicity of synthesis.<sup>59</sup> Moreover, such shells offer functional groups (amines or carboxylic acid) that have the ability to react with various biomolecules<sup>60</sup> such as proteins and enzymes. The use of alkoxy silane molecules to give a silica or polysiloxane coating layer has been demonstrated as biocompatible and water soluble SPIONs.<sup>61</sup> SPIONs, 2 nm in size with a 1 nm shell of silica were obtained by using a microemulsion technique in the presence of tetraethyl orthosilicate (TEOS). SPIONs, which are coated with TEOS, are usually then bound with (APTES) or analogous molecules in order to introduce amine groups onto the surface of the particles.<sup>62</sup> Magnetite ( $\text{Fe}_3\text{O}_4$ ) and maghemite ( $\gamma\text{-Fe}_2\text{O}_3$ ) have been directly coated with APTES.<sup>63,64</sup> In the present study, APTES is used to coat superparamagnetic magnetite particles with the APTES reacting with the iron oxide nanoparticles by adsorption or covalent bonding. In addition, the active amino group of APTES is able to bind with biomolecules, drugs and metals.<sup>63</sup>

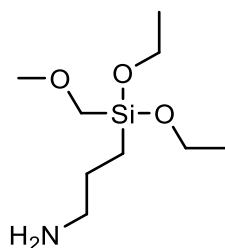


**Figure 4.11: (3-Aminopropyl) triethoxysilane**

#### 4.5 Literature Review

As mentioned before, the initial effort on the development of MRI contrast agents was focused on gadolinium complexes, some of which have been used clinically.<sup>18</sup> However, a range of MRI agents have been studied, such as SPIONs.

This chapter is focussed on SPIONs, as these nanoparticles exceed the contrast enhancement of a Gd agent, with less than a quarter of the injected dose.<sup>65</sup> Furthermore, and significantly, SPIONs have a negative enhancement effect on T<sub>2</sub>-relaxation time. The similarity between the behaviour of SPIONs and the paramagnetic substances, is the loss of their magnetisation when the removal of an external magnet. However, the magnetic moment of SPIONs is higher. Thus, the relaxivity of SPIONs is higher than those of Gd-agents. Thus, SPIONs are used to provide T<sub>2</sub>-relaxation effects, which bring about a signal decrease seen on T<sub>2</sub>-weighted images (negative contrast). The explanation for this phenomenon may be from the large magnetic field heterogeneity around SPIONs as water protons diffuse past. This diffusion results in dephasing of the proton magnetic moments causing short T<sub>2</sub>. These mechanisms have been extensively explained in the literature.<sup>66</sup> SPIONs uses as imaging agents have also been thoroughly examined.<sup>48,67</sup> Because of the exceptional physicochemical and biological properties of SPIONs, they are suitable for many biomedical applications, such as targeted drug delivery and hyperthermia therapy.<sup>68,69</sup>

There are some reports of the radiolabelling of SPIONs where their polymeric surface coatings contain chelators and isotopes. For example, DFO (desferrioxamine B) coordinated to <sup>89</sup>Zr, and DOTA (1,4,7,10-tetraazacyclododecane-1,4,7,10-tetraacetic acid) bound with <sup>64</sup>Cu (**Fig 4.12**).<sup>70,71</sup>



In 2010, Patel and co-workers synthesised SPIONs coated with 3-aminopropyl silane and then anchored them with a chelator capable of coordinating with a positron-emitting metal as a PET/MRI agent. Their properties, such as cell-labelling efficacy, cytotoxicity and relaxivity were investigated. These nanoparticles exhibited good biocompatibility and high cell uptake efficiency (**Fig 4.14**).<sup>72</sup>

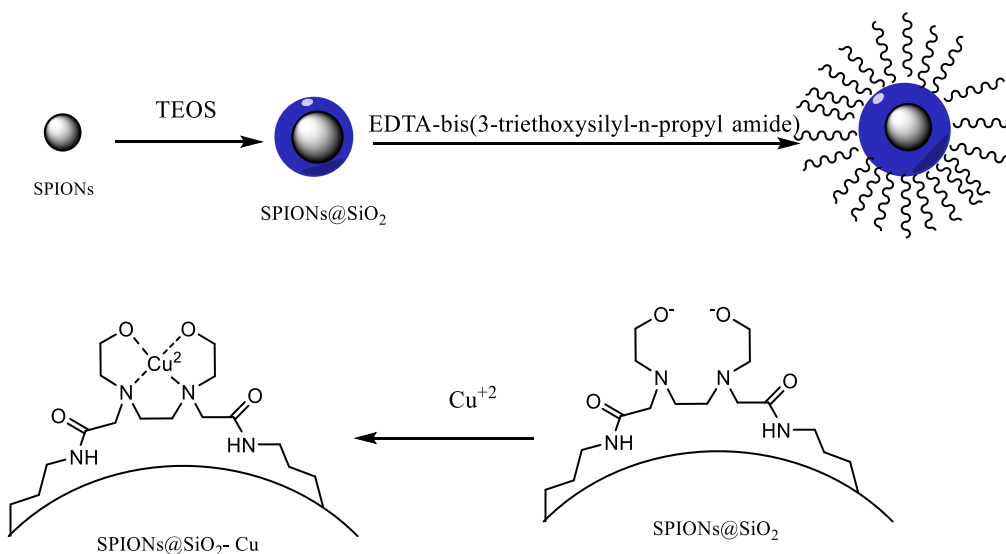


**Figure 4.14: Diagram of the SPIONs@SiO<sub>2</sub> with Cu<sup>2+</sup> and EDTA as a chelator**

In the present study, we have developed nanoparticles that are comprised of a superparamagnetic iron oxide coated with 3-aminopropyl silane (APTES) by using 3-aminopropyl triethoxysilane. The terminal amino group was reacted with one anhydride group of ethylenediaminetetraacetic acid anhydride (EDTAA) while the other anhydride function was bound to a fluorescent side chain (n-(2-aminoethyl)-1,8 naphthalimide and its derivative). These structures are able to form complexes with Cu<sup>2+</sup> ions (**Fig 4.15**). Potentially, this will allow the chelating of Cu<sup>64</sup> to be covalently bound to a tissue specific ligand either directly or through a single linker between EDTA and the ligand. These nanoparticles will provide a

novel class of trimodal imaging agent with MRI, PET and fluorescent allowing *in-vitro* and *in-vivo* cell evaluation. It is anticipated that the combination of these three imaging modalities will open a new gateway for accurate, precise and non-invasive imaging.

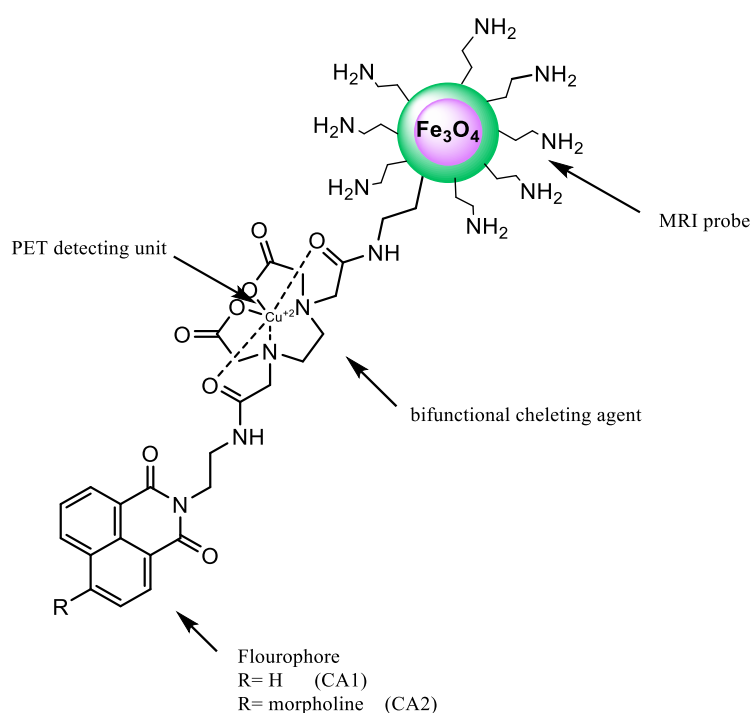


**Figure 4.15: Illustration of tri-modal nanoparticles**

In addition, new Schiff-base tailed silanes and metronidazole have been successfully synthesised and characterised by NMR, IR and HRMS. A novel MRI imaging agent conjugated to metronidazole and naphthalamide was also synthesised and characterised. This molecule was designed for hypoxia imaging purposes. SPIONs coupled with 2-nitroimidazole and naphthalimide as multi-modal nanoparticles for hypoxia tracking were synthesised here for the first time. In this report, we describe the synthesis, surface modification and characterisation of these nanoparticles and evaluate their optical properties.

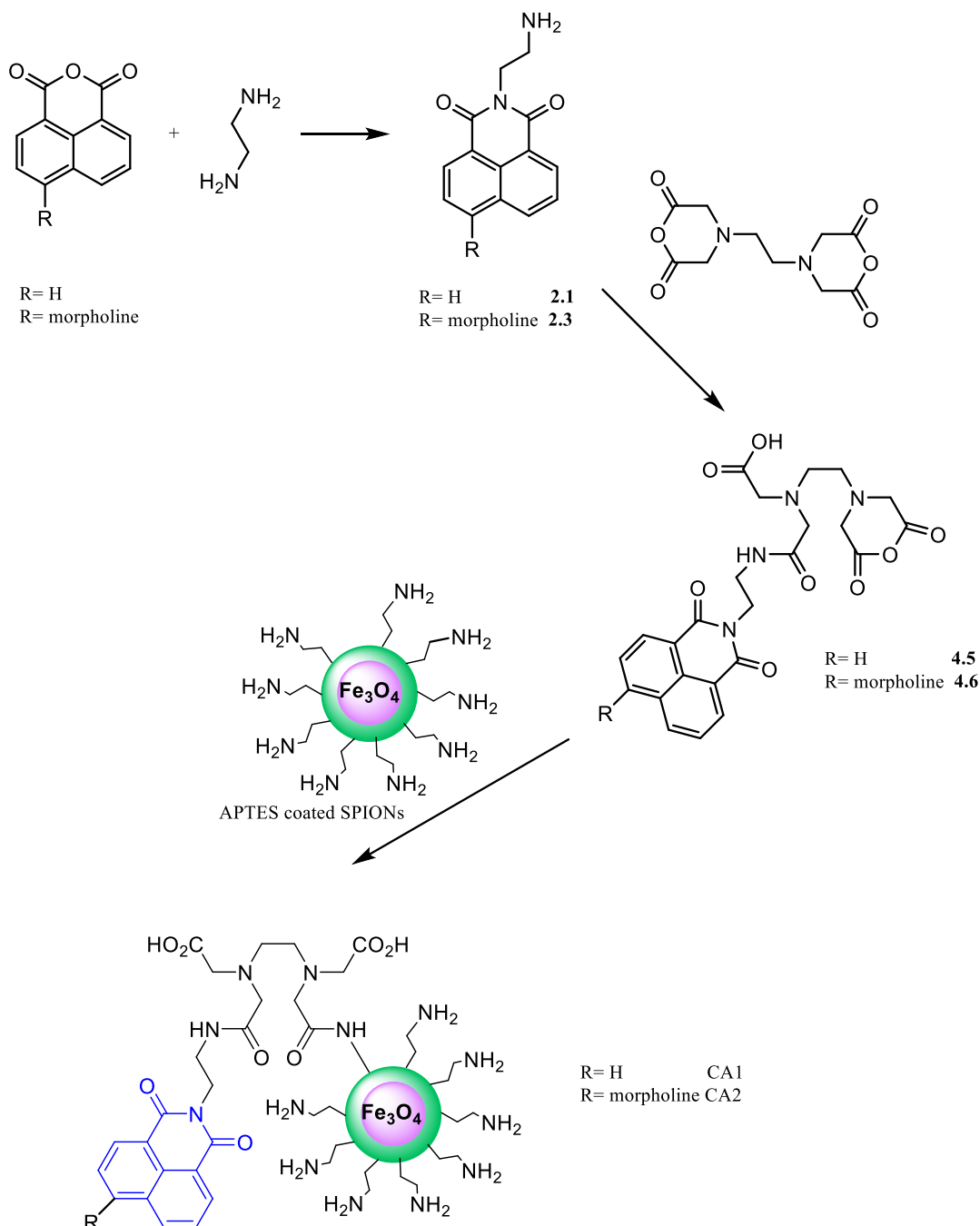
#### 4.6 Results and discussion

In this part, the following aspects will be discussed:

- 1- The synthesis and characterization of fluorescently labelled SPIONs CA1 and CA2.
- 2- The synthesis and characterisation of fluorescently labelled SPIONs conjugated to 5-nitroimidazole.
- 3- The synthesis and characterisation of fluorescently labelled SPIONs conjugated to 2-nitroimidazole.
- 4- Photochemical properties of the prepared nanoparticles including UV-vis and luminescence.
- 5- Diameter analysis of the prepared nanoparticles.
- 6- Inductively coupled plasma atomic emission spectroscopy (ICP-AES) of CA1.

#### 4.6.1 Synthesis and characterisations of fluorescently labelled SPIONs

The proposed route for the synthesis of naphthalimie-edta-APTES@Fe<sub>3</sub>O<sub>4</sub> (CA1) and morpholine-naphthalimie-edta-APTES@Fe<sub>3</sub>O<sub>4</sub> (CA 2) is shown below:



**Scheme 1: Preparation of the silica-coated magnetite nanoparticles and the surface modifications**

An APTES-coated SPION was targeted as a suitable starting material upon which to attach organic fragments. The co-precipitation technique of producing SPIONS is the easiest and fastest procedure. The co-precipitation approach under a N<sub>2</sub> atmosphere was also successfully applied but producing SPIONs rapidly in air is more practical and can yield the same product, although it is anticipated oxidation that will occur with time. In 2004, M. Yamaura *et al.*<sup>63</sup> reported that coating SPIONs with APTES provided water soluble nanoparticles. The coating process is not reported in detail, omitting the mass of SPIONs, the heating temperature, the duration of the heating and the volume of the solvent. The coated nanoparticles produced in this report were produced by heating to 70°C for 2 hours with a ratio of SPION to APTES of 0.25g to 2.8 ml. The product was soluble in diluted acetic acid but was not water soluble. These coated nanoparticles were conjugated to **4.5** and **4.6** to produce CA1 and CA2, respectively. Initially, before this step, many procedures were attempted to synthesise **4.5** and **4.6** (**Scheme 1**) by reacting EDTA bisanhydride with **2.1** and **2.3**, respectively in a 1:2 stoichiometric ratio; however, the <sup>1</sup>H NMR spectrum of the crude product showed a mixture of bisamide and monoamide products. Purification by column chromatography using DCM: methanol, hexane: ethyl acetate or ethanol for both reaction mixtures was not successful. Mass spectrometry of the reaction mixture indicated that the presence of compound **4.5** with the expected mass ion peak 515.18, (27%) for the monoamine. Characterisation using mass spectrometry for **4.6** presented the predictable M<sup>+</sup> ion peak 600.22, (100%) for the desired product as well as the M<sup>+</sup> ion peak 907.36 for the bisamide. This suggested that the reaction was successful; however, further purification is required. As the bis-amide would not react with the APTES-coated SPION in the next reaction step, it was decided to carry out a one pot reaction for producing CA1 and CA2, thereby avoiding the need to isolate the reactive anhydride intermediate. By using this synthetic procedure, we were able to separate the desired product from the crude product via an external magnet.

FT-IR spectra of synthesised  $\text{Fe}_3\text{O}_4$  are shown in **Fig 4.16**. As presented in all spectra, the distinctive absorption peak for magnetite nanoparticles was split into two peaks at about 518 and  $450\text{ cm}^{-1}$ .<sup>63</sup> Compared to naked SPIONs (a), APTES-modified iron oxide nanoparticles (b) showed additional peaks at  $1010\text{ cm}^{-1}$ ,  $1055\text{ cm}^{-1}$  and  $995\text{ cm}^{-1}$ . These absorptions corresponded to Si-O-Si and Si-O-H vibrations. The peak of  $\text{Fe}_3\text{O}_4$  nanoparticles can still be seen, representing the existence of the SPIONs. The peaks at  $930\text{ cm}^{-1}$  and  $855\text{ cm}^{-1}$  represent Si-O-H stretching and OH vibrations. The peak at  $2920\text{ cm}^{-1}$  which corresponds to C-H stretch and alkane, confirm the existence of propyl group in APTES.<sup>63</sup>

In the infrared analysis of n-(2-aminoethyl)-1, 8 naphthalimide, there were two absorption peaks at  $3350\text{ cm}^{-1}$  and  $3289\text{ cm}^{-1}$  that corresponded to N-H primary amine stretch frequency. Upon the coupling reaction of **CA1** and **CA2**, this region of the IR changed, and these peaks were not observed. This provides good evidence of the alkylation of primary amine and formation of an amide. The absorption at 1698, 1643 and 1600 were assigned for the carbonyl stretch of the amide bond and carboxylic acid stretch. Moreover, the presence of a peak at  $1400\text{ cm}^{-1}$  also suggests the synthesis of **CA1**. The absorption of this frequency corresponded to C=C aromatic bending in naphthalimide. Because of the similarity between **CA1** and **CA2** in the structure, infra-red absorptions of **CA2** were approximately at the same values.

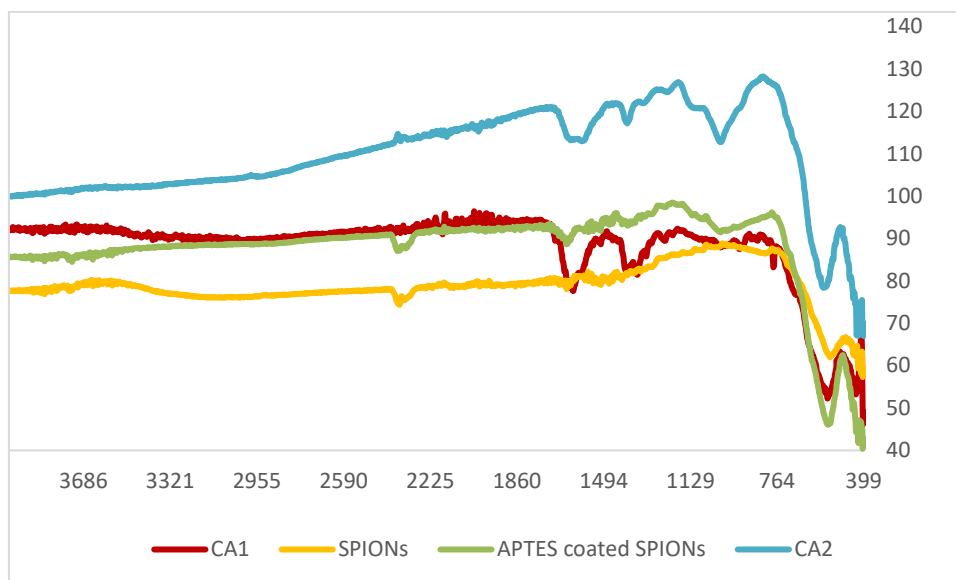


**Figure 4.16: IR spectra of uncoated SPIONs, APTES-coated SPIONs, CA1 and CA2**

#### 4.6.2 Coordination of CA1 with Cu<sup>2+</sup>

A fluorescence titration was carried out to determine if the co-ordination of Cu(II) to the EDTA moiety would induce quenching of the organic naphthalimide lumophore. Numerous literature reports exist of Pet (photo-induced electron transfer) quenching for the selective detection of Cu(II) ions.<sup>73</sup> To determine if CA1 and CA2 might be used as a sensor for Cu(II), a titration of CA1 with Cu(II) was carried out in the following manner:

Sodium acetate (0.1M) buffer pH 5, was prepared to keep the pH of the nanoparticles constant during the reaction. Nanoparticles CA1(200 mg) were dissolved in 100 ml of the buffer.

In the first attempt, the concentration of CA1 in each well was constant (3.645 ng/uL). In each well, 67.5 µml of CA1 was added and 0.1M CuSO<sub>4</sub> was used to vary the Cu(II) concentration.

Then, the concentration was increased from 10 mM to 75Mm while the concentration of the buffer was decreased gradually from 182.5 mM to 32,5 mM. The fluorescence of the naphthalimide was measured and was determined to be constant in all cases.

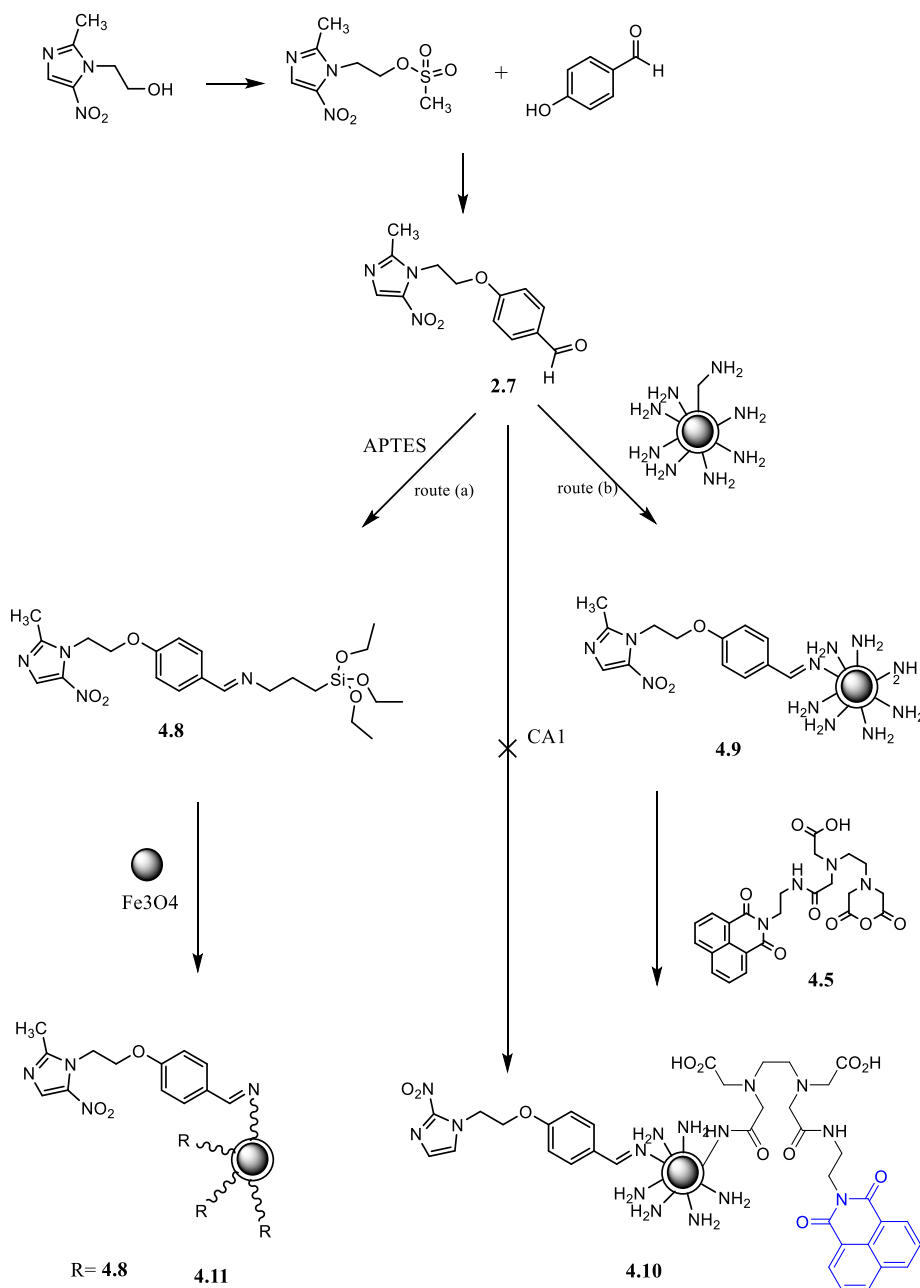
In a second experiment, the volume of the nanoparticles in sodium acetate buffer was reduced to 18.5  $\mu\text{ml}$  and accordingly the concentration of these nanoparticles was decreased to 1.00 ng/ $\mu\text{L}$ . Again, the volume and the concentration of CA1 remained constant during this attempt. A total of 18.5  $\mu\text{ml}$  of CA1 was added into each well. The concentration of  $\text{CuSO}_4$  was increased regularly throughout the wells from 10 mM to 75 mM. In this attempt, the decrease in ratio of the nanoparticles to copper ion was done in order to increase the opportunities of copper ions to chelate all the EDTA ligand of the nanoparticles, and consequently quench the UV light emitted by the naphthalimide of the ligand at 433 nm. Again, no obvious change occurred according to microplate reader fluorescence.

In order to investigate whether the co-ordination reaction was slow (which would be unusual for the typically labile  $\text{Cu(II)}$  ion), the time between the addition and measurement was increased from 30 minutes to 90 minutes. Unfortunately, the luminescence spectrum of the ligand remained the same.

To study the effect of increasing the ratio of Cu ions on the coordination ability of the nanoparticles, 1 M  $\text{CuSO}_4$  was used in this attempt and the concentration was varied from 100 mM to 750 mM while the concentration of the CA1 was constant and remained the same at 1.00 ng/ $\mu\text{L}$  in each well. There was a general downward trend in the luminescence intensity data suggesting that with high concentrations of  $\text{Cu(II)}$ , the successful coordination of copper ion to CA1 takes place.

#### 4.6.3 Synthesis and characterisation of fluorescently labelled SPIONs conjugated to 5-nitroimidazole

Having successfully labelled the SPIONs with a lumophore, we were interested in additionally labelling these particles with the hypoxia directing nitroimidazole groups. Such particles might localise in hypoxic tissue and could then be detected by luminescence *in vitro* and by MRI (or PET) *in vivo*.



Scheme 2: Synthetic route of 4.8, 4.9, 4.10 and 4.11

Two pathways were investigated to obtain SPIONs conjugated to metronidazole and both gave the desired product (Scheme 2, routes a and b). The first route involved the synthesis of a functionalised APTES derivative (**4.8**), which contained the nitroimidazole. By reacting **4.8** with SPIONs in EtOH (Scheme 2, route a), the desired product was formed. The other pathway was formed by reacting APTES-coated SPIONs with **7** (Scheme 2, route b). The synthesis and characterisation of **7** was fully described in Chapter 2.

The first pathway included the synthesis of **4.8** and **4.11**. The other pathway involved the formation of **4.9** the **4.10**. While at first glance compounds **4.9** and **4.11** may appear the same, the critical difference is that while **4.9** will have unreacted amines on the SPION surface, **4.11** will only have nitroimidazoles groups on its surface.

Attempts to react the fluorescent nanoparticles CA1 and CA2 with **2.7**, proved to be unsuccessful, with no incorporation of the nitroimidazole to the nanoparticle being detected. However, it was found that if the nitroimidazole was added first, in a controlled ratio, then addition of **4.5** to this product would yield the desired nanoparticle. One possible explanation for this observation may be due to the high loading of fluorophores in CA1, which would lead to the steric hindrance of the amino groups.

#### **Synthesis and characterisation of 4.8 and 4.11 (route a, scheme 2):**

The conditions for the reaction for preparing (E)-1-(4-(2-(2-methyl-5-nitro-1H-imidazol-1-yl)ethoxy)phenyl)-N-(3-(triethoxysilyl)propyl)methanimine **4.8** were adapted from reported Schiff base tailed silatranes preparations.<sup>74</sup> It was prepared by the condensation of **4.8** with APTES at a ratio of 1:1. APTES was added dropwise and vigorous stirring was continued for one hour. The reaction was carried out by using a dropping funnel and a Dean-Stark-trap. The reaction mixture was refluxed in toluene under nitrogen overnight. Next day, the H<sub>2</sub>O

collected in the Dean-Stark suggested that the reaction had been successful. The mechanism used is as follows:

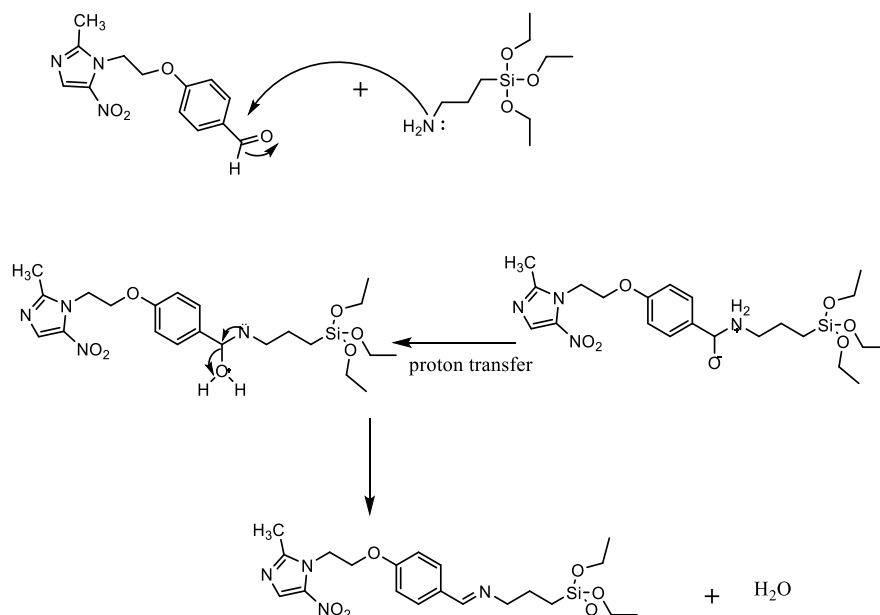


Figure 4.17: The suggested mechanism of 4.8

Dean-Stark-trap apparatus was employed in order to reduce the occurrence of the backward reaction. This is because water is a by-product of the reaction and it could re-enter the reaction causing hydrolysis of the imine group into aldehyde and primary amine. The Dean-Stark-trap apparatus assists in driving the reaction equilibria towards product formation and so increases the yield. When boiling, the reaction mixture forms a toluene-water azeotrope, which when condensed in the trap separates into water and toluene, with the more dense water settling at the bottom of the trap.<sup>75</sup>

This reaction was successfully achieved according to <sup>1</sup>H NMR spectra. The spectra indicated the presence of a peak at 8.37 ppm with an integral of one proton, indicative of the formation of an imine bond. In addition, the absence of the aldehyde proton of **2.7** is also a sign of imine bond formation. Compared to **2.7**, infrared analysis of the obtained product showed

additional peaks at 1180, 1186, and 1506  $\text{cm}^{-1}$  that were assigned to Si-alkoxy groups.<sup>76</sup> Moreover, the absence of stretching vibration of carbonyl group of **7** and disappearance of two  $\text{NH}_2$  stretching bands of APTES suggest imine bond formation. High resolution mass spectrometry showed the expected  $\text{M}^+$  ion peak (479.2334, 100%) for the desired product (**Fig 4.17**). This compound was prepared to be conjugated to iron oxide nanoparticles to be used potentially for MRI as a hypoxia tracer. In order to accomplish this target, naked SPIONs was directly reacted to **4.8**. The process and reaction conditions of this reaction are similar to the surface modification process for SPIONs by silanisation. In this reaction, **4.8** was added dropwise to a solution of SPIONs dispersed in ethanol. The reaction mixture was stirred and refluxed for 12 hours, then the nanoparticles were collected using an external magnet and washed with ethanol to remove any unreacted silane moiety. The resulting nanoparticles were analysed by infra-red spectroscopy, which shows, compared to uncoated SPIONs, absorptions at 1008 and 1188  $\text{cm}^{-1}$  assigned to Si-O-Si and Si-O-H vibrations (**Fig 4.18**) In addition, this spectrum shows all the absorbance of the 2- nitroimidazole moiety such as symmetric and asymmetric N=O bonds at 1363, and 1529  $\text{cm}^{-1}$ , respectively. The presence of the propyl and methyl groups were confirmed by C-H stretching vibrations that appeared at 2926  $\text{cm}^{-1}$ .

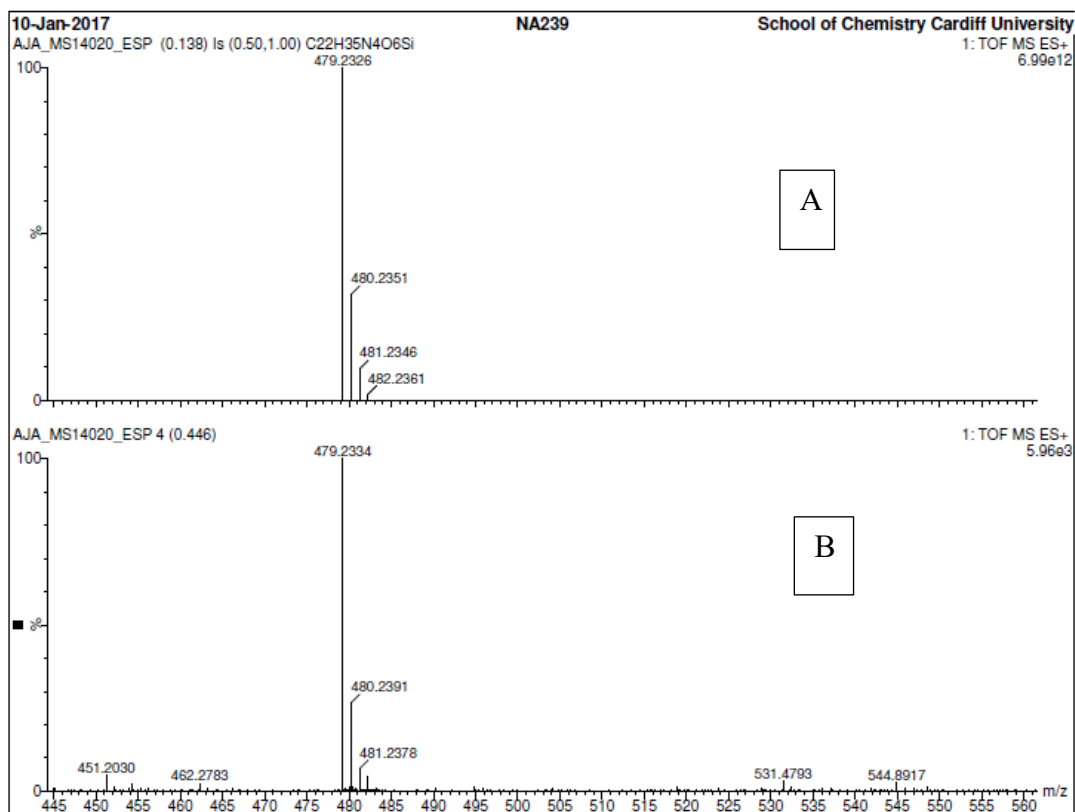


Figure 4.18: High resolution mass spectrometry 4.8, (A) theoretical spectrum, (B) experimental spectrum

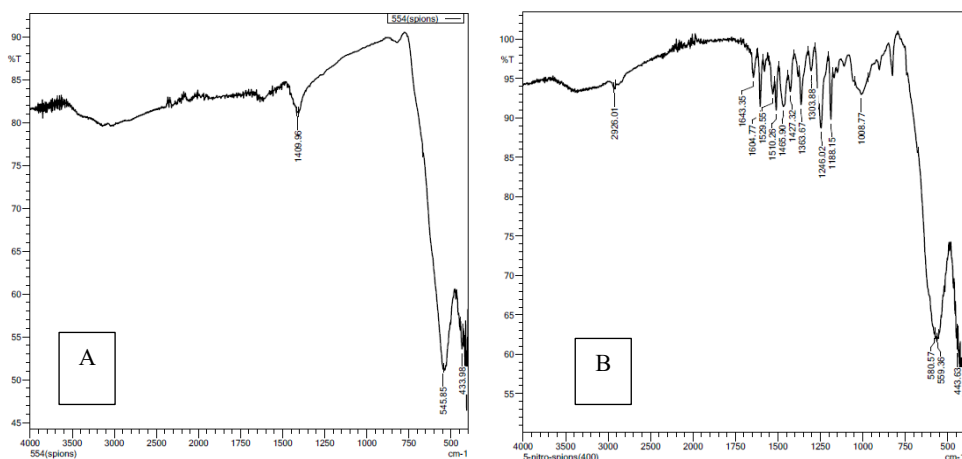


Figure 4.19: Infra-red spectrum of uncoated SPIONs (A) and 4.11 (B)

The direct conjugation between **2.7** and CA1 does not lead to the formation of fluorescently conjugated SPIONs with 5-nitroimidazole **4.10**. Ethanol was used as a solvent and the

reaction mixture was refluxed in atmosphere. In this reaction, it was expected that the primary amine on the surface of the SPIONs of CA1 would react with the aldehyde group of **2.7**. However, there is no evidence for any new product according to the infra-red spectrum. The reason for this may be that there are no free primary amine groups on the surface of the SPIONs and they have all coupled with EDTA, or that the equilibrium of the imine forming reaction lies towards the starting material. Thus, the preparation of CA1 was repeated and the amount of EDTA was reduced 3 times, 5 times and 10 times less than that of the original experiment. When the newly prepared CA1 species were reacted with **2.7**, the attempts were also unsuccessful. The reaction between **2.7** and CA1 was also screened under different solvents, such as DMF and acetonitrile under N<sub>2</sub>, in order to investigate the effect of these solvents and the inert atmosphere on the formation of imine bonds. Again, these attempts did not produce the desired product according to the IR spectrum. The failure of these reactions led to our attempt to produce **4.10** via route b.

**Synthesis and characterisation of 4.9 and 4.10 (route b, scheme 2):**

In the second pathway (route b, Scheme 2), SPIONs coated with APTES were synthesised using the coprecipitation method followed by surface modification by APTES. The terminal primary amine of these nanoparticles is theoretically able to react with the aldehyde group of **2.7** to form an imine bond of **4.9**. The infra-red data of this conjugation were in full agreement with the proposed structure (Scheme 2). Compared to APTES-modified SPIONs, the infrared analysis of the obtained nanoparticles showed additional peaks at 1533 and 1508 cm<sup>-1</sup> attributed to N=O asymmetric stretching (**Fig 4.19**). There were absorption bands at 1363 and 1306 cm<sup>-1</sup> which corresponded to N=O symmetric stretching. The success of this coupling can also be confirmed by the existence of imine absorption medium peak that appeared at 1647 cm<sup>-1</sup>.

In order to obtain fluorescently labelled SPIONs conjugated to metronidazole, compound **4.5** (scheme 2) was conjugated to **4.9** in a mixture of the solvents DMF and anhydrous ethanol as a one pot reaction, as mentioned previously in the synthesis of CA1. The desired product was collected by an external magnet and washed initially with DMF to remove any unreacted starting material, and then washed with DI water to remove the DMF. The desired product was dried under vacuum. These nanoparticles were characterised by IR, UV and luminescence and their successful synthesis was proven by IR (**Fig 4.19**). Compared to **4.9**, there are strong absorption bands at  $1653\text{ cm}^{-1}$  and  $1635\text{ cm}^{-1}$ , which are assigned to the carbonyl stretch of amide bond and carboxylic acid stretch. The presence of the anchored aromatic group of the naphthalimide group was confirmed by C–H stretching vibrations that appeared at  $3093\text{ cm}^{-1}$ .

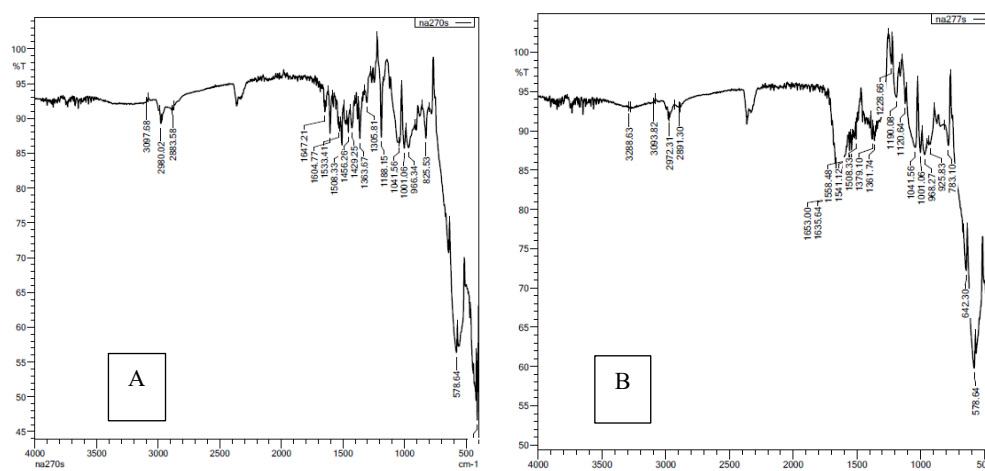
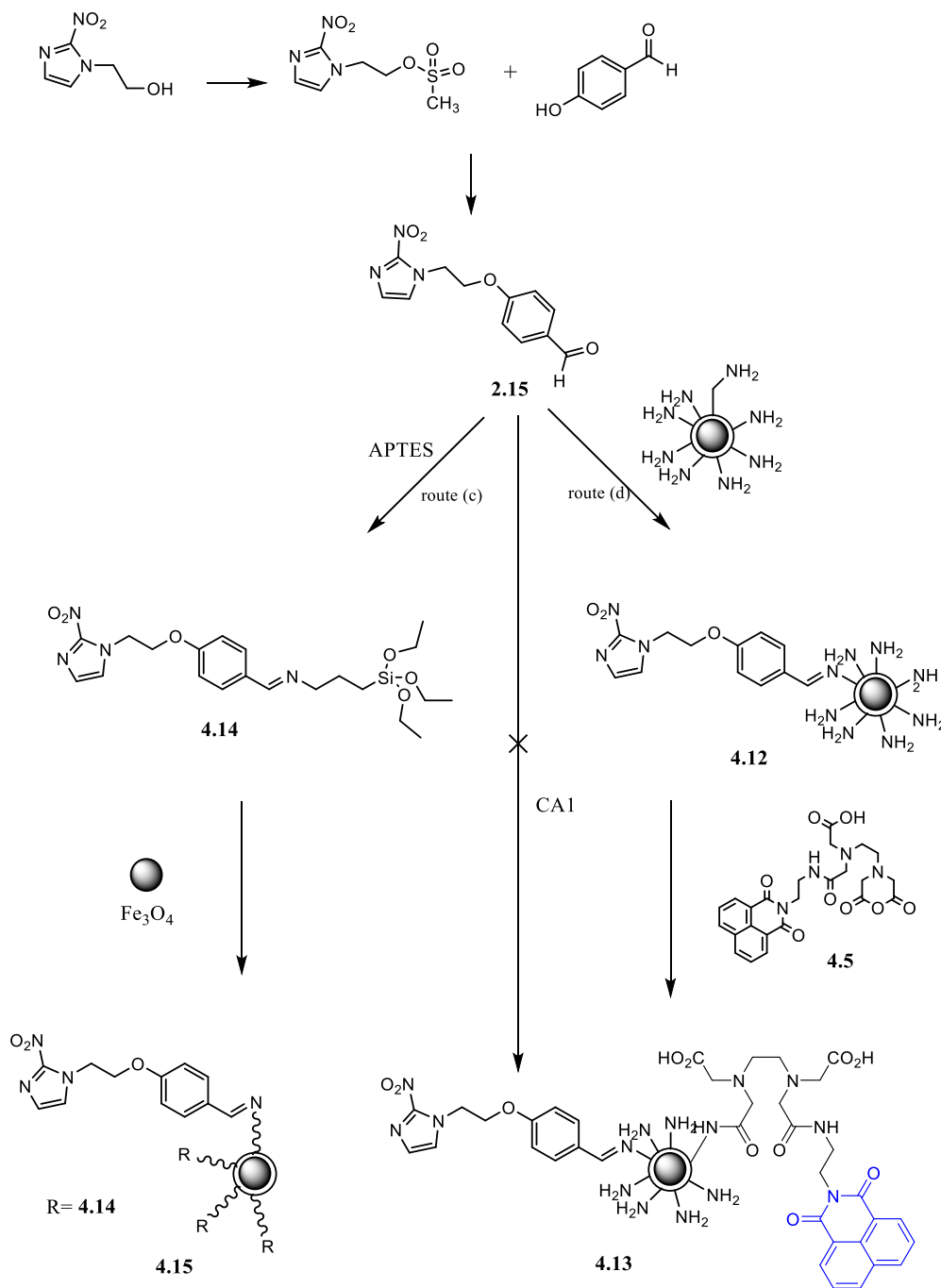


Figure 4.20: Infrared spectra of 4.9 (A) and 4.10 (B)

#### 4.6.4 The synthesis and characterisation of fluorescently labelled SPIONs conjugated to 2-nitroimidazole



Scheme 3: Synthetic route of 4.12, 4.13, 4.14 and 4.15

4-(2-(2-Nitro-1H-imidazol-1-yl)ethoxy)benzaldehyde **2.15** (scheme 3) was prepared as described in Chapter 2. With the aim of producing SPIONs conjugated to 2-nitroimidazole, **4.12** and **4.15** were synthesised. The same synthetic routes for **4.10** and **4.11** (Scheme 2) were applied to synthesis **4.12** and **4.15** (route c and d, Scheme 3). Fluorescently labelled magnetite coupled with 2-nitroimidazole was also synthesised **4.13**. The details of the synthesis and characterisation of these nanoparticles is described as follows:

#### 4.6.4.1 Synthesis and characterisation of **4.14** and **4.15**

(E)-1-(4-(2-(2-nitro-1H-imidazol-1-yl)ethoxy)phenyl)-N-(3-(triethoxysilyl)propyl)methanimine, **4.14**, (route c, scheme 3) was synthesised by applying the same reaction conditions as that of **4.8**. Although TLC showed the completion of the reaction and presence of a new product, the <sup>1</sup>H NMR spectra of **4.14** displayed the presence of one of the starting materials 4-(2-(2-nitro-1H-imidazol-1-yl)ethoxy)benzaldehyde **2.15**. To improve this, the ratio of APTES to **2.15** was doubled; however, the presence of aldehyde proton in <sup>1</sup>H NMR were still observed. The <sup>1</sup>H NMR spectra also confirmed the formation of this compound. One resonance was observed at 8.37 ppm with an integral of one proton, corresponding to the proton of an imide bond. As also seen in **4.8**, the infrared analysis of **4.14** illustrated the presence of extra absorptions at 1180, 1186, and 1506 cm<sup>-1</sup> that were assigned to Si-alkoxy groups<sup>76</sup> as well as small peaks at 1605 cm<sup>-1</sup> corresponding to imine group stretching. The disappearance of the carbonyl group absorption of **2.15** also suggests imine bond formation. Mass spectrometry showed the expected M<sup>+</sup> ion peak (465.22, 100%) for the desired product.

Compound **4.14** was synthesised to be reacted with SPIONs in order to produce contrast agent for MRI. Whether this compound is pure or not, it was decided to use it for the next step and

any impurities remaining in the mother liquor once the desired nanoparticles were washed and isolated using an external magnet.

In the next step, SPIONs were dispersed in anhydrous ethanol and a suspension of **4.14** in ethanol was added dropwise and refluxed for 12 hours. The desired nanoparticle **4.15** was collected using an external magnet and washed initially with DCM to remove any unreacted 2-nitro Schiff base tethered silatranes. These nanoparticles were dried on a vacuum line. The success of this conjugation was confirmed by the infra-red data, as shown in **Fig 4.20**.

Compared to uncoated SPIONs, the absorption of  $\text{Fe}_3\text{O}_4$  nanoparticles can still be seen, demonstrating the existence of the SPIONs. The peaks at 1018, 1006  $\text{cm}^{-1}$  represent Si–O stretching. The absorbances corresponding to the azomycin moiety were observed, such as N=O symmetric at 1361  $\text{cm}^{-1}$  and N=O asymmetric at 1508  $\text{cm}^{-1}$ . There was a medium absorbance at 1640  $\text{cm}^{-1}$  corresponding to the imide bond. The absorbance at 1249  $\text{cm}^{-1}$  could also be seen, which corresponded to C=C-N of imidazole. The aromatic ring has a characteristic weak overtone band that showed up at 1600  $\text{cm}^{-1}$ . The peak at 2924  $\text{cm}^{-1}$ , which corresponds to C–H stretching, confirmed the existence of a propyl group and methyl groups.

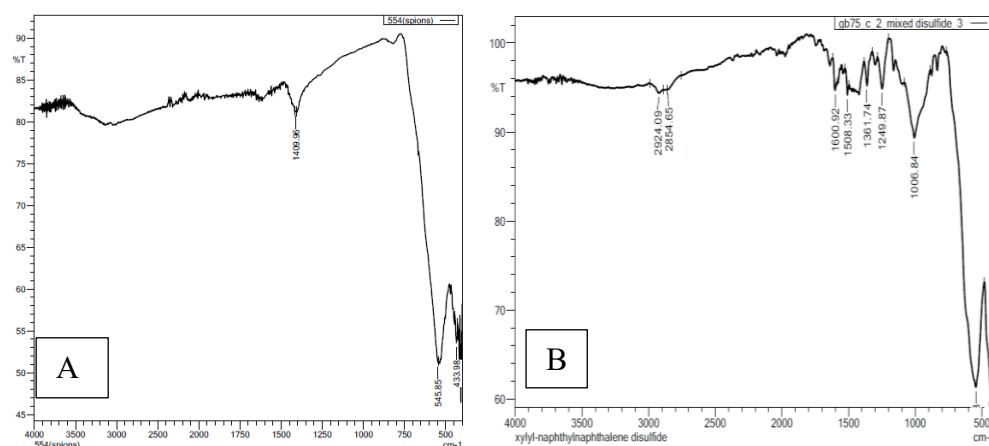


**Figure 4.21: Infra-red spectrum of uncoated SPIONs (A) and 4.15 (B)**

Again, as with the 5-nitroimidazole counterpart, the attempts to conjugate **2.15** to CA1 to produce fluorescently labelled SPIONs with 2-nitroimidazole were not successful according to the infra-red spectrum of the obtained nanoparticles. Thus, it was synthesised via the synthetic route b.

#### 4.6.4.2 Synthesis and characterisation of **4.12** and **4.13**

SPIONs coated with APTES were synthesised using the coprecipitation method and the surface was modified by using APTES. Then, the primary amine of APTES was condensed with the aldehyde group of 4-(2-(2-nitro-1H-imidazol-1-yl)ethoxy)benzaldehyde, **2.15**, to form an imine bond of **4.12** (Scheme 3, route d). This reaction was carried out in ethanol and refluxed for 12 hours in atmosphere. The desired nanoparticles were washed with DCM to remove any unreacted **2.15**. The success of this coupling was confirmed by IR (**Fig 4.21**). Compared to SPIONS@APTES, bands that showed up between 1512 and 1504  $\text{cm}^{-1}$  were attributed to N=O asymmetric stretching. There were also absorption bands between 1317 and 1361  $\text{cm}^{-1}$ , which corresponded to N=O symmetric stretching. Again, as seen in **4.15**, the absorbance peaks of C=C-N of imidazole could be observed at 1220 and 1265  $\text{cm}^{-1}$ . The absorption medium peak appeared at 1620  $\text{cm}^{-1}$ , which may correspond to C=N.

In order to obtain fluorescently labelled SPIONs conjugated to 2-nitroimidazole, **4.5** was conjugated to **4.12** in a mixture of solvents including DMF and anhydrous ethanol as a one pot reaction to produce **4.13** (route d, scheme 3). The same synthetic pathway for **4.10** was applied to produce **4.13**. In this reaction, the mixture was heated at 50<sup>0</sup>C for 15 hours. The modified nanoparticles were collected using an external magnet and characterised by IR, UV and luminescence analysis. The IR spectrum is shown in **Fig 4.21**. Compared to **2.12**, further absorptions occurred in the regions between 1662 to 1693  $\text{cm}^{-1}$  assigned to the carbonyl

stretch of the naphthalimide moiety. These overlap with the stretching peaks' imide bond, which was expected in these regions.

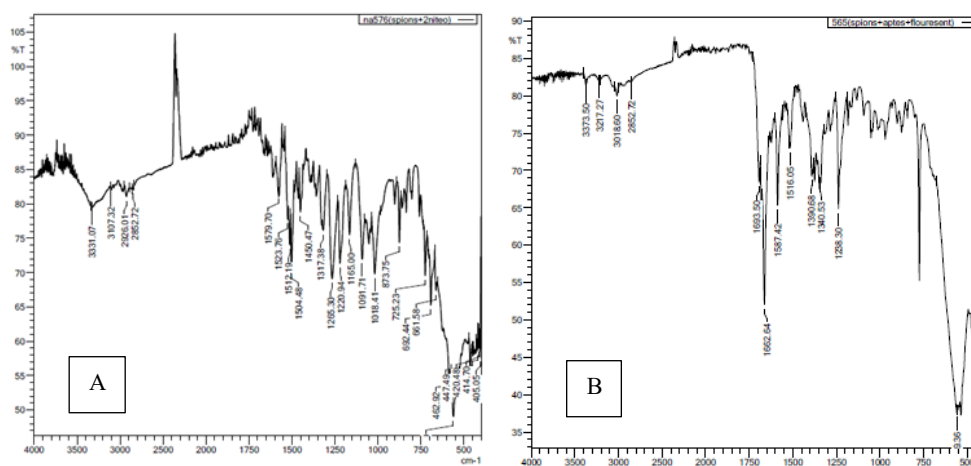


Figure 4.22: Infrared spectrum of 4.12 (A) and 4.13 (B)

#### 4.6.5 SPION diameter analysis

##### 4.6.5.1 Transmission electron microscopy (TEM)

In order to acquire more information on particle size and morphology, TEM analysis was carried out (Fig 4.22). The radius for about 25 nanoparticles of each sample were measured using ImageJ software, then the averages of these diameters were calculated.

As expected, all particles had a similar size as their cores were synthesised using the same co-precipitation method. The APTES magnetite particles showed an approximate spherical shape and an average diameter of 6.9 nm. However, CA1 and CA2 had less spherical particle sizes and an average diameter of 7.4 and 7.1 nm, which is only a few nanometres larger than that seen in SPIONs@APTES. Uneven size and shape were also seen, but as this irregularity is also seen in unfunctionalised particles it is unlikely to be due to the organic coating of the particles. The aggregation, shown as the darker spots in the images, was also observed in

these samples. This is probably due to the increase in electrostatic interaction as a result of the presence of both carboxylic acid and amine functional groups. The same phenomenon was seen in **4.9** and **4.10**, which had an average diameter of 9.8 nm and 9.5 nm, respectively. This diameter is larger than that of magnetite@APTES, perhaps suggesting that the aggregation phenomena accompanied the electrostatic interaction between the free amine group and carboxylic acid species. Both **4.9** and **4.10** seemed to have a less uneven shape. Table 9 summarises the calculated diameter for all samples.

**Table 9: Calculated diameters of APTES@SPIONs, CA1, CA2, 4.9 and 4.10; particle sizes were calculated using ImageJ software, taking 25 measurements for each sample**

Compound	Diameter / nm	Standard Deviation	Maximum / nm	Minimum / nm
APTES@SPIONs	6.909	1.15	9.399	4.925
CA1	7.483	1.55	11.32	5.43
CA2	7.17	1.10	11.32	5.43
<b>4.9</b>	9.8	2.65	17.68	6.671
<b>4.10</b>	9.546	2.86	18.208	6.704

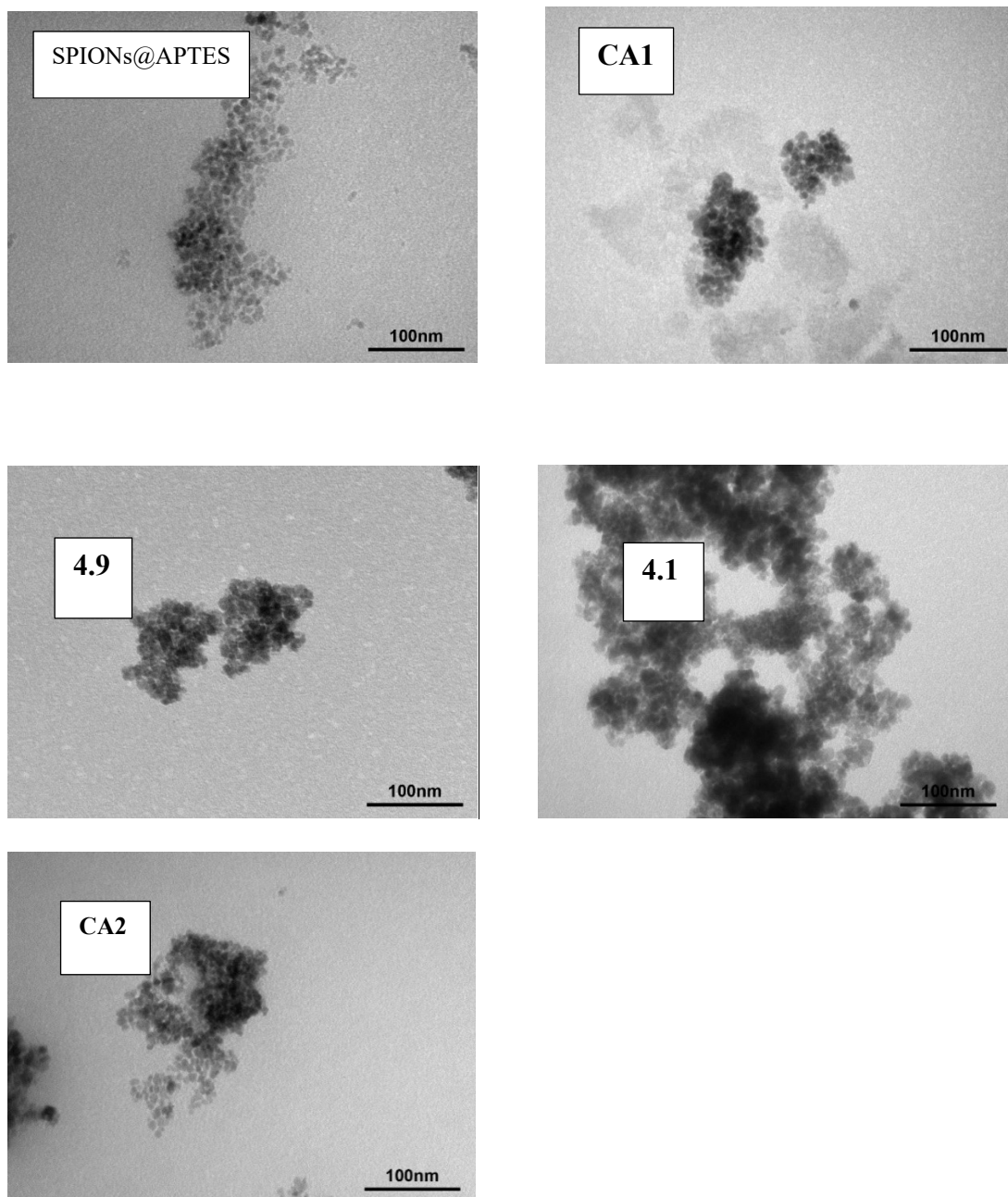


**Figure 4.23: Transmission electron microscopy for SPIONs@APTES, CA1, 4.9, 4.10 and CA2. The scale bar on the bottom right of each image corresponds to 100 nm.**

#### 4.6.6 Optical properties

##### 4.6.6.1 UV-Vis absorption spectroscopy

###### 4.6.6.1.1 UV-Vis absorption spectroscopy of CA1, CA2

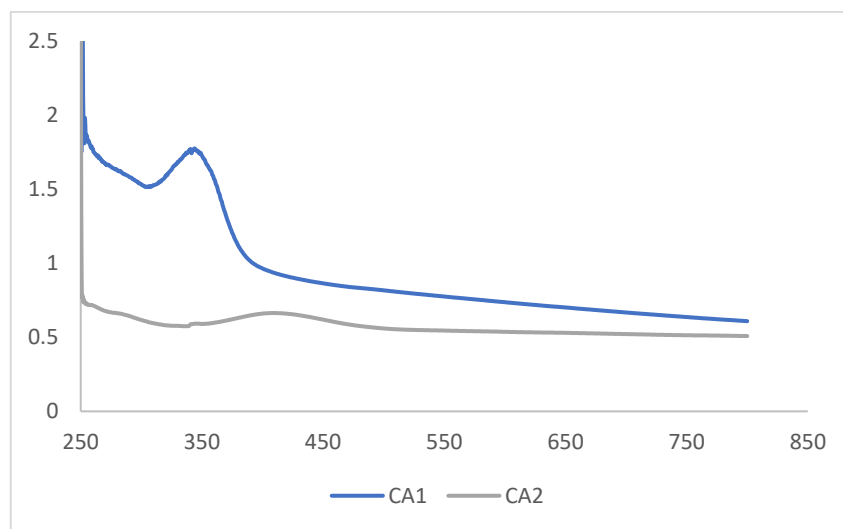


**Figure 4.24: UV-vis absorption spectra of CA1 and CA2**

The UV-vis absorption spectra were recorded in dilute acetic acid solution. For CA1, a characteristic absorption maximum ( $\lambda_{\text{max}}$ ) appeared at  $\sim 345\text{nm}$ , which is close to values reported for similar fluorescent, naphthalic anhydride-derived imides.<sup>77</sup> This value corresponds to an internal charge transfer (ICT) state arising from the  $\pi\text{-}\pi^*$  electron transfer (**Fig 4.24**).

CA2 showed a peak at  $\sim 400\text{ nm}$ , suggesting the presence of morpholine substituents on the 1,8-naphthalimide (**Fig 4.24**). This value is similar to the value reported for the other morpholine substituted naphthalimide dyes.<sup>78</sup> While an aqueous solution of CA1 was highly emissive, solutions of CA2 were found not to be fluorescent under UV lamp by the naked eye. While the excitation source may not be ideally tuned to the chromophore, it does perhaps

suggest that this lower energy luminescence is quenched by the iron oxide with its broad energy absorption band.

#### 4.6.6.1.2 UV-Vis absorption spectroscopy of 4.9, 4.10

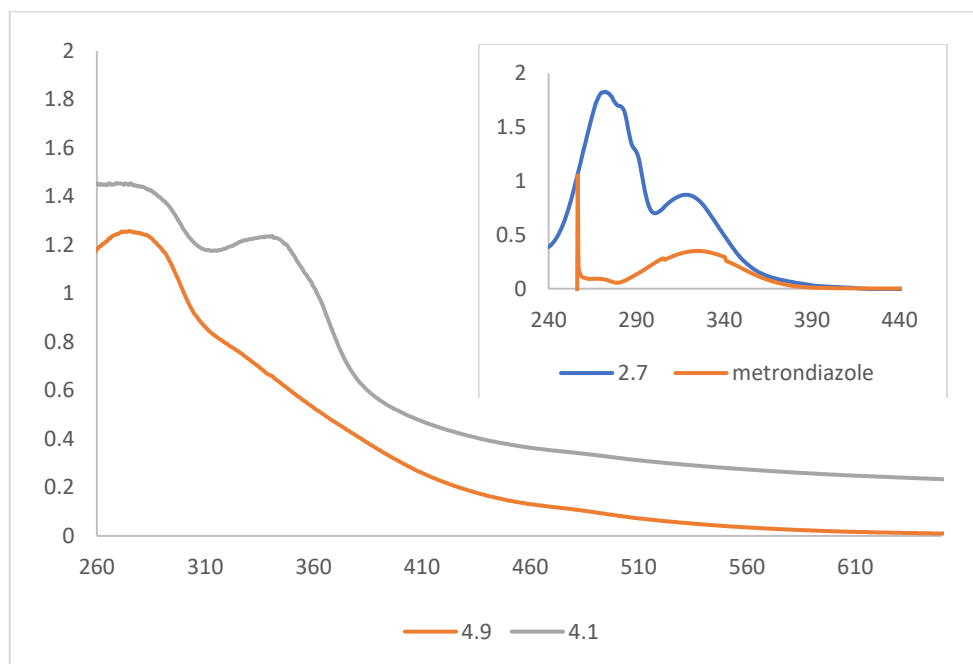


**Figure 4.25: UV-vis absorption spectra of 4.9 and 4.10. Inset shows the UV-vis absorption spectrum of metronidazole in DMSO at  $8.5 \times 10^{-6}$  M and 2.7 in DCM at  $1.3 \times 10^{-5}$  M**

As seen in **Fig 4.25**, inset, the UV-vis spectrum of metronidazole displays one peak at 325 nm. The same peak was seen in **2.7** which is in a good agreement with that of metronidazole. In addition, there is an intense peak was observed at 275 nm that perhaps is corresponded to the benzaldehyde fragment of **2.7**. This absorption was also seen in **4.9** and **4.10** in addition to the broad peak of SPIONs. However, the other the peak of metronidazole moiety could be hidden underneath the broad peak of SPIONs. Further peak was observed at 345 nm of **4.10** which confirms the existence of naphthalimide moieties in these nanoparticles.

#### 4.6.6.1.3 UV-Vis absorption spectroscopy of 4.12, 4.13

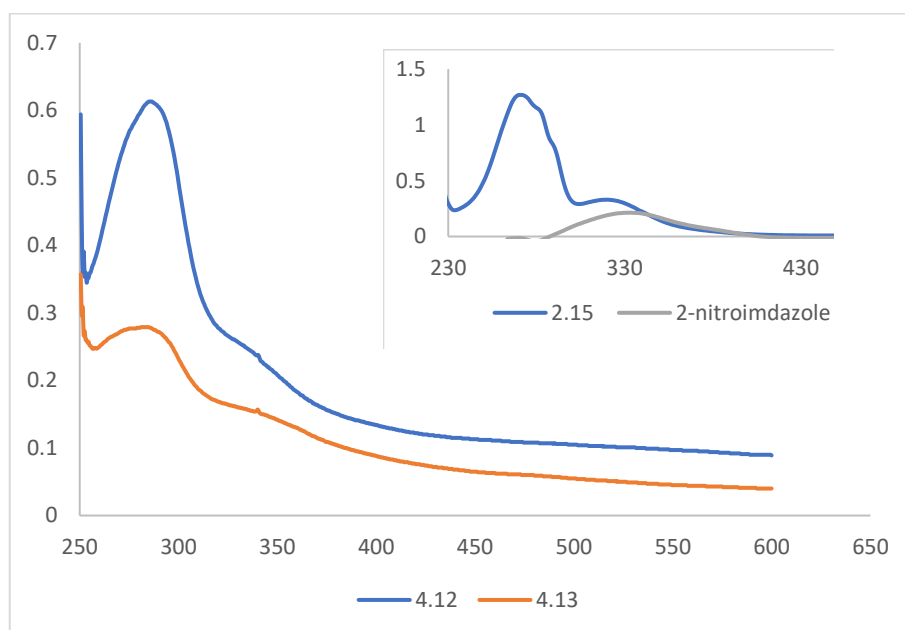


**Figure 4.26 :** UV-vis absorption spectra of 4.12 and 4.13. Inset shows the UV-vis absorption spectrum of 2-nitroimidazole in DMSO at  $5.6 \times 10^{-6}$  M and 2.15 in DCM at  $1.3 \times 10^{-5}$  M

2-Nitroimidazole has a peak at  $\sim 331$  nm while **2.15** shows two peaks; one at  $\sim 327$  nm which is corresponding to 2-nitroimidazole and an additional peak at  $\sim 273$  (Fig 4.26. inset) nm which perhaps corresponds to an internal charge transfer (ICT) state arising from the  $n-\pi^*$  and  $\pi-\pi^*$  electron transfer of benzaldehyde ring of **2.15**.

The solution state absorption spectra of **4.12** and **4.13** were recorded as acetic acid solutions. Both compounds showed a distinguishing absorption maximum ( $\lambda$  max), which appeared at  $\sim 285$  nm. There is an additional broad peak was displayed at 377 nm of **4.12** corresponds to 2-nitroimidazole moiety. This value cannot be seen in **4.14** as it is absorbed almost in the same region of the wavelength of naphthylamide. A weaker absorption was also observed at 345 nm of **4.13** consistent with the presence of naphthalimide group (Fig 4.26).

CA1, **4.10** and **4.13** have very similar UV-vis spectra exhibiting a peak at approximately 345 nm, which is similar to that previously reported for naphthalic anhydride-derived imides.<sup>77</sup>

#### 4.6.6.2 Luminescence spectroscopy

##### 4.6.6.2.1 Luminescence spectroscopy of CA1

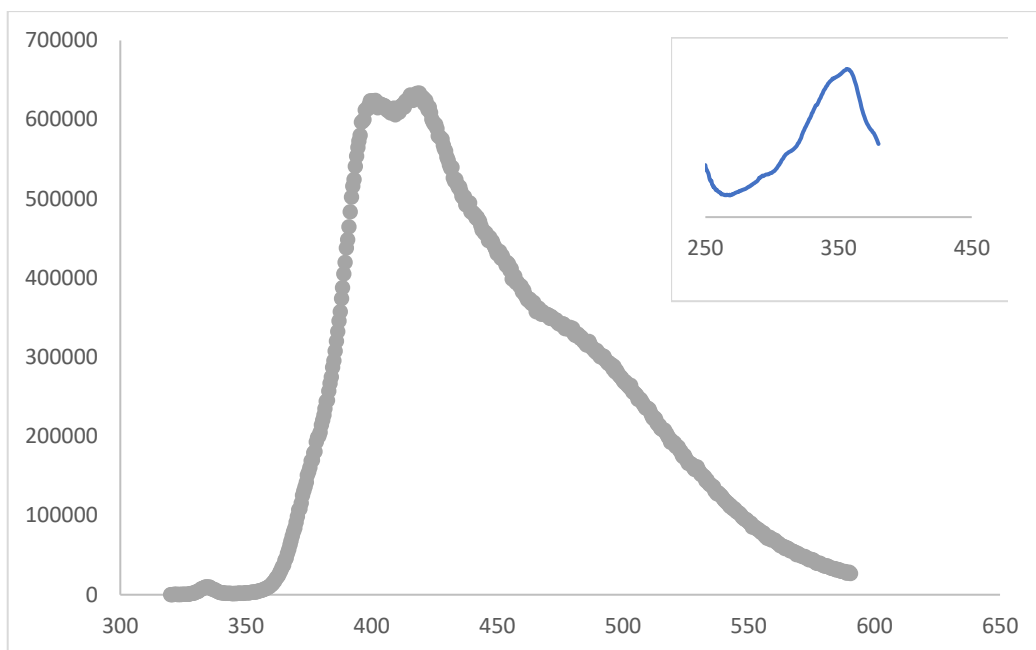


**Figure 4.27: Luminescence spectra for CA1, inset shows excitation spectra of CA1**

A luminescent spectrum was recorded for the excitation and emission of CA1. The excitation and emission wavelengths of CA1 were found to be 356 and 400 nm, respectively, which is close to values reported for similar fluorescents (Fig 4.27).<sup>77</sup> The excitation wavelength is in good agreement with the maxima observed in the electronic absorption spectrum. The lifetime recorded for CA1 was 2.3 ns.

#### 4.6.6.2.2 Luminescence spectroscopy of CA2

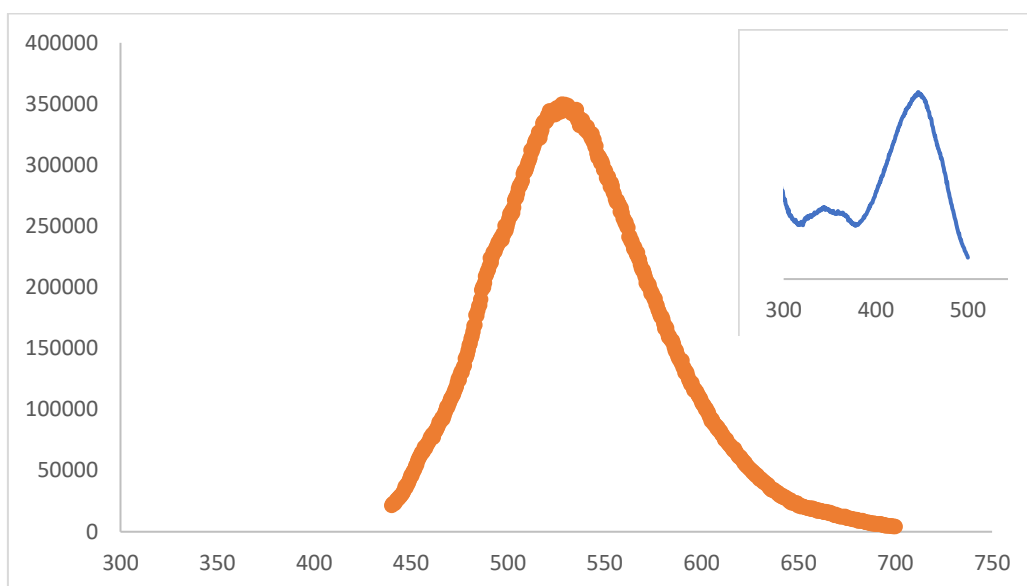


**Figure 4.28: Luminescence spectra for CA2, inset shows excitation spectra of CA2**

**CA2** revealed a visible emission band peaking at 563 nm, which is assigned to naphthalimide functionalised with morpholine (**Fig 4.28**). The corresponding excitation spectra gave a maxima at 446 nm, which was slightly higher than the maxima observed in the UV-vis spectrum (**Fig 4.28, inset**).<sup>78</sup> The lifetime recorded for CA2 was very low (less than 1 ns) (Table 2).

#### 4.6.6.2.3 Luminescence spectroscopy of 4.10

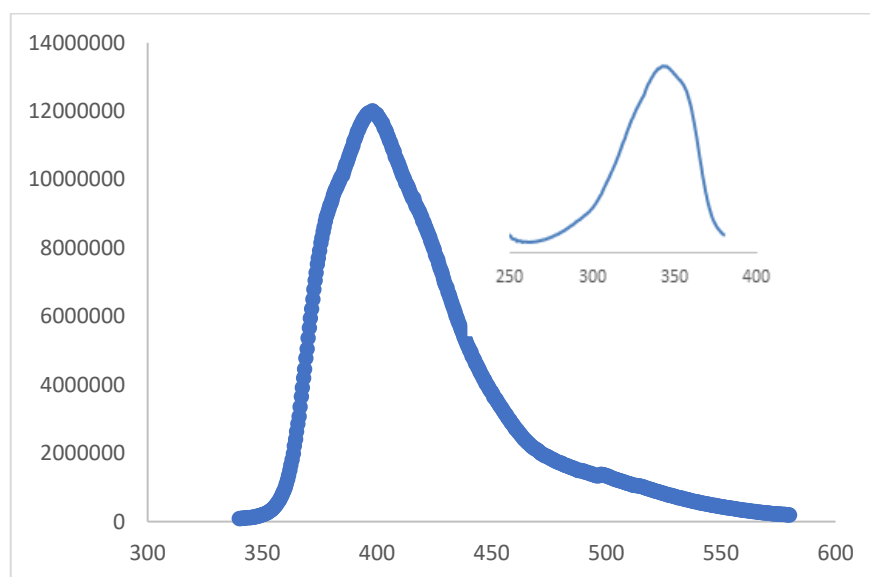


**Figure 4.29: Luminescence spectroscopy of 4.10, inset shows excitation spectra of 4.10**

Luminescence measurement of **4.10** was carried out on acetic acid solutions and the compound was found to be emissive. Similar to the CA1, there was a maxima at 400 nm, which is again in good agreement with literature examples (**Fig 4.29**). The corresponding excitation spectra gave a maxima at 345 nm, which was also in a good agreement with the maxima observed in the UV-vis spectrum (**Fig 4.29, inset**).<sup>77</sup> Time-resolved luminescence data was also recorded and showed lifetimes of 2.1 ns (**Table 2**).

#### 4.6.6.2.4 Luminescence spectroscopy of 4.13

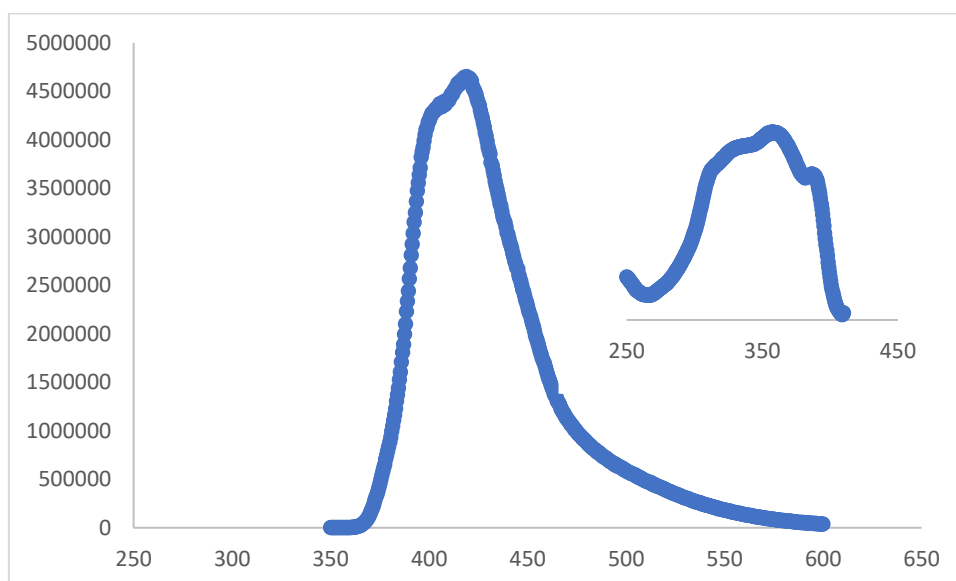


**Figure 4.30: Luminescence spectroscopy of 4.13, inset shows excitation spectra of 4.13**

Luminescence spectra was obtained by excitation at 345 nm, **4.13** displayed an emission band at 404 nm, with a lower energy shoulder at 420 nm (**Fig 4.30**). The corresponding excitation data exhibited a band between 311-388 nm (**Fig 4.30, inset**), which is in close agreement with observations from the UV-vis studies. With excitation of 345 nm and detection at about 400 nm, time-resolved lifetime measurements recorded exponential lifetimes 1.7 ns and 3.6 ns (78%).

**Table 10: Luminescence properties of CA1, CA2, 4.10 and 4.13**

Compound	$\lambda_{exc}/$ nm	$\lambda_{em}/$ nm	Stokes shift ( $\text{cm}^{-1}$ )	t/ns
CA1	356	400	3089	2.3
CA2	446	563	4659	1
4.10	345	400	3985	2.1
4.13	345	404	4233	1.7, 3.6

According to the luminescence properties of these nanoparticles, as shown in Table 10, there is a similarity in the excitation, emission and Stokes shift values for the nanoparticles, which involved the naphthalimide moiety. The CA2, which contains the naphthalimide functionalised with morpholine, had significantly higher excitation and emission values and higher Stokes shift values. However, in CA2, the lifetime was slightly lower than that of CA1, **4.10** and **4.13**.

#### **4.6.7 Inductively coupled plasma atomic emission spectroscopy (ICP-AES)**

##### **4.6.7.1 MP-AES Analysis of Cu<sup>+2</sup> Incorporation**

Here, we looked at the incorporation of Cu<sup>+2</sup> ion for the potential preparation of a dual modality imaging agent. <sup>64</sup>Cu is a PET isotope that can be produced in a cyclotron and is be used later in this research.

Atomic emission spectroscopy has been used to quantify the incorporation of Cu into the CA1 nanoparticles. The samples were injected into plasma and the intensity measured at a number of wavelengths specific to Cu. The wavelengths used for measurement were 324.754 and 377.395 nm. The intensity at each of these wavelengths was measured for four calibration solutions 1 ppm, 2 ppm, 5 ppm and 10 ppm to generate calibration plots for these solutions of unknown concentration (Table 11). However, the values obtained for the samples of these two wavelengths were very close. For this reason, we took the average of both wavelengths and the rest of the experiment was performed accordingly.

**Table 11: Standard Cu<sup>2+</sup> solutions**

<b>Standard solution of Cu<sup>2+</sup></b>	<b>Cu (count) 324.754 nm (C/S)</b>	<b>Cu 377.395 nm (C/S)</b>
<b>1 ppm</b>	175669	85289
<b>2 ppm</b>	311404	150031
<b>5 ppm</b>	814644	394984
<b>10 ppm</b>	1553366	759533

Preparation of the samples was carried out as follows:

Sample 1: 10 ml of 1 ppm Cu<sup>+2</sup> was added to **CA1** (20 mg)

Sample 2: 10 ml of 2 ppm Cu<sup>+2</sup> was added to **CA1** (20 mg)

Sample 3: 10 ml of 5 ppm Cu<sup>+2</sup> was added to **CA1** (20 mg)

Sample 4: 10 ml of 10 ppm Cu<sup>+2</sup> was added to **CA1** (20 mg)

Sample 5: 10 ml of 100 ppm Cu<sup>+2</sup> was added to **CA1** (20 mg)

Sample 6: 10 ml of 1 ppm Cu<sup>+2</sup> was added to SPIONs (20 mg). This sample was prepared as a reference for all the other samples.

Then, the reaction mixture was stirred for 16 hours. The nanoparticles were collected using an external magnet and washed with DI H<sub>2</sub>O to remove any unreacted copper ions. The solute of this sample was then collected and 1 ml of this solute was diluted to 100 ml for MP-AES analysis.

For all the previous samples, the nanoparticles were collected and washed with DI H<sub>2</sub>O. The solute was collected (samples 1-6). These samples were then injected into plasma and the intensity was measured at the number of wavelengths specific to Cu. This step was done in order to calculate the concentration of the unreacted copper ions and determine if CA1 is capable of chelating the Cu<sup>+2</sup>. As shown in Table 12, once the unreacted Cu<sup>+2</sup> is counted, the

reacted  $\text{Cu}^{+2}$  can be counted, and consequently, the mole of the EDTA of CA1 can be determined.

**Table 12: The percentage of  $\text{Cu}^{+2}$  which coordinated to the nanoparticle.**

Sample	Mass of CA1 added	Mass of $\text{Cu}^{+2}$ added	Measured [Cu] /ppm	Mass of unbonded $\text{Cu}^{+2}$	Mass $\text{Cu}^{+2}$ bound	% $\text{Cu}^{+2}$ bound
Sample 1	20 mg	0.01 mg	0.961	0.00961 mg	0.00039 mg	0.039%
Sample 2	20 mg	0.02 mg	1.479	0.01479 mg	0.00521 mg	0.51%
Sample 3	20 mg	0.05 mg	4.070	0.0407 mg	0.0093 mg	0.93%
Sample 4	20 mg	0.1 mg	7.554	0.07554 mg	0.02446 mg	2.44%
Sample 5	20 mg	1 mg	0.76	0.076 mg	0.924	92.4%
Sample 6	20 mg of naked SPIONs	0.01 mg	0.007	0.0007	0.0093 mg	0.93%

In conclusion, regarding inductively coupled plasma atomic emission spectroscopy (ICP-AES), it was found that the mass of  $\text{Cu}^{+2}$  coordinated to CA1 cannot be determined by using this technique. This is because  $\text{Cu}^{+2}$  ions can also be chelated by the naked SPIONs, as shown in Table 12.

#### 4.7 Experimental procedures

##### SPIONs synthesis:

SPIONs were synthesised according to the previous literature<sup>79</sup>.  $\text{FeCl}_2$  (0.317, 1.59 mmol) and  $\text{FeCl}_3$  (0.810, 2.9 mmol) were dissolved in 50 ml of degassed and deionised water and stirred for 30 minutes. The water was purged with argon for 20 minutes before addition of the iron salt. Then, ammonium hydroxide (50 ml, 25%) was added rapidly and stirred vigorously for an additional 30 minutes. The nanoparticles were collected using an external magnet, washed

thoroughly with distilled water and dried under vacuum. A black crystal was obtained yield 0.307g; IR:438(vs), 545(vs). 620(vs)cm<sup>-1</sup>.

#### **Coating with APTES:**

The coating procedure was adapted from reported procedures.<sup>80</sup> SPIONs (0.25 g) were sonicated in (20 ml) ethanol/water solution (volume ratio, 1:1) and APTES (2.8 cm<sup>3</sup>) were added to the SPION suspension. The mixture was heated at 70°C for 2 hours and stirring was performed under N<sub>2</sub> atmosphere. Then, the nanoparticles were collected using an external magnet and washed three times with ethanol (10 ml) to remove unreacted APTES and dried under vacuum. The yield was 0.310g; IR: 2901,1107, 1004, 545, 438.

#### **One pot reaction of naphthalimie-edta-APTES@Fe<sub>3</sub>O<sub>4</sub> (CA1):**

n-(2-Aminoethyl)-1,8naphthalimide (0.240 g, 1 mmol) was dissolved in anhydrous DMF (5 ml) and added to the EDTAA solution (0.256 g, 1 mmol) in anhydrous DMF (5 ml) slowly and dropwise for 30 minutes. The reaction mixture was stirred over night at room temperature under N<sub>2</sub>. Then it was added dropwise to a dispersion of APTES-modified SPIONs (0.200 g) in a mixture of the solvents DMF (30ml) and anhydrous ethanol (50ml). The reaction mixture was then stirred and heated at 50 °C for 16 hours under N<sub>2</sub>. The nanoparticles were separated using a magnet and re-dispersed in cold DMF (10 ml) and centrifuged for 20 minutes. The product was collected using a magnet and washed initially with DMF (5ml), and then with distilled water (50 ml). During the washing process, particles were re-dispersed by a sonication and separated by an external magnet (5 times) so that nonmagnetic impurities could be removed. The resulting nanoparticles were dried in the vacuum line and obtained as a dark grey powder yield (0.317g). IR: 3315(w), 3010(w), 2820(w), 1698(s), 1643(s), 1600(s),1110(b), 780(s), 553(s), 440(s) cm<sup>-1</sup>; UV-vis 345 nm.

**One pot reaction of morpholine- naphthalimie-edta-APTES@Fe<sub>3</sub>O<sub>4</sub> (CA 2):**

A solution of EDTA bisanhydride (0.256 mg, 1 mmol) in anhydrous DMF (5ml) was added dropwise to a solution of 2-(2-aminoethyl)-6-morpholino-1H-benzo[de]isoquinoline-1,3(2H)-dione (0.325g, 1.00 mmol) in anhydrous DMF (5 ml). The reaction mixture was stirred for 24 hours at room temperature under N<sub>2</sub>. Then it was added dropwise to a dispersion of APTES-modified SPIONs (0.20 g) in a mixture of the solvents DMF (15ml) and anhydrous ethanol (20ml). The reaction mixture was stirred and heated at 50 °C for 16 hours under N<sub>2</sub>. The nanoparticles were separated magnetically and washed initially with DMSO (50 ml), then with distilled water (50 ml). During the washing process, particles were re-dispersed by a sonication and magnetically confined from the solution by placing an external magnet next to the reaction vessel so that any unreacted starting material and nonmagnetic impurities could be removed. The desirable nanoparticles were obtained as brown to black magnetite (yield: 403g). IR:1643(s), 1600(s),1101(s), 553(s), 440(s) cm<sup>-1</sup>; UV-vis 400 nm.

**(E)-1-(4-(2-(2-methyl-5-nitro-1H-imidazol-1-yl)ethoxy)phenyl)-N-(3-(triethoxysilyl)propyl)methanimine, 4.8:**

In a 25 mL round bottom flask fitted with a condenser and a Dean-Stark-trap, a solution of 4-(2-(2-methyl-5-nitro-1H-imidazol-1-yl)ethoxy)benzaldehyde (0.137 g, 0.5 mmol) in toluene (15 mL) was heated to reflux. Then, 3-aminopropyltriethoxysilane (0.110 ml, 0.5 mmol) was added dropwise and the contents were heated under reflux for 16 hours until the completion of water formation (as indicated by the water collected in the trap). Then, the solvent was removed under vacuum to afford the product as a yellow powder yield (273, 91%); <sup>1</sup>H NMR (400-DMSO): 0.6 (3H,t), 1.15 (9H,t),1.65 (2H,t), 3.71(2H,t), 3.8 (6H, m), 4.38 (3H,t), 4.73(3H,t), 6.93 (2H, d), 7.64 (2H,d), 8.04 (s,1H), 8.22 (s, 1H).IR: 1180, 1186, 1305, 1361,

3126(w), 2927(w), 2883(w), 1683(m), 1558(m), 1508(s), 1445(m), 1425(m), 1381(s)  $\text{cm}^{-1}$ .

HR.ESI MS [M+H] calcd for  $[\text{C}_{22}\text{H}_{34}\text{N}_4\text{O}_6\text{Si}] = 479.2326$ . found = 479.2334.

**SPIONs@(E)-1-(4-(2-(2-methyl-5-nitro-1H-imidazol-1-yl)ethoxy)phenyl)-N-(3 (triethoxysilyl)propyl)methanimine, 4.11:**

SPIONs (0.50 g) and (E)-1-(4-(2-(2-methyl-5-nitro-1H-imidazol-1-yl)ethoxy)phenyl)-N-(3-(triethoxysilyl)propyl)methanimine (0.170 g) were dispersed in ETOH (5 ml). The reaction mixture was refluxed for 14 hours and the resulting nanoparticles were collected using a magnet and washed with ethanol (30 ml) to remove any excess (E)-1-(4-(2-(2-methyl-5-nitro-1H-imidazol-1-yl)ethoxy)phenyl)-N-(3 (triethoxysilyl)propyl)methanimine. The yield was 0.398g; IR; 2926, 1643, 1604, 1529, 1510, 1464, 1363, 1188, 1008, 580, 443.

**SPIONs@APTES conjugated to 4-(2-(2-nitro-1H-imidazol-1-yl)ethoxy)benzaldehyde, 4.9:**

The mixture of APTES-coated SPIONs (0.200 g) 4-(2-(2-nitro-1H-imidazol-1-yl)ethoxy)benzaldehyde (0.040 g) was dispersed in ETOH (5 ml) and the reaction mixture was refluxed for 14 hours. The resulting nanoparticles were collected using a magnet and washed with chloroform (30 ml) to remove any excess of aldehyde moiety. Yield 0.179g; IR: 3097, 2980, 2883, 1647, 1604, 1533, 1508, 1456, 1363, 1188, 1041, 1001, 642, 578, 434.; UV-vis 279, 325 nm.

**Reaction of 4.9 with 2,2'-((2-((carboxymethyl)(2-((2-(1,3-dioxo-1H-benzo[de]isoquinolin-2(3H)-yl)ethyl)amino)-2-oxoethyl)amino)ethyl)azanediyl)diacetic acid , 4.10:**

n-(2-Aminoethyl)-1,8naphthalimide (0.240 g, 1 mmol) was dissolved in anhydrous DMF (5 ml) and added to the solution of EDTAA (0.256 g, 1 mmol) in anhydrous DMF (5 ml) slowly and dropwise for 30 minutes. The reaction mixture was then stirred over night at room

temperature under N<sub>2</sub>. Then it was added dropwise to a dispersion of **4.9** (130 mg) in a mixture of the solvents DMF (15ml) and anhydrous ethanol (25ml). The reaction mixture was stirred and heated at 50 °C for 16 hours. Then, the nanoparticles were collected using a magnet and washed repeatedly with DMSO and distilled water. The resulting nanoparticles were dried in a vacuum line to obtain a dark brown magnetite yield of (142 g). IR; 3093(w), 2972(w), 2891(w), 1653(s),1635(s), 1541(m),1508(m), 1361(m),1190(m), 1041(m), 1001(m), 642(vs),578(vs), 433(vs) cm<sup>-1</sup>; UV-vis: 279,325, 345 nm.

**(E)-1-(4-(2-(2-nitro-1H-imidazol-1-yl)ethoxy)phenyl)-N-(3-(triethoxysilyl)propyl)methanimine, 4.14:**

In a 25 mL round bottom flask fitted with a condenser and a Dean-Stark-trap, a solution of 4-(2-(2-nitro-1H-imidazol-1-yl)ethoxy)benzaldehyde (0.130 g, 0.5 mmol) in toluene (15 mL) was heated to reflux. Then, 3-aminopropyltriethoxysilane (0.110 ml, 0.5mmol) was added dropwise and the contents were heated under reflux for 16 hours, until the completion of water formation (as indicated by the water collected in the trap). Then, the solvent was removed under vacuum to afford the product as a yellow powder. HRMS calcd for [C<sub>21</sub>H<sub>32</sub>N<sub>4</sub>O<sub>6</sub>Si]: 464.21; found: 465.22.

**SPIONs@(E)-1-(4-(2-(2-nitro-1H-imidazol-1-yl)ethoxy)phenyl)-N-(3-(triethoxysilyl)propyl)methanimine, 4.15:**

(E)-1-(4-(2-(2-nitro-1H-imidazol-1-yl)ethoxy)phenyl)-N-(3-(triethoxysilyl)propyl)methanimine (0.232g, 0.5mmol) in ethanol was added dropwise to SPIONs 0.189 g in ethanol (10 ml). The reaction mixture was refluxed for 14 hours. Then, the coated nanoparticles were collected by an external magnet and washed with DCM to yield

(0.203 g) dark brown nanoparticles; IR: 2924(w), 2854(w), 1600(w), 1361(m), 1249(m), 1006(w), 642(s), 545(vs), 433(vs)cm<sup>-1</sup>.

**Conjugating SPIONS@APTES to 4-(2-(2-nitro-1H-imidazol-1-yl)ethoxy)benzaldehyde,**

**4.12:**

The mixture of APTES-coated SPIONs (0.200 g) and 4-(2-(2-nitro-1H-imidazol-1-yl)ethoxy)benzaldehyde (0.040 g) was dispersed in ETOH (5 ml). The reaction mixture was refluxed for 14 hours. The resulting nanoparticles were collected by a magnet and washed with DCM (30 ml) to remove any excess of aldehyde moiety. The yield was 0.099 g; IR: 3107(w), 2926(w), 1620(s), 1512(m), 1512(m), 1504(m), 1450(m), 1361(m), 1317(m), 1265(m), 1221(w), 1191(w), 1018(w), 661(vs), 578(vs), 433(vs) cm<sup>-1</sup>; UV-vis: 285, 327 nm.

**Reaction of 4.12 with 2,2'-((2-((carboxymethyl)(2-((2-(1,3-dioxo-1H-benzo[de]isoquinolin-2(3H)-yl)ethyl)amino)-2-oxoethyl)amino)ethyl)azanediyl)diacetic acid , 4.13:**

n-(2-Aminoethyl)-1,8naphthalimide (0.240 g, 1 mmol) was dissolved in anhydrous DMF (5 ml) and added to the EDTAA solution (0.256 g, 1 mmol) in anhydrous DMF (5 ml) slowly and dropwise for 30 minutes. The reaction mixture was stirred over night at room temperature under N<sub>2</sub>. Then it was added dropwise to a dispersion of **4.12** (130 mg) in a mixture of the solvents DMF (15ml) and anhydrous ethanol (25ml). The reaction mixture was stirred and heated at 50 °C for 16 hours. Then, the nanoparticles were collected using a magnet and washed repeatedly with DMSO and distilled water. The obtained nanoparticles were dried in the vacuum line to obtain a dark brown magnetite yield (129g); IR: 3018(w), 2927(w), 2852(w), 1693(s), 1662(s), 1578(m), 1518(m), 1456(m), 1390(m), 1340(m), 1188(w), 1064(w), 578(vs), 450(vs) cm<sup>-1</sup>. UV-vis: 285,327, 345 nm.

#### 4.8 References

- 1 R. Weissleder and U. Mahmood, *Radiology*, 2001, **219**, 316–333.
- 2 C. G. Hadjipanayis, H. Jiang, D. W. Roberts and L. Yang, *Semin. Oncol.*, 2011, **38**, 109–118.
- 3 *Med. Phys.*, 2012, **39**, 1152–1153.
- 4 T. Metens, M. Pezzullo, E. Coppens, J. Absil and K. Coenegrachts, in *Reference Module in Biomedical Research*, 2015.
- 5 F. Patriarca, F. Carobolante, E. Zamagni, V. Montefusco, B. Bruno, E. Englaro, C. Nanni, O. Geatti, M. Isola, A. Sperotto, S. Buttignol, R. Stocchi, P. Corradini, M. Cavo and R. Fanin, *Biol. Blood Marrow Transplant.*, 2015, **21**, 1068–1073.
- 6 T. Holly, B. Abbott, M. Al-Mallah, D. Calnon, M. Cohen, F. DiFilippo, E. Ficaro, M. Freeman, R. Hendel, D. Jain, S. Leonard, K. Nichols, D. Polk and P. Soman, *J. Nucl. Cardiol.*, 2010, **17**, 941–973.
- 7 M. A. Toth K, Helm L, *The chemistry of contrast agents in medical magnetic resonance imaging.*, Wiley, Chichester, 2001.
- 8 S. R. Cherry, *Annu. Rev. Biomed. Eng.*, 2006, **8**, 35–62.
- 9 M. P. Melancon, Y. Wang, X. Wen, J. A. Bankson, L. C. Stephens, S. Jasser, J. G. Gelovani, J. N. Myers and C. Li, *Invest. Radiol.*, 2007, **42**, 569–578.
- 10 *Medical imaging : technology and applications*, 2014.
- 11 M. S. Judenhofer, H. F. Wehrl, D. F. Newport, C. Catana, S. B. Siegel, M. Becker, A. Thielscher, M. Kneilling, M. P. Lichy, M. Eichner, K. Klingel, G. Reischl, S. Widmaier, M. Rocken, R. E. Nutt, H.-J. Machulla, K. Uludag, S. R. Cherry, C. D. Claussen and B. J. Pichler, *Nat Med*, 2008, **14**, 459–465.
- 12 H. Young, R. Baum, U. Cremerius, K. Herholz, O. Hoekstra, A. A. Lammertsma, J. Pruim and P. Price, *Eur. J. Cancer*, 1999, **35**, 1773–1782.
- 13 M. S. Judenhofer, C. Catana, B. K. Swann, S. B. Siegel, W.-I. Jung, R. E. Nutt, S. R. Cherry, C. D. Claussen and B. J. Pichler, *Radiology*, 2007, **244**, 807–814.
- 14 A. Louie, *Chem. Rev.*, 2010, **110**, 3146–3195.
- 15 P. W. (Peter W. Atkins, *Atkins' physical chemistry*, Eleventh edition., 2017.
- 16 A. Farzadnia, F. Faeghi and S. Shanehsazzadeh, *Appl. Magn. Reson.*, 2017, **48**, 597–607.
- 17 Y. Jun, J. W. Seo and A. Cheon, *Acc. Chem. Res.*, 2008, **41**, 179–189.
- 18 P. Caravan, J. J. Ellison, T. J. McMurry and R. B. Lauffer, *Chem. Rev.*, 1999, **99**, 2293.
- 19 A. S. Boyd, J. A. Zic and J. L. Abraham, *J. Am. Acad. Dermatol.*, 2007, **56**, 27–30.
- 20 A. Lu, E. L. Salabas and F. Schüth, *Angew. Chemie Int. Ed.*, 2007, **46**, 1222–1244.
- 21 A. S. Teja and P.-Y. Koh, *Prog. Cryst. Growth Charact. Mater.*, 2009, **55**, 22–45.
- 22 B. Bonnemain, *J. Drug Target.*, 1998, **6**, 167–174.
- 23 A. F. Orchard, *Magnetochemistry*, Oxford University Press, Oxford, 2003.
- 24 J. Frenkel and J. Doefmam, *Nature*, 1930, **126**, 274.
- 25 C. P. Bean and J. D. Livingston, *J. Appl. Phys.*, 1959, **30**, 5120–5129.
- 26 M. D. Bartholomä, A. S. Louie, J. F. Valliant and J. Zubieta, *Chem. Rev.*, 2010, **110**,

- 2903–2920.
- 27 T. J. Wadas, E. H. Wong, G. R. Weisman and C. J. Anderson, *Chem. Rev.*, 2010, **110**, 2858–2902.
- 28 W. A. Volkert, *Nucl. Med. Biol.*, 2003, **30**, 791.
- 29 A. Obata, E. Yoshimi, A. Waki, J. S. Lewis, N. Oyama, M. J. Welch, H. Saji, Y. Yonekura and Y. Fujibayashi, *Ann. Nucl. Med.*, 2001, **15**, 499–504.
- 30 N. A. Spaldin, Ed., in *Magnetic Materials: Fundamentals and Applications*, Cambridge University Press, Cambridge, 2nd edn., 2010, pp. 48–64.
- 31 M. Mahmoudi, S. Sant, B. Wang, S. Laurent and T. Sen, *Adv. Drug Deliv. Rev.*, 2011, **63**, 24–46.
- 32 A. B. Chin and I. I. Yaacob, *J. Mater. Process. Technol.*, 2007, **191**, 235–237.
- 33 Y. Lu, Y. Yin, B. T. Mayers and Y. Xia, *Nano Lett.*, 2002, **2**, 183–186.
- 34 E. H. Kim, H. S. Lee, B. K. Kwak and B.-K. Kim, *J. Magn. Magn. Mater.*, 2005, **289**, 328–330.
- 35 J. Wan, X. Chen, Z. Wang, X. Yang and Y. Qian, *J. Cryst. Growth*, 2005, **276**, 571–576.
- 36 M. Kimata, D. Nakagawa and M. Hasegawa, *Powder Technol.*, 2003, **132**, 112–118.
- 37 G. Salazar-Alvarez, M. Muhammed and A. A. Zagorodni, *Chem. Eng. Sci.*, 2006, **61**, 4625–4633.
- 38 S. Basak, D.-R. Chen and P. Biswas, *Chem. Eng. Sci.*, 2007, **62**, 1263–1268.
- 39 I. Martínez-Mera, M. E. Espinosa-Pesqueira, R. Pérez-Hernández and J. Arenas-Alatorre, *Mater. Lett.*, 2007, **61**, 4447–4451.
- 40 A. C. Nunes and Z.-C. Yu, *J. Magn. Magn. Mater.*, 1987, **65**, 265–268.
- 41 L. Babes, B. Denizot, G. Tanguy, J. J. Le Jeune and P. Jallet, *J. Colloid Interface Sci.*, 1999, **212**, 474–482.
- 42 S. Thurm and S. Odenbach, *J. Magn. Magn. Mater.*, 2002, **252**, 247–249.
- 43 R. Massart, *Magn. IEEE Trans.*, 1981, **17**, 1247–1248.
- 44 S. Laurent, D. Forge, M. Port, A. Roch, C. Robic, L. Vander Elst and R. N. Muller, *Chem. Rev.*, 2008, **108**, 2064–2110.
- 45 E. J. W. Verwey, *J. Phys. Colloid Chem.*, 1947, **51**, 631–636.
- 46 R.-Y. Hong, J.-H. Li, S.-Z. Zhang, H.-Z. Li, Y. Zheng, J.-M. Ding and D.-G. Wei, *Appl. Surf. Sci.*, 2009, **255**, 3485–3492.
- 47 N. M. Griбанov, E. E. Bibik, O. V Buzunov and V. N. Naumov, *J. Magn. Magn. Mater.*, 1990, **85**, 7–10.
- 48 S. Mornet, S. Vasseur, F. Grasset, P. Veverka, G. Goglio, A. Demourgues, J. Portier, E. Pollert and E. Duguet, *Prog. Solid State Chem.*, 2006, **34**, 237–247.
- 49 B. Derjaguin and L. Landau, *Prog. Surf. Sci.*, 1993, **43**, 30–59.
- 50 M. Baalousha, *Sci. Total Environ.*, 2009, **407**, 2093–2101.
- 51 H. Unterweger, L. Dézsi, J. Matuszak, C. Janko, M. Poettler, J. Jordan, T. Bäuerle, J. Szebeni, T. Fey, A. R. Boccaccini, C. Alexiou and I. Cicha, *Int. J. Nanomedicine*, 2018, **13**, 1899–1915.
- 52 Y. C. Park, J. B. Smith, T. Pham, R. D. Whitaker, C. A. Sucato, J. A. Hamilton, E. Bartolak-Suki and J. Y. Wong, *Colloids Surfaces B Biointerfaces*, 2014, **119**, 106–114.

- 53 J.-H. Kim, K. Park, H. Y. Nam, S. Lee, K. Kim and I. C. Kwon, *Prog. Polym. Sci.*, 2007, **32**, 1031–1053.
- 54 M. Muthiah, I.-K. Park and C.-S. Cho, *Biotechnol. Adv.*, 2013, **31**, 1224–1236.
- 55 D. Portet, B. Denizot, T. E. Rump, J.-J. Lejeune and P. Jallet, *J. Colloid Interface Sci.*, 2001, **238**, 37–42.
- 56 R. M. Cornell, *The iron oxides : structure, properties, reactions, occurrences, and uses*, Wiley-VCH, Weinheim, 2nd, compl edn., 2003.
- 57 L. Zhang, R. He and H.-C. Gu, *Appl. Surf. Sci.*, 2006, **253**, 2611–2617.
- 58 Y. Sahoo, H. Pizem, T. Fried, D. Golodnitsky, L. Burstein, C. N. Sukenik and G. Markovich, *Langmuir*, 2001, **17**, 7907–7911.
- 59 C. Sun, J. S. H. Lee and M. Zhang, *Adv. Drug Deliv. Rev.*, 2008, **60**, 1252–1265.
- 60 Y. Zhang, N. Kohler and M. Zhang, *Biomaterials*, 2002, **23**, 1553–1561.
- 61 B. K. Sodipo and A. A. Aziz, in *ISESCO Conference on Nanomaterials and Applications 2012*, Trans Tech Publications, 2013, vol. 756, pp. 74–79.
- 62 K. Woo, J. Hong and J.-P. Ahn, *J. Magn. Magn. Mater.*, 2005, **293**, 177–181.
- 63 M. Yamaura, R. L. Camilo, L. C. Sampaio, M. A. Macêdo, M. Nakamura and H. E. Toma, *J. Magn. Magn. Mater.*, 2004, **279**, 210–217.
- 64 K. Can, M. Ozmen and M. Ersoz, *Colloids Surfaces B Biointerfaces*, 2009, **71**, 154–159.
- 65 M. Saeed, M. F. Wendland, M. Engelbrecht, H. Sakuma and C. B. Higgins, *Eur. Radiol.*, 1998, **8**, 1047–1053.
- 66 J. W. M. Bulte, R. A. Brooks, B. M. Moskowitz, L. H. Bryant and J. A. Frank, *Magn. Reson. Med.*, 1999, **42**, 379–384.
- 67 J. W. M. Bulte and D. L. Kraitchman, *NMR Biomed.*, 2004, **17**, 484–499.
- 68 Z. Nemati, S. M. Salili, J. Alonso, A. Ataie, R. Das, M. H. Phan and H. Srikanth, *J. Alloys Compd.*, 2017, **714**, 709–714.
- 69 D. K. Chatterjee, P. Diagaradjane and S. Krishnan, *Ther. Deliv.*, 2011, **2**, 1001–1014.
- 70 D. L. J. Thorek, D. Ulmert, N.-F. M. Diop, M. E. Lupu, M. G. Doran, R. Huang, D. S. Abou, S. M. Larson and J. Grimm, *Nat. Commun.*, 2014, **5**, 3097.
- 71 H.-Y. Lee, Z. Li, K. Chen, A. R. Hsu, C. Xu, J. Xie, S. Sun and X. Chen, *J. Nucl. Med.*, 2008, **49**, 1371–1379.
- 72 D. Patel, A. Kell, B. Simard, J. Deng, B. Xiang, H.-Y. Lin, M. Gruwel and G. Tian, *Biomaterials*, 2010, **31**, 2866–2873.
- 73 A. P. de Silva, *J. Phys. Chem. Lett.*, 2011, **2**, 2865–2871.
- 74 R. Mutneja, R. Singh, V. Kaur, J. Wagler, S. Fels and E. Kroke, *New J. Chem.*, 2016, **40**, 1640–1648.
- 75 E. W. Dean and D. D. Stark, *J. Ind. Eng. Chem.*, 1920, **12**, 486–490.
- 76 A. L. Smith, *Spectrochim. Acta*, 1960, **16**, 87–105.
- 77 J. Wang, L. Yang, C. Hou and H. Cao, *Org. Biomol. Chem.*, 2012, **10**, 6271–6274.
- 78 L. Song, X.-D. Sun, Y. Ge, Y.-H. Yao, J. Shen, W.-B. Zhang and J.-H. Qian, *Chinese Chem. Lett.*, 2016, **27**, 1776–1780.
- 79 O. Karaagac, H. Kockar, S. Beyaz and T. Tanrisever, *IEEE Trans. Magn.*, 2010, **46**, 3978–3983.

- 80 A. Ebrahimezhad, Y. Ghasemi, S. Rasoul-Amini, J. Barar and S. Davaran, *Colloids Surfaces B Biointerfaces*, 2013, **102**, 534–539.

---

## **CHAPTER 5**

### **Conclusion**

**CHAPTER 5      Conclusion**

In Chapter Two we have reported the successful development of a new synthetic route to prepare a series of fluorescently labelled nitroimidazoles. We have investigated many methods to produce these reagents and it was found that the easiest way was to synthesise molecules conjugated by an imine group. The imine was formed by condensing an aldehyde with a primary amine. Although the resulting reagents are air stable, the stability testing was achieved to investigate how these reagents will cleave hydrolytically. This could be useful for some applications, but it limits the general use of these reagents. We have also investigated the synthesis of fluorescently labelled nitroimidazoles by using an active ester instead of the aldehyde. In this study we found that the reagent was more stable in aqueous solution. While this synthesis was successful for one reaction, the syntheses of other species was not successful as the purification steps of such reaction was problematic and the separation of the impurities by chromatography was also impracticable. For further work, further investigation of conjugation via amide bond formation could be carried out. In particular, the use of coupling reagents such as EDC, EDAC or DCC in conjunction with a carboxylic acid terminated nitroimidazole. These could be reacted with primary amine of a fluorophore, or even metal complex or a nanoparticulate construct.

We have carried out some very preliminary investigations into their use in confocal microscopy imaging using a variety of yeast cells. This was mainly done due to the availability of these cells and the ease in handling them. However, it is known that small molecules diffuse much more slowly through the membrane of a yeast cell compared to animal cells<sup>1</sup> and passive labelling may be more difficult. However, with an extended labelling time, we were able to label yeast cells, with *Schizosaccharomyces Pombe* cells showing the greater tendency to take up the reagents. For further work these compounds should be tested with

animal (tumour) and bacterial (anaerobic) cells under normoxic and hypoxic conditions to evaluate their ability to differentiate oxygen levels within the cells.

In chapter three, two novel ligands based on terpyridine and containing 2- nitroimidazole or metronidazole were successfully synthesised. Structures of the ligands were confirmed by means of  $^1\text{H}$  NMR,  $^{13}\text{C}$  NMR, high resolution mass spectrometry, infrared and UV-vis spectra. The metronidazole based terpyridine,  $\text{L}^1$ , was further characterised by X-ray crystal diffraction. The electrochemical behaviour of the ligands was compared, but this did not show that 2-nitroimidazoles were more readily reduced than 5-nitroimidazole and the voltammograms appear dominated by the redox activity of the terpyridine group. On reflection, the desired electrochemistry of the nitroimidazole is proton coupled and the reactions occur in water. These protons are important in such electrochemical reaction in order to convert the nitro group of imidazole to hydroxyl amine. As the cyclic voltammograms were obtained in non-aqueous conditions, we did not simulate the actual environment for a living cell, and we have done these reactions in organic solvents such as DCM that does not have protons and consequently does not allow the required process. Thus, different electrochemical process has occurred, if any at all. Moreover, these ligands contain terpyridine which are also readily reduced to radical species. Similarities in the CVs of the 2 and 5 nitroimidazole perhaps indicate that it is the activity of the terpyridine that is been observed.

In this chapter, a series of novel Fe(II),Co(II), Ni(II), Pd(II), Cu(II) and Zn(II) complexes of these two ligands was synthesised and fully characterised. The electrochemical behaviour of these complexes was studied using cyclic voltammetry to determine the suitability for their intended application. These complexes could be used potentially as drugs for hypoxia as it has two reducible sites. However further investigation of the electrochemical behaviour must be

done in aqueous solution instead of organic solvent to precisely simulate the actual environment of the human body. In case of copper complexes of both ligands, both PET and SPECT could be used to image tumour hypoxia with markers labelled with  $^{64}\text{Cu}$  and  $^{67}\text{Cu}$ , respectively. Metal complexes of terpy are able to bind nucleic acid to be used as anticancer drugs.<sup>2</sup> Thus for further work, the behaviour of these newly synthesised complexes should be evaluated with (tumour) of preclinical animal models .

In chapter 4, we have developed superparamagnetic iron oxide with a silica coating which contain EDTA and bound to a fluorescent side chain (n-(2-aminoethyl)-1,8 naphthalimide and its derivative) CA1 and CA2. These structures are able to form complexes with  $\text{Cu}^{2+}$  ions which could potentially coordinate with  $^{64}\text{Cu}$ . These nanoparticles will provide a novel class of trimodal imaging agent with MRI, PET and fluorescent allowing *in-vitro* and *in-vivo* cell evaluation. However, after using Inductively coupled plasma atomic emission spectroscopy (ICP-AES) to investigate the copper concentration that have been coordinated with CA1, we found that the naked SPIONs have chelated more copper than CA1. While this is extremely interesting and means that labelling of these SPIONs with  $^{64}\text{Cu}$  should be facile, we will need to evaluate the stability of these complexes *in vivo*, to determine how readily  $\text{Cu(II)}$  is lost from the SPION. In addition, the tendency of the SPION to bond with  $\text{Cu(II)}$  (presumably in the  $\text{Fe}_3\text{O}_4$  core, which is known)<sup>3</sup>, means that assessing the ability of CA1 and CA2 as  $\text{Cu(II)}$  responsive luminescent sensors is very problematic as the  $\text{Cu(II)}$  may preferential interact with the SPION core.

SPIONS containing 2-nitroimidazole or 5-nitroimidazole were reported for the first time in this chapter. Such compounds may have application for hypoxia imaging purpose as an MRI (T2) imaging agent. The synthesis of both samples was successfully achieved and confirmed by infra-red spectrum and UV-vis analysis. Fluorescently labelled (2/5) nitroimidazole

conjugated to SPIONs were successfully synthesised as potential probes for use in MRI (*in vivo*) and luminescence (*in vitro*) to detect hypoxic cells. The photophysical properties of these nanoparticles such as UV-vis and luminescence were investigated. The nanoparticles sizes of these nanoparticles were studied by TEM and it was consistently found that the diameters of the resulting nanoparticles were of the order of 6-9 nm with slightly larger diameters than the starting APTES coated SPIONs.

## 5.1 References

- 1 J. Valdez-Taubas and H. R. B. Pelham, *Curr. Biol.*, 2003, **13**, 1636–1640.
- 2 Z. Naseri, A. N. Kharat, A. Banavand, A. Bakhoda and S. Foroutannejad, *Polyhedron*, 2012, **33**, 396–403.
- 3 X. Yang, J. He, Q. Yang, R. Jiao, G. Liao and D. Wang, *J. Colloid Interface Sci.*, 2019, **551**, 16–25.